The influence of salt walls on deformation band formation and implications for reservoir quality

PHILIP PETER DAVIES

How to cite:

DAVIES, PHILIP PETER (2020) The influence of salt walls on deformation band formation and implications for reservoir quality. Masters thesis, Durham University.

The influence of salt walls on deformation band formation and implications for reservoir quality

By

Philip Peter Davies

Thesis submitted for the Degree of Master of Science by Research

Department of Earth Science
Durham University

2020

Abstract

A significant number of hydrocarbon reservoirs globally are found in sedimentary sequences affected by salt diapirs and salt walls. As a result, the hydrocarbon industry routinely drills near salt walls. Significant stress perturbations arise in this environment due to the rising salt and associated withdrawal imposing an additional load on the adjacent sediments. The strength of these sediments and their response to external loading is a function of their loading history since deposition. It is therefore critical to account for the stress history in those environments close to salt walls where significant additional loading has been imposed by halokinesis. This study investigates the Triassic fluvial sandstones of the Skagerrak Formation, Central Graben, North Sea where deformation bands are frequently observed in wells drilled adjacent to salt walls, focussing on wells 22/29-2S1 and 22/29-3 in the Seagull Field. Well logs, optical microscopy and statistical analysis are utilised to fully appreciate the salt-sediment interaction and improve our understanding of stress changes near salt walls in mini-basins and how these stresses influence the sediments through their early lithification (<500 m) and later physical and chemical diagenesis. Preferential infiltration of meteoric water and clay material along the complex network of dilational shear (disaggregation) bands has resulted in widespread diagenesis in the sediment adjacent to the salt wall, reducing porosity in sandstones at the margin of the mini-basin. Further analysis of the preserved deformation band orientations reveal that the principal stresses changed over time, reflecting irregular lateral and vertical salt wall movements and minor far-field influence (approximately 1000 m away). This study demonstrates the need to consider the implications of early sandstone deformation coupled with diagenetic processes on the long-term reservoir quality of complex HPHT mini-basin sandstones proximal to salt structures.

Table of Contents

Acknowledgements

First and foremost, I would like to thank my supervisors Stuart Jones and Jonathan Imber for their knowledge, support, guidance and immense patience.

To Stephan Stricker for his limitless knowledge on the North Sea sediments and providing solid grounding for the geological background.

To my neighbours in our bay, especially Jack Lee and George Lodwick for providing much needed relief during hard times.

To all in the Earth Science Department, whether staff or student, for providing a welcoming environment during my time in the department.

To ShellShock! Improvised comedy society for always managing to make me laugh.

Huge thanks go to my family for their love, support and encouragement.

And to Honey, grrr, bark, woof, good girl!

Chapter 1. Introduction

1.1 Rationale

Sandstones bodies found in salt provinces serve as useful hydrocarbon reservoirs due to the typically porous nature of the sandstones and stacked, thick sandstone successions (Archer et al., 2012; Banham & Mountney, 2013b). The preservation of the thick sandstone successions is aided by the relatively rapid subsidence into salt-walled mini-basins providing accommodation space for later sediment and reducing the likelihood of sediment erosion prior to lithification. However, interactions at the contact between the rising salt-walls and subsiding sediment may cause small-scale deformation of the rock, leading to degradation of the sandstone quality (McKie et al., 2010; Stricker et al., 2018). As high-production hydrocarbon reservoirs in thicker sedimentary units at the mini-basin centre become depleted and production decreases, future prospects may be located closer to salt walls where the reservoir quality is likely to be poorer than towards the basin centre, due to diagenesis and deformation bands (Stricker et al., 2018). Deformation bands are currently difficult to identify in seismic surveys, and so the best method of confirming the presence of reservoir-compromising deformation bands is drilling and coring exploration wells, a costly and time-consuming procedure (Fossen & Hesthammer, 1998; Dusseault et al., 2004). Understanding the relationship between salt tectonics and early deformation in unconsolidated sediments could yield improved predictions of how sandstones in salt provinces will be impacted by early deformation processes.

Previous research has studied how deformation bands form in unconsolidated sediments (Desrue & Viggiani, 2004), how deformation bands impact the reservoir quality of sandstones (Du Bernard et al., 2002; Fossen et al., 2007; Exner et al., 2013), and how salt structures affect sedimentation and deform those sediments (Alsop et al., 1996; Banham & Mountney, 2013a, b; Nikolinakou et al., 2014; Heidari et al., 2017). However, these findings have not been thoroughly applied to the Skagerrak Formation in the CNS, where deformation features have been identified as negatively impacting reservoir quality, but with no further extensive investigation regarding what caused the formation of these features, how the deformation bands developed over time, the range of influence the salt wall has on sediment deformation, or the wider implications for hydrocarbon reservoirs in other halokinetic provinces (McKie et al., 2010; Stricker et al., 2018). This thesis aims to utilise the findings from the previously mentioned studies in addition to the substantial volume of literature concerning the Skagerrak Formation (Goldsmith et al., 2003; McKie et al., 2010; Archer et al., 2012; Karlo et al., 2014; Stricker et al., 2018) to investigate the mechanics of how the salt walls influenced the formation of the deformation bands, how the deformation features were preserved in the Skagerrak Formation, and how they are able to impact reservoir quality. By investigating the evolution of the deformation bands from their formation to the modern day, consideration of the factors that affect the formation and preservation of deformation bands, and exploring the range of influence the salt wall has on mini-basin sediment deformation, this will allow for the application of the findings from this thesis to aid predictions of reservoir quality in other halokinetic provinces.

1.2 Aim of thesis

The null hypothesis of this thesis is that the abundance of deformation bands increases closer to the salt walls in a salt-walled mini-basin, with a secondary hypothesis being that the orientations of the deformation bands are controlled by the salt wall. These hypotheses assume that the deformation bands directly result from movement of the salt wall and act as records for halokinesis. Testing this will involve investigating the structural and petrophysical properties of the deformation bands to ascertain the timing of formation, and the orientations of the deformation bands will reveal the nature of the palaeostresses imposed on the sediment.

Key areas of investigation are:

1. To use thin section analysis and wireline logs to assess the quality of deformation band-bearing sandstones in close proximity to a salt wall. This considers the formation and evolution of the deformation band over time during burial and diagenesis. Dilation bands are some of the earliest deformation features to form, and are rarely preserved at depth. Light microscopy inspection will reveal how the dilation bands were preserved at depth and the interaction between the deformation band and host rock.
2. How movement of the salt wall would produce deformation bands in adjacent sediments. Deformation bands form as a result of brittle failure caused by stresses and strains imposed on the sediments, with the orientation of the deformation bands being influenced by the orientation and intensity of principal stresses. Therefore, the original stress state imposed on the sediment can be inferred. Analysis of deformation band orientations could therefore be used to reconstruct the flow of salt through the salt wall.
3. To investigate the range of influence that the salt wall has on deformation features on distal sediments (up to 1000 m) away from the salt wall. If deformation bands in wells proximal and distal to the salt wall show similar orientation variations, this would imply an unprecedented range of influence the salt wall has on sediments in a salt-walled mini-basin.
4. To investigate the proliferation of deformation bands in wells adjacent to salt walls. The presence of deformation bands across several mini-basins would show that deformation of sediments adjacent to salt walls is a common occurrence within salt-walled mini-basins.

1.3 Soft sediment deformation

The study of unconsolidated shallow sediments (<500 m burial depth) and their influence during burial is frequently overlooked in the literature concerning deformation structures. This is in part due to the poorly lithified nature of the sediments and that early processes and structures are rarely preserved due to overprinting by later mechanical and chemical compaction. The deformation bands found in the Skagerrak Formation of the Central North Sea (CNS) would require a degree of competence and strength to be formed at depth (e.g. Fossen et al., 2007; McKie et al., 2010). However, structures formed in shallow sediments may have evolved and propagated into more conventional deformation bands at depth, or allowed accumulation of minerals which would aid preservation of the sediment (Du Bernard et al., 2002; Fossen et al., 2007).

1.3.1 Soil mechanics and strain experiments

Unconsolidated sediment near the surface is referred to as soil, and the deformation of soil under strain is termed 'soil mechanics' (Bardet, 1990; Desrues & Viggiani, 2004). Although the sediment has not yet been cemented and compacted to form a lithified rock, unconsolidated sands can still maintain a high enough stress to develop localised shear bands (Bolton, 1986). The point of peak strength of sand, which is usually associated with the maximum rate of dilation, is defined as $(-d\varepsilon_V/d\varepsilon_1)_{max}$ where ε_V is the volumetric strain and ε_1 is the major principal strain (both defined positive in compression). In order to generate dilatancy within the soil, the grain structure would have to be densely packed and the stress imposed on the soil would have to be less than the stress required to fracture the grains (Bolton, 1986). If the grains were not densely packed, the grains would be compacted together, removing some of the pore space. If the stress exceeded the strength of the grains, then there would also be a loss in porosity as the fragments from the fractured grains would cause the soil to become poorly sorted, reducing the pore space between grains.

A series of strain experiments were carried out on drained sand specimens in to investigate how strain localises within unconsolidated sands (for details see Desrues & Viggiani, 2004; Desrues et al., 2007). The method used to monitor the deformation involved stereophotogrammetry, which produces a false three-dimensional representation of the magnitude of deformation. The reason the three-dimensional representation is considered false is because the stereophotograms are taken within a very short time of each other, so the images appear similar with any minor differences indicating movement of the grains. Combining this method with a method for measuring density, and thus the void ratio or pore volume across the sample, allows for the identification of porosity loss or porosity increase within the samples. Findings from the collection of experiments show that shear bands can form in unconsolidated sands at very low confining stresses (100 – 1000 KPa) when an axial stress is applied (Desrues et al., 2007). Other experiments show that higher confining stresses (10 – 60 MPa), also produce shear bands in the unconsolidated sand. Specifically, within the range of confining effective stress (10 and 30 MPa) a few parallel shear bands would form, and higher confining stress ranges (40 – 60 MPa) produced conjugate shear bands (Bésuelle et al., 2000; Desrue et al., 2007). As the mean effective stress increased, the shear band formed at greater axial strains. This adds to the idea that less axial stress is required to shear soils closer to the surface, which would experience smaller mean effective stresses than sediments at greater depths. The stereophotogrammetry method used in these experiments also reveal that as the stress imposed on the sediments increases, the strain 'condenses' and localises into a thin and tabular band (Fig. 1.1). The bottom row of Figure 1.1 illustrates that strong dilatancy is associated with the localisation process (Desrues et al., 2007).

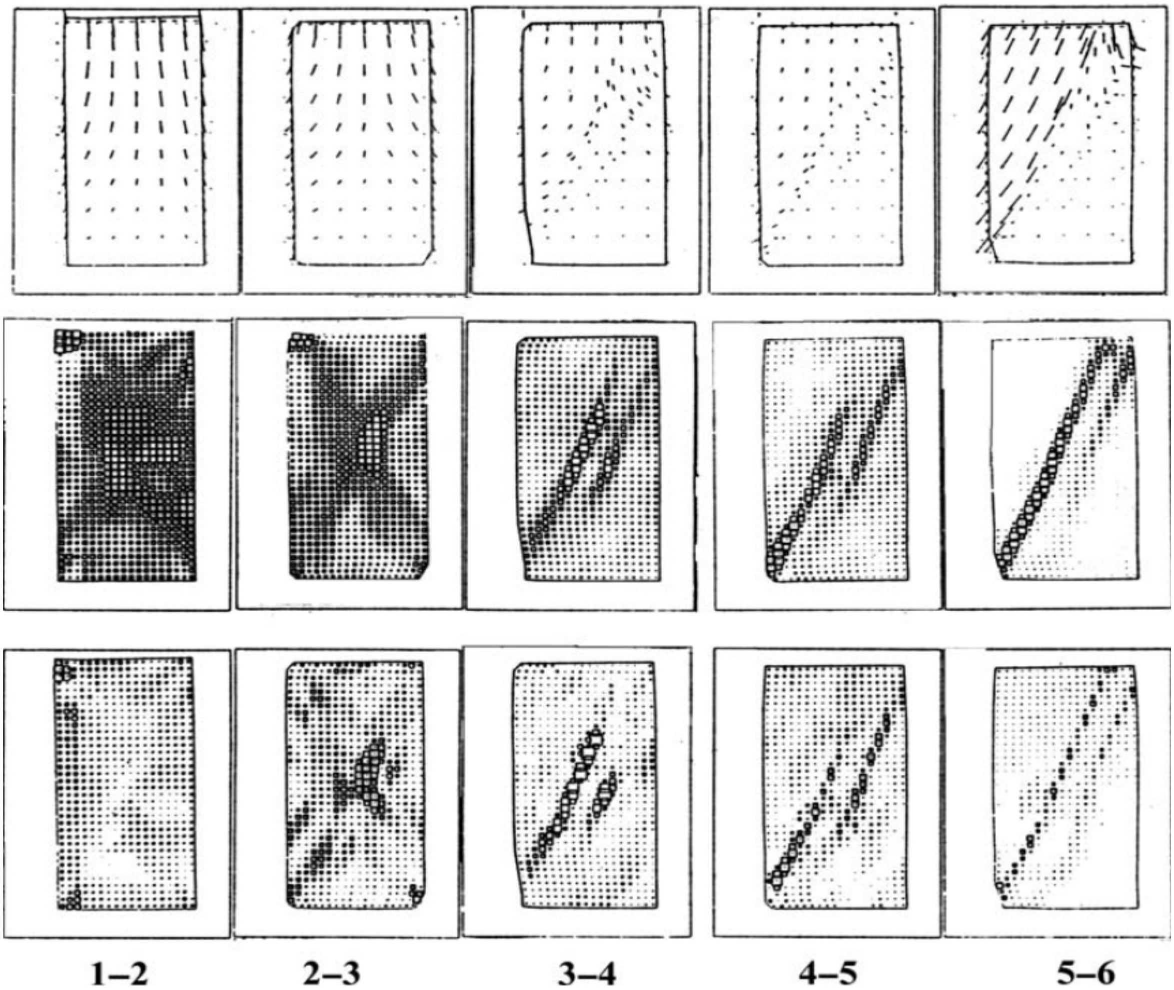

Figure 1.1: Stereophotogrammetric measures of incremental deformation during a soft sediment strain experiment. Numbers specify the deformation increments displayed, such that 2 – 3 is the increment between photographs 2 and 3. Top row shows incremental displacement. Middle row shows the corresponding incremental shear intensity. Bottom row shows volumetric strain. Sizes of symbols are proportional to the value of the scalar quantity being plotted. (From Desrues et al., 2007).

1.3.2 Failure of porous soil

When describing failure of porous sediment samples, a variant of the Mohr circle diagram is used to graphically represent the failure envelope of the sample. This is referred to as the *q*-*p* diagram (Fig. 1.2). The horizontal axis *p* is equal to $\sigma_1 + \sigma_2 + \sigma_3$, identified as the mean stress, rather than the just the normal stress on a particular plane. The vertical axis *q* is reduced to $\sigma_1 - \sigma_3$ from a more complex expression (below) (Schultz & Siddharthan, 2005):

$I_1 = \sigma_1 + \sigma_2 + \sigma_3$,

$I_2 = \sigma_1\sigma_2 + \sigma_2\sigma_3 + \sigma_1\sigma_3$,

$I_3 = \sigma_1\sigma_2\sigma_3$,

$q = \sqrt{I_1^2 - 3I_2}$

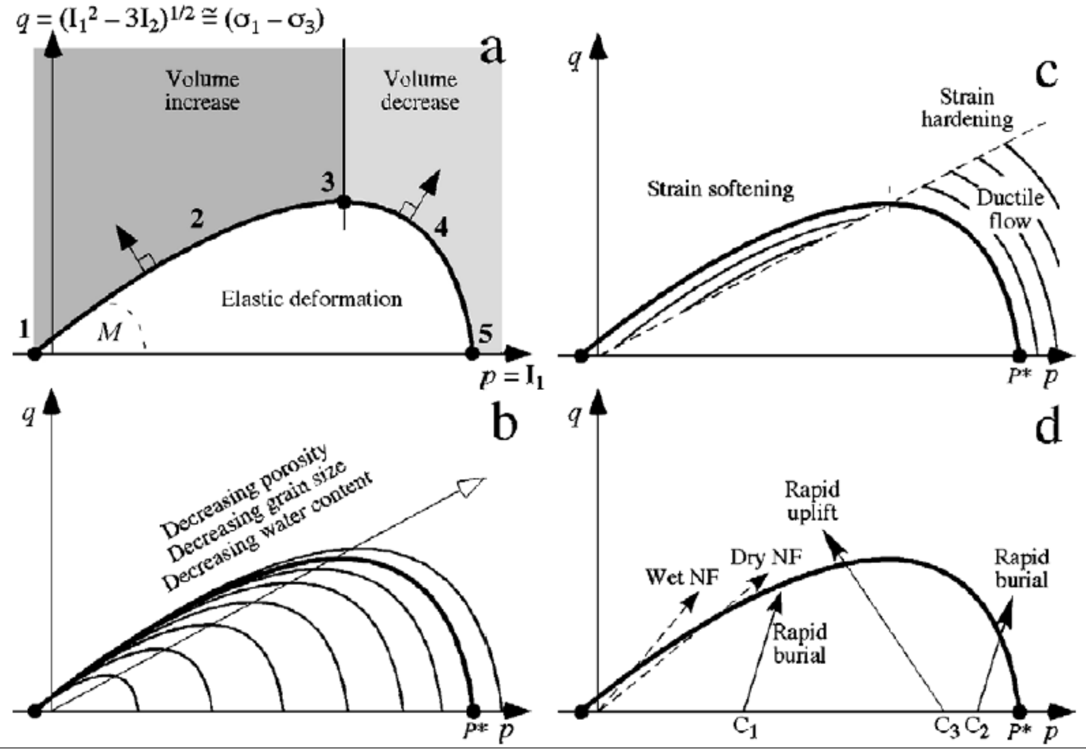

Figure 1.2: Basic elements of the *q*-*p* diagram applied to porous rocks. (a) Yield surface (bold curve) with slope *M* showing approximate regions of deformation band nucleation. (b) Yield surface expands for decreasing host-rock porosity, decreasing average grain size, and/or decreasing water content. *P**, grain crushing pressure. (c) Movement of yield surface is inward toward critical state line (dashed) for strain softening deformation; cap moves outward toward critical state line for strain hardening deformation. (d) Representative loading paths with arrows showing direction of progressive loading. Dashed lines, normal faulting (NF) regime for hydrostatic pore-fluid conditions in the crust (wet NF, $\sigma_1/\sigma_3 = 3$) and anhydrous conditions (dry NF, $\sigma_1/\sigma_3 = 2$); rapid burial, increasing σ_1 from $\sigma_1 = \sigma_2 = \sigma_3$ (initial confining pressure C_3). (From Schultz & Siddharthan, 2005).

The value of *q* is equal to the diameter of the Mohr circle and provides a measure of the shear stress supported in the rock. Stresses applied to the diagram are defined as being effective stresses in order to include the influence of pore fluid pressure when applied to rock strength and failure.

The locus of stress states that separates the elastic (the sediment can fully recover from deformation) from the inelastic yielding regimes is called a “yield surface” (Fig. 1.2). Through experimental and theoretical methods, it has been found that decreasing the porosity, grain size, or water content can cause the yield surface to increase and trend towards the right of the diagram, where the mean stress increases.

1.4 Deformation bands

Soil mechanics described above provides the conditions and processes that produce deformation features in shallowly buried, poorly lithified sediments. Deformation bands (previously referred to as granulation seams) are a general term for localised tabular features which tend to form in porous sandstones or unconsolidated sediments (soils) at relatively shallow depths (<500 m) and low confining pressure, potentially resulting in a minor increase in porosity (disaggregation or dilation) or significant decrease in porosity (compaction or cataclasis) relative to the surrounding sandstone (Aydin, 1978; Pittman, 1981; Antonellini et al., 1994; Shipton & Cowie, 2001; Desrues & Viggiani, 2004; Aydin et al., 2006; Fossen et al., 2007; Fossen & Bale, 2010). The formation and evolution of a deformation band involves a significant amount of grain rotation and translation, and can include grain crushing or merely rotation and frictional sliding along grain boundaries depending on conditions in the sediment, such as grain size, sorting, grain shape, and porosity (Griffiths et al., 2016). This means that deformation bands are typically characterised by prominent reorganisation of the grain framework which can increase or decrease porosity in the deformation band relative to the host rock (Aydin et al., 2006; Fossen et al., 2007; Fossen & Bale, 2008). The enhanced porosity of dilation bands is typically overprinted by compaction of the sediment during burial. However, subsequent emplacement of allogenic or authigenic minerals can further deteriorate the porosity within the deformation band relative to the host rock, and preserve the dilation in the form of a cementation band (Du Bernard et al., 2002; Fossen et al., 2007; Exner et al., 2013; Lommatzsch et al., 2015) (further explored in Section 2.1.3).

1.4.1 Classification of deformation bands

Multiple methods of categorising deformation bands have been proposed, based on the microstructure and localisation characteristics (Antonellini et al., 1994), the kinematic properties of the band (Aydin et al., 2006), or the dominant mechanism that formed the deformation band (Fossen et al., 2007).

1.4.1.1 Classification based on microstructure and localisation

The system that is based on the microstructure and localisation of the deformation band (Antonellini et al., 1994) can be broadly divided into three categories based on if the band i) contains cataclastic material, ii) does not contain cataclastic material, iii) contains clay smearing. These groups can be divided further into subgroups based on volume change in the band, the amount of cataclasis formed during deformation, or the amount of clay mineral within the band (Table 1.1).

Table 1.1: A classification of deformation bands from Antonellini et al. (1994).

Major Groups	**Subgroups**
1. Deformation bands with no cataclasis	1a. Deformation bands with dilatancy
	1b. Deformation bands with no volume change
	1c. Deformation bands with compaction
2. Deformation band with cataclasis	2a. Deformation bands with poorly-developed cataclasis
	2b. Deformation bands with well-developed cataclasis
3. Deformation bands with clay smearing (localised shear zones)	3a. Deformation bands with clay smearing in high porosity (>20%) and low clay content (~ 5-7%) host rocks – with cataclasis
	3b. Deformation bands with clay smearing in low porosity (<15%) and high clay content (~15%) host rocks – with poorly developed cataclasis

1.4.1.2 Classification based on the kinematic properties

The kinematic properties of deformation bands (Aydin et al., 2006) focus on the volume changes within the band indicated by the change in grain framework density by establishing three 'end-members' of deformation (Fig. 1.3). These end-members are compaction (volume decrease), dilation (volume increase), and shear (no volume change). There are very few examples of these pure end-member deformation bands preserved in outcrop, with the majority of the deformation bands being a combination of compaction with a shear component or dilation with a shear component (Du Bernard et al., 2002).

1.4.1.3 Classification based on the dominant deformation mechanism

The most recent way of classifying deformation bands involves using their dominant deformation mechanism (Fossen et al., 2007). These deformation mechanisms include: a) granular flow (disaggregation), b) phyllosilicate smearing, c) cataclasis and d) diagenetic mineral growth (Fig. 1.4). However, it is important to note that the dominant deformation mechanism may change over time, such as a disaggregation band developing into a cataclastic band when buried and reactivated at greater depths. This type of deformation classification system does not consider significant changes to the grain framework density, and most of the deformation mechanisms apply to bands with a component of shear offset.

The various classification methods for describing a deformation band allows for multiple descriptions of the same deformation feature. A disaggregation band in fig. 1.4a can be kinematically described as a dilational or compactional shear band (Fig. 1.3), depending on the volume change during deformation.

Disaggregation bands and dilational bands typically form at shallow depths (< 500 m) due to the low confining pressures, weak grain bindings, and low contact forces between grain surfaces (Bésuelle, 2000; Du Bernard et al., 2002; Fossen et al., 2007). Many early disaggregation bands are related to local, gravity-controlled deformation such as local shale diapirism, underlying salt movement and glaciotectonics (Andersen et al., 2005).

Cataclastic and compactional bands form at greater burial depths where the increased confining pressure produce higher forces at the contacts between grains, promoting grain breakage and cataclasis. Further burial of the cataclastic bands can increase the degree of cataclasis, potentially resulting in cataclastic flow (Fig 1.5). There are occurrences of cataclastic bands forming at shallow depths of burial, but these can be attributed to sudden increases of stress associated with

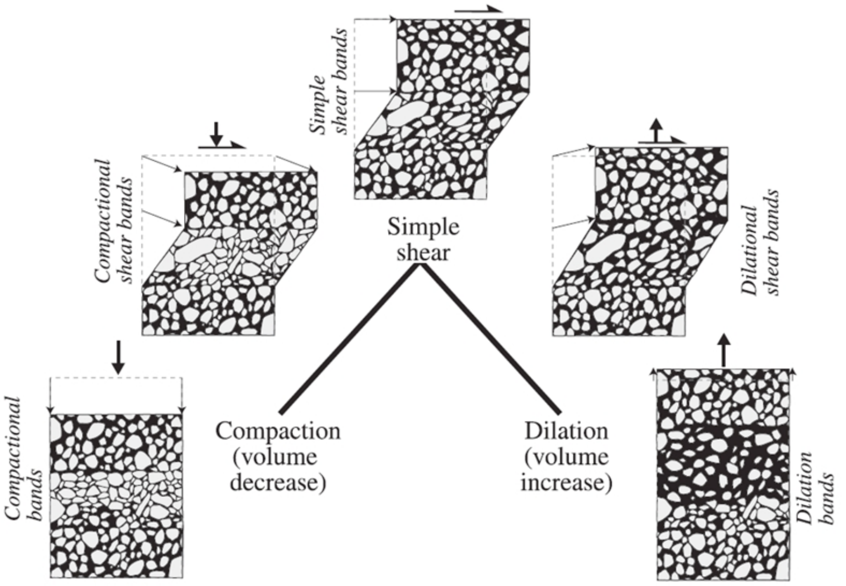

Figure 1.3: Kinematic classification of deformation bands based on Aydin et al. (2006). This study focusses on dilatant shear bands (From Fossen et al., 2007).

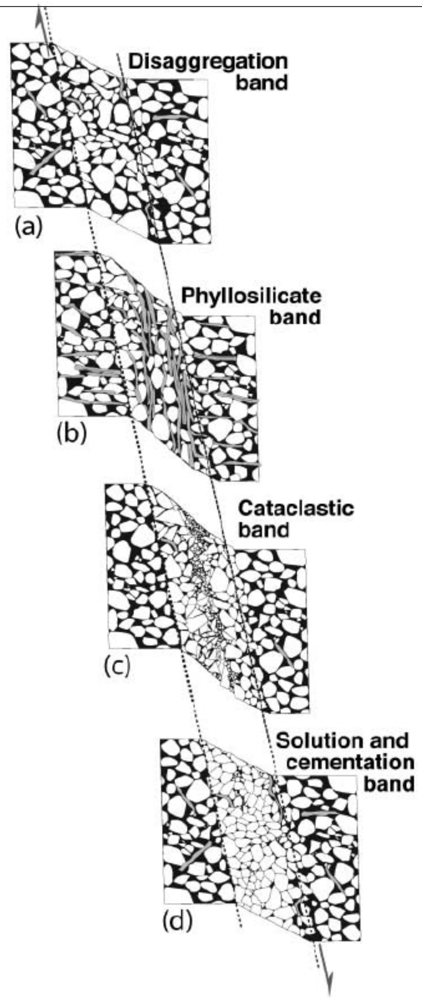

Figure 1.4: Classification of deformation bands based on dominant mechanism. The order of the deformation mechanisms (a – d) indicates the relative depths where these mechanisms would occur. This study focusses on disaggregation bands (From Fossen et al., 2007).

localised earthquakes and other seismic events (e.g. Rosetti et al., 1999; Rawling & Goodwin, 2003; Cashman et al., 2007).

Phyllosilicate band formation is not dependant on burial depth or confining stress and can occur at any burial depths that induce shearing. The main requirement for phyllosilicate band formation is a significant abundance of phyllosilicate minerals within the sediment (exceeding 10-15%) (Fig. 1.5; Fossen et al., 2007).

Solution and cementation bands typically require significant burial or compaction and precursor dilation bands, respectively. The materials required for solution bands are derived from pressure dissolution at grain-grain contacts as compaction bands experience larger stresses at greater depths. Cementation bands form from the preferred authigenic precipitation of minerals (e.g. carbonate, quartz and clay) along a dilation band due to the increased permeability generated by the increased pore space (Figs 1.4 and 1.6; Du Bernard et al., 2002; Exner et al., 2013; Lommatzsch et al., 2015a).

This thesis will refer to the deformation features using the general term deformation bands, but will combine elements of the kinematics of the deformation band (1.4.1.2) and the dominant deformation mechanisms (1.4.1.3) when referring to specific types of deformation features (Aydin et al., 2006; Fossen et al., 2007).

1.4.2 Factors which influence deformation band formation

The initiation and development of deformation bands can be influenced by many factors. This includes mineralogy, grain size, porosity, sorting, cementation, and stress fields. Griffiths et al. (2016) investigated the lithological controls on deformation band formation in the Triassic Sherwood sandstone, focussing on the link between host rock properties and the deformation bands formed. This study found that rocks with higher amounts of feldspars formed cataclastic bands more easily than bands with a lower abundance of feldspar grains. This is thought to be due to the relative weakness of feldspars compared to quartz grains, which would therefore fracture at lower differential stresses (Griffiths et al., 2016). Time can also be considered a factor for deformation band development due to the previously mentioned stress fields changing as the product of fluctuating burial depths and tectonic environments as well as the introduction of diagenetic cementation (Figs. 1.5 & 1.6) (Fossen et al., 2007). These factors and their impact on reservoir sandstone quality will be explored further in section 2.1.

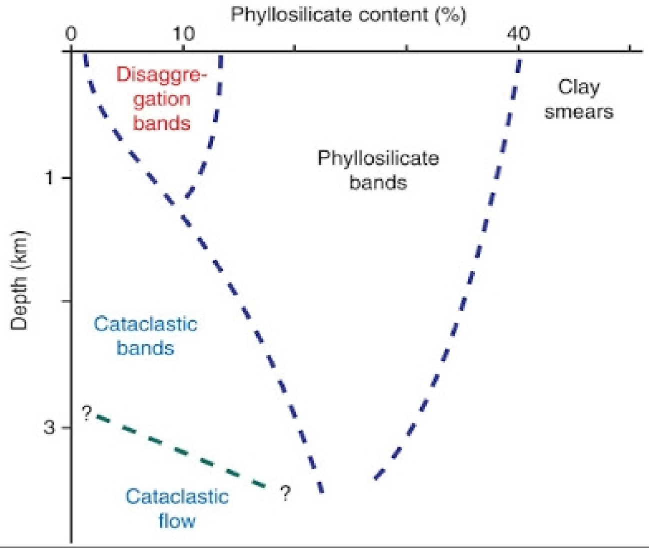

Figure 1.5: Diagram showing the likely conditions under which different types of deformation bands would form. The two factors considered here are depth (km) and phyllosilicate content (% abundance). (From Fossen et al., 2007).

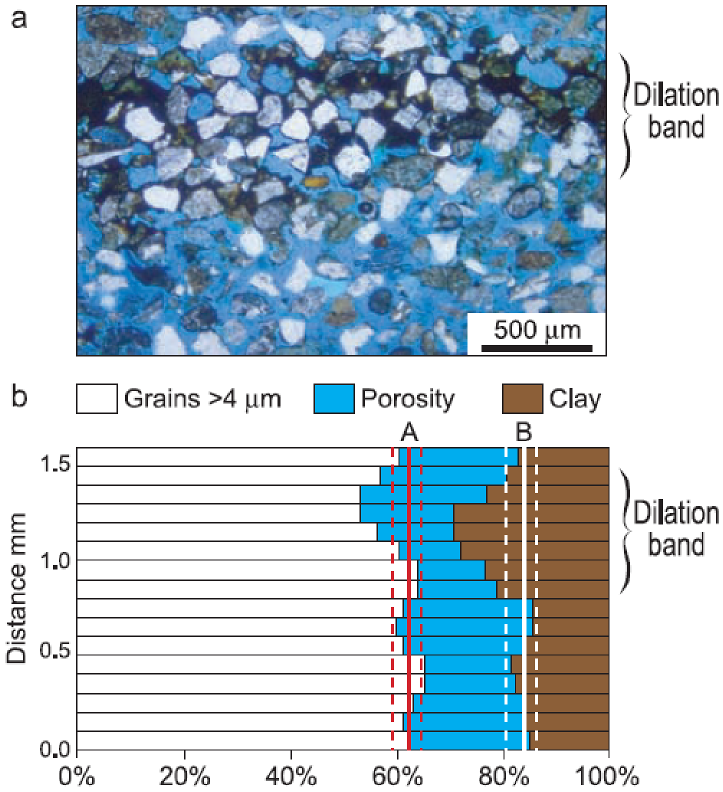

Figure 1.6: (a) Photomicrograph of a cemented dilation band. Pore space is impregnated with blue epoxy, and the interstitial space among the sand grains within the band is preferentially filled with a dark cement composed of clay minerals, iron oxide, and organic matter. (b) Frequency diagram of rock constituents and pore space based on point counting traverses across a dilation band. The band is characterised by a decrease in detrital grain abundance compared to undeformed sand. Solid lines indicate mean values in detrital grain abundance ("A") and residual porosity ("B") away from bands, dashed lines indicate +2σ error. (From Du Bernard et al., 2002).

1.5 Salt-wall mini-basins

Marine and continental sedimentary successions deposited on top of thick salt layers commonly result in the generation of multiple discrete mini-basins in response to differential subsidence related to salt flow driven by sediment loading (Hudec & Jackson, 2007). Salt-wall mini-basins are 'synkinematic basins' that subside into relatively thick, allochthonous or autochthonous salt (Jackson & Talbot, 1991). True mini-basins are not preferentially controlled by basement tectonics and commonly have polygonal plan-form shapes (Rowan & Vendeville, 2006). However, in many examples the location of inherited basement structure features is important (Smith et al., 1993; Banham & Mountney, 2013a, b). The initiation and evolution of mini-basins involves a variety of local and regional controls. Local factors include both salt withdrawal, which influences the rate and style of subsidence, and salt inflation, which influences the topographic expression of growing diapirs (Andrie et al., 2012; Giles & Rowan, 2012). The style of mini-basin development is also dependent on regional changes in climate, tectonic regime and rates of sediment supply (Hodgson et al., 1992; Barde et al., 2002; Prochnow et al., 2006; Buck et al., 2010; Newell et al., 2012; Banham & Mountney, 2014). While salt bodies can be identified on a seismic line, the salt structure does not typically have strong internal seismic reflectors (acoustically homogeneous), such that little has been known about how the salt walls develop internally as they evolve adjacent to the mini-basin pod until relatively recently (Jackson et al., 2014). The development of salt-wall mini-basins is driven by a positive feedback loop of sediment subsidence into the salt layer providing accommodation space for more sediment, resulting in further loading and thus subsidence of the sediment into the salt. This is an environment with significant stress perturbations, because the rising salt imposes an additional load on adjacent sediments (Alsop, 1996; Davison et al., 2000; Quinta et al., 2012; Nikolinakou et al., 2014; Heidari et al., 2017). The stress imposed by salt walls is sufficient enough to hinder drilling and cause additional expense, or the additional load can even result in abandonment of the well (Bradley, 1978; Willson et al., 2003; Dusseault et al., 2004). Improving the prediction of the formation of sub-seismic structures and their petrophysical properties is essential for realistic characterisation of deformed sandstone reservoirs especially in close proximity to salt diapirs and within salt-wall mini-basins. Both the burial history and the diagenetic history of the sediment determine the strength of the sediment, and therefore how it will react to external loading (Terzaghi et al., 1996; Laubach et al., 2010). Therefore, considering the stress history of potential sandstone reservoirs adjacent to salt walls that have mobilised and undergone substantial geological deformation is important.

Globally, there exist in excess of 120 provinces in which evaporite basins are known to have been influenced by salt deformation (Hudec and Jackson, 2007; Banham & Mountney, 2013b; Fig. 1.7).

Numerous studies have been previously conducted to demonstrate how various sedimentary environments are influenced by coeval halokinesis that results in high rates of basin subsidence (i.e., Prather et al., 1998; Banham & Mountney, 2013b), diversion of sediment transport pathways by uplifting topography (e.g., Kneller and McCaffrey, 1995; Banham and Mountney, 2013a, b), and reworking of uplifted sediments or diapir-derived detritus (Lawton and Buck, 2006). Of these and other studies, only a modest number have attempted to document the influence on sedimentation in salt-walled mini-basins. Of particular recent interest has been the Paradox Basin, Utah; Central Graben, North Sea, and Gulf of Mexico, amongst others (Matthews et al., 2007; Kane et al., 2012; Banham & Mountney, 2013b; Sathar & Jones, 2016).

Sediments deposited within layers of salt are likely to form hydrocarbon reservoirs since the salt layers can act as side and top seals, and the salt can distribute the sediment to form stratigraphic traps (Archer et al., 2012). Salt-walled mini-basins form an economically and volumetrically significant component of many basins and passive margins, yet they are comparatively poorly studied relative to the larger body of literature that focusses on the salt bodies and especially diapirs (Alsop, 1996; Davison et al., 2000; Nikolinakou et al., 2014).

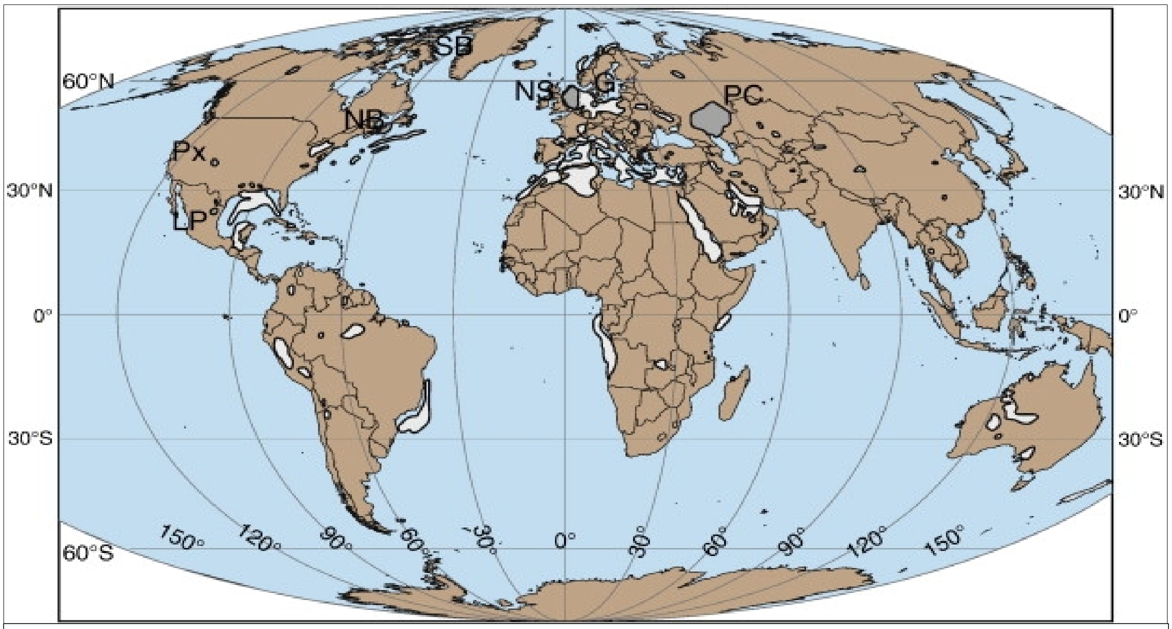

Figure 1.7: Overview of some of the major halokinetic provinces worldwide. Dark grey shows provinces discussed in Banham & Mountney (2013b) and light grey areas represent the halokinetic provinces that were not discussed in that paper. Each of these minibasins show significant salt tectonics. G: German case studies; LP: La Popa Basin; NB: New Brunswick; NS: North Sea; PC: Precaspian Basin; Px: Paradox Basin; SB: Sverdrup Basin. (From Banham & Mountney, 2013b).

1.6 Area of study

The wells studied all occur within the Central Graben, North Sea, within Quads 22 and 29 of the UK sector (Fig. 1.8). The Central Graben can be defined as the southern arm of the North Sea's trilete rift system, with the western arm forming the Moray Firth Basin, and the northern arm consisting of the Viking Graben. The Central Graben has been divided into the East and West Central Graben (ECG and WCG, respectively), with Quads 22 and 29 located between the Forties-Montrose High and the Josephine High. The faults in the underlying Rotliegend trend run from NW-SE, as do the salt walls surrounding the sedimentary mini-basins (Fig. 1.9) (Stricker et al., 2016). These faults were active during the Permo-Triassic and are likely to have initiated halokinesis of the Zechstein salt layer in the area (Hodgson et al., 1992; McKie, 2014). The faults

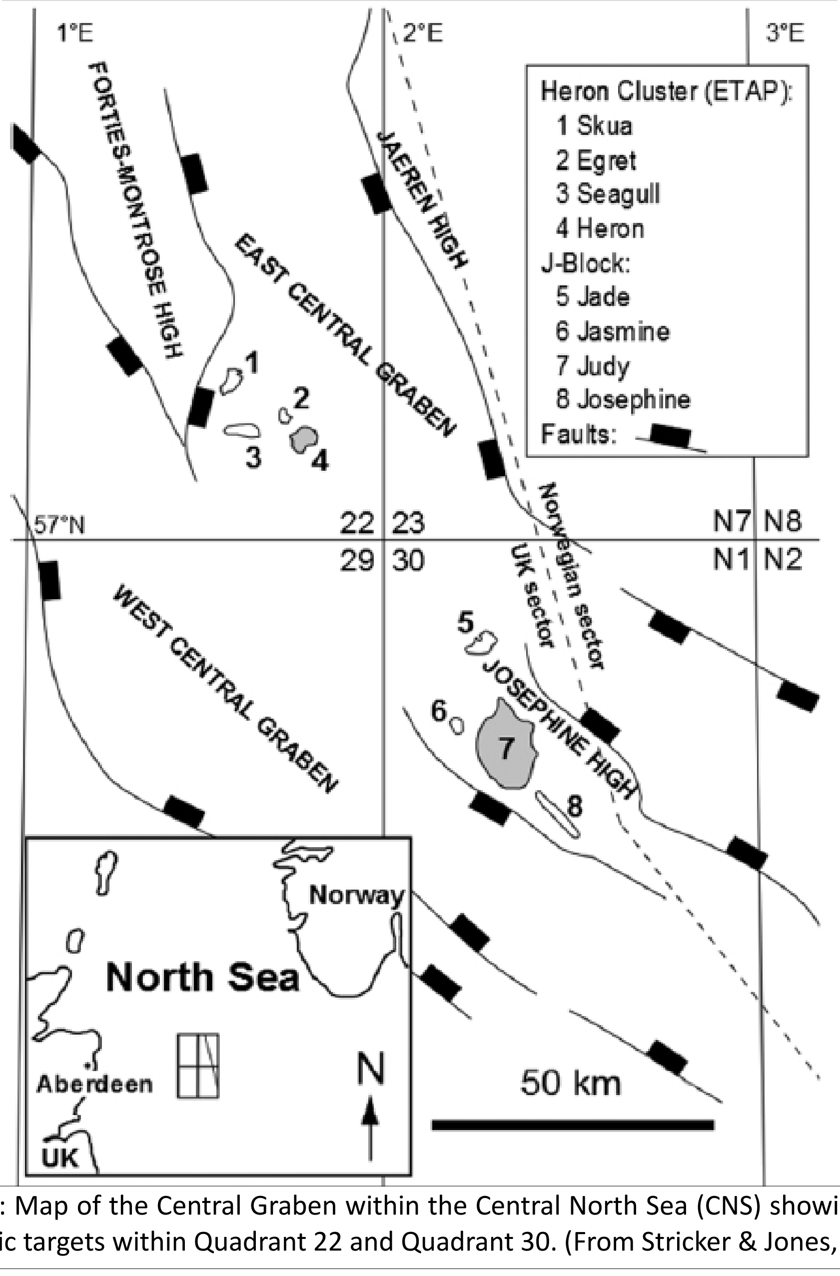

Figure 1.8: Map of the Central Graben within the Central North Sea (CNS) showing major faults and Triassic targets within Quadrant 22 and Quadrant 30. (From Stricker & Jones, 2016).

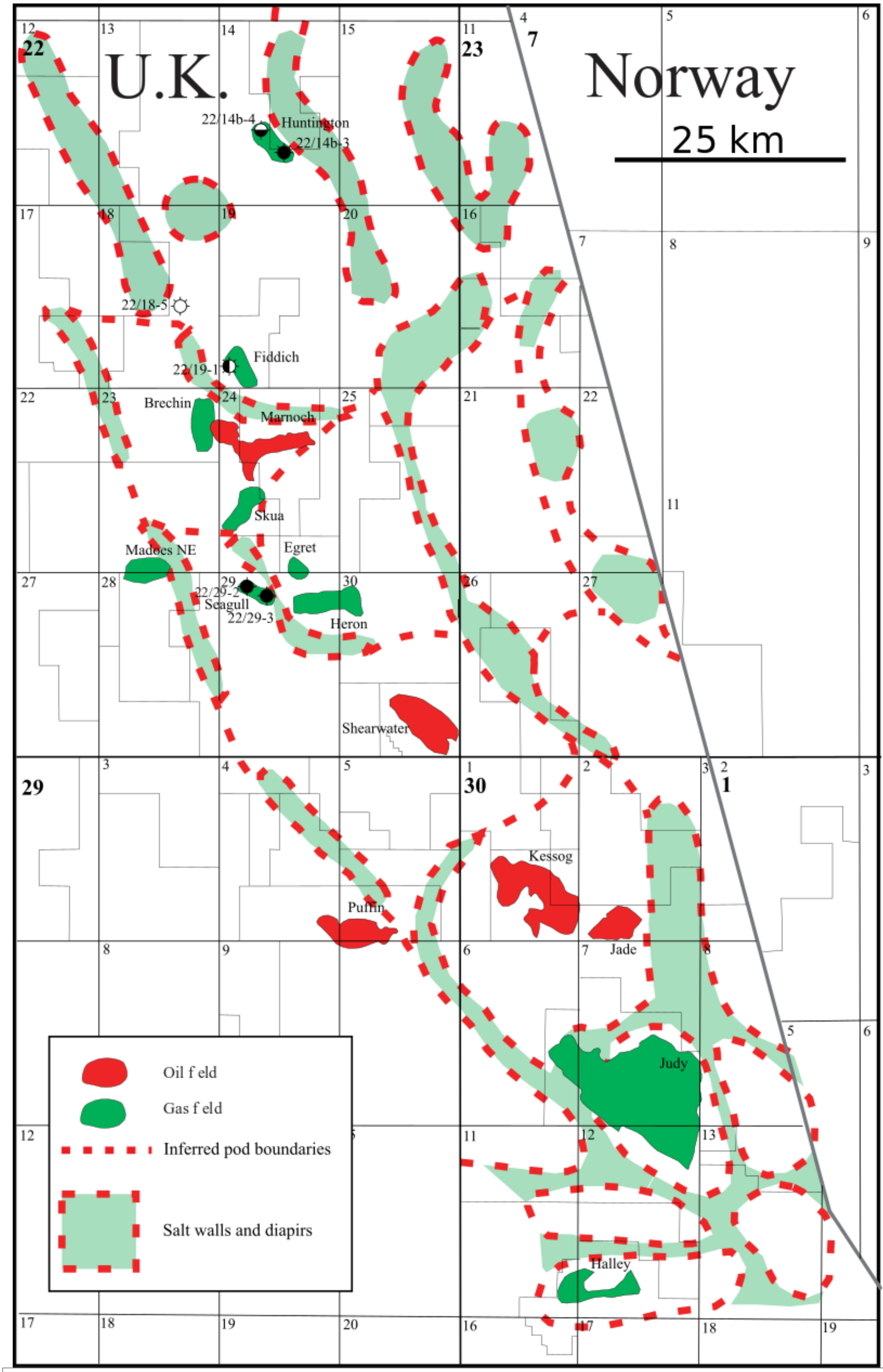

Figure 1.9: Map of salt walls across the Central Graben within the Central North Sea (CNS) within Quadrant 22 and Quadrant 30. The map also includes the location of hydrocarbon fields (oil and gas).

and salt were active throughout the Triassic and potentially influenced the development of deformation bands near the surface.

The stratigraphy considered in this thesis can be divided into the Permian (Rotliegend and Zechstein Formation), the Triassic (Smith Bank Formation, Bunter Sandstone and Skagerrak Formation), and the Mid-Late Jurassic (Pentland Formation) all of which will be explored further in section 2.2. Particular focus will be applied to the Skagerrak Formation, which can be further sub-divided into the three sandstone members (Judy, Joanne, and Josephine), interbedded with three mudstone members (Julius, Jonathan, and Joshua) (Goldsmith et al., 1995; Mouritzen et al., 2017). The sandstone members include sheetflood deposits and stacked channel sandbodies, while the mudstone members include extensive floodplain and playa lake deposits (Stricker et al., 2018).

Triassic sediments were deposited into salt-walled mini-basins, and due to the kinematics of the salt walls altering the topography of the CNS and grounding of the mini-basins, there are variations between the sedimentary infills of the salt-walled mini-basins (Hodgson et al., 1992; Matthews et al., 2007). Previous studies have correlated between the mini-basin sediments and developed a generalised stratigraphy for the CNS (Goldsmith et al., 1995; McKie, 2014; Mouritzen et al., 2017). The Early Triassic Smith Bank and Bunter Formation sandstones were deposited directly onto the salt layer and are comprised of silty mudstones and a thin layer of coarse sand, respectively (Goldsmith et al., 2003). The sediments of the Skagerrak Formation deposited during the Middle to Late Triassic are a thick series of interbedded sandstone and mudstone from continental meandering and braided fluvial deposits as well as terminal fluvial fan deposits with lacustrine facies.

Jurassic stratigraphy records post-Triassic tectonic events. One notable post-Triassic event evident from most wells in the CNS is a significant unconformity between the Late Triassic sandstones and the overlying Mid-Jurassic sediments, referred to as the Mid-Cimmerian Unconformity (Goldsmith et al., 2003). This Mid-Cimmerian Unconformity may have been caused by thermal doming uplifting, isolating the area from sediment influx and favouring erosion of the Early Jurassic sediments (Erratt, 1993). This erosion was further aided in some areas by the exhaustion of the salt layer beneath the Triassic stratigraphy, exposing the shallow deposits to erosion (Goldsmith et al., 2003; Archer et al., 2010). Minor subsidence of Late Jurassic sediments show the continuing development of the mini-basins and the effect of sediment pod 'grounding' on the underlying basement rock (Hodgson et al., 1992; Karlo et al., 2014).

Chapter 2. Deformation Band Formation, Petrography and Morphology

2.1 Introduction

This chapter will investigate the factors that influence the deformation of sediment, and the impact that these deformation features can have on the reservoir quality of sandstones, both at the petrographic level and at larger scales. This chapter also includes a detailed stratigraphy of the varied formations across the CNS, followed by an in-depth description of the reservoir quality of the Skagerrak Formation sandstones derived from structural and petrographic factors. The aim of this chapter is to then investigate the petrography and morphology of the deformation bands observed in the Skagerrak Formation at the microscale and macroscale to determine the conditions under which the deformation bands formed and how the bands developed over time. Classification of the deformation band in terms of dominant deformation mechanism and kinematics will constrain the magnitude of the stress imposed on the sediment thus providing an estimation for the depth of formation (Fossen et al., 2007). The petrography of the deformation bands should highlight how the deformation bands evolved during burial in terms of diagenetic alteration (Exner et al., 2013). Interactions of the deformation bands with other deformation bands and sedimentary features can reveal multiple periods of deformation band formation, highlighting that deformation adjacent to salt walls is a continuous or intermittent process. Utilising other data sources such as wireline logs and UV photographs can further reveal the impact of the deformation bands on the porosity and permeability of the sandstone. Assessing reservoir quality risk is especially important in plays and prospects where potential sandstone reservoirs have been exposed to elevated temperatures (>～100°C) and/or high effective stresses for significant periods of geological time (Stricker & Jones, 2016). Occurrences of high quality reservoir sandstone that deviate from normal porosity-depth trends are attributed to processes or conditions that have preserved porosity through limited compaction and/or cementation or contributed to porosity enhancement by dissolution of grains or cements.

2.1.1 Deformation band formation: Changing the cohesion and stress state of soft sediments

Although deformation bands can form in unconsolidated sand, the strength and competence of soils can be influenced by other factors. There have been several studies on factors that can change the physical properties of the sediment, or external influences may impose brief changes in the stress field that can cause the stresses acting on the sediment to suddenly shift into a state where they may not deform in a ductile manner. Increasing the cohesion of the sediment could allow fractures and dilation bands to remain open long enough to allow the infiltration of meteoric water and clay minerals into the sediment.

2.1.1.1 Altering fluid content

A possible way of increasing the cohesion of sediments could simply be adding water or fluids in general (Kemper & Rosenau, 1984; Kim et al., 2009). A study by Kim et al. (2009) found that wet sand (0.5 – 4% of the sands mass consisting of water) could sustain a tensile strength of 400 Pa (at 0.5% water weight) to between 850-950 Pa (at 4% water weight) due to capillary bonding forces arising from 'water bridges' between the grains. While not a significant increase in cohesion and tensile strength compared to lithified rock, in the context of $q - p$ diagrams, where stresses that cause soil to deform can be at KPa scales this could allow a soil at the surface to maintain a strain high enough to exceed the yield surface and mechanically fail (Schultz & Siddharthan, 2005; Desrues et al., 2007). However, higher water content (>5 % water weight) within the sand resulted in the water pressure exerted on the sand grains exceeding the capillary forces between the grains, weakening the sediment. Based on the tension test, the water content required for the pore pressure to overcome the cohesion provided by water bridges would need to exceed pressures at the scale of $10^2 - 10^3$ Pa. This would likely happen soon after burial of the sediment, or at the point where the soil becomes oversaturated.

2.1.1.2 Clay minerals and biogenic substances

Similarly to the above example, clays and biogenic substances can also increase the cohesion of sediments (Kemper et al., 1987; Gerbersdorf & Wieprecht, 2015; Malarkey et al., 2015; Jones 2017). The influence of clay materials and extracellular polymeric substances (EPS) can even have an influence on the development of dune bedforms in subaqueous conditions (Parsons et al., 2016). The results showed that although both mud and EPS both had a significant influence on the bedforms, the EPS had a more significant impact on reducing the bedform dimensions and steepness due to the stronger interparticle bonding. This increased interparticle bonding inhibits the height and length of the mixed mud-EPS bedforms, with high amounts of EPS reducing the bedform type from dunes to ripples and then, ultimately, to flat beds.

2.1.1.3 Seismicity and sudden changes to the local stress

Owen (1987) describes how deformation mechanisms are processes that enable a typically solid-like substance to deform in a ductile manner. This is likely achieved by the liquefaction or fluidisation of the sediments. However, sand could act as a brittle solid in certain circumstances, and a plastic solid in others.

Subsequent studies on the influence of seismic waves on the deformation of unconsolidated sediments have found that faults can generate cataclastic bands in shallow sediment, due to the seismic shock from the faults suddenly altering the stress field and causing the local sediments to enter the brittle deformation regime (Rossetti, 1999; Cashman et al., 2007). However, fault zones were also found to produce ductile deformation features that disappeared rapidly with depth, suggesting that the features were unable to develop fully (Rossetti, 1999).

The soft sediment deformation features described here may change as they are buried and exposed to higher confining stresses and diagenetic alteration. These changes can produce structures broadly referred to as deformation bands in the literature, although the exact terminology for specific types of deformation bands can differ between studies (Antonellini et al., 1994; Aydin et al., 2006; Fossen et al., 2007).

2.1.2 Lithological controls on deformation band formation

In terms of porosity, rocks with higher porosities would undergo volumetric reduction deformation since the grain framework would be weaker and less resistant to mechanical compression. For well-sorted sands composed of sub-round to rounded grains, larger grains were found to fracture at lower stress conditions than finer grains. This behaviour is likely to do with larger grains having fewer point contacts with other detrital grains, which therefore leads to higher stress concentrations at these point contacts and subsequent fracturing of the grains. Conversely, poorly sorted rocks with a non-uniform grain-size distribution would allow smaller grains to redistribute the stress concentrations between grains, reducing the likelihood of cataclasis. Therefore, a host rock with a high quartz content, but poorly sorted, sub-round grains and a fine-grain size would be less likely to undergo cataclasis and grain fracturing than a coarse-grained, well-sorted rock with well-rounded grains (e.g. Griffiths et al., 2016).

The effect of lithology can also play an important role on the distribution of deformation bands next to or within a fault damage zone (Johansen & Fossen, 2008). Johansen and Fossen (2008) looked at deformation bands in aeolian sandstones, siltstones and shales from two study areas, the San Rafael Desert, and the Moab Desert of Utah, USA. Their findings establish that the coarse aeolian sandstones had the widest zones of deformation band clusters, followed by the siltstone, with the shale having very few deformation bands or clusters. This was attributed to the change in deformation mechanism between the different lithologies. The cataclasis in the sandstone was likely caused by the coarseness of the grains, the higher strength of the surrounding host rock, and the effect of strain hardening, a process where increased stress on sediments increases the strength of the sediments, which meant that the clustering of the bands was more intense closer to the fault surface. The siltstones showed greater offset, but a thinner damage zone compared to the sandstone (Johansen & Fossen, 2008). This would imply that strain hardening had a lesser effect in the siltstone, or was absent altogether based on the lack of grain fracture and breakage.

The finer grain size would have also diffused the stress at grain contacts, reducing the likelihood of grain fracturing, as mentioned above. Interestingly, the mudrock showed no evidence of sequential deformation band growth, with little to no strain hardening (Johansen & Fossen, 2008). This was attributed to the very fine grain size, and the presence of phyllosilicate minerals. The alignment of the platy minerals would have allowed the grains to slip past each other, promoting strain softening (when the resistance of a material to deformation reduces with continuous deformation of the material) and early slip surface formation. The deformation bands were also found to form conjugate sets which dipped in the range of 50-80°. However, the orientations of the bands became more complex within sections of the damage zone which had the highest frequencies of deformation bands (Johansen & Fossen, 2008).

The type of stress regime can also influence the development of deformation bands (Solum et al., 2010; Zuluaga et al., 2017). Deformation bands that form close to reverse faults were found to be more likely to feature cataclasis compared to deformation bands near normal faults, and did not feature any dilational bands (Solum et al., 2010; Zuluaga et al., 2017). It was concluded that deformation bands formed in a thrust regime are more likely to degrade the reservoir quality and compartmentalise the sandstone compared to deformation bands in a normal-faulted extensional setting due to the thrust fault regime favouring the production of lower permeability cataclastic bands compared to disaggregation bands found in a normal fault regime (Solum et al., 2010).

2.1.2.1 Summary of factors that influence deformation band development

Given the various types of deformation bands and their different effects on fluid flow, it is important to understand the underlying conditions that control when and where they form in clastic sediments. A number of factors are influential, including burial depth, tectonic environment (state of stress), and host rock properties, such as mineralogy, grain size, sorting, grain shape and degree of lithification. Some of these factors, particularly mineralogy, grain size, rounding, grain shape and sorting, are more or less constant for a given sedimentary rock bed but can be strongly influenced by internal bed heterogeneities (sedimentary structures, graded bedding, etc.). However, properties may vary from layer to layer, which is why rapid changes in deformation band development may be seen from one layer to the next. Other factors, such as porosity, permeability, confining pressure, stress state and cementation, are likely to change with time. The result may be that early deformation bands are different from those that formed at later stages in the same porous rock layer, for example at deeper burial depths (Fossen et al., 2007). Hence, the sequence of deformation structures in a given rock layer reflect the physical changes that the sediment has experienced throughout its history of burial, lithification and uplift.

2.1.3 How deformation bands impact reservoir quality

2.1.3.1 The impact of deformation bands on reservoir quality

Deformation bands can significantly influence reservoir quality through the direct impact on porosity, permeability and fluid flow within the sandstone, as well as reducing connectivity between volumes of porous and permeable sandstone, leading to compartmentalisation within reservoir rocks. (Chuhan et al., 2002; Bense et al., 2003; Sternlof et al., 2004; Fossen & Bale, 2007; McKie et al., 2010; Torabi et al., 2013). Deformation bands with a dilational component would initially increase porosity and permeability in the sandstone along the length of the band, aiding subsurface fluid flow. However, preferential fluid flow along the enhanced porosity and permeability of the deformation band allows for the deposition of authigenic clays and new cements (Fig. 1.6) (Du Bernard et al., 2002; Exner et al., 2013; Lommatszch et al., 2015a, b). Dilation bands, as previously described (1.4.1.3), initially have an increased porosity compared to the host rock. However, as dilation bands are buried the overburden pressure will most likely erase the enhanced pore space and reduce porosity within the deformed sediment. Although, there are examples where deformation bands show little or no pore volume changes, such as disaggregation features (Fossen & Bale, 2007). Deformation bands that are mechanically compacted and reactivated so as to develop grain breakage along their length, usually termed as cataclastic bands, have been shown to have a significant impact on the permeability properties of sandstone (Fig. 1.4) (Sternlof et al., 2004; Fossen & Bale, 2007; Torabi & Fossen, 2009). The grain fracturing, fragmentation and comminution during cataclasis would increase the variety of grain sizes in the sandstone, shifting the grain sorting of the sandstone towards a more poorly sorted configuration (Fig. 2.1). Poorly-sorted sandstones have lower porosities than well-sorted sandstones and generally function as less effective hydrocarbon reservoirs (Main et al., 2000; Ogilvie & Glover, 2001). Further burial and subsequent reactivation of the cataclastic bands can result in the development of cataclastic flow, which produces finer and finer grains until a highly impermeable fault gouge forms along the deformation band surface (Fossen et al., 2007).

Cemented disaggregation bands or dilational bands have the potential to become a barrier or baffle to fluid flow perpendicular to the planar surface of the deformation band (Exner et al., 2013). Examples of cementation bands observed in the Vienna Basin (Exner et al., 2013), accounted for a decrease in porosity of between 2 – 9% in contrast to the surrounding rock, where porosity measured between 20 – 31.5%. The reason for the decrease in porosity is the preferred precipitation of Fe-rich dolomite cement within the deformation bands. Additionally, the grain size of detrital grains is reduced relative to the host rock by grain fracturing and fragmentation of the mineral surface (spalling). However, timing would be an issue when developing cementation bands since the enhanced porosity from the dilation would be quickly removed due to mechanical compaction as the dilation band was buried.

Phyllosilicate bands that consist of aligned platy minerals (typically micas) could significantly inhibit subsurface fluid flow perpendicular to the deformation band depending on the continuity of the phyllosilicate planar surface (Fisher & Knipe, 1998). These phyllosilicate bands would not necessarily require a change in grain size or the precipitation of a new authigenic cement to influence subsurface fluid flow.

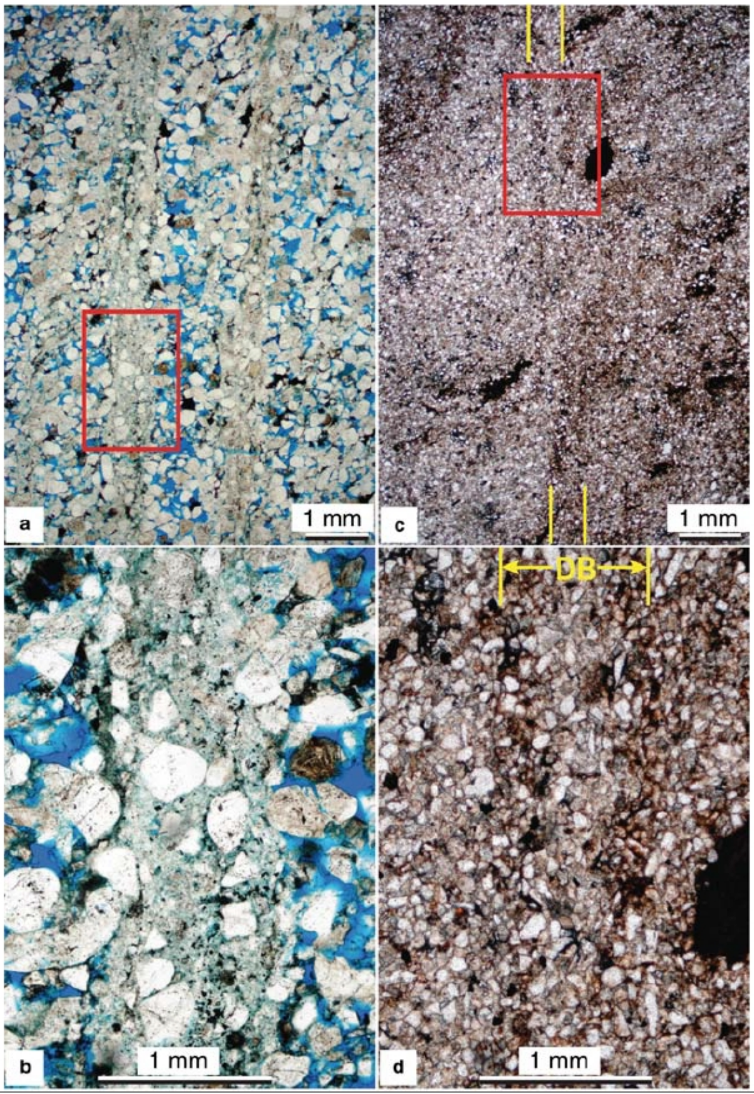

Figure 2.1: **(a)** Cataclastic bands in sandstone with grain-size reduction. **(b)** Magnification of the red box in (a). **(c)** Disaggregation band in siltstone showing grain reorganisation. **(d)** Magnification of the red box in (c). (From Johansen & Fossen, 2008).

2.1.3.2 Compartmentalisation of sandstones due to deformation bands

Compartmentalisation can complicate the structure of a reservoir and possibly reduce the total amount of fluids that can be recovered from the reservoir. The compartmentalising barriers can be caused by changes in stratigraphy, by tectonic structures, by dense networks of deformation bands, or by a combination of these factors (Sternlof et al., 2004; Archer et al., 2010; McKie et al., 2010; Laubach et al., 2010).

While individual deformation bands may influence porosity and permeability at the centimetre scale, the spatial orientation, density of deformation band clusters, as well as the continuity and thickness of the deformation band must be considered when investigating the implications at the reservoir scale. Sternlof et al. (2004) focussed on the effect various patterns of cataclastic bands have on permeability. The patterns considered are parallel sets of bands, cross-hatched sets of bands, and anastomosing sets of bands (Figs 2.2 & 2.3). It has been identified that thick, densely-packed clusters of deformation bands could generate a significant anisotropy across a sandstone and substantially impact fluid flow. Although Sternlof et al. (2004) recognised that single cataclastic bands were unable to maintain a significant pressure difference perpendicular to their orientation, non-continuous nature, and variable band thickness, it is still possible that cataclastic bands may act as baffles to fluid flow. However a combination of deformation bands and diagenesis can have a greater influence on sandstone reservoir quality compared to deformation bands alone (i.e. Laubach et al., 2010).

Overall, while some deformation bands can initially be beneficial for porosity in sandstones, the majority of deformation bands are detrimental or have little impact on the porosity and permeability of sandstones. The presence of deformation bands in a reservoir is highly likely to reduce the quality of the sandstone when buried at depth due to reactivation of the bands, and precipitation of new diagenetic minerals along the deformation bands (McKie et al., 2010). The ability of deformation bands to inhibit fluid flow may also allow them to promote compartmentalisation of a sandstone reservoir, although the capability of deformation bands to influence large-scale subsurface fluid flow will not be as effective compared to lithological barriers or clay smears (McKie et al., 2010; Stricker et al., 2018).

Figure 2.2: Typical anastomosing pattern of deformation (compaction) bands in the Aztec Sandstone, Utah. (From Sternlof et al., 2004).

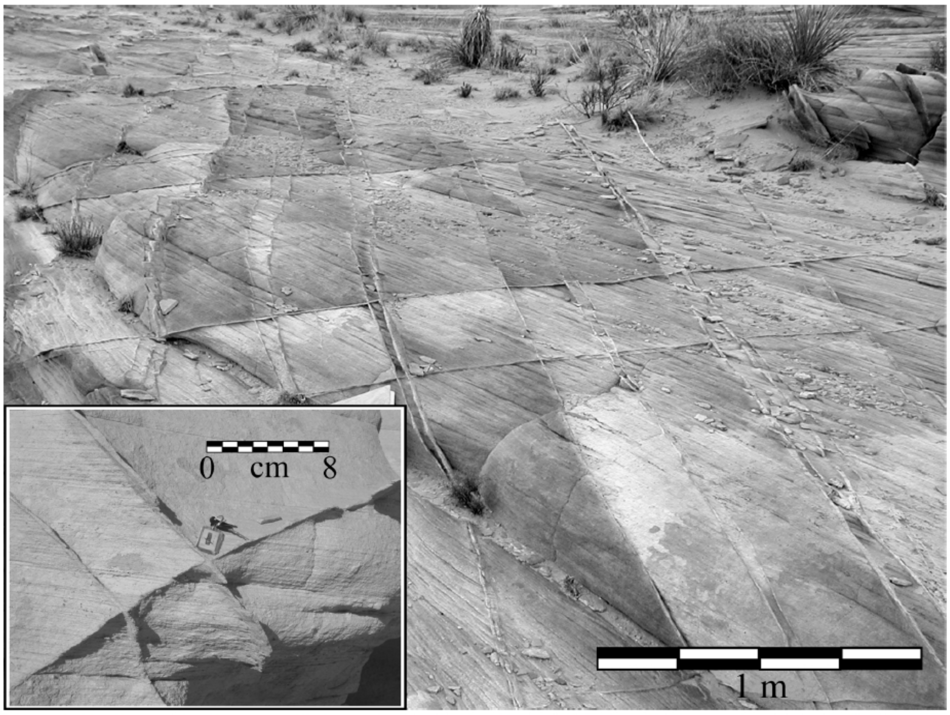

Figure 2.3: Typical cross-hatch pattern of deformation (compaction) bands in the Aztec Sandstone. Bands are set at a high angle to each other and to the bedding. (From Sternlof et al., 2004).

2.2 Stratigraphy of the Central North Sea

2.2.1 Stratigraphy of the Rotliegend and Zechstein Groups

The stratigraphy and composition of the Permian deposits will be described here since this salt layer would drive the development of the Triassic and Jurassic stratigraphy. The Permian stratigraphy of the CNS can be split into two major components, the Rotliegend Group and the Zechstein Group (Glennie et al., 2003) (Fig. 2.4). The lower Rotliegend Group is mostly made up of sandstones with local basal volcanics and the overlying Zechstein Group consists of carbonates and evaporites. Prior to the Permian – Triassic rifting event a layer of marine-derived evaporites were deposited on top of the Rotliegend over a period of 5 million years (250 – 245 Ma) (Tucker, 1991). The salt layer that did finally accumulate over the Rotliegend varied in thickness between locations, with the evaporite layer reaching up to 2400 m in thickness in some areas (Smith et al., 1993) (Fig. 2.5).

The Shearwater Salt Layer, a component of the Zechstein Group, had a thickness prior to the onset of halokinesis of at least 500 m in most areas and could be as thick as 1500 m (Glennie et al., 2003). However, the problem with reconstructing the thickness of the Zechstein salt layers prior to sediment deposition during the Triassic is that the Zechstein salt has been heavily deformed into salt walls and other structures by the later sediment load. A backstripping technique was used to restore a series of regional seismic lines in order to estimate the contoured thickness of the Zechstein Formation (Smith et al., 1993). The restored isopachs of the Shearwater Salt Formation indicate separate basinal development on either side of the Central Graben, likely caused by the Josephine High and Forties-Montrose High and suggesting that these are long-lived structures (Glennie et al., 2003).

2.2.2 Stratigraphy of the Smith Bank Formation and Bunter Sandstone Formation (Early Triassic)

The first sediments to be deposited on the Zechstein salt layer were comprised mostly of silty mudstones (the Smith Bank Formation). The inferred initial depositional setting and climate is an arid to semi-arid playa lake (Smith Bank Formation) or distal sheet flood (Bunter Sandstone Member) environment, based on the low energy required to deposit the very-fine grained mud and the indication that the pre-existing sediments had been reworked (Mange-Rajetzky, 1995; Goldsmith et al., 2003). Widespread evidence of a hyper-arid phase during the Early Triassic has been identified across north-western Europe, although this has not been confidently observed in the CNS area (Bourquin et al., 2011; McKie & Shannon, 2011). The high-sphericity of the grains and a ‘frosted’ appearance would suggest that aeolian deposits (loess) could have also been

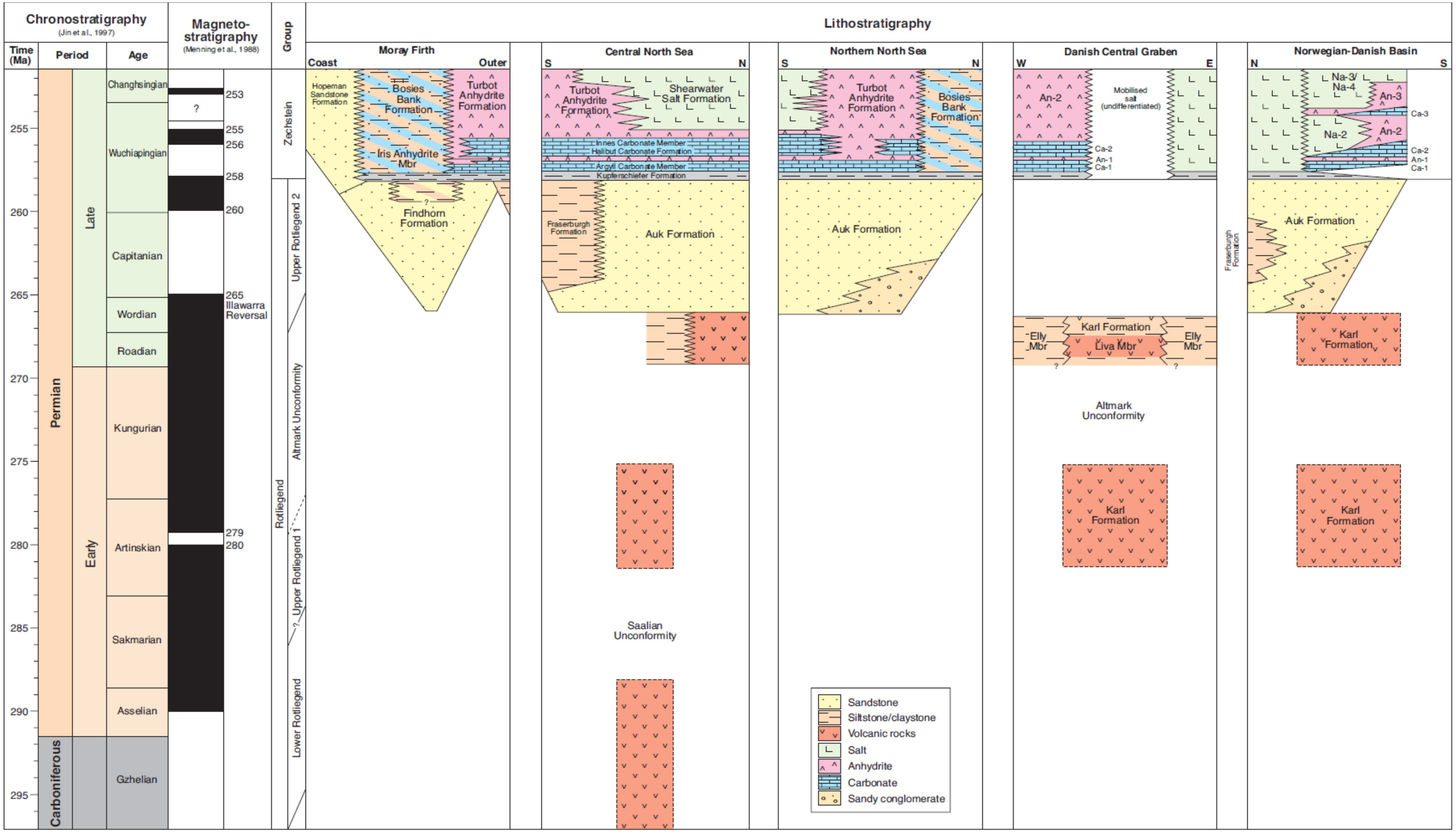

Figure 2.4: Permian stratigraphy of the North Sea area, including the Central North Sea. The relevant groups for this section are the Upper Rotliegend 2 Group (referred to in this thesis as Rotliegend Group) and the Zechstein Group. (From Glennie et al., 2003).

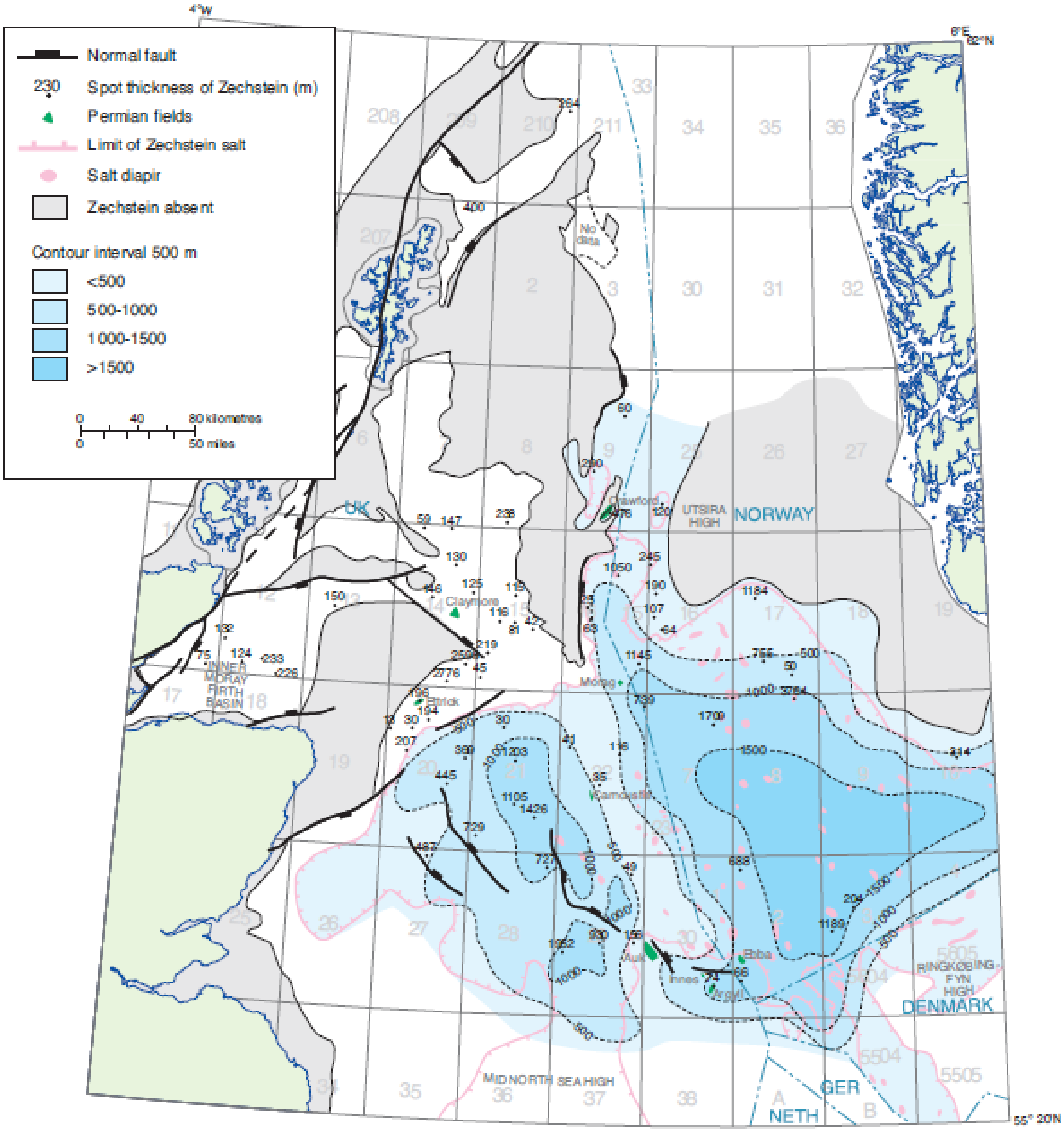

Figure 2.5: The thickness of the Zechstein Group over the Central North Sea. The current diapiric nature of the salt would produce meaningless contours of the present day Zechstein salt layer. The backstripping technique used to calculate the original thickness of the Zechstein is taken from Smith et al. (1993). It should be noted that there was separate development on either side of the Central Graben indicating that the west Central Graben and east Central Graben were separated by the Forties-Montrose High at the time of deposition. Also note that the Highland Boundary Fault further aided salt confinement (From Glennie et al., 2003).

important contributors to the Smith Bank Formation (Wilkins et al., 2018). Combined with the observations that there was little to no communication between the Northern Permian Basin and Southern Permian Basin, it would imply that the Smith Bank Formation could be considered as a terminal deposit in an endorheic basin. (McKie, 2014).

An influx of coarse sediment from the Fennoscandian Shield towards the end of the early Triassic resulted in the deposition of the Bunter Sandstone Formation across the CNS (10 – 130 m thick) (Goldsmith et al., 2003, McKie, 2014). The contact between the Bunter Sandstone Formation and the Smith Bank Formation can vary from sharp, featuring mud clasts and desiccation cracks, to a gradual transition between the mudstones and the sandstones (McKie, 2014).

2.2.3 Stratigraphy of the Skagerrak Formation (Mid-Late Triassic)

The loading induced by the Smith Bank Formation and Bunter Sandstone Member sediments caused the withdrawal of salt from underneath the sedimentary pods and into the continually developing salt wall structures. This resulted in the salt walls forming topographic elements that influenced fluvial pathways which would cause the subsequent deposition of the Skagerrak Formation to be more laterally confined compared to the playa lake depositional environment of the Smith Bank Formation (Fig 2.6) (McKie, 2014; Banham & Mountney, 2013 a, b). The climate during this period fluctuated between semi-arid to arid conditions, based on the interfingering layers of sandstone and mudstone deposits that are found throughout the Triassic stratigraphy in the CNS (Fig. 2.7) (Goldsmith et al., 2003; Archer et al., 2010; Bourquin et al., 2011). The evidence for burrowing activity and vegetation across the Skagerrak Formation floodplains shows that there was a significant amount of soil moisture available year round (McKie & Shannon, 2011). The fluvial network in the CNS during the Mid-Triassic was a terminal system, so catchment run-off could not drain out of the CNS. As such, wetter periods have been associated with the expansion of fluvial fans in the CNS without any influence from sea level fluctuations (McKie & Shannon, 2011). It is thought that warm periods would lead to the wetter episodes and increased monsoonal activity via increased evaporation (McKie & Williams, 2009).

The Triassic Skagerrak Formation is dominated by thick fluvial channel sandstone bodies, with interfingered mudstones (Fig. 2.7). Due to topographical elements caused by the salt walled mini-basins, some of the mini-basin pods could become sediment-starved compared to other neighbouring pods, with pods becoming isolated in extreme circumstances (Hodgson et al., 1992). This has caused difficulty when correlating sediment deposits between the various basins found across the Central Graben in the North Sea. General correlations can be made across the Central Graben, but a common approach is to focus on the stratigraphy of individual fields. The main fields

MIDDLE TRIASSIC

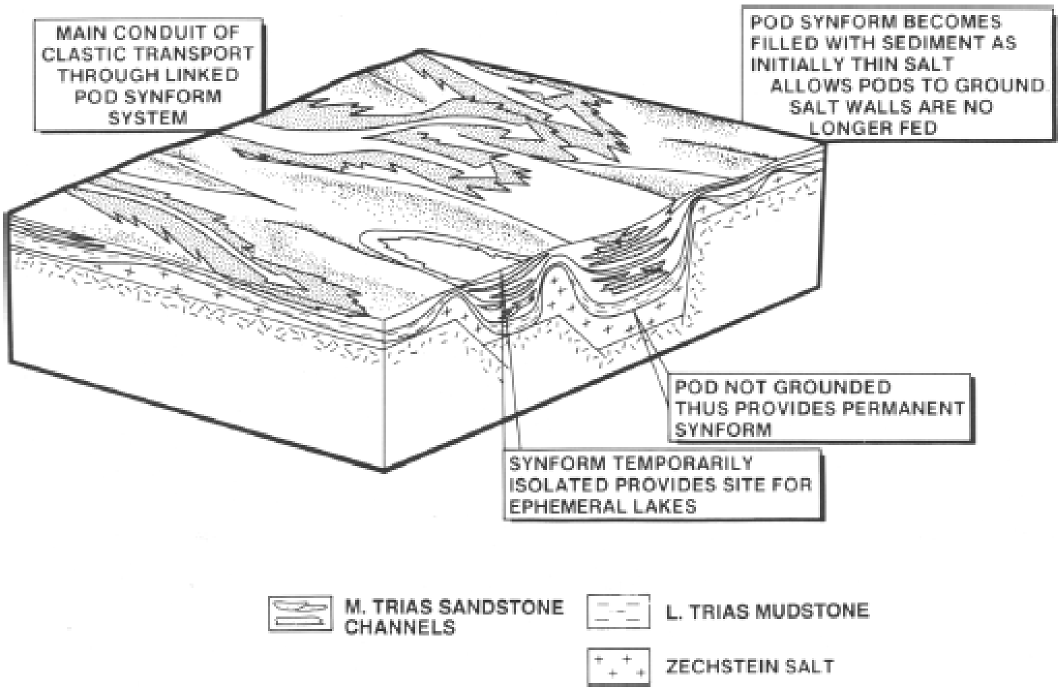

UPPER TRIASSIC

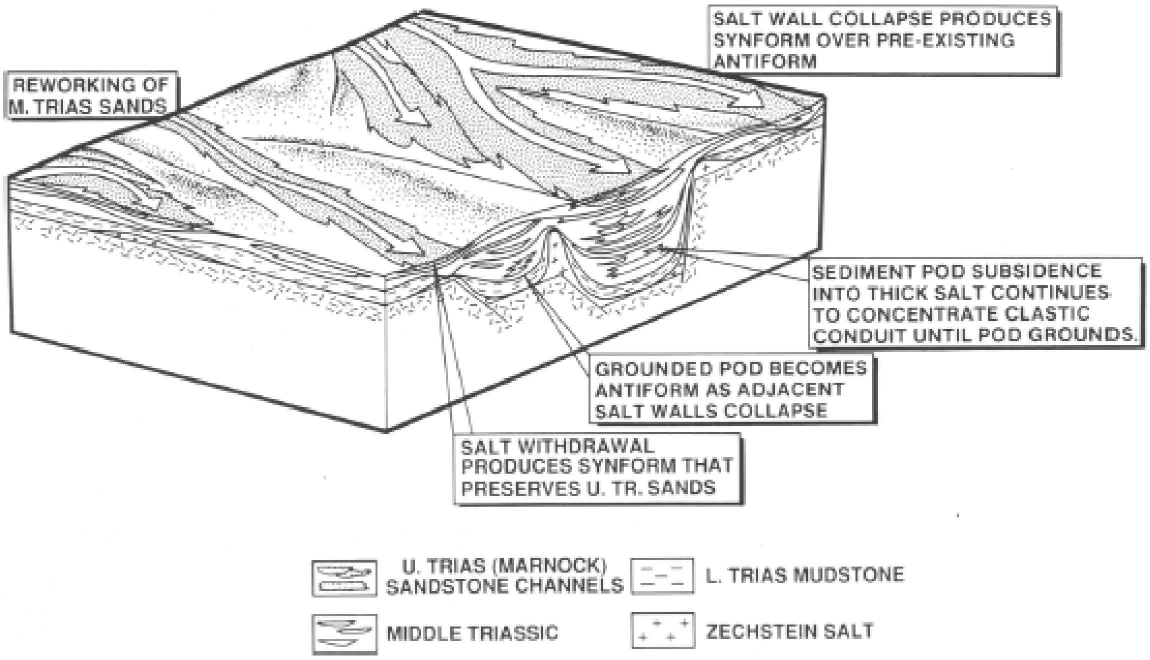

Figure 2.6: Middle and Upper Triassic depositional models. These models show how the topography of the CNS changed over time as the minibasin pods began to ground on the underlying basement rock. (From Hodgson et al., 1992).

Figure 2.7: Summary of controls on Triassic sedimentation. A wetter or more humid climate is shown to drive an increase in the grain size of deposited sediment, as opposed to Goldsmith et al. (2003) where it was thought that a wetter climate would result in finer-grained sediment being deposited in a wetland setting. (From Archer et al., 2010).

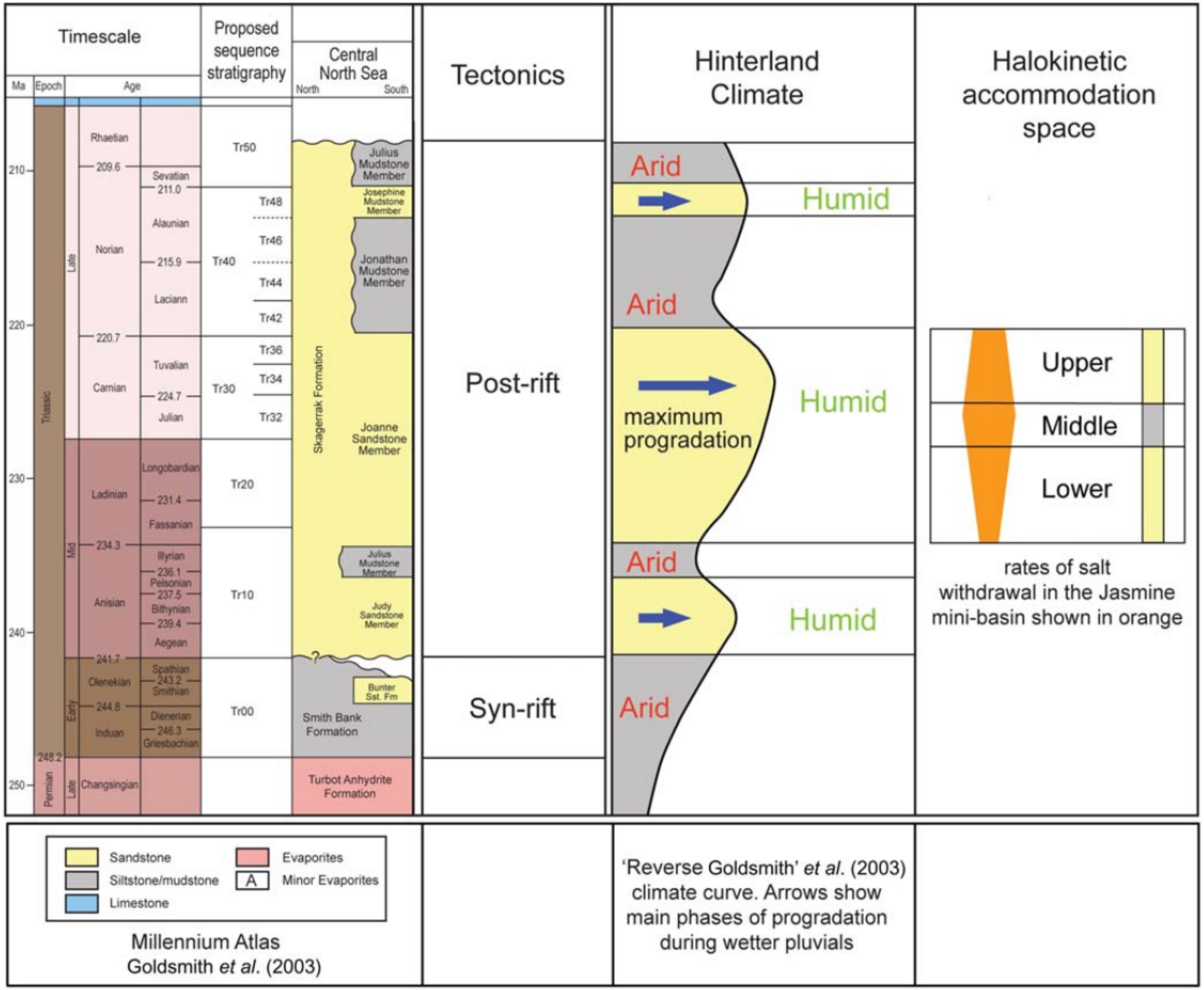

that have recently been focussed on in the Central Graben are the Jasmine Field in the J-Block area (Archer et al., 2010) and the Heron Cluster (McKie et al., 2010; Stricker et al., 2016). The source of the sediments for Skagerrak successions is likely to have been the west and northeast Scottish and the Scandinavian Caledonian Highlands, north of the CNS area (Archer et al., 2010). The sediments for the Skagerrak Formation across the CNS are quartz (>75%), with feldspar and minor micas (Stricker et al., 2018). The grain sizes range from very fine- to fine-grained, with silt and mudstone units interfingered within the sandstone units. The grains are typically sub-angular to sub-rounded and poorly- to moderately-sorted. The majority of Triassic sandstones within Quad 22 and 30 of the CNS area are classified as sub-arkosic to arkosic arenites (Goldsmith et al., 2003; Nguyen et al., 2013; Stricker et al., 2016).

The Skagerrak Formation contains equally important and significant mudstone Members (Fig. 2.7). These mudstone Members act as seals to the adjacent sandstone units and were deposited in a semi-arid playa lake environment (McKie 2010; Archer et al., 2010).

The thickness of the Triassic Skagerrak Formation sandstones will vary depending on accommodation space due to the amount of salt that was able to withdraw out from underneath the sediment pods and/or grounding of the sediment body on the underlying basement, but the sandstones of the Skagerrak Formation are typically 500 – 1000 m thick (Goldsmith et al., 1995; Nguyen et al., 2013).

2.2.4 Skagerrak sedimentary architecture

In the case of the Skagerrak Formation sandstones the fluctuation between semi-arid and arid conditions produced several end member facies throughout the depositional history of the Skagerrak Formation (Fig 2.7). The lower Skagerrak interval contains erosively-based channel fill deposits with a variety of internal fabrics, ranging from dewatered to horizontal and gently inclined parallel lamination (McKie, 2014). These deposits indicate confined channels, but the dewatered fabric would suggest either bank collapse or brief periods of rapid deposition from a diminishing, sediment-rich flow. Terminal splay complexes can be identified throughout the lower Skagerrak as they form coarsening-upward cycles. The sandstones in these cycles display climbing current ripples and plane bedding, which reflect unconfined flow, with the coarsening upwards implying progradation (McKie et al., 2010).

The transition from dominantly terminal splay facies in the lower Skagerrak Formation to a fluvial dominated system in the upper Skagerrak is marked by an increase in confined fluvial facies (McKie et al., 2010). The facies in the lower Skagerrak can be divided into a lower terminal splay-prone section, characterised by fine-grained, planar cross-bedded and ripple laminated sandstones (McKie & Audretsch, 2005). The facies in the upper interval is dominated by channel-fill deposits organised into fining upward packages with coarse lag deposits commonly occurring at the base. The channel-fill deposits are characterised by well-sorted cross-bedded sandstones that can be further divided into channel and sheet-dominated sandstones (McKie & Audretsch, 2005).

The dominant facies in the upper Skagerrak is the channel belt deposit, which can be identified by the cross stratification and low angle plane-bedding of the sandstone. This facies can be interpreted as a confined channel flow, with the cross-stratification and plane bedding being part of shallow bars and channels in a shallow stream. Other forms of facies identified involve perennial and ephemeral lakes and floodplain deposits with calcic palaeosols, providing a significant amount of the finer-grained material found within the sandstones (Fig. 2.8) (McKie et al., 2010).

Previously, the preserved Skagerrak Formation stratigraphy across the CNS (Quadrant 22) overlain by Mid-Jurassic sediments due to the Mid-Cimmerian Unconformity, has been referred to as the Judy Sandstone Member (McKie & Audretsch, 2005 & McKie et al., 2010). However, heavy mineral analysis and biostratigraphy indicates that the Josephine Sandstone Member and Jonathan Mudstone Member are much more widespread than previously speculated (Mouritzen et al., 2017). While this suggests that the Josephine Sandstone Member is potentially sampled in this study, Mouritzen et al. (2017) did not confirmed that the Josephine Sandstone Member is present in the wells investigated in this study. Therefore, the term ‘Judy Sandstone Member’ will be used when referencing studies that specify the term Judy Sandstone Member, otherwise the term ‘Skagerrak Formation’ will be used to refer to the preserved Triassic stratigraphy studied in this thesis.

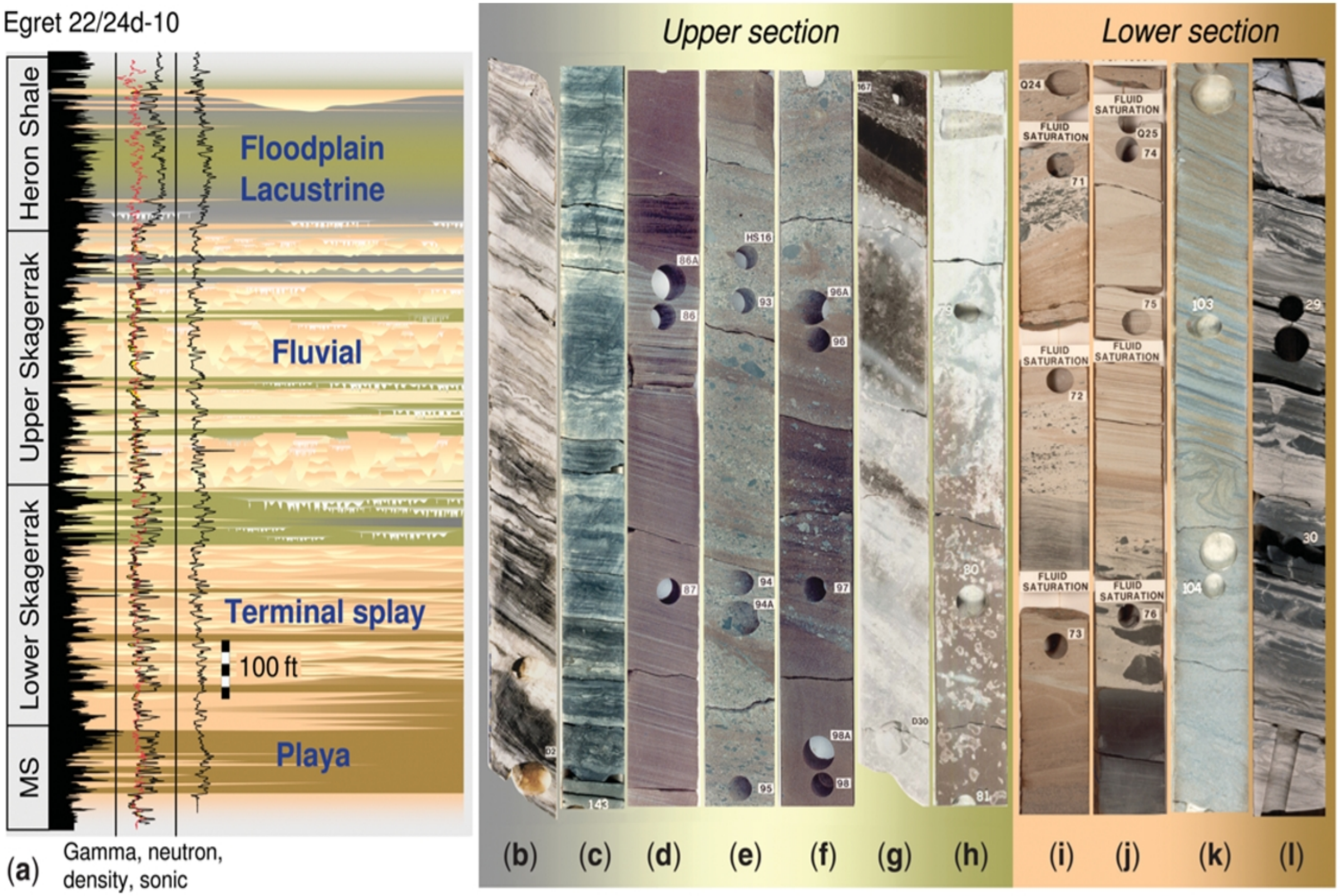

Figure 2.8: Stratigraphic section from Egret well 22/24d-10 showing (**a**) the overall facies architecture of the Skagerrak as well as (**b** – **l**) representative core sections from across the Heron Cluster area showing the main facies. (**b**) and (**c**) show palustrine facies, (**d**), (**e**) and (**f**) show upper Skagerrak channel belt sandstones, (**g**) shows bioturbated and rooted sheet deposits cemented by groundwater carbonate, (**h**) shows a well developed calcic palaeosol profile within floodplain mudrocks, (**I**) and (**j**) show mudclast mantled scour and channel-fill deposits from the lower Skagerrak section, (**k**) shows micaceous, plane bedded and dewatered lower Skagerrak splay sandstones, and (**l**) shows heterolithic playa deposits. All core sticks are 1 m long. (From McKie et al., 2010).

2.3 Reservoir quality of the Skagerrak Formation

2.3.1 Depositional controls on reservoir quality

The Skagerrak Formation has an overall moderate net-to-gross ratio due to the presence of the mudstone layers between the sandstone units. For the Judy Field, the net-to-gross ratio averages out at 0.61 (range 0.48 – 0.94) (Goldsmith et al., 2003). The mudstones were deposited during arid phases, so may not have been as widespread as the fluvial deposits during the more humid climate.

Sandstones with a coarser grain size and with well-sorted grains tend to have higher permeabilities and porosities compared to sandstones with a finer grain size and poorer sorting. Therefore the very-fine grained deposits in the terminal splay facies towards the base of the Skagerrak would form a poorer sandstone reservoir compared to the confined channel sandstone in the middle-upper sandstones of the Skagerrak Formation (McKie et al., 2010; Grant et al., 2014). The thickness of these sandstone units should also be considered when discussing the quality of the sandstone reservoirs. Thicker intervals of sandstone between the mudstone layers would reduce stratigraphic compartmentalisation and increase the amount of hydrocarbons that could be stored and recovered from the sandstone.

The initial porosity of the sandstones is controlled at deposition, influenced by the composition of the sediment, as well as the size, sphericity, and roundness of the grains. If the sandstone contains mineral grains weaker than quartz, such as feldspars and phyllosilicates, then less stress is required to compact these softer minerals (Rawling & Goodwin, 2003). The initial clay content can also determine how much porosity is lost during compaction, as the clay minerals can reduce the friction between mineral grains and cause the sandstone to compress at lower stresses (Fossen et al., 2007). Therefore, the initial composition of the sandstone can determine the extent of mechanical compaction as the sediment is buried.

The degree of mechanical compaction can vary between individual mini-basins due to the different geological history and development of each mini-basin across an area. An example of this is the high primary porosity preserved in fields found across the Heron Cluster due to the formation of grain coatings (Stricker et al., 2016), and the pore-filling chlorite found throughout the Triassic sandstones of the Seagull area (Stricker et al., 2018). The major loss of porosity has been identified as being due to compaction for the Heron Cluster (Nguyen et al., 2013; Grant et al., 2014; Stricker et al., 2018).

The discrepancy of the degree of diagenesis between the different mini-basin infills indicates the difference in initial composition of the sandstones. While meteoric water can infiltrate the sediments and alter the composition of the pore water, the initial composition of the sandstone has the greatest influence on the final diagenetic products as the sediment is buried and compacted.

2.3.2 Compartmentalisation of the Skagerrak Formation

For the Triassic sediments across the CNS, vertical compartmentalisation of the sandstones within the mini-basins would have initiated during deposition as the interfingering mudstones between the sandstone units would create effective barriers to vertical migration of fluids, along with calcrete palaeosols and calcrete lags (McKie & Audrestch, 2005; McKie et al., 2010). However, the effectiveness of these mud layers and calcrete deposits as barriers to fluid flow would depend on their lateral continuity. The mud layers are typically thick enough to maintain a significant pressure difference, but erosion, lateral facies change, and tectonic processes may have thinned out and eroded the mudstone layer until it could not maintain a high pressure difference across its thickness. The areal extent of calcrete palaeosols and calcrete lags was limited, but significant enough to cause local baffling and increase compartmentalisation across the reservoir sandstone (McKie & Audretsch, 2005).

Horizontal migration of fluids can be inhibited by the development of faults or fractures. This could be through the creation of fault gouge along the fault planes which has low perpendicular permeability (kh), by the fault offset juxtaposing permeable lithologies against low-permeability lithologies in the stratigraphy, or by cementation along the fault plane (McKie et al., 2010). The faults may also cross-cut an impermeable mud or shale layer and smear the low permeability material along the fault plane. While the effectiveness of this lithological barrier would still rely on extensive lateral continuity of the smeared lithology, this process could provide an effective barrier to fluid flow if combined with fault gouge formation, juxtaposed stratigraphy, or cementation along the fault.

Compartmentalisation of the sandstones in the J-Block is evident based on the varying height of the hydrocarbon – water contact (HWC) between the reservoirs, as well as the differing pressures within the reservoirs (Archer et al., 2010). The variable height of the HWC contact between the sandstone members is likely to be as a result of stratigraphic barriers, with the varying pore pressures between horizontally adjacent sandstones caused by faulting, since the presence of fault gouge or stratigraphic juxtaposition inhibits communication between the wells, so the pore pressure in some sandstones cannot leak out of the compartmentalised sandstone units and equilibrate across the formation.

2.3.3 Diagenetic controls on reservoir quality

The diagenetic alteration of sediments can begin soon after deposition, dependent on the composition of fluids in the intergranular pore space, the composition of the sediment, the infiltration of clay particles, thermal conditions, and the rate of burial (Carr, 2003). However, the composition of the pore fluids can change over time due to the dissolution and alteration of detrital grains as pressure and temperature increase at depth. Typically the burial rate and thermal conditions are related through a geothermal gradient that is used to estimate the temperature of sandstone at depth. Yet, the presence of a salt layer has been found to alter the geothermal gradient for sediments adjacent to salt structures (Mello et al., 1995; Davison et al., 1996). Vertical salt structures have been found to thermally conduct heat away from the sediments at the base of the salt structure and transfer the heat towards the surface at the top of the salt structure (Mello et al., 1995; Davison et al., 1996). This means that sediments at the base of salt structures are not as thermally mature as predicted by the geothermal gradient, while sediments towards the top of the salt structure are more thermally mature than predicted. A result of this is that the extent of diagenesis in sediments at the base of the salt structure would be less than expected for sediments at that depth.

While salt can have the ability to alter the temperature history of sandstones, and therefore diagenetic maturity, certain types of diagenetic minerals can aid the preservation of primary porosity by inhibiting the growth of pore-filling minerals and grain overgrowths that would nucleate from grain surfaces, as observed in the Skagerrak Formation in the CNS (Nguyen et al., 2013; Stricker et al., 2016; Stricker et al., 2018). Combining the early formation of porosity-preserving diagenetic grain coatings and the inhibition of thermal maturation, which could form pore-filling diagenetic minerals, results in the highly likely scenario of preserving porosity within the sandstones and potentially preserving the increased porosity produced by dilation bands formed at the surface.

Phases of diagenetic mineral growth can be grouped in three ways (Pichat et al., 2016):

- Eodiagenesis – Diagenesis which occurs from deposition of the sediment until buried beyond the influence of surface processes.
- Mesodiagenesis – Diagenetic processes that occur while the sediment is beyond the influence of surface diagenetic processes.

- Telodiagenesis – Diagenetic processes that occur when the buried sediments are uplifted to the surface and erosion occurs, forming unconformities.

After deposition of the Skagerrak Formation and burial of the sediments, diagenetic processes can have had a significant influence on the development of the sandstones. Towards the end of the Triassic and the deposition of the Skagerrak Formation, the accumulated sediments were approximately 500—1000 m thick. Thermal models of various wells throughout the CNS (Nguyen et al., 2013; Stricker et al., 2016) show that the Skagerrak Formation was buried to a depth of 1000—2000 m, where it remained until approximately 90 Ma when the formation rapidly subsided to its present-day depth of 4000—5000 m (Fig. 2.9). During this rapid burial (4000-5000 m), several diagenetic minerals influenced the petrophysical properties of the sandstone reservoir including chlorite, illite and some minor halite (Nguyen et al., 2013; Stricker et al., 2018).

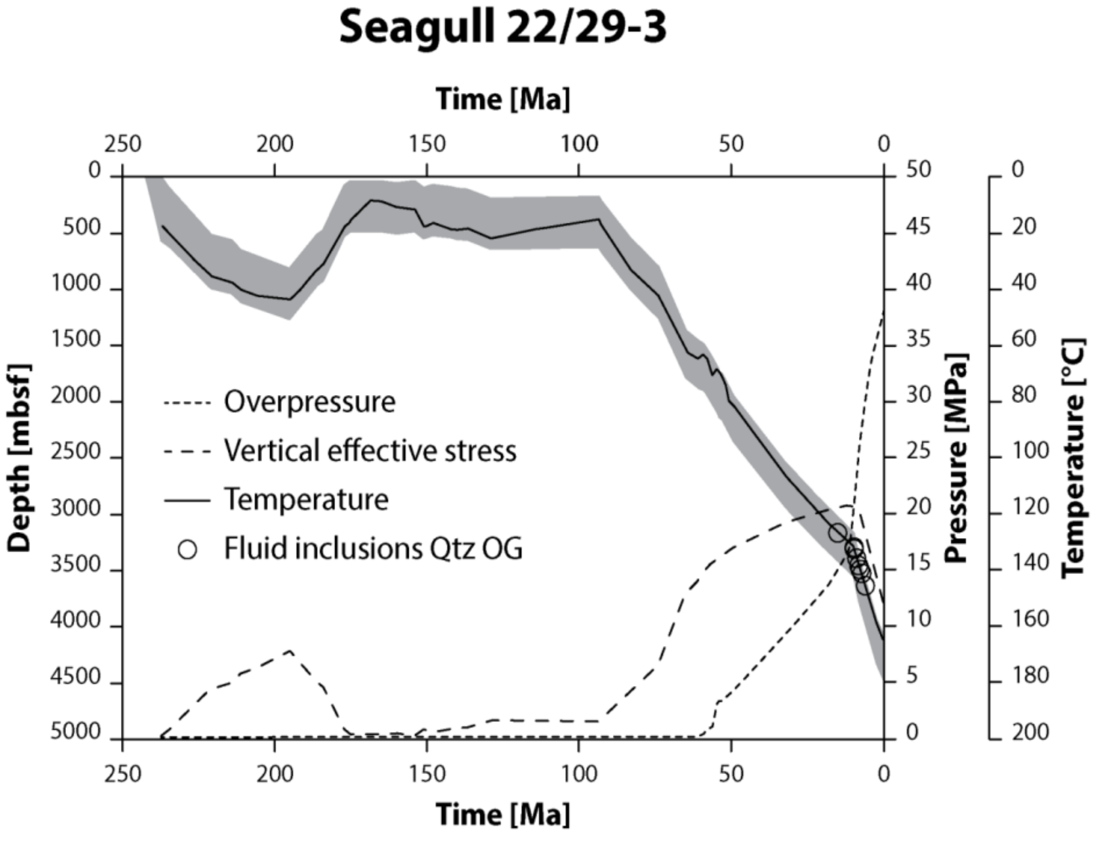

Figure 2.9: Burial history of the top of the Judy Sandstone Member in the Skagerrak Formation for well 22/29-2 and well 22/29-3. Graphs include temperature evolution, overpressure evolution and vertical effective stress (VES), including aqueous fluid inclusion temperatures enclosed in quartz overgrowth (Qtz OG). (From Stricker et al., 2018).

2.3.3.1 Chlorite

One of the early diagenetic minerals to form was chlorite grain coatings on the surface of quartz grains. The chlorite grain coatings reduced the available porosity and permeability by partly infilling the pore space or by forming clay coat bridges across pore throats. On the other hand, these grain coatings inhibited the development of macroquartz overgrowths, which have been found to significantly reduce porosity in sandstones without extensive chlorite grain coatings (Nguyen et al., 2013). This has resulted in porosities exceeding 30% at 3-4 km depth in some Skagerrak Formation sandstone reservoirs (Stricker & Jones, 2016). Although the formation of chlorite has preserved the primary porosity in some areas of the Skagerrak Formation, later deposition of pore-filling chlorite has reduced the porosity in the sandstones, notably in the Seagull area (Quad 22/29) (Stricker et al., 2018). The later chlorite formation can be characterised by the growth of blocky, pore-filling chlorite, which significantly reduced the porosity in those sandstones (Nguyen et al., 2013). Along with the grain-coating chlorite and pore-filling chlorite, a minor amount of chlorite was also generated by replacement of detrital feldspar and biotite grains (Humphreys et al., 1989). However, the amounts generated would not have any discernible influence on the reservoir quality compared to the other types of chlorite found.

The grain-coating chlorite is largely confined to the facies towards the top of the succession, whereas the pore-filling chlorite is found throughout the Skagerrak Formation (Humphreys et al., 1989). The grain-coating chlorite could be an alteration of a precursor swelling chlorite or corrensite cement deposited as part of the marginal marine facies, while the origin of the pore-filling chlorite is likely to be that it precipitated from pore fluids (Humphreys et al., 1989). There is also an inverse relationship between the abundance of pore-filling chlorite and dolomite cement, which could indicate competition for the magnesium available in the rock. This is in contrast to the Jurassic sediments which did not contain elements conducive to chlorite growth i.e. Fe-poor, significant organic content, coastal plain to marine depositional setting (Smith et al., 1993).

2.3.3.2 Illite

Another major diagenetic mineral found in the Skagerrak Formation is illite, which is a common diagenetic mineral found in sandstones (Guven et al., 1980; Worden & Morad, 2003). There are several ways of producing illite depending on the temperature of the sandstone and available materials (Worden & Morad, 2003). For example, diagenetic illite can form from precursor smectite in the sandstone, with the smectite being replaced by the illite on a layer-by-layer basis. There are two chemical routes that can convert smectite to illite. Generally, one route requires minimal silica, but necessitates a supply of aluminium. The other requires minimal aluminium, but produces excess silica that could be deposited as quartz cement. Illitisation of smectite has the potential to release considerable amounts of Mg^{2+}, Fe^{2+}, Na^{+}, and Ca^{2+}. These ions are then utilised in diagenetic reactions within the same rock or adjacent lithologies. Illite can also be sourced from the transformation of K-feldspar and kaolin. The transformation of kaolinite into illite would occur at temperatures greater than 70^{O}C, but becomes pervasive at 130^{O}C. This process releases quartz which may be precipitated as quartz overgrowths (Worden & Morad, 2003).

The source of illite in the CNS is likely to be from the transformation and alteration of detrital smectite and mixed-layer clays (Bjørlykke & Aagaard, 1992; Weibel, 1999). However, the illite found in the Skagerrak Formation is similar in composition to the illite found in the Rotliegend sandstones (Smith et al., 1993). This type of illite is thought to be formed in highly saline waters, as would be found in proximity to a salt wall, at temperatures in excess of 100°C (Smith et al., 1993).

The prevalence of illite and smectite clays in the lower Triassic sandstones compared to kaolinite, a clay that is found in the upper Triassic sediments, indicates that the climate may have become more humid in the Late Triassic (Spark & Trewin, 1986; Weibel, 1999). The propensity for illite to form in highly saline waters and requiring a supply of potassium would suggest that illite formation would be localised in sediments adjacent to salt walls (Stricker et al., 2018).

2.3.3.3 K-Feldspar

It should be noted that dissolution of K-feldspar did produce some amount of secondary porosity (up to 5%), and another product from the dissolution of the K-feldspar was the release of potassium which would contribute to the formation of late stage illite (Worden & Morad, 2003; Nguyen et al., 2013). However, the dissolution of K-feldspar was only recognised as occurring at great depth (>3200 m) where most of the materials that would produce illite would have already been incorporated into other diagenetic minerals (Nguyen et al., 2013). Overall, at depths greater than 3200 m, the dissolution of K-feldspar would have provided a minor amount of increased porosity compared to the decrease in porosity caused by the illite formed from the potassium released by the K-feldspar (Nguyen et al., 2013).

3.3.3.4 Halite

A minor impact that has been discussed in a previous study is that brine could have infiltrated the sandstone and deposited halite within the pore space (Nguyen et al., 2013). The brine is likely to have been sourced from dissolution of the salt walls by meteoric fluids, and would therefore be an eodiagenetic process that would be more prevalent closer to the salt walls. This would have initially decreased porosity but it would have also resisted any mechanical compaction as the formation was buried. After burial, dissolution of the halite after exposure to water in the formation would free up the preserved pore space (Nguyen et al., 2013). It was believed from the study that this would have had little influence compared to other methods of porosity preservation, and if it did have a significant local impact, the diagenetic halite would not be extensive enough to substantially alter the petrophysical properties of the entire sandstone reservoir. However it could be hypothesised that the extent of halite would be greater for sandstones closer to the salt walls due to the proximity to a source of halite and the presence of deformation bands with enhanced porosity allowing for the pervasive infiltration of pore fluids into the surrounding sediment compared to undeformed sandstones within the mini-basin.

2.4 Methodology

2.4.1 Well selection and core photographs

Multiple core samples from wells in the Central Graben, North Sea were investigated using the British Geological Society (BGS) online database, which included photographs of the core sections. These core photographs consist of ~0.9 m (3ft.) core sections imaged at high resolution under white light. The cylindrical core samples from wells are cut in half along the length of the core sample to display the internal features prior to photographic imaging. The main purpose of using the photographs was to identify the wells that displayed the greatest abundance of deformation bands for further investigation. These core photographs were of sufficient quality that the pale deformation bands could easily be picked out from the darker coloured host rock (e.g. Fig. 2.18). The photographs were also used to identify significant features of the bands, such as the thickness of the bands, the interaction between cross-cutting sets of deformation bands, and relationships between the bands and visible sedimentary bedding features. Wells were selected using a 'pod' map (Neil Meadows (pers. Comm.)) which showed the locations of salt walls in relation to boreholes across the CNS, and was used in this study to identify wells that were on the margins of the mini-basins (Fig. 2.10). Used in conjunction with the core photographs from the BGS database, the aim was to find wells that were on the margin of salt walls and contained photographed core sections of the Skagerrak Formation (Fig. 2.10). Unfortunately, some wells did not have any core section photographs or the photographs available did not sample the Skagerrak Formation. Out of the wells that were proximal to a salt wall and sampled the Skagerrak Formation, five wells (including a sidetrack well) were selected which displayed an abundance of well-developed deformation bands (Table 2.1). The core photographs are complemented by the lithology analysis and interpretation included in the various well reports and well logs (Shell Exploration & Production (1991, 1992, 1993a, 1993b)). However, a factor to be considered is that the core runs,

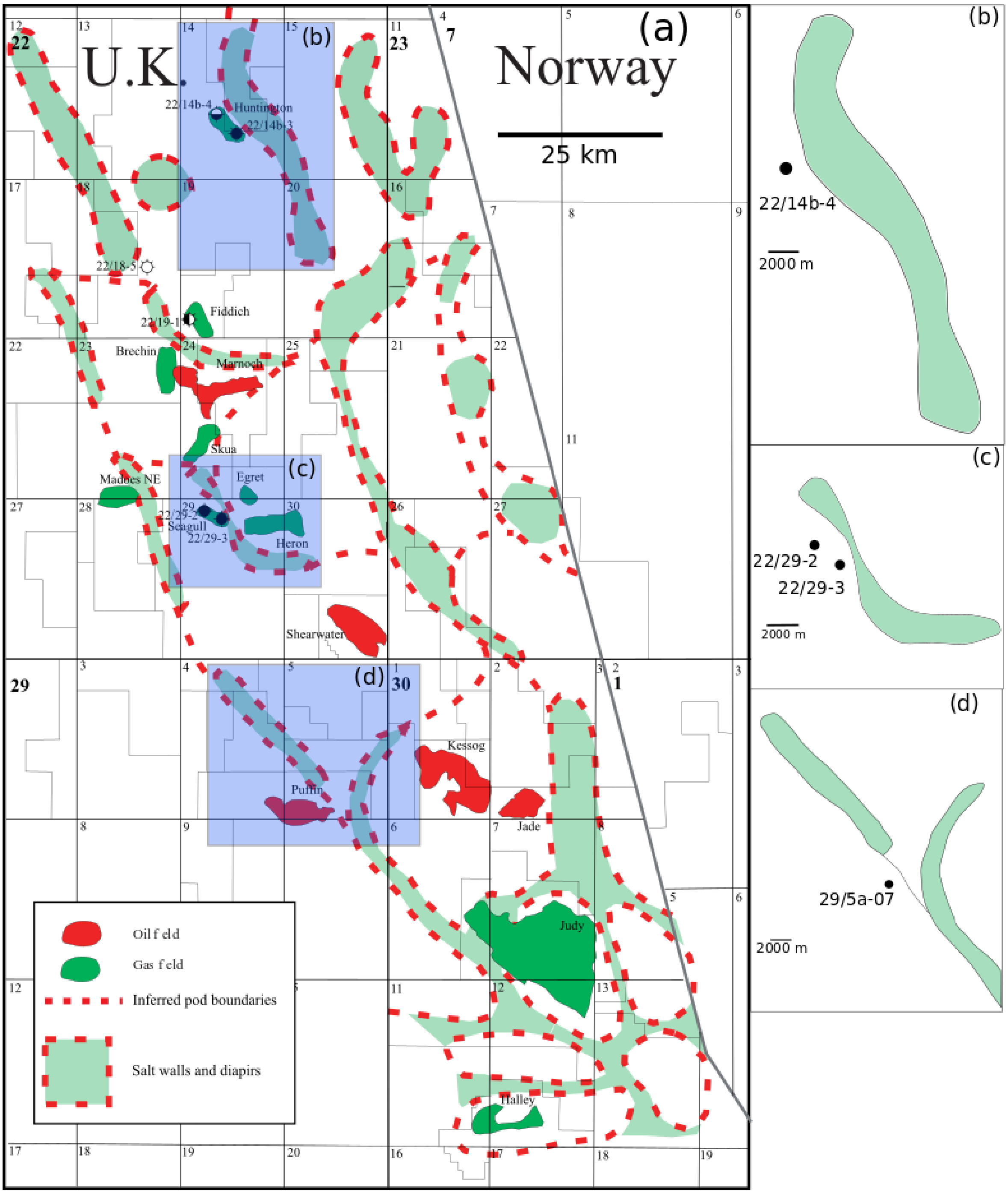

Figure 2.10 (a) Edited map of figure 1.9 highlighting the locations of wells used in this study and their proximity to modern day salt walls. (b) displays the proximity of the well in the Huntington field. (c) displays the proximity of the wells in the Seagull field. (d) displays the proximity of the well in the Puffin field. Tabulated distances of the wells from the salt walls are included in table 2.1.

Table 2.1: A list of wells which fulfilled the criteria of being located proximal to a salt wall and having available core photographs sampling the Skagerrak Formation. Wells are listed using the assigned well number, the specific field in the CNS that they occur, the cored interval (Measured Depths (MD) along the borehole from the drilling floor datum), and the datasets used in this study from each well. It should be noted that the proximity to the salt wall refers to the proximity of the well to the modern day location of the salt wall, and may not reflect the closest distance between the well sediments and salt wall in the wells history.

Well Number	**Field**	**Proximity to salt wall (m)**	**Core interval- Borehole depth m (ft.) MD**	**Datasets**
Well 22/14b- 4	Huntington	900	3725.9 – 3862.4 m (12224 – 12672 ft.)	Core Photographs UV Photographs Core data log
Well 22/29- 2	Seagull	1200	4073.0 – 4232.1 m (13363 – 13885 ft.)	Core Photographs Wireline logs
Well 22/29- 2S1 (offshoot)	Seagull	1200	4050.8 – 4480.6 m (13290 – 14700 ft.)	Interpreted FMI logs (dip logs)
Well 22/29- 3	Seagull	500	4137.1 – 4270.9 m (13573 – 14012 ft.)	Core Photographs, UV photographs, interpreted FMI logs (dip logs), core goniometry tables, thin sections, wireline logs.
Well 29/5a- 07	Puffin	1000	4420.8 – 4501.3 m (14504 – 14768 ft.)	Core Photographs

and thus core photographs, show varying degrees of continuity along the well (Fig. 2.11). This is due to the core samples being divided into core runs, which are non-regular sub-divisions of core sample over a specific length of an exploration well. Table 2.2 contains the well core data for well 22/29-3, which is separated into 6 core runs of varying length. It should be noted that the core runs for both well 22/29-2 and well 22/29-3 sampled Jurassic sediments along with the Skagerrak Formation, however, the tapered nature of sediment deposits in salt-wall mini-basins results in the retrieved core runs for well 22/29-3 sampling Mid- and Late- Jurassic sediments (Pentland Formation, Heather Formation, and Kimmeridge Clay Formation), whereas the core runs for well 22/29-2 sampled the Triassic and some of the Mid- and Late- Jurassic sediments (Pentland Formation and Kimmeridge Clay Formation) (Fig 2.11). The absence of core between core runs may or may not omit dense clusters of deformation bands from the core photograph database. Lithological observations in the well reports, such as grain size and facies type, are also omitted from core logs between core runs. It should therefore be noted that although the core photographs are not a fully comprehensive record of the sampled Skagerrak Formation within a well, it is assumed for this thesis that the available core photographs for a well are representative of the sampled Skagerrak Formation for that interval.

Ultraviolet (UV) photographs of the core section utilise UV light instead of white light to highlight fluorescence in core sections due to hydrocarbon staining in the well. These photographs were recorded alongside the white-light core photographs, and allow for comparison between features observed in the core section and the effect they had on fluorescent material abundance. Since hydrocarbons fluoresce under UV light, this method can indicate the prospectivity of the sampled section, depending on the intensity of fluorescence from the core section. In the context of this study, if differential staining of the sandstones on either side of the deformation bands can be observed, it may provide an indication of the ability of the band to act as a baffle to hydrocarbon migration. Another effect of UV light is that some mineral deposits within the deformation band may fluoresce, helping to identify the bands if they cannot be easily seen in the standard photographs. Tests have shown that illite can fluoresce under UV light instead of being a remnant of hydrocarbons and has been used to observe relationships between diagenetic illite and other authigenic phases (Lemon & Cubitt, 2009). The uncertainty involved in this process is if there is no hydrocarbon staining within the sandstone, any potential baffling effect may not be observed. Fluorescent diagenetic or detrital material in the sandstones could also give a false positive for the presence of hydrocarbons. UV photographs were available for well 22/14b-4 and well 22/29-3 (Table 2.1)(Shell Exploration & Production, 1991, 1993b).

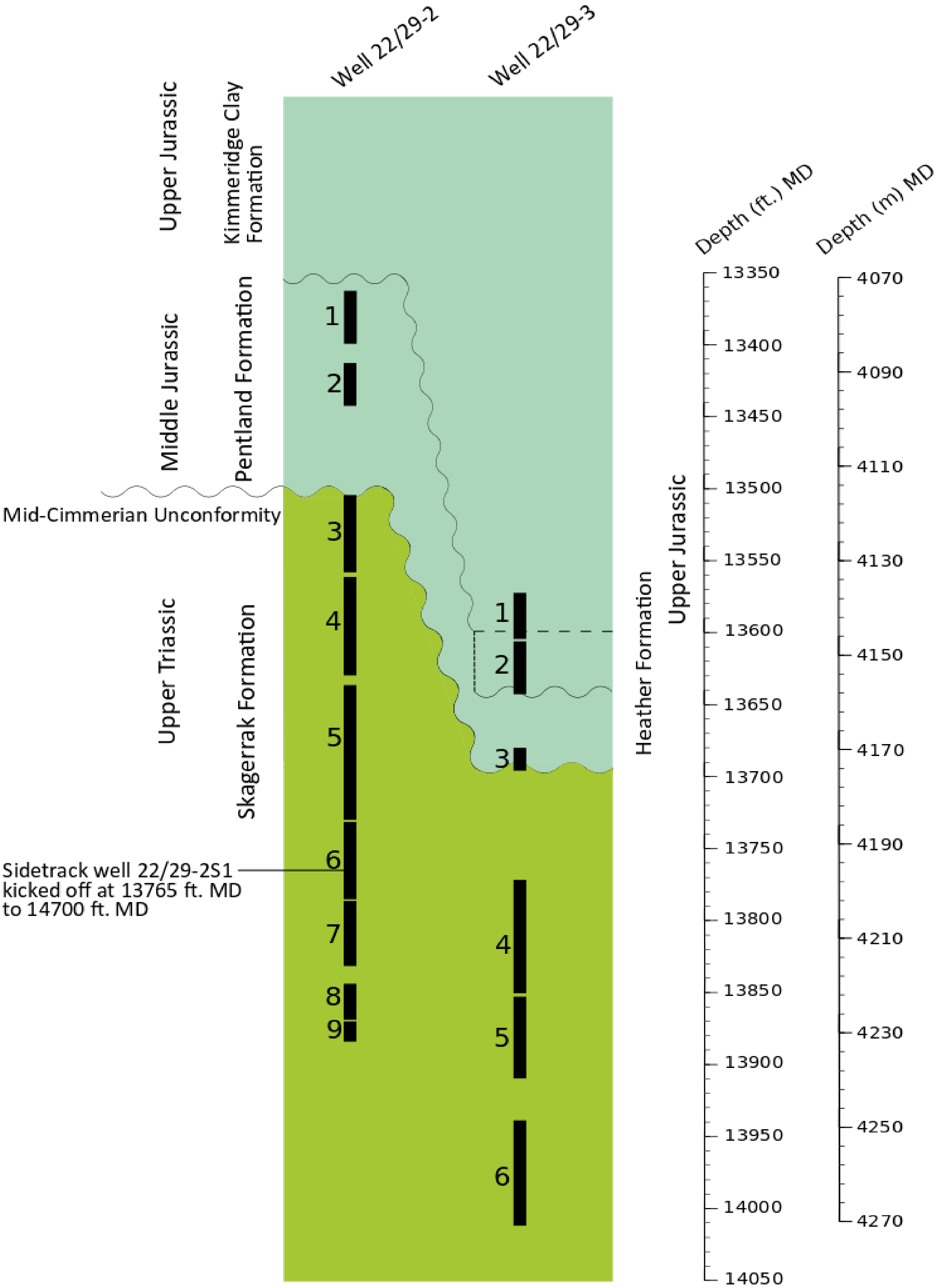

Figure 2.11: Simplified stratigraphic column highlighting the studied intervals from well 22/29-2 and well 22/29-3, based on interpreted wireline logs (Shell Exploration and Production, 1993a). Both wells sample the Skagerrak Formation, Middle Jurassic Pentland Formation and Upper Jurassic Kimmeridge Clay Formation, but the Upper Jurassic Heather Formation is present only in well 22/29-3 (core run 2). The numbers and black bars are representative of the core run intervals at depth. The sidetrack well 22/29-2S1 kickoff is included, although this well does not contain individual core runs.

Table 2.2: An example of core run divisions using well 22/29-3, in which both Jurassic and Triassic formations are sampled. This table shows the lack of continuity across the core runs, as well as the variable lengths sampled by individual core runs. The largest gap between core runs occurs between core run 3 and core run 4 (22.8 m/ 75 ft.).

Well 22/29-3			
Depth Interval (ft.) MD	**Depth Interval (m) MD**	**Core Run Number**	**Formation Sampled**
13573 - 13605	4137.1 – 4146.8	Core Run 1	Kimmeridge Formation
13607 - 13642	4147.4 – 4158.1	Core Run 2	Heather Formation
13680 - 13696	4169.6 – 4174.5	Core Run 3	Pentland/Skagerrak Formation
13771 - 13850	4197.4 – 4221.5	Core Run 4	Skagerrak Formation
13853 - 13910	4222.4 – 4239.8	Core Run 5	Skagerrak Formation
13939 - 14012	4248.6 – 4270.9	Core Run 6	Skagerrak Formation

Table 2.3: Depths of the thin section samples from well 22/29-3 with facies association and grain sizes based on the well report for well 22/29-3. Grain sizes refer to sandstone.

Depth m (ft.) MD	**Facies**	**Grain size**
4203.34 (13790.5)	S3	Fine grained
4212.27 (13819.8)	C3	Fine grained
4219.16 (13842.4)	C4	Fine to very-fine grained
4228.34 (13872.5)	S3	Very fine grained
4234.83 (13893.8)	S2	Fine grained

2.4.2 Thin sections

Large thin sections (approximately 40 mm x 40 mm) from Seagull well 22/29-3 containing deformation bands were prepared using blue-stained epoxy to highlight porosity within the thin section. The depths of these samples are representative of the channel-fill and terminal splay facies found within the Skagerrak Formation sandstone member, based on the stratigraphy and lithofacies associations presented in the well reports (Shell Exploration & Production, 1993a). Table 2.3 presents the sample depths, lithofacies and grain size for each sample, based on the well report. The lithofacies associations from the well report are as follows:

- S2—Sheetflood deposit with a typical sequence showing evidence for a rapidly falling water level towards the end of a flooding event.
- S3 – Sheetflood deposit which displays low energy deposits and is inferred to have been a distal sheetflood deposit.

- C3 – Incomplete channel bar accretion or the development of minor sandflats initiated by the emergence of cross-channel bars.
- C4 – Deposits within minor, very ephemeral, braided channels.

The main focus when analysing the thin sections was to identify the relationship between the deformation bands and the surrounding grain framework, with lithological analysis supplemented by other studies. Where possible, the relationships between intersecting bands was also visually analysed to see if the relative history of formation could be ascertained.

Point counting was used to provide an estimate of the variation in mineral grain abundance and clay minerals between the deformation bands and the host rock. This method was performed on straight deformation bands which displayed a uniform thickness in thin sections representative of channel deposits and sheetflood deposits. Point counts of grains, clay minerals and porosity were conducted along multiple transects parallel to the deformation band. This was used to generate a graph of thin section constituents against transect distance across the deformation band (method from Du Bernard et al., 2002).

Further analysis was carried out using composite wireline logs for well 22/29-2 and well 22/29-3, which recorded gamma ray intensity, borehole compensated sonic log, composite neutron density, compensated density logs, resistivity, porosity, and permeability (Appendices A + B) (Shell Exploration and Production, 1993a). Comparison of these values over depth intervals with a high density of deformation bands, and a negligible abundance of deformation bands within various types of facies can further reveal the influence of deformation bands on sandstones. Gamma ray logs measure the radioactivity of the formation (American Petroleum Institute (API) units), and act as a proxy for the amount of shale in a formation. “Clean” sandstone units (<50 API) comprised mainly of quartz typically display low radioactivity, while inclusions such as feldspars and micas can increase the gamma ray count. Density logs measure the density of the formation and neutron logs (measured in units of porosity (PU)) act as a proxy for pore space based on the presence of hydrogen (from water or hydrocarbons) in pore spaces, and combining these logs indicate the porosity along the formation. Resistivity (measured in ohm metres) measures the resistivity of the formation and provides an indicator for fluids in the pore spaces. Hydrocarbons have a higher resistivity compared to saline water, while freshwater will have a higher resistivity compared to hydrocarbons. Porosity and permeability are directly measured by extracting core plug samples, which are then plotted onto the composite wireline log.

2.5 Results

2.5.1 Core analysis

Deformation bands in the selected wells were identified in the core sections due to their pale colouration compared to the host rock. Most deformation bands display a uniform thickness of 1 mm with some examples exceeding thicknesses of 15 – 20 mm within dense clusters of deformation bands. Apparent dips of the deformation bands ranged from sub-vertical to horizontal, with most of the apparent dips tending towards >30° and <60° from horizontal, along with examples of oppositely dipping conjugate sets. However, measuring apparent dips from core photographs may not reflect accurate orientation data, these apparent dips can act as an indicator of deformation band steepness when measured against horizontal bedding features. This is rectified for well 22/29-2S1 and well 22/29-3, where orientated FMI data and core goniometry are available for the deformation bands (Chapter 3).

2.5.1.1 Deformation band distribution

For this section depths are given as measured depths along the borehole (MD) with the datum set at the drilling floor. Equivalent True Vertical Depths (TVDSS) can be found plotted on the wireline logs (Appendices A + B). Deformation band abundances are unlikely to correlate across all the selected wells since each well occurs adjacent to different salt walls, with the exception of wells 22/29-2 and 22/29-3.

2.5.1.1.1 Well 22/14b-4

For well 22/14b-4 in the Huntington Field (3725.9 – 3840.8 m MD/ 12224 – 12601 ft. MD), all of the observed deformation bands occur within the top 36.5 m (120 ft.) of the core section (3725.9 – 3763.6 m MD/ 12224 – 12348 ft. MD). Higher abundance of deformation bands (> 7 bands per metre) are found at multiple intervals within this top 36.5 m interval at 3725.9 m MD (12224 ft. MD); 3738.7 m MD (12266 ft. MD); and 3752.7 m MD (12312 ft. MD). There is a sparse abundance of deformation bands between these intervals of < 3 bands per metre prior to the absence of deformation bands at depths greater than 3762.8 m MD (12345 ft. MD). Although this well contained the lowest number of deformation bands from the wells observed, primarily due to the short depth range over which the bands were observed, the abundance density of deformation bands are comparable to the other wells investigated.

The modal thickness of the deformation bands in well 22/14b-4 was observed to be 1 mm in thickness (47%) (Fig 2.12). The thicknesses of bands that were less than 1 mm and 2 mm are both similarly abundant (22% and 25%, respectively). Thicker bands of width 5 mm and 10 mm are observed in decreasing abundance (4% and 2%, respectively). The thickest band observed in the cored interval was 10 mm (3727.09 m (12228.0 ft.) MD).

It must be noted that the above deformation band thicknesses are observed thicknesses rather than measured thicknesses due to the core photographs being 2-dimensional representations of planar band features.

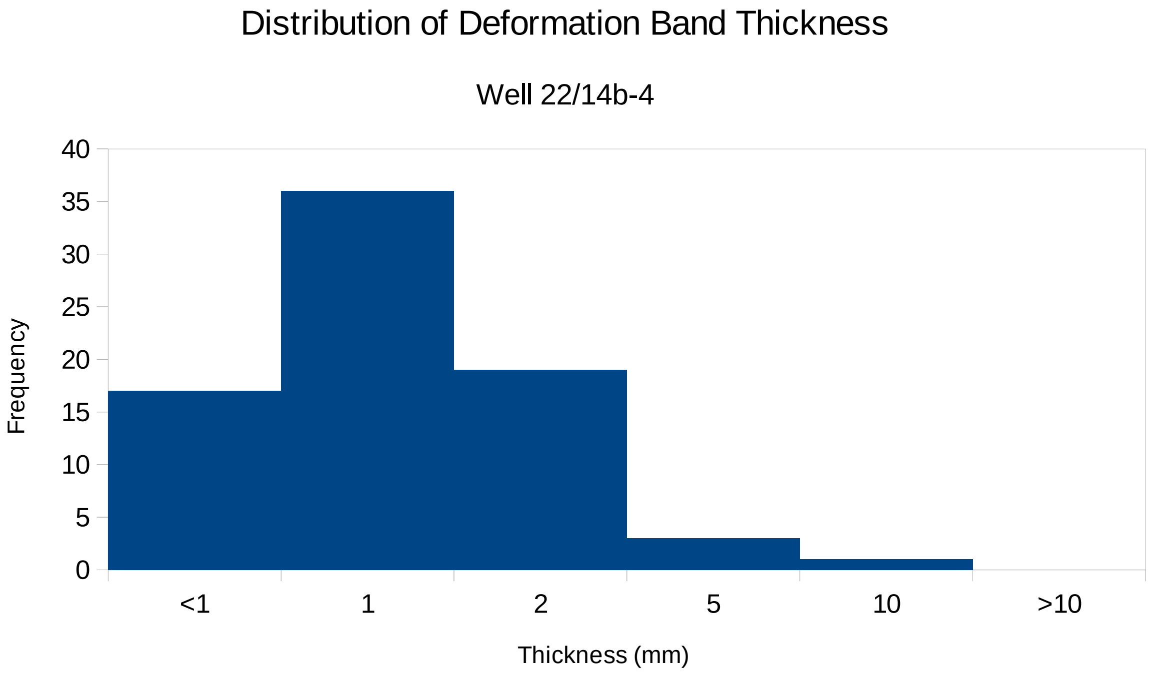

Figure 2.12: Graph showing the distribution of deformation band thicknesses for well 22/14b-4, based on core photographs (BGS).

2.5.1.1.2 Well 29/05a-7

For well 29/05a-7 in the Puffin Field, high abundances of deformation bands were observed throughout the whole core section (4420.8 – 4501.3 m MD/ 14504 – 14768 ft. MD), with each core run displaying zones with high abundances of deformation bands (> 10 bands per metre). This well contained the highest abundance of deformation bands out of the wells observed.

The modal thickness of the deformation bands in well 29/05a-7 was observed to be 1 mm in thickness (43%) (Fig 2.13). The thicknesses of bands that were less than 1 mm and 2 mm are both similarly abundant (24% and 22%, respectively). Thicker bands of width 5 mm, 10 mm, and > 10 mm are observed in decreasing abundance (6%, 3%, and 2%, respectively). The thickest band observed in the cored interval was 30 mm (4485.3 (14715 ft.) MD) as part of a dense population of bands.

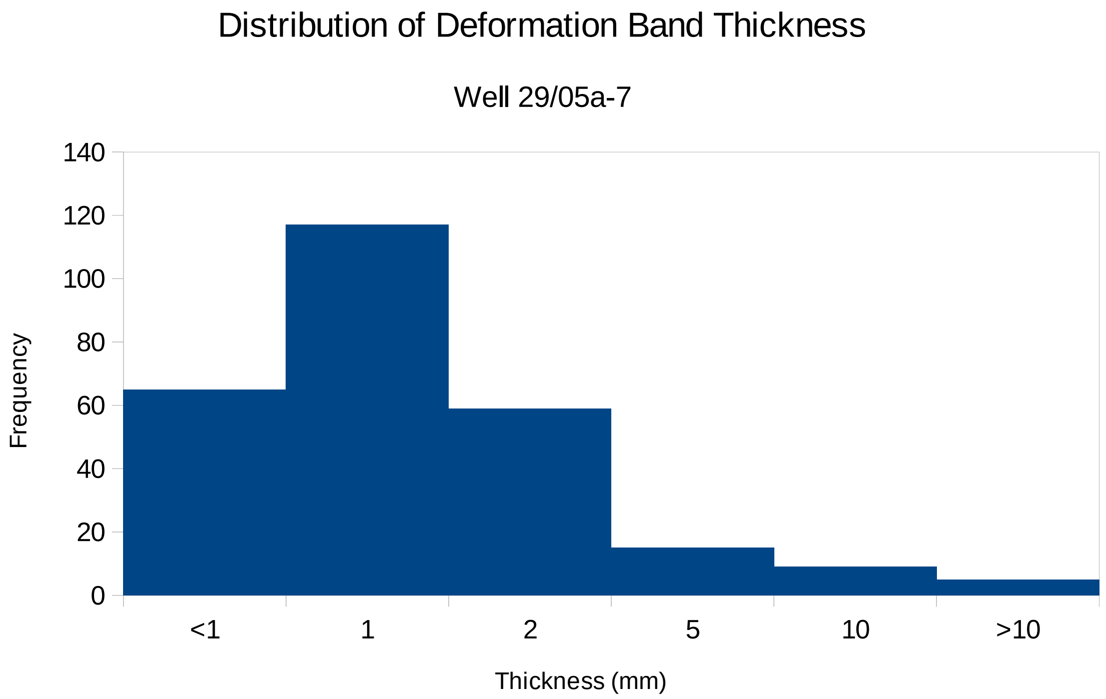

Figure 2.13: Graph showing the distribution of deformation band thicknesses for well 29/05a-7, based on core photographs (BGS).

2.5.1.1.3 Well 22/29-2 and 22/29-2S1

Well 22/29-2 in the Seagull Field displays deformation bands throughout most of the sampled Skagerrak Formation core section (4133.7 – 4232.1 m MD/ 13562 – 13885 ft. MD) (Fig. 2.14), but the frequency of the deformation band distribution is much lower than that of well 29/05a- 7. There are intervals along well 22/29- 2 that contain little to no deformation bands, with core run #2 (4088.3 – 4097.4 m MD/ 13413 – 13443 ft. MD) showing only one zone that contains deformation bands (4093.8 – 4094.6 m MD/ 13431.0 – 13433.7 ft. MD). Due to the absence of available core photographs for well 22/29-2S1, it is assumed that well 22/29-2 is representative of the deformation band abundance present in the sidetrack well (22/29-2S1).

The modal thickness of the deformation bands in well 22/29-2 was observed to be 1 mm in thickness (44%) (Fig 2.15). The thicknesses of bands that were less than 1 mm and 2 mm are both similarly abundant (24% and 22%, respectively). Thicker bands of width 5 mm, 10 mm, and > 10 mm are observed in decreasing abundance (6%, 2%, and 1%, respectively). The thickest band observed in the cored interval was 15 mm (4209.44 m (13810.5 ft.) MD).

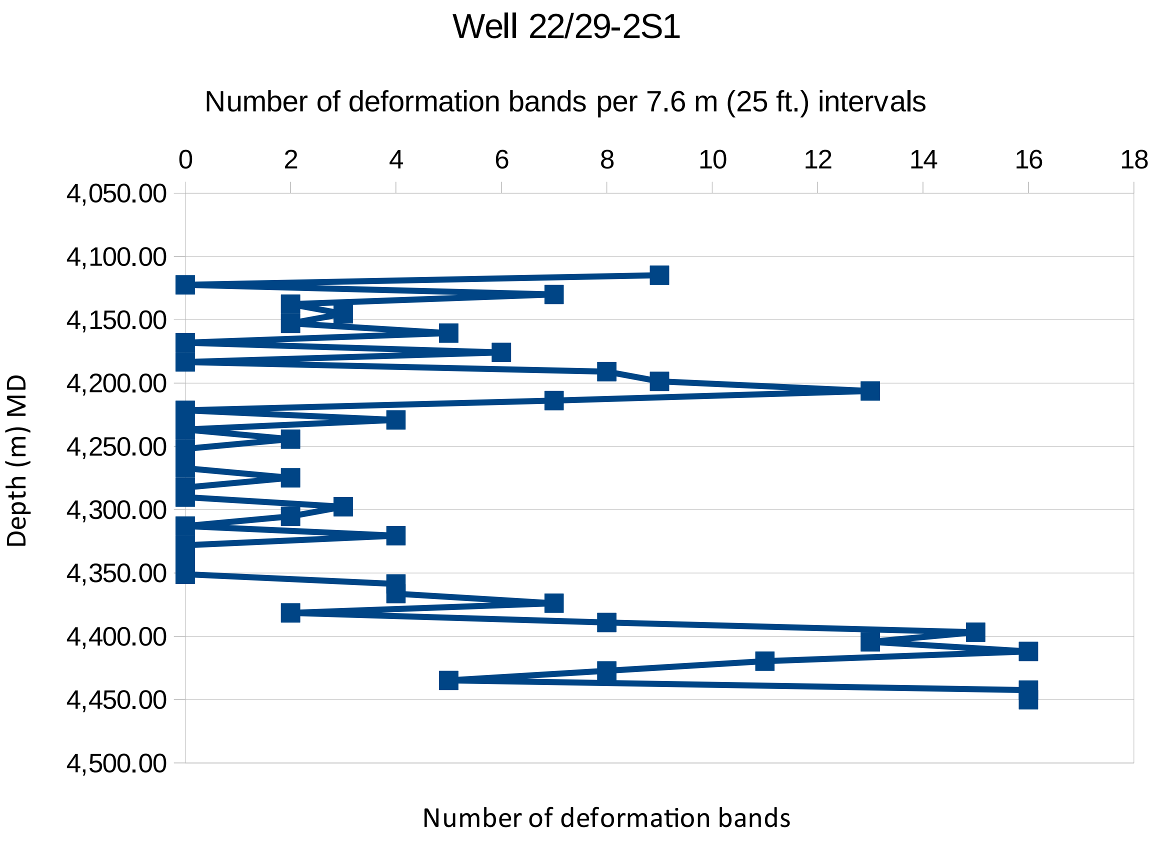

Figure 2.14: Graph showing the number of deformation bands per unit depth (7.6 m/ 25 ft. intervals) for well 22/29- 2 S1. Depths are shown as measured depths (MD) from the drilling floor datum. Data from interpreted FMI data (Shell Exploration and Production, 1992b).

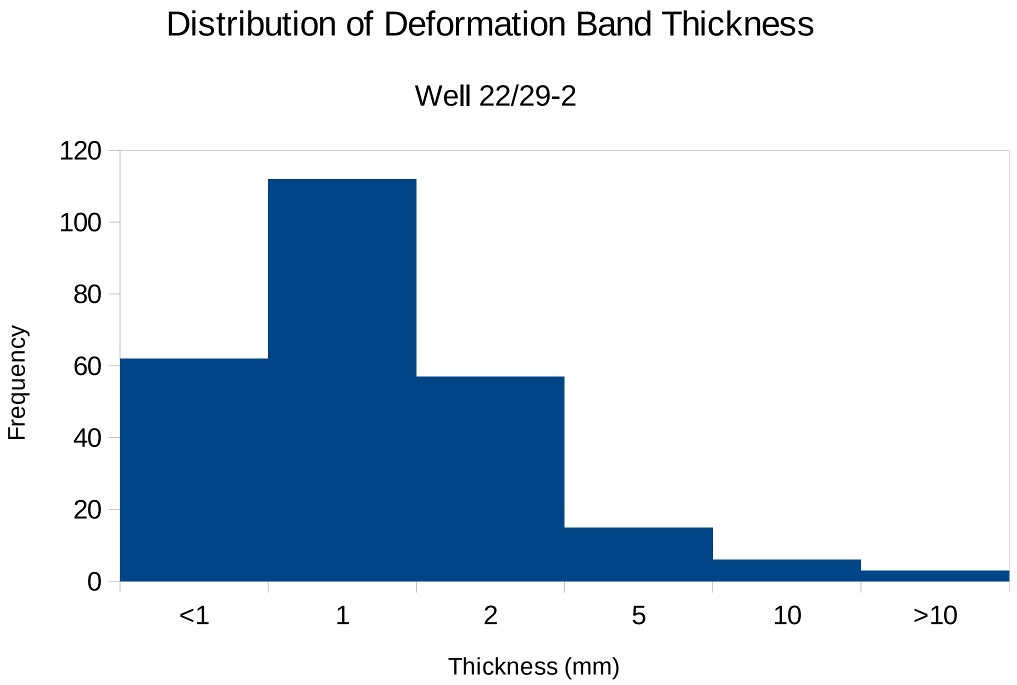

Figure 2.15: Graph showing the distribution of deformation band thicknesses for well 22/29-3, based on core photographs (BGS).

2.5.1.1.4 Well 22/29-3

The sampled Judy Sandstone Member of well 22/29-3 (4174.2 – 4270.9 m MD/ 13695 – 14012 ft. MD) displays a significant abundance of deformation bands throughout the cored intervals (Fig. 2.16). The abundance of deformation bands significantly decreases in the core photographs along core run #6 (4248.6 – 4270.8 m MD/ 13939 – 14012 ft. MD) with few zones displaying deformation bands. Although this well samples a shorter portion of the Upper Skagerrak Formation compared to well 22/29-2, well 22/29-3 shows consistently higher densities of deformation bands in the available section (> 5 per metre). This well also samples overlying Middle and Late Jurassic sediments (Fig.2.10), which both display significantly fewer deformation bands compared to the Judy Sandstone Member (averaging < 1 band per metre).

The modal thickness of the deformation bands in well 22/29-3 was observed to be 1 mm in thickness (45%) (Fig. 2.17). The thicknesses of bands that were less than 1 mm and 2 mm are both comparably abundant (25% and 20%, respectively). Thicker bands of width 5 mm, 10 mm, and > 10 mm are observed in decreasing abundance (5%, 3%, and 2%, respectively). The thickest band observed in the cored interval was 45 mm (MD 13872.5 ft.), although this may result from the planar surface of the deformation band being cross-cut by the core image at a similar angle to the deformation band orientation.

As previously mentioned, the measurements given are apparent thicknesses as opposed to measured thicknesses.

2.5.1.2 Wireline Logs

This section compares wireline log measurements between zones of high deformation band abundance and low deformation band abundance along well 22/29-2 and well 22/29-3 (Shell Exploration and Production, 1993) (Figs. in appendices A + B). The comparisons focus on the relationship between the reservoir quality of the sandstones, the facies and lithologies identified along the formation, and the abundance or absence of deformation bands along the wells. Unfortunately, the facies interpretation included with the composite wireline log for well 22/29-2 is not included for core runs 5 – 9. However, another wireline log for well 22/29-2 includes core runs 5 – 9, but did not include grain size data or measured porosity and permeability data. Specific intervals of the composite wireline logs will be utilised when investigating features observed along the core section (sections 2.5.1.3 – 2.5.1.5).

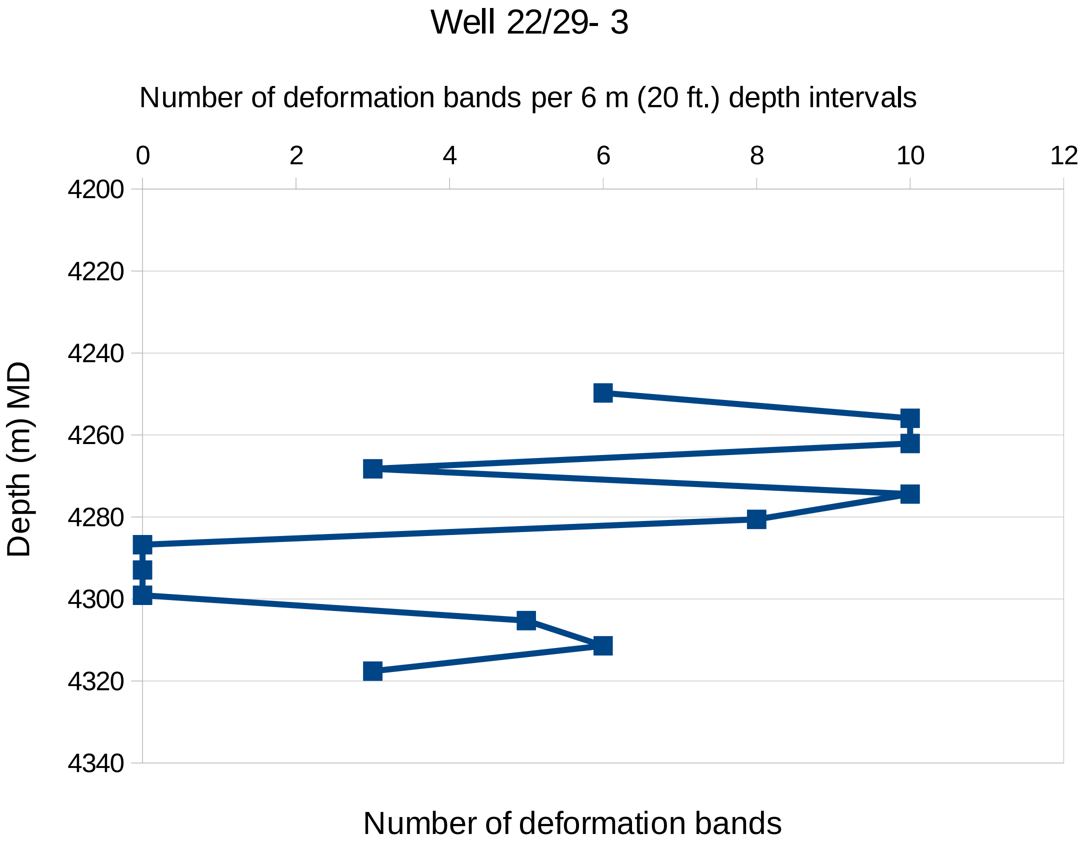

Figure 2.16: Graph showing the number of deformation bands per unit depth (6 m/ 20 ft. intervals) for well 22/29-3. Depths are shown as measured depths (MD) from the drilling floor datum. Data from core goniometry data (Shell Exploration and Production, 1993b).

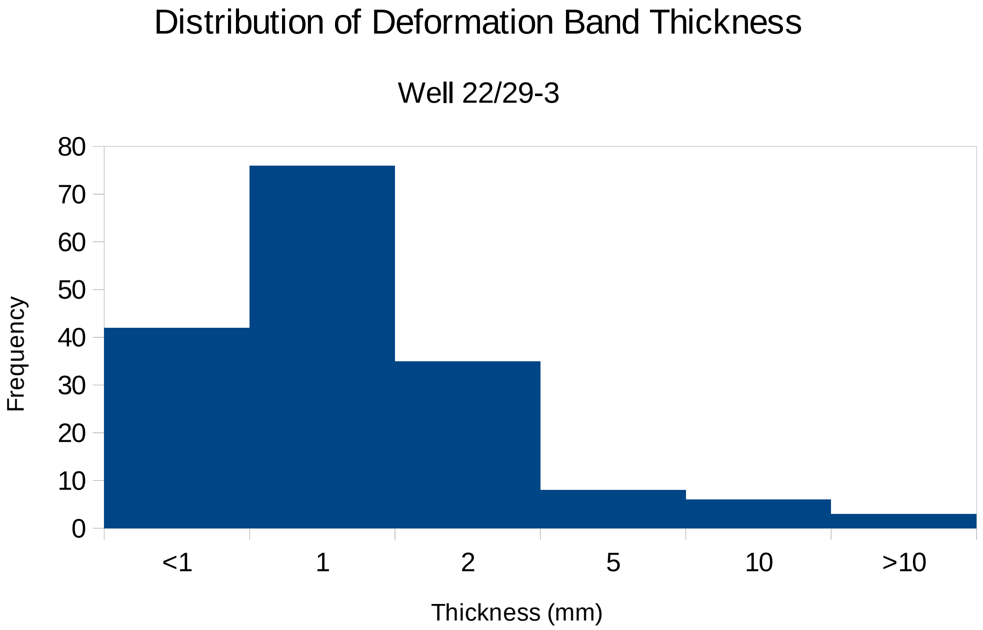

Figure 2.17: Graph showing the distribution of deformation band thicknesses for well 22/29-3, based on core photographs (BGS).

2.5.1.2.1 Wireline logs in Well 22/29-2

The interpreted wireline log indicates that the entirety of the cored interval in well 22/29-2 is from the hydrocarbon leg of the Pentland Formation and Skagerrak Formation reservoir, without any indication of intersecting a hydrocarbon-water contact (HWC). Drill stem testing (DST) was successfully performed, although the production rates from the DSTs were not available for this study.

For well 22/29-2, the Mid-Cimmerian Unconformity is identified at 4112.67 m (13943 ft.)MD, with the Skagerrak Formation sampled by core run 3 to core run 9 (4116.02 m – 4232.15 m (13504 ft. - 13885 ft.) MD).

The wireline log across the Mid-Cimmerian Unconformity displays a decrease in GR from 84 API to 61 API with the sonic log decreasing from 91 µsecs/ft. to 80 µsecs/ft. across this interval. The formation density log and neutron log measured a decrease from 2.55 gr/cc to 2.42 gr/cc and a decrease from 32 PU to 15 PU respectively. Resistivity recorded an increase from 1 ohm metre to approximately 2 ohm metres.

Core run 3 contains an interval that does not contain any deformation bands (4121.5 – 4129.4 m (13522 – 13548 ft.) MD). The gamma ray log for this zone fluctuated between 45 API and 75 API with lower peaks associated with coarser units. Sonic density fluctuated between 85 µsecs/ft. and 95 µsecs/ft. with resistivity exhibiting no fluctuations and remaining between 1 ohm metres and 2 ohm metres for this interval. The formation density log and neutron log measured an increase from 2.26 gr/cc to 2.39 gr/cc and fluctuated between 14 PU and 19 PU respectively. Helium porosity in this interval peaked at 28% and remained above 10% porosity. Horizontal permeability ranged from 1 mD to 100 mD, with the higher permeabilities occurring within the coarser-grained lithologies.

The gamma ray log for the sections of core run 3 that contain deformation bands ranges from 35 API to 75 API, with the weaker gamma rays measured in the coarser-grained lithologies. Sonic density fluctuated between 85 µsecs/ft. and 95 µsecs/ft. for this interval. The formation density log and neutron log measured an increase from 2.26 gr/cc to 2.39 gr/cc and fluctuated between 14 PU and 19 PU respectively. Resistivity decreased down the core run from 4 ohm metres to 1 ohm metres. Helium porosity ranged between 12% and 23%, with higher porosity values occurring in coarser-grained units. Lower porosities typically coincided with finer-grained lithologies although a porosity low of 12% occurred in a medium-grained sandstone unit 4119.7 m (13516 ft.) MD). Horizontal permeability ranged between 1 mD and 500 mD, with lower permeabilities typically measured in finer-grained lithologies, apart from the exception mentioned above in porosity.

Core run 4 contains two intervals that do not contain any deformation bands at 4145.3 – 4148.3 m (13600 – 13610 ft.) MD) which samples a very-fine grained to silty sandstone, and 4149.5 – 4153.8 m (13614 – 13628 ft.) MD which samples a medium-grained sandstone. The gamma ray log for these zones fluctuated between 42 API and 66 API with lower peaks associated with the more coarse unit. Sonic density fluctuated between 76 µsecs/ft. in the coarser interval and 84 µsecs/ft. in the finer-grained interval. The formation density log measured 2.35 gr/cc in the finer-grained interval and 2.20 gr/cc and in the coarser interval with the neutron log measuring 12 PU in the finer-grained interval and 15 PU in the coarser interval. Helium porosity for the very-fine grained interval was 14% and peaked at 27% in the coarser interval. Horizontal permeability in the fine-grained interval decreased from 100 mD to 1 mD, while permeability peaked at >100 mD in the coarser interval.

The gamma ray log for the sections of core run 4 that contain deformation bands ranged from 42 API to 75 API, with no apparent correlation to changes of the grain size within the varying facies. Sonic density fluctuated between 34 µsecs/ft. and 43 µsecs/ft. for this interval. The formation density log and neutron log measured fluctuations between 2.22 gr/cc to 2.40 gr/cc and fluctuations between 17 PU and 23 PU respectively. Helium porosity ranged between 11% and 26%, with the lowest porosity measured in a conglomerate layer (4138.9 m (13579 ft.) MD), although other conglomerate layers present in core run 4 did not display significant drops in porosity. Horizontal permeability typically ranged between 1 mD and 100 mD, with one exception at 4148.0 m (13609 ft.) MD where permeability dropped to 0.1 mD within a very-fine grained sandstone unit. Overall, higher horizontal permeabilities were measured in coarser units (medium-grained) than finer units (fine-grained).

2.5.1.2.2 Wireline logs in Well 22/29-3

The interpreted wireline log indicated that cores 1 – 5 are above the HWC (4249.82 m (13943 ft.) MD), with core run 6 located below the HWC. Drill stem tests were performed, although similar to well 22/29-2, production rates from the DSTs were not available for this study.

For well 22/29-3, the Mid-Cimmerian Unconformity is identified at 4173.93 m (13694 ft.) MD, with the Skagerrak Formation sampled by core run 4 to core run 6 (4197.40 m – 4270.86 m (13771 ft. - 14012 ft.) MD).

The wireline log across the Mid-Cimmerian Unconformity displayed a decrease in GR from 67 API to 40 API with the sonic log decreasing from 88 µsecs/ft. to 80 µsecs/ft. across this interval. The formation density log and neutron log measured a decrease from 2.30 gr/cc to 2.43 gr/cc and a decrease from 32 PU to 24 PU respectively. Resistivity recorded an increase from 1 ohm metre to approximately 2 ohm metres.

The majority of core runs 1, 2, and 3 (4137.1 – 4174.5 m (13573 – 13696 ft.) MD) displayed a low abundance of deformation bands, as did the core samples below 4260.5 m (13978 ft.) MD. It should also be noted that these core runs do not sample the Skagerrak Formation.

Core run 4 contains two intervals that did not contain any deformation bands at 4200.1 – 4202.9 m (13780 – 13789 ft.) which sampled a fine-grained sandstone unit, and 4213.9 – 4218.1 m (13825 – 13839 ft.) MD, which sampled a very fine- to silty- sedimentary unit with a medium-fine grain size sedimentary unit within the interval. The gamma ray log for these zones fluctuated between 53 API and 58 API for the fine-grained interval and 67 API in the silty unit, decreasing to 38 API in the medium-fine grained unit. Sonic density decreased slightly from 91 µsecs/ft. to 82 µsecs/ft. in the fine-grained deposit, while the silty and medium-fine grained deposit displayed a relatively consistent sonic density of approximately 77 µsecs/ft. across both units. The formation density log measured a decrease from 2.45 gr/cc to 2.36 gr/cc for the fine-grained deposit and fluctuated between 2.40 gr/cc and 2.50 gr/cc for the silty and medium-fine grained deposit, with no significant measured differences between the different grain sized deposits. The neutron log for the fine-grained interval decreased from 28 PU to 22 PU. The neutron log in the mixed grain-size deposit measured 18 PU in the silty component and 22 PU in the coarser grained deposit. Helium porosity for the fine-grained interval peaked at 20% and decreased to 15%, while helium porosity for the silty deposit increased from 7% to 15% in the coarser deposit. Horizontal porosity in the fine-grained deposit decreased from ~100 mD to 0.1 mD while the porosity in the silt deposit increased from 0.01 mD to 5 mD in the coarser deposit.

The gamma ray log for the sections of core run 4 that contained deformation bands fluctuated between 48 API and 78 API, with the sonic log fluctuating between 77 µsecs/ft. and 81 µsecs/ft. over the interval. The lower gamma ray values and lower sonic measurements for this interval occurred in the coarser deposits. The formation density log fluctuated between 2.55 gr/cc and 2.40 gr/cc and the neutron log displayed a range of 20 PU to 28 PU with the lower neutron values occurring in silty/clay deposits. The helium porosity fluctuated between 10% and 15%, with the horizontal permeability fluctuating between 0.01 mD and 5 mD along the interval, although there was no significant difference between grain size and porosity/permeability fluctuations in this interval.

The gamma ray log for the sections of core run 5 that contained deformation bands fluctuated between 48 API and 78 API, with the sonic log fluctuating between 77 µsecs/ft. and 81 µsecs/ft. with the lower gamma ray values and lower sonic measurements occurring in the coarser deposits. The formation density log fluctuated between 2.55 gr/cc and 2.40 gr/cc and the neutron log displayed a range of 20 PU to 28 PU. The helium porosity fluctuated between 10% and 15%, with the horizontal permeability fluctuating between 0.01 mD and 5 mD along the interval.

Core run 5 contained deformation bands along the entire core run (4222.39 – 4239.77 m (13853 – 13910 ft.) MD), but deformation bands above 4229.1 m (13875 ft.) MD were less cemented than other deformation bands in this interval. The gamma ray log measured a gradual decrease from 95 API to 50 API over the interval 4224.5 m (13860 ft.) MD to 4233.6 m (13890 ft.) MD, which occurred in conjunction with a gradual increase in grain size from silty to fine-grained. However, the sonic density for this increasing grain size remained relatively constant at 80 µsecs/ft. (±2 µsecs/ft.). The formation density and neutron log for this increasing grain size interval decreased from 2.60 gr/cc to 2.40 gr/cc and 30 PU to 20 PU, respectively. Although it should be noted that the neutron log decreased to 16 PU at 4230.01 m (13878 ft.) MD before increasing to 20 PU in the coarser deposits. Helium porosity in this interval fluctuated between 7% and 18% with a dip also at 4230.01 m (13878 ft.) MD, where the porosity decreased to 8%. Permeability also fluctuated along this interval, but displayed an overall trend from 0.01 mD to 5 mD also with a dip to 0.05 mD at 4230.01 m (13878 ft.) MD. It should be noted that the core sample at 4230.01 m (13878 ft.) MD is absent from the core photographs.

Core run 6 contained cemented deformation bands along the entire core run and thus comparison with lesser deformed intervals or cemented intervals was difficult. The gamma ray log fluctuated between 50 API and 75 API, although it tended towards 70 API below 4265.1 m (13993 ft.) MD, which was possibly due to the decrease in grain size towards very-fine grained. Sonic density tended towards 95 µsecs/ft. above 4265.1 m (13993 ft.) MD, and 91 µsecs/ft. below the grain size decrease. Formation density was also measured to have a gradual overall increase across this transition from 2.40 gr/cc to 2.55 gr/cc with neutron density displaying an overall decrease across this transition from ~25 PU to ~17 PU. Helium porosity fluctuated between 9% - 18% above the transition, and fluctuated between 7% and 14% below the transition. Similarly, the permeability above the transition fluctuated between 0.02 mD and 5 mD, and fluctuated between 0.01 mD and 1 mD below the transition.

2.5.1.3 Offsets along the deformation bands

The deformation bands in the core photographs are observed cross-cutting other deformation bands and some stratigraphic features, such as sedimentary bedding. Almost all deformation bands that were observed to cross-cut bedding or deformation features display a degree of shear offset (mm – cm scale) with a few examples of deformation bands not producing a shear offset when cross-cutting other deformation bands or bedding features (Figs. 2.18 & 2.19). However, not all deformation bands were observed to cross-cut planar features, so it was not possible to accurately quantify the amount of deformation bands which have a shear component against the amount of deformation bands which were only dilational. The average offset observed across the wells was <10 mm, with some exceptions exceeding 20 mm of offset, although no correlation was observed between the thickness of the deformation band and the degree of offset along their length (Fig. 2.18d & e). The narrow width of the core sections (<100 mm) may have excluded offsets further along horizontal bands, but this would have had little effect on sub-vertical bands where the entirety of the offsets can be observed. It should be noted that only the vertical component of offsets could be observed due to the 2-dimensional perspective of the core section photographs not presenting an indicator of lateral offset. Where shear displacements are observed, the offset is typically in the down-dip direction, akin to normal faulting. While offsets are commonly observed along deformation bands, Fig. 2.19 shows an example of a deformation band cross-cutting planar features with no visible offset. The wireline log measurements for Figure 2.18d display a GR intensity of 52 API, formation density log and neutron log of 2.5 gr/cc and 16 PU respectively. Resistivity records a value of less than 2 ohm metres. These values do not exceed the range for undeformed sandstone in this well. The wireline log measurements for the conjugate set observed in figure 4.3e display a GR intensity of 53 API, formation density log and neutron log of 2.43 gr/cc and 21 PU. Helium porosity for the interval is 12% and horizontal permeability measures less than 1 mD. Grain density is observed to decrease from 2.61 g/cc to 2.56 g/cc. These values do not exceed the range of values measured in undeformed sandstone intervals for this well. The wireline log for Figure 2.18e is included with the analysis of the wireline log for the deformed interval of core run 4 in well 22/29-3 and also does not exceed the range of measurements observed (section 2.5.1.2.2).

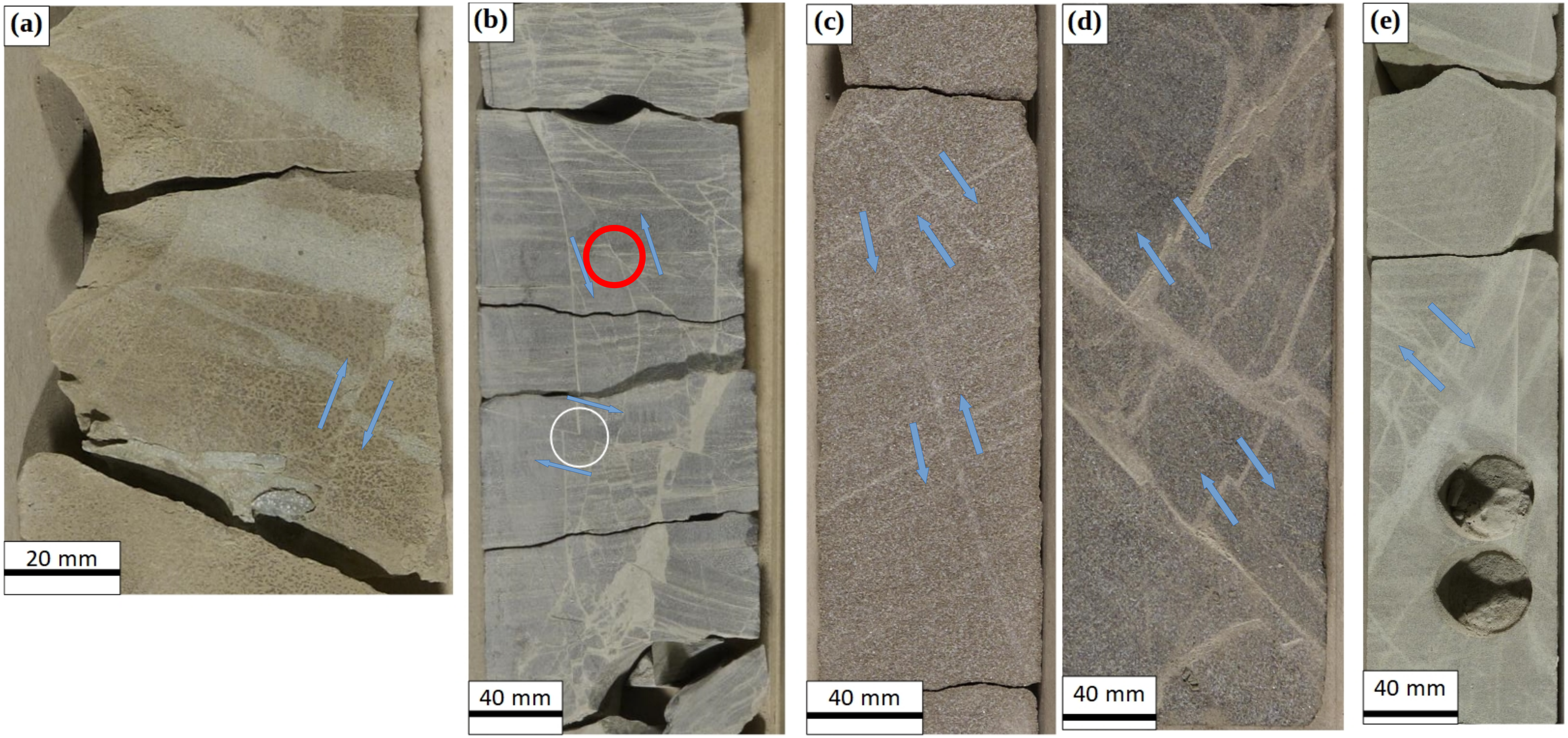

Figure 2.18: Core section photographs demonstrating offsets observed along deformation bands. All core section photographs are oriented the correct way up. Blue arrows indicate displacement direction (**a**) Offset along a vertical deformation band [well 22/14b-4 (3729.07 m MD/ 12234.5 ft. MD)]; (**b**) Examples of both vertical and horizontal offsets along deformation bands (white circles) [well 29/05a-7 (4478.91 m MD/ 14694.6 ft. MD)]; **(c)** Two steeply dipping deformation bands displaying downthrow offsets of parallel features from a central horst [well 22/29-2 (4119.90m MD/ 13516.9 ft. MD)]; **(d)** Multiple offsets observed between oppositely-dipping deformation band sets [well 22/29-2 (4180.27 m MD/ 13714.8 ft. MD)]; **(e)** Offsets along oppositely dipping deformation bands of varying thicknesses [well 22/29-3 (4212.09 m MD/ 13819.2 ft. MD)].

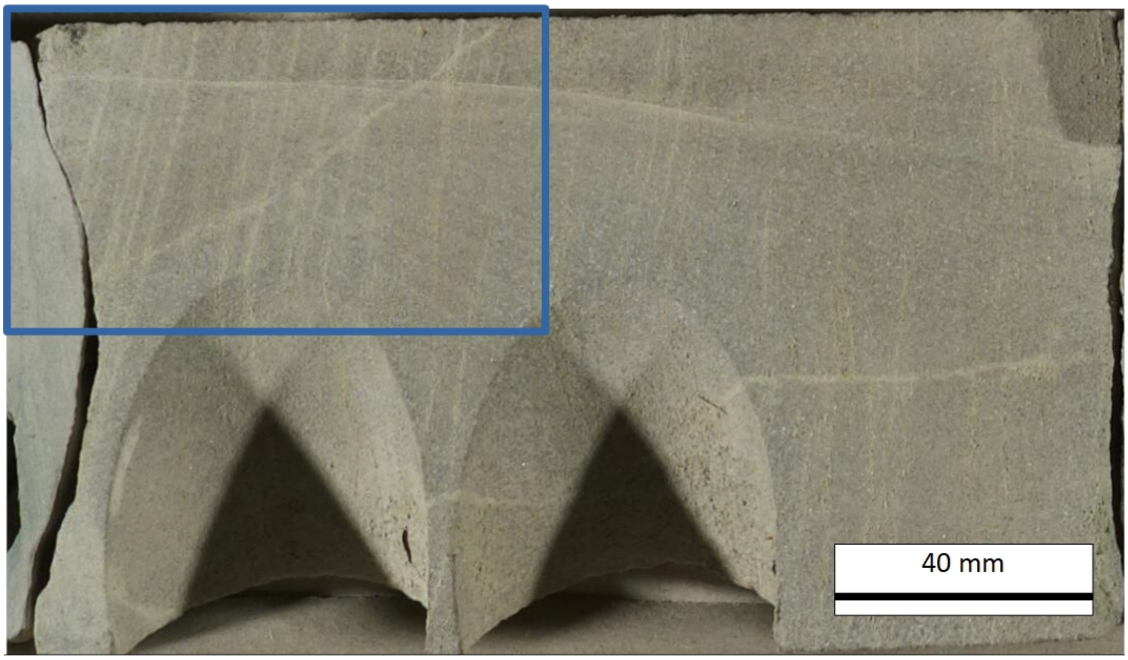

Figure 2.19: Core photograph of a deformation band cross-cutting several horizontal planar features with no visible offset (highlighted in blue). There is also an example of a vertical deformation band fading out towards the right of the image[well 22/29-3 (4198.37 m MD/ 13774.2 ft. MD)]. Left side of image is towards the top of the core section.

2.5.1.4 Deformation band terminations and initiations

In this study deformation band initiations and terminations refer to the occurrence when the deformation band stops within the sampled core due to lithological or morphological factors and may provide insight into their formation and evolution. While these features are rarely observed in the core photographs, the clearest examples of deformation band initiations and terminations occurred across changes in lithology (Fig 2.20a & b). This style of deformation band termination occurred at sharp contacts between the lithologies, with the deformation band displaying a similar colour to the overlying lithology. In some cases the sub-vertical deformation bands which occurred towards the top of the core section appear to originate from thicker wedges as evidenced by the identical colouration and appearance between the deformation band interior and the overlying lithology (Fig 2.20a). The wireline log measurements for the conjugate set observed in Figure 2.20b displayed a decrease of GR intensity from 80 API to 53 API, the formation density log decreased from 2.50 gr/cc to 2.44 gr/cc and the neutron log decreased from 27 PU to 25 PU. Helium porosity for the transition is 10% and increased to 19% within the deformed lithology. Horizontal permeability measured an increase from 0.1 mD to approximately 1 mD. Grain density was observed to increase from 2.60 g/cc to 2.66 g/cc across the lithology change.

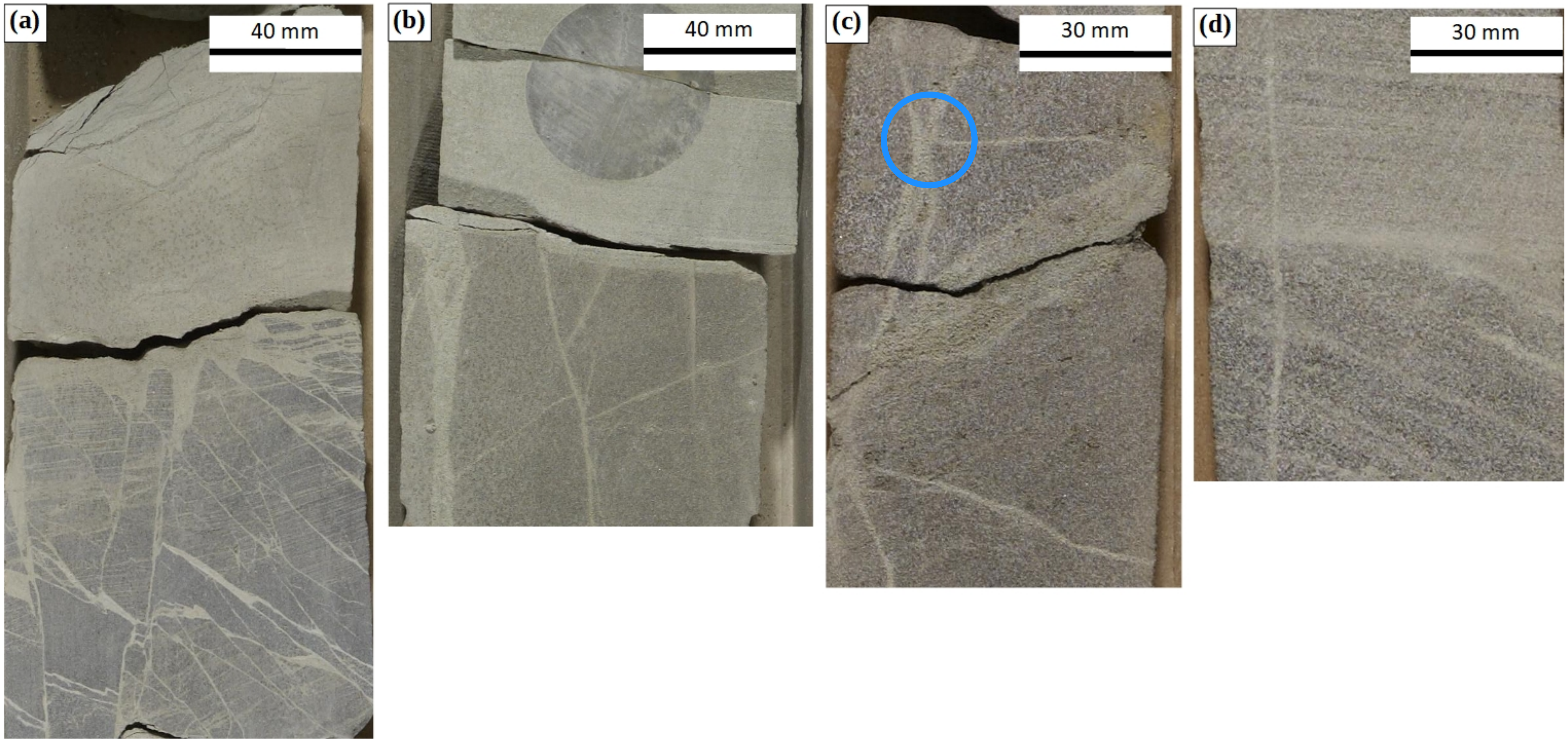

Figure 2.20: Core photograph images demonstrating deformation band interactions with changes in lithology and other deformation bands. All photographs are correct way up. **(a)** deformation bands in the underlying lithology do not appear in the overlying lithology. The contact between the lithologies is irregular with wedges of the overlying lithology intruding into the lower lithology [well 29/05a-7 (4485.16 m MD/ 14715.1 ft. MD)]; **(b)** Deformation bands terminating upon contact with a planar contact between different lithologies [well 22/29-3 (4234.61 m MD/ 13893.1 ft. MD)]; **(c)** A deformation band terminating at the contact between an oppositely dipping set of conjugate bands (blue circle) [well 22/29-2 (4207.21 m MD/ 13803.2 ft. MD)]; **(d)** A deformation band occurring across an erosive contact between different lithologies [well 22/29-2 (4211.63 m MD/ 13817.7 ft. MD).

Although changes in lithology were the most common form of deformation band termination, deformation bands were observed to exist across changes in lithology (Fig. 2.20d). The interpreted lithology on the wireline log indicated that this deformation feature occurred above a change in lithology. Therefore, the following measurements were taken from above the change in interpreted lithology. The wireline log measurements for the conjugate set observed in Figure 2.20d displayed a decrease of GR intensity from 52 API to 38 API, the formation density log increased from 2.35 gr/cc to 2.40 gr/cc and the neutron log fluctuated between 28 PU and 30 PU.

Another variety of continuity loss along a deformation band observed is when a deformation band encountered another deformation band. This is distinct from the offsets described previously since the continuation of the deformation band is not observed on both sides of the intersecting deformation band. This type of deformation band termination occurred in all studied wells. This relationship was more noticeable when the angle between the steeply-dipping and shallowly-dipping deformation band intersection was between 60° – 90°, and there was an occurrence of a deformation band terminating at the intersection between a conjugate pair of deformation bands (Fig. 2.20c).

The final type of band termination was the gradual thinning of the deformation band to an imperceptible level within the core section, giving the band the appearance of 'fading-out' along the core sample (Fig. 2.21). This was observed to happen for deformation bands oriented both parallel and obliquely to the sedimentary layering without encountering a change in lithology. This was rarely observed across the core sections, with well 29/05a-7 containing the majority of examples for this type of deformation band termination.

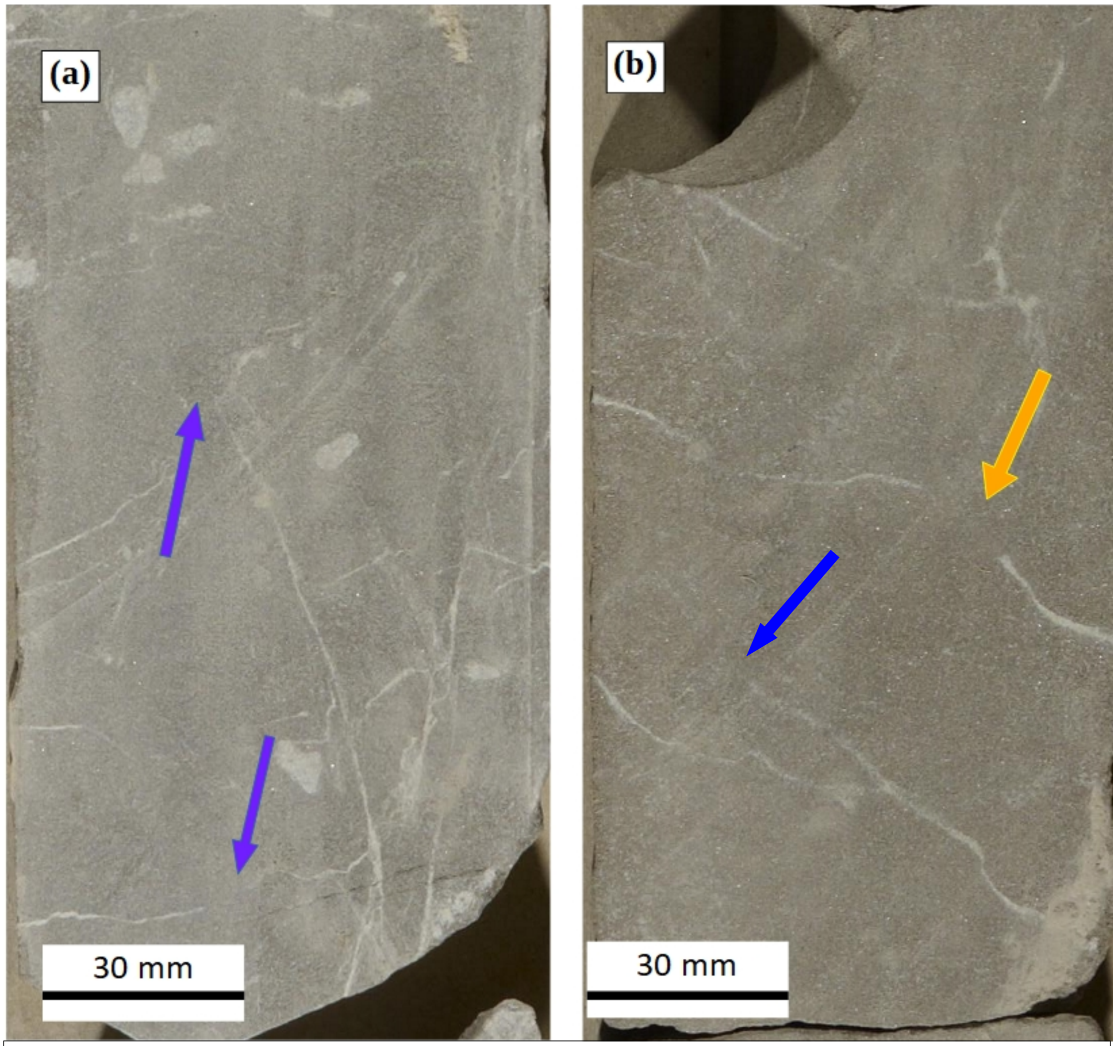

Figure 2.21: Deformation bands terminating without encountering a contact between lithologies or another deformation band. **(a)** horizontal and vertical deformation bands becoming imperceptible across the core section (blue arrows) [well 29/05a-7 (4447.45 m MD/ 14591.4 ft. MD)]; **(b)** a deformation band terminating (blue arrow) and becoming imperceptible along the length of the band (orange arrow) [well 29/05a-7 (4429.72 m MD/ 14533.2 ft. MD)].

2.5.1.5 UV Analysis of core

The purpose of the ultraviolet (UV) photographs was to identify changes in fluorescence across deformation bands, potentially indicating inhibition of hydrocarbon migration across the deformation band. Examples from well 22/14b-4 and well 22/29-2 showed that differential fluorescence did occur across deformation bands in conjunction with shear displacement of the host rock resulting in juxtaposed lithologies (Fig. 2.22). The composite wireline log for Figure 2.22 displayed a GR intensity of 65 API, formation density log and neutron log of 2.45 gr/cc and 31 PU respectively. Both deep and shallow resistivity logs recorded less than 1.5 ohm metres at this depth. There were also samples which contained a significant abundance of deformation bands that did not show differential staining across the deformation bands within fluorescent host rock (Fig.2.23).

Figure 2.22: Section of core with **(a)** photographed under white light and **(b)** photographed under UV light. A difference in fluorescence is observed across a set of steeply dipping deformation bands possibly indicating that the deformation band acted as a baffle during hydrocarbon migration [well 22/29-2 (4173.99 – 4174.32 m MD/13694.2 – 13695.3 ft. MD)].

It should be noted that the samples in Figure 2.23 were taken from core above the HWC. The composite wireline log for Figure 2.23 displayed a GR intensity of 74 API, formation density log and neutron log of 2.45 gr/cc and 14 PU respectively. Both deep and shallow resistivity logs recorded less than 2 ohm metres at this depth without any major fluctuations above 2 ohm metres immediately above or below this depth. Some deformation bands were found to display stronger fluorescence compared to the host rock when viewed under UV light. However, not all deformation bands fluoresced when exposed to UV light (Fig. 2.23). Fluorescence was not present in the host rock for some of the core sections (Fig. 2.23) 4203.04 – 4203.8 m MD/ 13789.5 – 13792 ft. MD), so not all of the deformation bands for well 22/14b-4 and well 22/29-3 could be investigated for acting as a baffle to in-situ subsurface fluid flow.

Figure 2.23: Comparison between white light photography **(a)** and UV core photographs **(b)** of deformation bands in well 22/29-3 over the measured depth interval 4196.3 – 4203.8 m MD (13774 – 13792 ft. MD). Several examples of deformation bands with various thicknesses (1 – 10 mm) could be observed throughout this section with no visible difference in fluorescence in the host rock across the deformation band. The host rock towards the end of the section (4202.1 – 4208.3 m MD/ 13789.8 – 13792.0 ft. MD) did not display any fluorescence with the exception of trace fluorescence along the deformation bands.

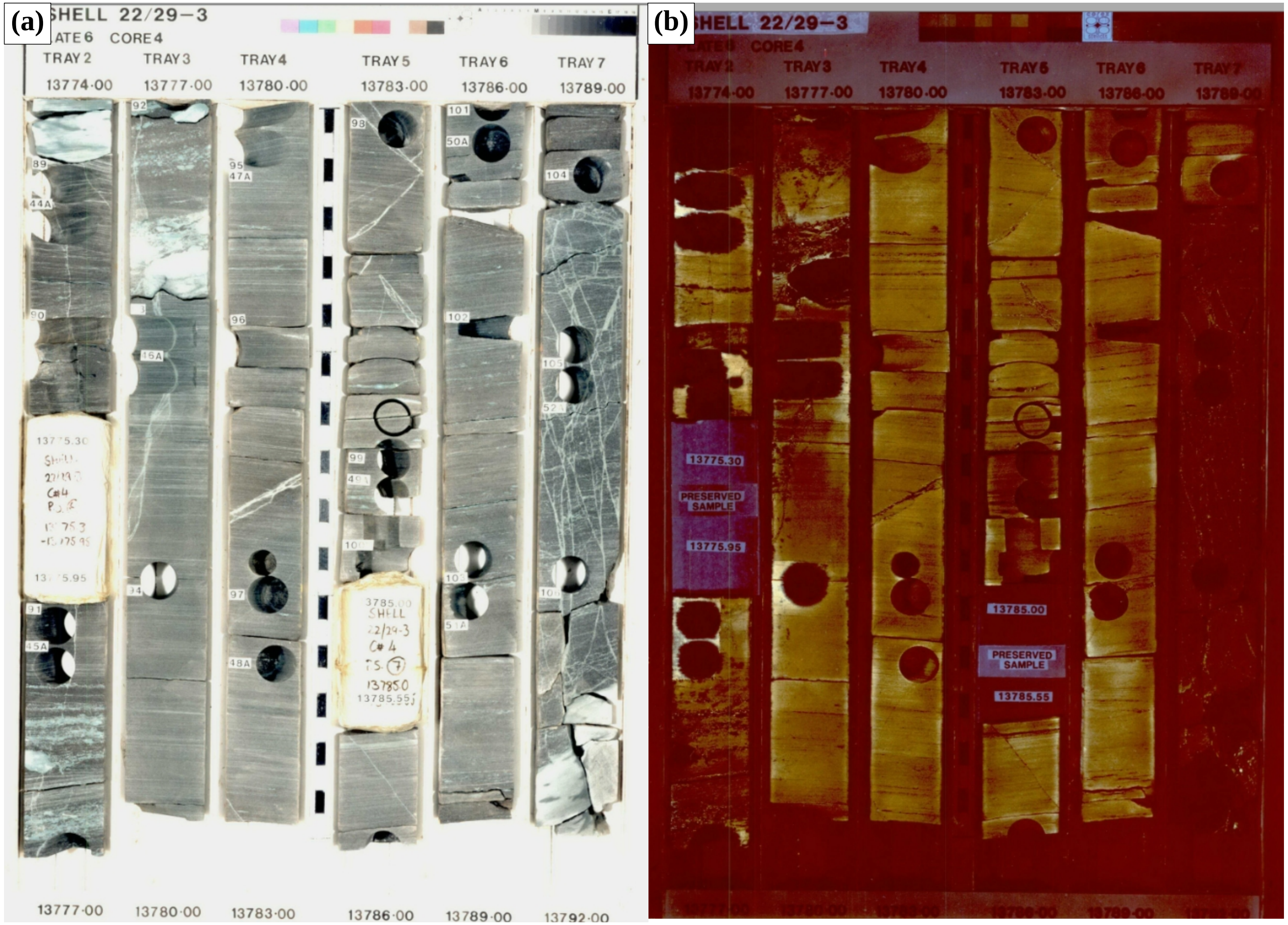

2.5.2 Thin section petrography

In order to determine the kinematic evolution and porosity of the deformation bands, analysis of the lithology, diagenetic and microstructural features of the sampled material was undertaken. The deformation bands could already macroscopically be distinguished from the host rock as distinct anastomosing and contrasting bands. Under the optical microscope, thin section analyses of the host rock and the deformation bands identified the cause for this macroscopic appearance to be caused by localised concentrations of clay minerals within the deformation bands.

2.5.2.1 Lithology in thin section

The lithology of the channel sediments in thin section comprise of very fine to fine grain sizes with high angularity and poor to moderate grain sorting. For the floodplain deposits, the average grain sizes ranged from very fine to fine, with a higher proportion of very-fine mineral grains compared to the channel deposits. Mineral abundances categorise the sandstone deposits as minor variations of subarkose, with mineral grains suggestive of immature sediments. The most notable observation in the thin sections was the abundance of diagenetic minerals including grain coats and pore-filling clays (> 20%). (Table 2.4). There was no evidence of significant grain fracturing in the host rock or the deformation bands in any of the thin sections. Optical intergranular porosity was very low with the exception of irregular voids and open fractures adjacent to the deformation bands. Alignment of mica grains and low sphericity grains in the host rock tending towards horizontal, independent of the orientation of the deformation band, was common in the thin sections. The orientation of mica grains within the deformation bands could not be observed due to the absence of visible mica grains within the deformation bands.

Table 2.4: Petrographic analysis of the host rock of the well 22/29-3 thin sections. The porosity listed refers to optical porosity observed during point counting.

Well 22/29-3							
Depth m (MD)	Depth m (TVDSS)	Quartz (%)	Feldspar (%)	Lithic (%)	Mica (%)	Clay (%)	Porosity (%)
4203.34	4177.44	54.3	12.7	5.7	4.0	21.3	2.0
4212.27	4186.37	47.3	15.0	8.0	3.0	24.7	2.0
4219.16	4191.18	48.0	15.7	4.3	8.3	19.3	4.3
4228.34	4202.43	42.0	12.3	4.7	3.7	34.7	2.7
4234.83	4208.92	51.3	10.3	6.7	2.3	27.7	1.7

2.5.2.2 Diagenetic cements

Diagenetic cements which have previously been identified in the sandstones of the Skagerrak Formation across the CNS are quartz overgrowths, dolomite and other carbonate minerals, chlorite and illite. The thin sections contained trace amounts of the dolomite and carbonate minerals, as well as minor quartz overgrowths. The main diagenetic phases present in the thin sections were chlorite and illite, which both occurred as grain coats and pore filling clay minerals.

When viewed in thin section, the deformation bands were identified by the higher proportion of darker clay minerals compared to the host rock. The darker intergranular clay minerals within the deformation bands were observed to form sharp contacts with the host rock (Fig. 2.24).

The abundance of diagenetic cements across the deformation bands were measured using point-counting on representative thin sections for the facies found throughout the sampled Skagerrak Formation. The graphs showed an increase in clay content across the transect from the host rock to the deformation band (Fig. 2.24, 2.25, 2.26, & 2.27).

2.5.2.3 Petrographic distribution in cores from well 22/29-3

Abundances of mineral grains, clay minerals, and porosity were measured along transects parallel to the deformation bands. The resulting graphs showed that the abundance of mineral grains decreased from the host rock across the deformation band (Figs. 2.22, 2.23, 2.24, & 2.25a). The grain mineral constituent was comprised of quartz grains, feldspar grains, mica grains and lithic fragments. The clay mineral constituent was comprised of intergranular authigenic clay minerals such as illite and chlorite, based on previous literature (Humphreys et al., 1989; Stricker et al., 2018) (Appendix C). The porosity constituent was comprised of macroporosity including open fractures caused by core section retrieval, thin section production, and voids caused by grain dissolution (Figs. 2.25b & c).

Figure 2.24: Micrographs and graphs of rock constituent frequency for the micrographs. The blue line highlights the deformation band and the red line shows the distance over which the transects were taken. The blue box on the frequency diagram highlights the deformation band width. **(a)** shows the dark clay-filled deformation bands appearing to terminate across the micrograph (right to left); **(b)** shows a deformation band with an adjacent open fracture (blue arrow). The fracture developed after coring. Both micrographs are from well 22/29-3 (4228.34 m (13872.5 ft.) MD).

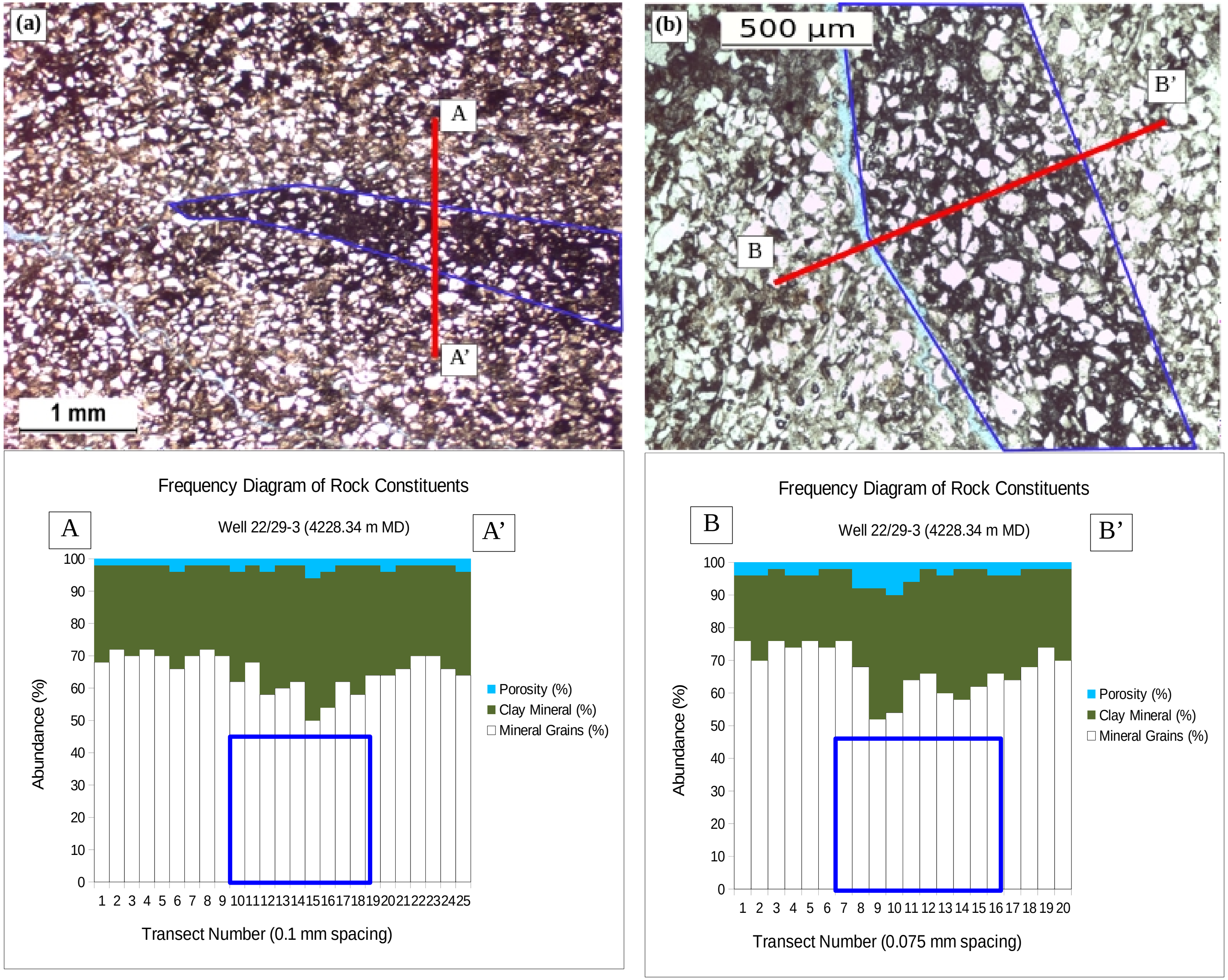

Figure 2.25: Micrographs and graphs of rock constituent frequency for the micrographs. The blue line highlights the deformation band and the red line shows the distance over which the transects were taken. The blue box on the frequency diagram highlights the deformation band width. **(a)** at the macro-scale, the thin section left of the blue line is visible as a deformation band [well 22/29-3 (4203.34 m MD)]; **(b)** the blue line is positioned along the length of a deformation band [22/29-3 (4212.27 m MD)].

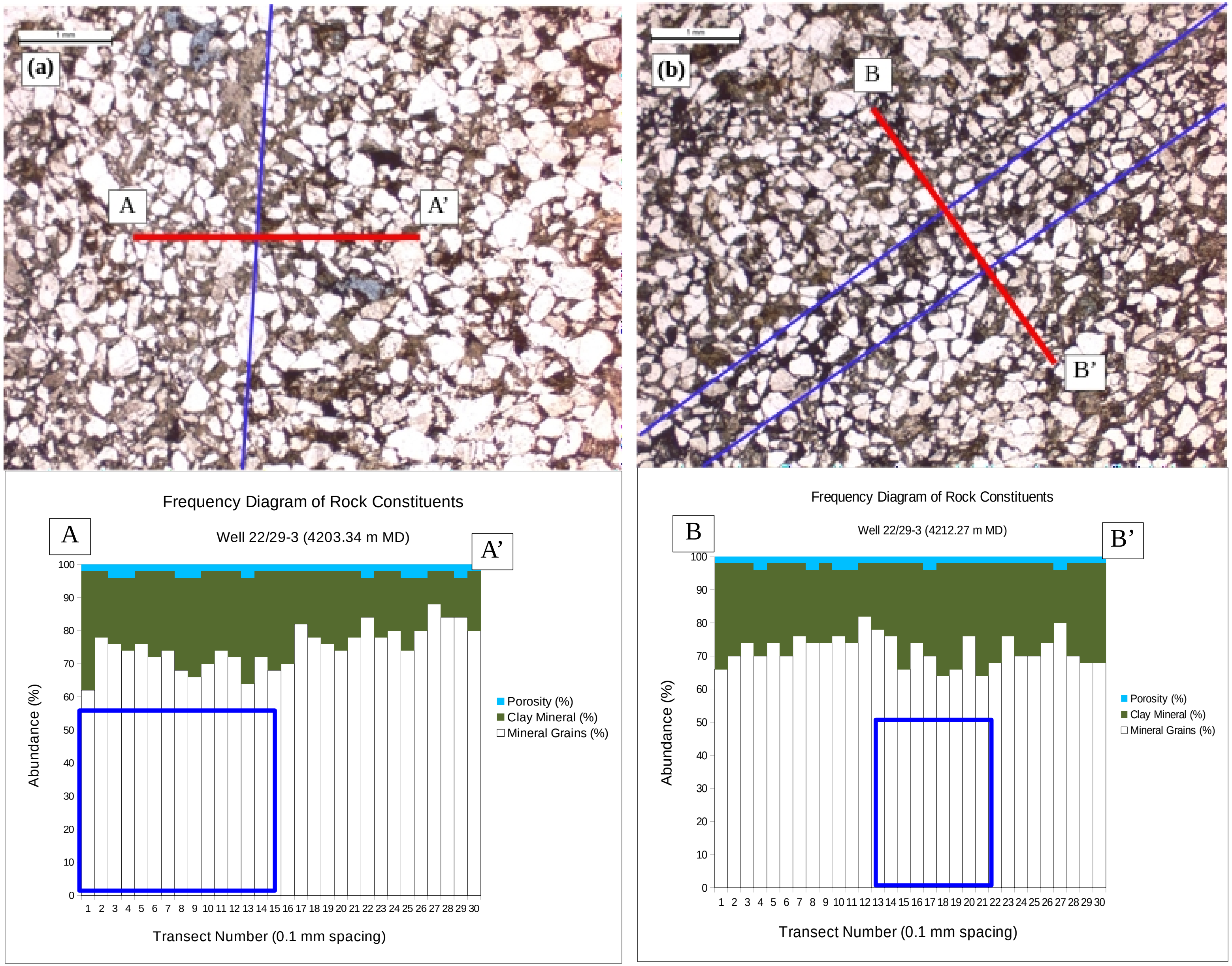

Figure 2.26: Micrographs and graphs of rock constituent frequency for the micrographs. The blue line highlights the deformation band and the red line shows the distance over which the transects were taken. The blue box on the frequency diagram highlights the deformation band width. **(a)** a micrograph and mineral constituent frequency diagram of a moderately dipping deformation band (~ 30^{O} from horizontal) [well 22/29-3 (4234.83 MD)]; **(b)** the orientation and mineral constituent frequency diagram for a deformation band cross-cutting the deformation band observed in **(a)** [well 22/29-3 (4234.83 MD).

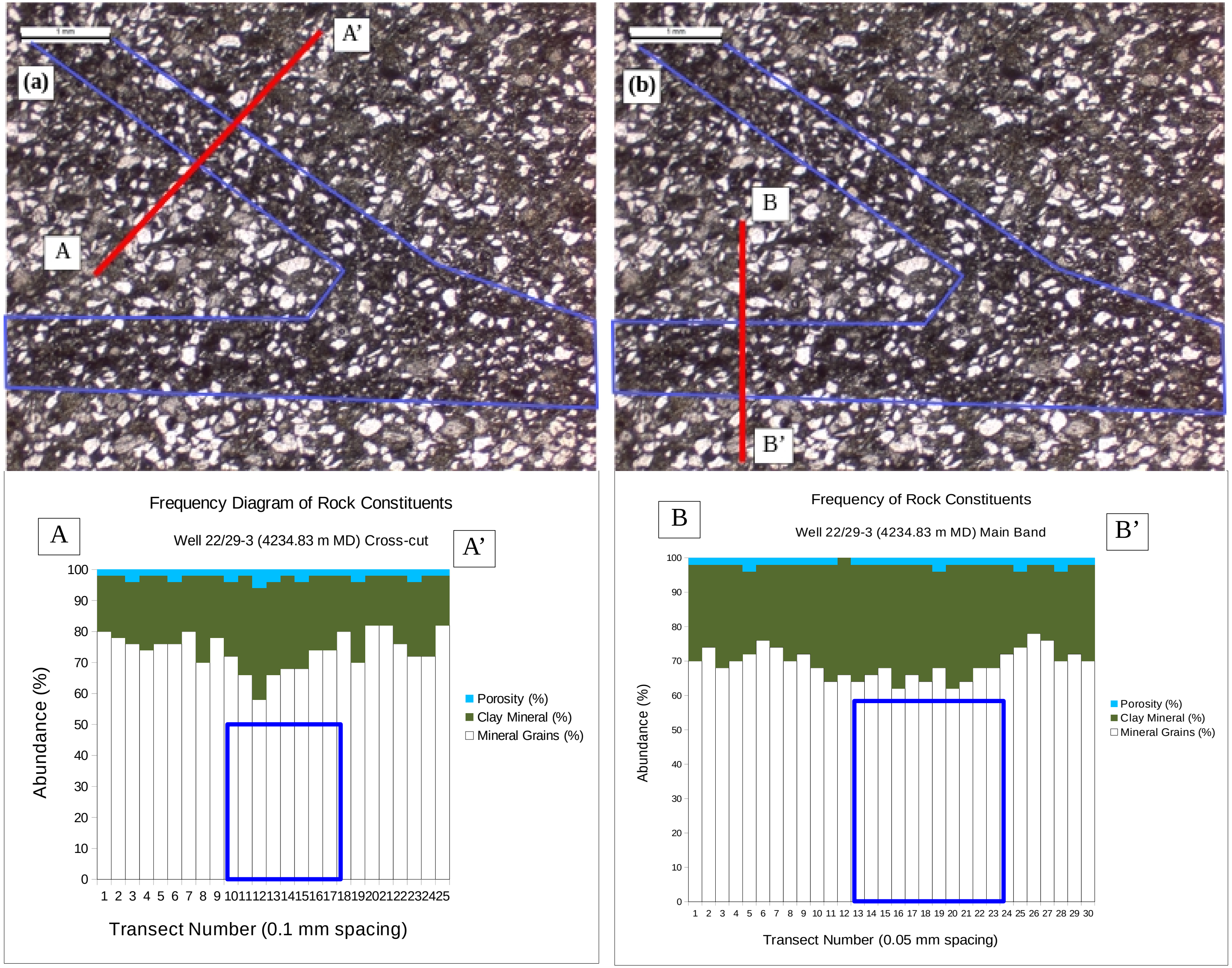

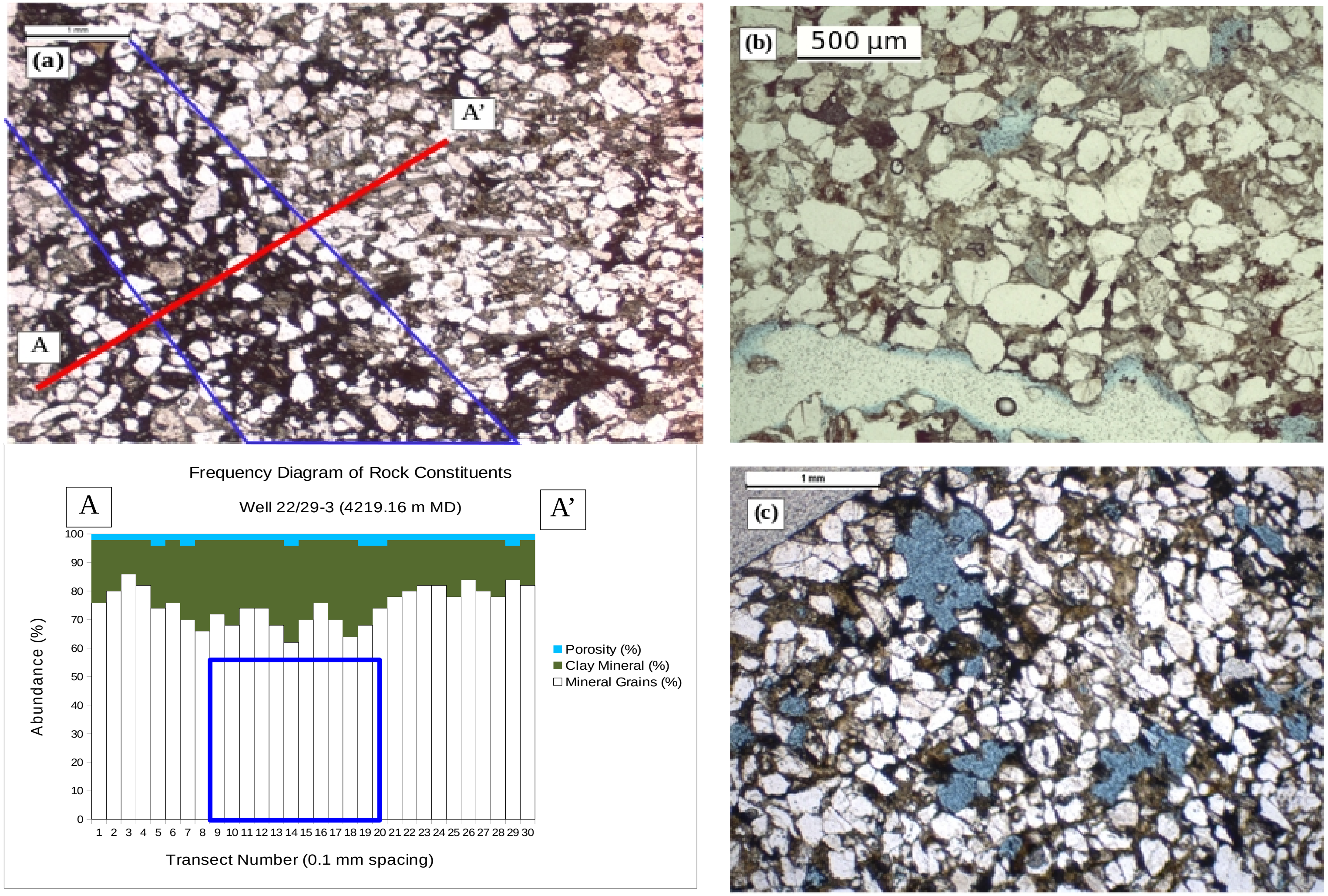

Figure 2.27: Micrographs and a frequency diagram of thin sections from well 22/29-3 **(a)** Micrograph and graph of rock constituent frequency for the micrograph. The blue line highlights the deformation band and the red line shows the distance over which the transects were taken. The blue box on the frequency diagram highlights the deformation band width. The micrograph illustrates the deformation band with a darker colour compared to the host rock [well 22/29-3 (4219.16 m MD)]; **(b)** a micrograph of an open fracture containing some blue epoxy resin and some examples of macro-porosity in the form of irregular voids containing minor amounts of blue epoxy resin [well 22/29-3 (4203.34 m MD)]; **(c)** a micrograph displaying a high density cluster of grain voids filled with blue epoxy resin [well 22/29-3 (4212.27 m MD)]

2.6 Discussion

2.6.1 Deformation band interactions and terminations

A variety of deformation band morphologies can be found across the core photographs. It should be noted that well 29/05a-7 illustrated extremely complex deformation band morphologies and interactions. Since the only data available for this well were the core photographs, any interpretation of the band morphology cannot be confidently made without more data such as lithologies and burial history. However, deformation band features that occurred in well 29/05a-7 may share a similar evolution to deformation features in other wells. Therefore these figures were included to show more complex deformation band morphologies that may occur in other mini-basins.

The fluctuating abundance of deformation bands along the wells appears to be independent of facies as deformation bands are found to occur in all facies identified in the wells. The thin sections of well 22/29-3 then show that deformation bands show similar traits in both fine grained channel sandstones and very fine grained sheetflood sediments. Figure 2.18b, d, & e highlighted that different thicknesses of deformation bands could occur within the same facies. This may imply that the facies variations have little to no impact on the kinematic formation of the deformation bands, including minor control on the thickness of the deformation bands, which have been shown in the literature to be dependant on grain size (Johansen & Fossen, 2008; Griffiths et al., 2016).

The production of thicker bands (>10 mm) could be indicative of strain hardening, with the proposed shallow depth of formation not imposing a high enough stress for cataclasis of the grains, as evidenced by the lack of grain fracturing in the thin sections (Figs. 2.15 & 2.17) (further explored in section 2.6.2). This increased strength would arise from the early infiltration of water and clay minerals along the deformation bands increasing the strength of the bands relative to the host rock. Multiple deformation events were indicated by both the strain hardening of deformation bands into thicker bands, as well as the cross-cutting relationships observed between different sets of deformation bands throughout the wells (Fig. 2.18).

Offsets between bands of identical thickness and colour, indicative of similar internal petrography, would have occurred at shallow depths (<500 m) prior to the onset of diagenesis since post-diagenetic bands would not display the same internal band petrography and morphology as earlier bands. Offsets of deformation bands by other bands with minimal thickness (<1 mm) would occur at mesodiagenetic depths (>500 m) since the infiltration of clay minerals within the band is reduced compared to bands formed at shallower depths and any clay material along the thinner bands would be sourced from the cross-cut deformation band. The greater depths that these thinner bands formed at would lead to an increased overburden stress on the sediments, possibly resulting in early signs of mineral breakage and cataclasis along these thinner cross-cutting deformation bands.

Most deformation bands were observed to terminate upon contact with another lithology, with some exceptions (Fig. 2.20). In the cases where the deformation band terminated into the overlying lithology, the contact between the lithologies was typically a discrete horizontal planar contact (Fig. 2.20b). This contact may be interpreted as representing an erosional contact between the lithologies, and the lithology with deformation bands was eroded post-lithification, after infiltration of the clay minerals. The wireline log measurements for this transition reflected a top-down change in lithology into a less shaley (cleaner) sandstone, based on the decrease in GR intensity. The decrease in formation density and increase in grain density indicated a transition from a silty shale into a fine-grained sandstone, reflected by the increase in porosity and permeability. This increase in porosity and permeability is likely to have allowed for the infiltration of diagenetic material into the host rock, compared to the overlying lithology. For the few instances of deformation bands terminating into the underlying lithology a potential hypothesis is that the underlying lithology was more consolidated than the overlying lithology and required greater stresses to deform, which may also explain the above observation. The wireline log measurements for Figure 2.20d suggested a transition into cleaner, coarser sandstone based on the decrease in GR intensity and increase in formation density. The increase in grain size would be expected to coincide with an increase in pore space that would be reflected in the neutron log, however, the absence of major fluctuations in the neutron log may indicate the influence of pore-filling diagenetic material. Unfortunately, the wireline log did not include grain-size data for this interval so further interpretations could not be confidently made.

In the case of Figure 2.21b, the deformation bands could be linked outside of the visible plane of the core section, although core plug samples may confirm this hypothesis.

Multiple instances of open fractures developing along the orientation of deformation bands were also observed (Fig. 2.24b). In thin section, these fractures were found to form adjacent to the deformation bands and appear to be expansion cracks formed during retrieval of the core sections. The tendency of these open cracks to appear along the orientation of the deformation bands suggest that the deformation bands have a significantly different strength competency compared to the host rock.

Dilational bands are thought to form as a result of accommodating shear offsets of adjacent deformation bands (Du Bernard et al. 2002). This could be a potential explanation for examples of deformation bands which terminated upon contact with another deformation band. Although Du Bernard et al., (2002) showed that compaction bands may also form, the poorly consolidated sediment would have had a high porosity which would not show significant indicators of compaction.

2.6.2 Deformation band formation, cementation and reservoir quality

Comparing the composite wireline logs between the deformed and undeformed lithology within the wells indicated that helium porosity in intervals that contained a significant abundance of deformation bands and intervals that did not contain a significant abundance of deformation bands both ranged within 10% to 28% in well 22/29-2, and 7% to 25% in well 22/29-3. These porosities demonstrated that well 22/29-2 had a higher porosity on average compared to well 22/29-3, which concurs with the findings in Stricker et al. (2018). It should also be noted that porosity did not typically fluctuate according to changes in deformation band abundance, but increased in coarser-grained lithologies and facies and decreased in finer-grained lithologies. Although the spike in multiple measurements for the cemented band at 4230.01 m (13878 ft.) MD, suggests that a cemented deformation band has the potential to be picked out in a wireline log, but it is not a reliable method of identifying deformed sandstone units. Overall, the observations made from the wireline logs of the Skagerrak Formation indicated that facies type and lithology usually have a greater influence on porosity fluctuations than the presence of deformation bands. It is likely that the pervasive nature of the pore-filling diagenetic clay minerals throughout the host rock and deformation bands obscures any significantly measurable differences between deformed and undeformed lithology within this well.

At the micro-scale, the thin sections of the deformation bands did not show a significant grain size reduction or grains fracturing compared to the host rock, indicating that little to no cataclasis took place during deformation (Figs. 2.24 – 2.27). The abundance of rock constituent graphs demonstrated that all deformation bands observed display a decrease in grain mineral abundance and increase in clay mineral abundance. Assuming that the clay minerals were indicative of the pore space prior to mechanical compaction and represent the grain framework density of the deformation band, then the graphs signified that all of the deformation bands have a dilational component with shear displacement. The low abundance of phyllosilicates within the thin sections also prevented the development of phyllosilicate bands. This would mechanically categorise the deformation bands as disaggregation bands in thin section (Fossen et al., 2007). Combined with the research into soil mechanics and how unconsolidated sediment deforms under low-levels of stress (100—800 KPa) (Desrues & Viggiani, 2004), the disaggregation bands would have formed at shallow depths (< 500 m) prior to the onset of lithification. While research suggests that deformation bands can form from sudden changes in stress caused by localised earthquakes or seismic events, the thin sections did not show the grain fracturing or disturbed sedimentary beds associated with these events (Rosetti et al., 1999; Rawling & Goodwin, 2003; Cashman et al., 2007). This was likely due to the stress required for brittle failure of the unconsolidated sediment being less than the stress required for the fracturing of fine-grained quartz along with the high initial porosity of the sediment. However, it should also be considered that dilatant shear bands can form to accommodate the shear from adjacent disaggregation (shear) bands (Du Bernard et al., 2002).

The shallow formation depth would concur with the hypothesis that the clay minerals found within the bands infiltrated the sediment during the influx of meteoric water, either through rainfall or palaeoriver flooding events (Stricker et al., 2018). The higher porosity within the disaggregation bands compared to the host sediment would have therefore provided a preferential pathway for the infiltration of meteoric water and clay minerals. It is then possible that a combination of hydrostatic forces, calcic palaeosols from floodplain deposits, or biofilms (polymers excreted by microorganisms) could have then preserved the enhanced porosity long enough for the clay minerals to infiltrate the sediment (Kemper & Rosenau, 1984; Kim et al., 2009; Jones, 2017). The sharp contact between the deformation bands and host rock could be caused by larger particles of smectite able to infiltrate the increased pore space along the deformation band, but being too large to infiltrate further into the relatively smaller pore spaces of the host rock. The dissolved pore fluid components are then able to percolate further into the host rock and deposit diagenetic material into the host rock. The sharp contact between the deformation bands and host rock may therefore represent the transition from pore spaces large enough to accommodate the detrital smectite along the deformation band into the reduced pore space too small to allow further transport of the smectite.

The meteoric influx would have also produced hypersaline pore fluids due to the proximity to the salt wall (<1000 m). The location and abundance of deformation bands proximal to a salt wall has the potential for enhanced meteoric influx, enhanced clay mineral infiltration, and hypersaline pore fluid chemistry. As evidenced by the poor porosity found in the thin section samples, this combination of factors has resulted in the significant propagation of pore-filling diagenetic clays throughout well 22/29-3. Although, it is likely that the thermal property of salt to transfer heat at depth and alter the geothermal gradient would have had a minimal influence on the diagenetic maturity of the clay minerals due to the shallow depths over which these processes would have occurred (Mello et al., 1995; Davison et al., 1996). Although hydrocarbons were found in both well 22/29-2 and well 22/29-3, the UV photographs do not show consistent evidence of deformation bands acting as a baffle to fluid flow, although this is the case for cementation bands in other studies (Fig. 2.23) (Du Bernard et al., 2002; Exner et al., 2013; Lommatzsch et al., 2015a). The inability of the deformation bands to consistently inhibit subsurface hydrocarbon flow could be caused by the timing of deformation band formation and diagenetic development (Exner et al., 2013), or that the deformation band is not a continuous planar surface (Sternlof et al., 2004).

For the wells in this study, this is likely due to the poor permeability and porosity of the host rock that developed prior to the migration of hydrocarbons, thus inhibiting the flow of fluids in proximity to the salt wall (Stricker et al., 2018). Instances of differential fluorescence across deformation bands is can be explained as the juxtaposition of offset lithologies (Fig. 2.22). Several studies on porosity loss in the wells across the Heron Cluster and J Block state that porosity loss is primarily through compaction rather than diagenetic cementation (Nguyen et al., 2013; Stricker et al., 2016).

While a high abundance of deformation bands has been observed adjacent to salt walls, further investigation into unfaulted wells towards the mini-basin centres would be required to confirm that the abundance of deformation bands is highest adjacent to salt walls and their frequency decreases towards the mini-basin centre.

The sandstone units investigated in this chapter comprise of the Upper Skagerrak which was syn-depositional to the salt movement. Assuming a correlation between the intensity of salt movement and abundance of deformation bands would suggest that periods of increased salt mobility would produce more deformation bands. Periods of high salt mobility produce more accommodation space for sediment influx, therefore leading to thicker sandstone units containing higher abundances of deformation bands. Unfortunately the Early and Mid-Triassic sedimentary units across the Heron Cluster (sub-Josephine sandstone and mudstone units) are unconformably overlain by Mid-Late Jurassic sediments, and so this hypothesis cannot be tested in this study.

2.7 Summary

- Variation in sedimentary facies has a minimal impact on the kinematic formation of the deformation bands as deformation bands are observed in various facies. Variable thicknesses of the deformation bands within the same facies suggest band thickness is controlled by multiple factors other than facies type.

- Stress imposed on shallow sediments (<500 m depth) adjacent to the salt wall resulted in the rearrangement and rotation of the sediment grains to form tabular zones of higher porosity compared to the host rock (deformation/ disaggregation/ dilational shear bands).
- The higher porosity along the deformation band formed a preferential conduit for the mechanical infiltration of a clay minerals (likely smectite) and meteoric fluid influx. The meteoric influx also caused dissolution of the proximal salt wall and could result in hypersaline pore fluids permeating the sediment along the disaggregation bands.
- The pore fluid chemistry during burial allowed for the precipitation of chlorite grain coatings prior to the development of quartz overgrowths. Precursor clay minerals (i.e. smectite) could also react with the pore fluids and form grain coatings of illite. The chlorite and illite grain coatings could then form thick layers, closing pore throats and occupying the remaining pore space.
- The pore spaces in wells closer to the salt wall (well 22/29-3) become almost entirely occluded and fluid flow through the sandstone adjacent to the salt wall was minimal.
- Offsets observed between deformation bands are indicative of multiple deformation events during burial of the sediments. Cross-cutting between deformation bands with identical colouration and thickness occur at shallow depths (<500 m) while offsets between bands of different thicknesses occur at greater depths. The offset of a deformation band by a band with no or minimal visible diagenetic infill would also occur at depths greater than 500 m beyond the range of surface processes and clay mineral infiltration. These offsets occur independently of lithofacies type.
- Some macro-porosity was produced as grain dissolution creates voids in the host lithology, as well as open fractures developing either due to expansion of the samples during core retrieval or during the production of the thin sections.
- UV core photographs did not indicate significant inhibition of the migration of fluorescent materials across the deformation bands, although instances of different intensities of fluorescence across the deformation bands could be found.

Chapter 3. Deformation Band Orientations and the Influence of Halokinesis

3.1 Introduction

The deformation bands described in this study are identified in core from wells sampling the Triassic Skagerrak Formation across the Central Graben. These deformation features have been clearly identified in core sections from the Skagerrak Formation and previous studies of similarly recognised deformation features in core sections have been ascribed as the result of movement of the proximal salt wall (McKie et al., 2010; Stricker et al., 2018). This chapter initially investigates the factors that influence salt-wall mini-basin formation, how sedimentation in mini-basins can be affected by salt movement, and how salt structures can impart stresses on local sediments. This chapter will then describe the tectonic history of the CNS during the Permian, Triassic, and Jurassic, as well as the interplay between halokinesis and the deposition of the Triassic sediments. Finally, this chapter specifically aims to analyse the orientations of the deformation bands observed in well 22/29-2S1 and well 22/29-3 of the Seagull Field, CNS. Well 22/29-3 is situated closer to a salt wall than well 22/29-2S1 and allows for the comparison of deformation band orientations within sediment proximal and distal to a salt wall (Fig. 2.10c). Analysis of these deformation band orientations will allow for the interpretation of the stresses imparted on local and more distal sediments by the salt wall with the aim of reconstructing palaeostresses in unconsolidated syn-halokinetically deposited sediment adjacent to a salt wall.

3.1.1 Evaporite accumulation and properties

Salt-wall mini-basins are relatively small structures (1 – 10 km across) comprised of sediment subsiding into a thick layer of salt (Fig. 3.1). Accumulating a thick layer of salt would require an area to become flooded with saline fluids which would be cut off from any drainage pathways

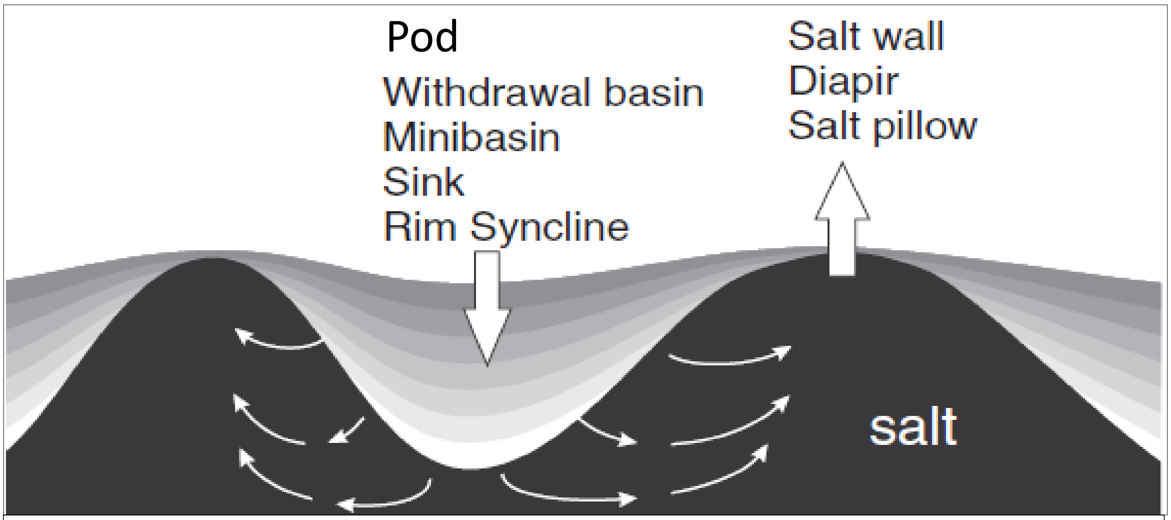

Figure 3.1: A basic diagram showing the major elements of a salt withdrawal basin, or salt-wall mini-basin. Alternative names for the areas of salt depletion and salt accumulation are given. (From Peel, 2014).

whilst under arid conditions to reduce the likelihood of dissolution via meteoric water. The water would then evaporate and deposit a layer of salt, a process that would need to happen multiple times to amass a salt layer several kilometres thick. It has been calculated that for standard seawater, 1000 m of seawater would only generate at most 15 m of salt. This means that 66,000 m of seawater would be required to produce a 1000 m thick layer of evaporites (Brun & Fort, 2011). Evaporites can also precipitate out of hypersaline seawater where the concentration of salt in the seawater is such that the seawater reaches a saline saturation point and any excess salt in the water precipitates out of solution and is eventually deposited on the sea bed.

These evaporite deposits can consist of different types of salt such as halite, anhydrite, and gypsum. On geological timescales, the rheology of salt means that it can deform in a viscous manner under certain circumstances, such as flowing on a slope and deforming due to gravity loading (Hudec et al., 2009). Salt is also less dense compared to compacted and lithified sediments, and therefore more buoyant. This means that salt can rise through overlying rock towards the surface, potentially forming a salt diapir. There are two principal types of flow, Poiseuille flow and Couette flow (Fig. 3.2a). Poiseuille flow typically applies to when salt flows from beneath a salt body into a rising salt structure and the salt experiences viscous shear forces, causing boundary drag. Therefore salt in contact with the sedimentary bodies and basement rock flow slower than salt in the central part of the salt layer (Fossen, 2016).

Couette flow, on the other hand, typically happens to salt when acting as a decollement beneath a sliding block. In this case, the salt is subject to simple shear so that salt flows more rapidly at the top of the layer and velocity decreases linearly towards the base of the salt layer, where the velocity typically reaches zero (Fig. 3.2b) (Fossen, 2016).

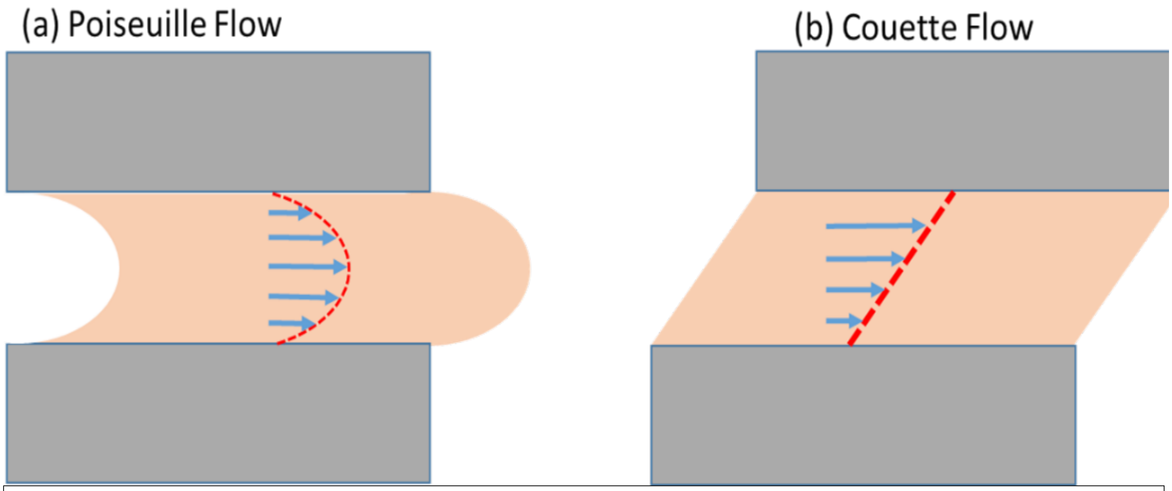

Figure 3.2: Simple diagram showing the difference in flow velocities (blue arrows) within a salt layer (orange) between (a) stationary and (b) mobile surfaces (grey). The dashed red lines show the resulting displacement from an initially vertical line.

These two types of flow are end-members, so hybrid salt flows can occur in certain situations. When describing salt flow, the viscosity of salt must also be considered. The different types of salt will have different viscosities, as well as if the salt is wet or dry. For instance, wet carnallite may have a viscosity as low as 10^8 Pa s, whereas dry halite may have a viscosity around 10^{18} Pa s (Davison et al., 1996). However, the triggering of diapirism is mainly dependent on the strength of the overburden and the buoyancy force produced by the salt, rather than the viscosity of the salt. Estimates for sedimentary rock: evaporite rock viscosity ratios range from 50 – 10^4 (Davison et al., 1996).

3.1.2 Initiation of halokinesis

While mini-basin evolution is thought to be due to gravity loading of the sediment into the salt, the exact mechanisms by which a sediment load may initiate salt movement and displacement have yet to be accurately identified (Hudec et al., 2009). The previous mechanism, which was density-driven, required that the average density of the sediment exceeded the average density of the salt. Considering the sediment at the surface would be loose and unconsolidated, the sediment would have to reach an unrealistic thickness. In the case of the Gulf of Mexico, it was calculated that the sediment would need to be 2600 m thick in order to compact the underlying sediment sufficiently so that it would be denser than the salt (Hudec et al., 2009). Several processes have been proposed (Hudec et al., 2009; Ings & Beaumont, 2010) which consider if the basins are forming in an extensional or compressional regime. Other initiation mechanisms considered subsalt folding or faulting, or gravitational decay of salt topography on an inclined plane, both of which would produce bathymetric lows in the salt surface that would then be filled in by sediment. Another proposed mechanisms is diapir shortening (Hudec et al., 2009), which was then broadened into a viscous pressure ridge mechanism (Ings & Beaumont, 2010).

3.1.3 Salt structures

When mobile and flowing, salt can form many structures in the subsurface and a few that penetrate to the surface. While most rising salt structures are referred to as salt diapirs, some salt structures can be classified more specifically (Fig. 3.3). Salt diapirs typically develop from salt pillows, which are small salt structures that are not large enough to break through the overlying sediment. Growth of these salt pillows into salt stocks allows the salt to break through the overlying layers by causing the buoyancy of the salt to exceed the strength of the overburden. The characteristic salt diapir forms when the top of the salt stock inflates, producing the distinctive diapir head, or bulb. The salt stock then forms the stem of the diapir, providing a pathway for the

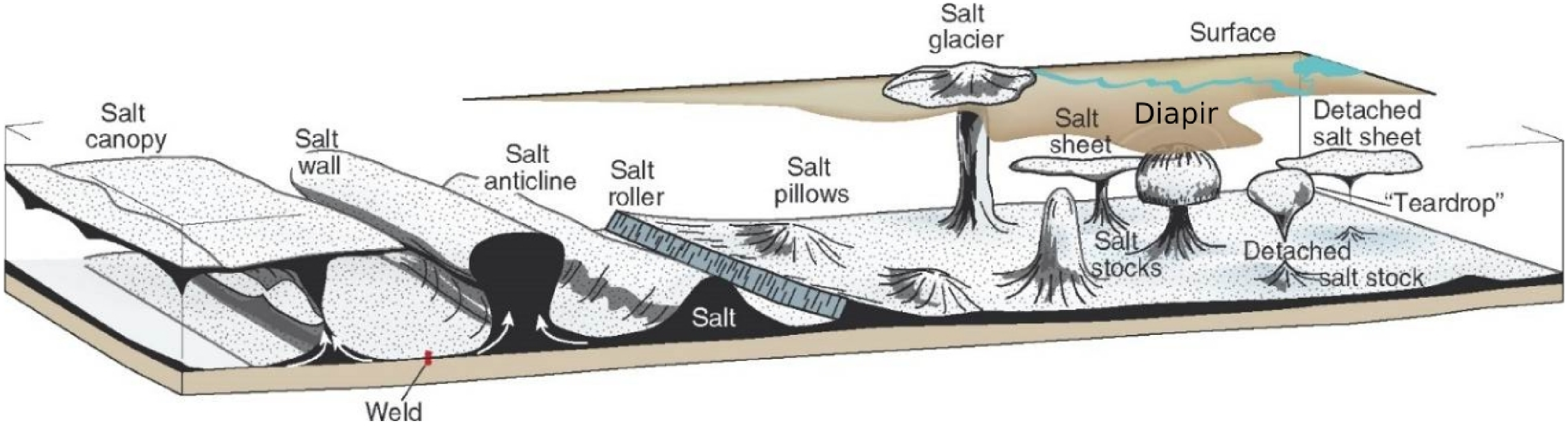

Figure 3.3: Different types of salt structures, with names and geometries. Maturity of the structures increases from the centre of the figure towards the left and right. This study focusses on salt walls and their tectonic influence on Skagerrak Formation sandstones (left from centre). (From Fossen, 2016).

salt supply. If the salt supply ceases, then the stem would collapse and the salt bulb would become detached from the source layer. If a salt diapir breaches the surface and a sufficient amount of salt flows from the breach point, a salt structure known as a salt glacier would develop. Salt sheets develop when the salt encountered a stratigraphic layer where the overburden strength exceeded the buoyancy of the salt, and would therefore flatten out, growing laterally from the salt source supply point (Hudec & Jackson, 2007; Fossen, 2016).

Salt anticlines, salt walls and salt canopies are all elongated salt structures at various stages of maturity after the formation of a salt roller (Fig. 3.3). A salt roller is when salt is overlain by a normally faulted layer and they are widely recognised in association with tilted blocks or listric fault rollover systems. The salt roller will then rise into a short salt anticline, before continuing to rise into a salt wall if the salt supply is sufficient enough. When a salt wall is observed along its length, the profile would look similar to a salt diapir, with the characteristic inflated salt head. As the salt wall continues to inflate and rise, eventually the salt supply will become exhausted and the upper salt layer will flatten into a salt canopy. This could also happen if the rising salt encounters a stratigraphic layer that is too competent for the buoyancy of the salt to break through (Fossen, 2016).

3.1.4 Summary of halokinetic development

In summary, there are many factors that can influence the rate of salt mobility and subsequent subsidence, including in salt-wall mini-basins:

- Basement geometries (Smith et al., 1993; Trudgill, 2011),
- Total thickness of the salt (Smith et al., 1993; Trudgill, 2011),
- Evaporite properties (purity of the salt layer) (Jackson & Talbot, 1986),
- Geothermal controls (warm salt has a lower viscosity than cool salt) (Jackson & Talbot, 1986),
- Climate (Infiltration of meteoric water can soften the salt, reducing its viscosity) (Jackson & Talbot, 1986), and
- Dissolution rate (Banham & Mountey, 2013b).

These factors all have an effect on the rate that the mini-basin as a whole subsides and develops, but the rate of mini-basin subsidence can also have an effect on the sediment-fill style and surface topography (Hodgson et al., 1992; Fort et al., 2004; Banham & Mountney, 2013a, b).

3.1.5 Sedimentary fill in salt-wall mini-basins

Within salt-walled mini-basins, the pattern of sediment deposition is governed by the movement of salt. However, the movement of salt can be driven by the deposited sediment, if the rate of sedimentation is high and fairly constant (Banham & Mountney, 2013b; Venus et al., 2015).

If a high and constant sediment supply is deposited into a slowly subsiding mini-basin (therefore with a slow rate of accommodation creation), any fluvial systems that would develop within the mini-basin would avulse and migrate laterally with the sedimentary deposits being reworked as a consequence. This would therefore only preserve lower, coarse-grained channel-fill elements. If the sediment supply was less than the rate of accommodation space formed, the conditions would favour the preservation of complete fluvial deposition cycles. Finer-grained sediment and a larger proportion of argillaceous deposits would also be present, which are indicative of floodplains (Banham & Mountney, 2013b).

More globally, if the sediment is deposited on salt on an incline, then two distinct syn-sedimentary deformation features could occur within the resulting mini-basin (Fort et al., 2004). This involves mostly extension up-slope, and contraction down-slope. Extension would be accommodated by brittle faulting to form 'rafts' and graben structures, as well as the upwelling of salt through extensional diapir formation. Contraction downslope would be accommodated by the early initiation of polyharmonic fold and thrust faults, as well as late-stage squeezing of diapirs (Fort et al., 2004). The basal slope angle influences the overall structure, but the rate of sedimentation controls the types of structures that developed in the structural domains. Polyharmonic folding occurs when a smooth, long-wavelength anticline is superimposed on earlier, short-wavelength folds (Rowan et al., 2004).

When all the salt has withdrawn from beneath the major salt-walled mini-basins, the sediment pods then ground on the underlying basement rock. The time between initiation of the sediment subsidence into the salt layer and the grounding of the sediment pod onto the underlying basement rock is dependent on the thickness of the salt layer, the exact composition of the salt (which would influence the viscosity of the salt, and therefore the rate of salt flow into the diapirs), and the rate of sediment infill. According to Hodgson et al. (1992) during the Late Jurassic and Early Cretaceous the interpod salt-wall highs across the CNS start to deflate and collapse vertically, due to a combination of dissolution at the surface and salt withdrawal towards the salt-wall base. The collapsing salt wall then creates smaller, secondary mini-basins between the larger mini-basins (Fig. 3.4). However, it is argued that such interpod basins form due to rafting and lateral movement of thin-skinned sediments on top of the salt layer (e.g. Penge et al., 1993; Karlo et al., 2014).

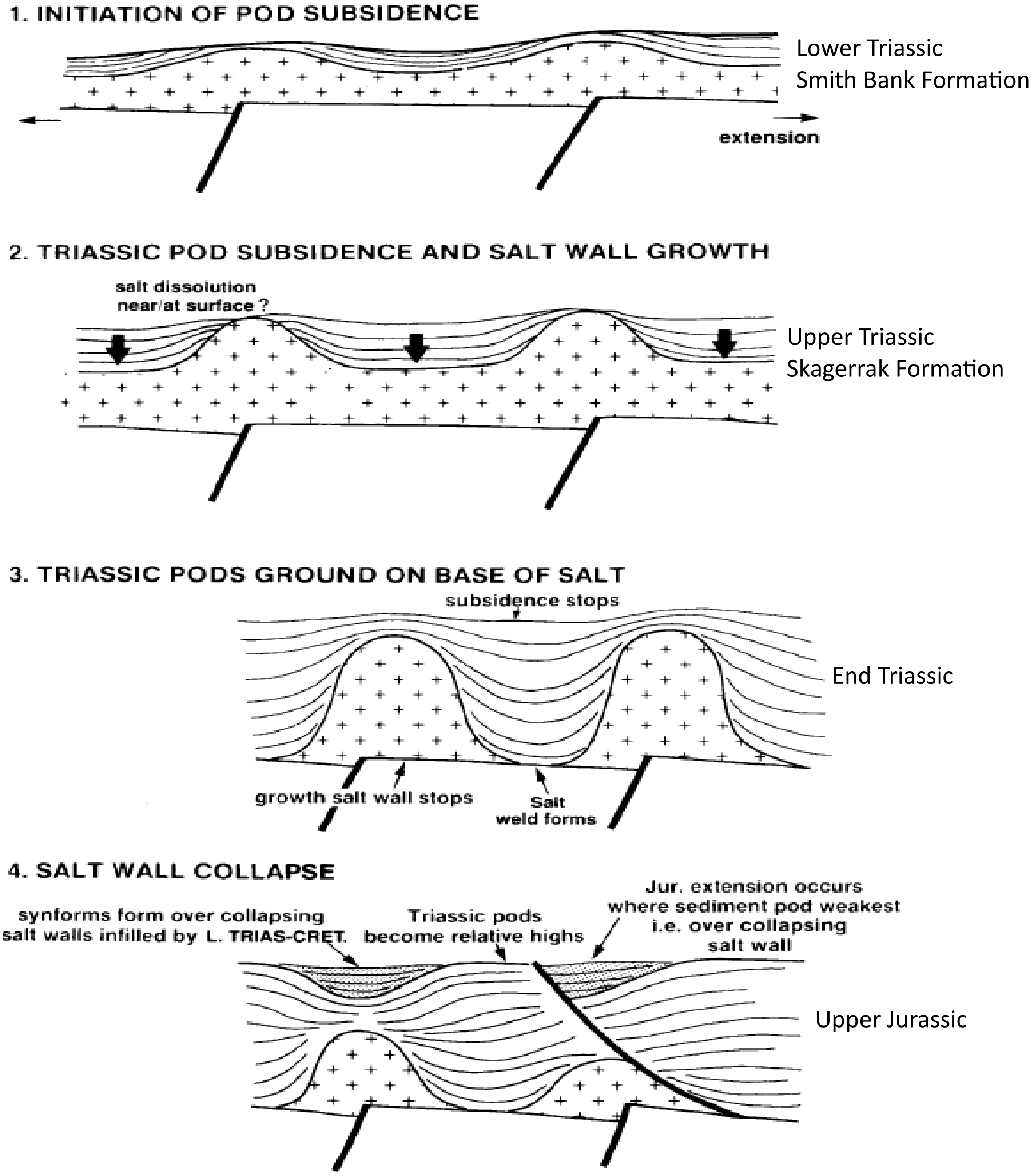

Figure 3.4: Diagram showing the possible evolution of salt walled minibasins in the CNS. This involves the vertical movement of salt resulting in the formation of secondary sedimentary minibasins found above former salt walls. This is termed as the 'podology' model. The timing of each stage along with the respective sedimentary unit has been included (From Hodgson et al., 1992).

3.1.6 Mini-basin induced stress

The rising salt-walls and diapirs can confer stress on the overlying sediments, resulting in brittle and ductile deformation within the overburden. The orientation of the resulting deformation, if brittle, can form concentric or radial patterns (Withjack & Scheiner, 1982; Quinta et al., 2012). However, if there is also a regional stress present, then the two stress fields would interact with each other and could produce brittle deformation features with varying orientations, indicative of a transition from one stress regime to another (regional to salt-wall related; Quinta et al., 2012).

Several studies have focussed on modelling the stress field around mobile salt structures and commonly salt diapirs (Withjack et al., 1990; Alsop, 1996; Rowan et al., 2006; Nikolinakou et al., 2014; Heidari et al., 2017). However, while previous literature has focussed on stresses around a single diapir rising through an overburden with some cohesive strength, there are very few studies that look at the link between salt movement and deformation bands in contemporaneous sediment. The stresses around a rising diapir may not be directly relatable to salt movement in the North Sea during the Triassic, this section will provide an insight into the way that the movement of salt can deform sediment at the macro-scale (faults and folding) and could link to how sediments deform at smaller scales. However, since the major difference in structure between a salt diapir and a salt wall is that a salt wall has a significantly longer length compared to its width, whereas diapirs are usually modelled as having a circular horizontal cross-section in plan-view. Therefore, a vertical cross-section perpendicular to the length of the salt wall should appear similar to a vertical cross-section of a salt diapir, and thus the variations in stress can be considered similar (Figs. 3.1 & 3.5).

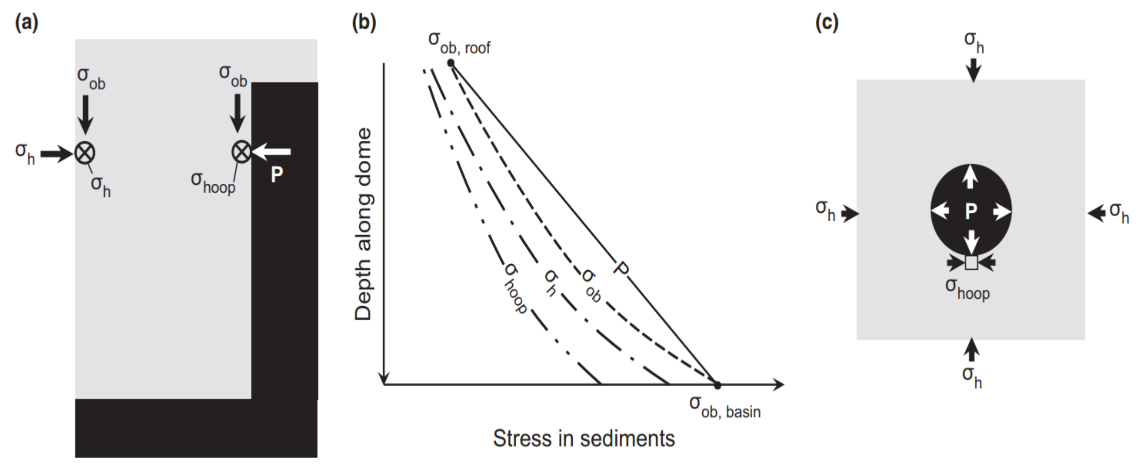

Figure 3.5: Principal stresses in sediments adjacent to the salt dome. σ_{ob} is the overburden pressure, *P* is the salt pressure, σ_h is the in situ (regional) lateral stress, and σ_{hoop} is the hoop (out-of-plane) stress. (a) Direction of principal stresses in a vertical cross-section of salt dome. (b) Schematic curves showing the variation and the relative magnitude of principal stresses in wall sediments. (c) Direction of principal stresses in a horizontal section through the dome. (From Heidari et al., 2017).

When salt rises and intrudes through the overlying sediment, it will exert a stress on the adjacent and overburden sediments. The movement of the salt is assumed to be density-driven, as the salt is typically more buoyant than the overlying sediment and results in passive flow. The stress exerted by the sediment can be modelled in the vertical orientation above the rising salt diapir, and radially in the adjacent sediments surrounding the diapir length (Heidari et al., 2017). This study showed that the maximum principal stress in sediments adjacent to the salt wall was normal to the salt wall (Fig. 3.5). Thicker units of sediment would become more compact and denser due to sediment loading, so the stress exerted on the salt would increase in thicker basins. Overall, this simple analytical model indicated that basin compaction had a critical influence on the evolution and development of salt domes.

If the rising salt structures intrude into the overburden, the salt may cause the overburden to fold and fracture. The evolution of these folded and faulted structures has been modelled in several studies (Withjack et al., 1990; Alsop, 1996; Nikolinakou et al., 2014; Heidari et al., 2017). When creating a model to investigate the impact of salt on the overburden, a factor to consider is how to model the strength of the overburden. Some models may estimate the overburden as a rigid layer that deforms in the brittle regime, while other models consider that the overburden is more visco-elastic (Davison et al., 1996). Some models are variations of sandbox models, using sand to represent the sedimentary overburden, and clay to model the viscous salt layer. When a single diapir is rising and the diapiric head starts ballooning into a competent overburden, it was found that a flat-topped dome formed from an irregular set of polygonal tensile fractures (Alsop, 1996). The central ring fault would then typically be surrounded by radial tensile fractures (Fig. 3.6). It was also found that source layer extension was a major factor in controlling how the geometry of the diapiric structures evolved over time. While the salt structures in the North Sea tend to be more elongated in plan-view compared to the more rounded diapirs, this study showed a rough evolution of fractures around a rising salt body. This model could be used to estimate the orientation of faults and their accompanying deformation bands in proximity to a rising salt body, dependant on when the bands developed during the evolution of the fracture patterns.

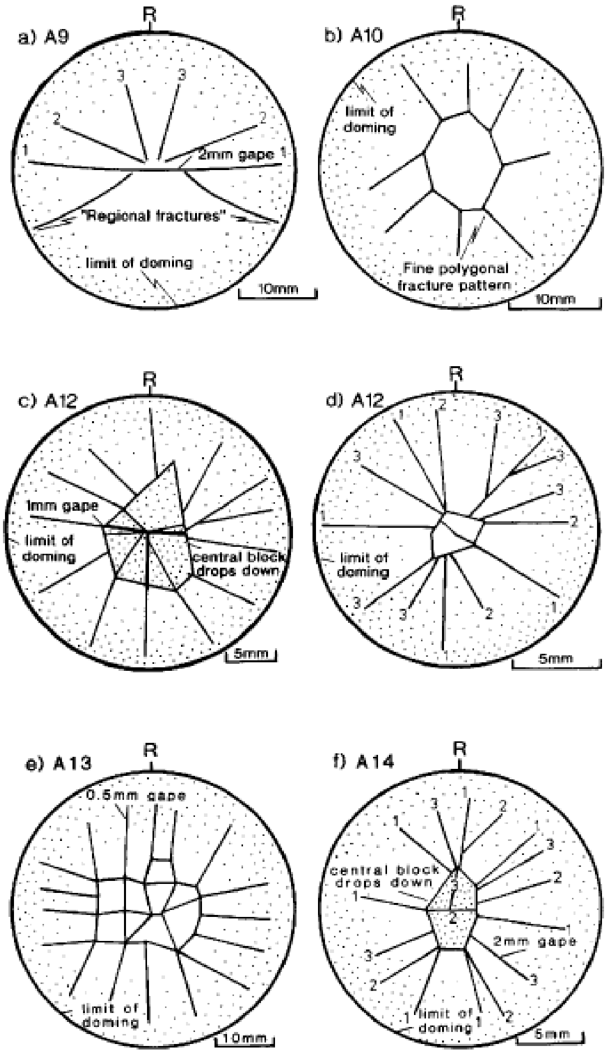

Figure 3.6: Plan view line drawings illustrating the pattern and order of development of fractures in and sand-clay mix horizon directly above the diapir. Fracture patterns are typically radial and may incorporate a central ring fault with downthrown hub. (From Alsop, 1996).

The mechanism by which salt can intrude into thick layers of overburden is not necessarily by active salt injection (Davison et al., 2000). The salt diapir head and flanks caused the overlying sediment to form intense extensional faults, tensile fractures and pressure solution. These processes helped to thin and weaken the overburden, allowing the buoyant salt to rise through the thinned sedimentary layer. However, as the salt continued to rise and breached the surface, it caused the thin layers of sediment to slide off the salt and produce slump folds. As the salt rises towards the surface, the overlying beds might fold as the salt column continues to rise (Giles & Rowan, 2012). The sedimentary beds would become upturned, but there are two proposed end-members. One is a hook sequence, in which the deformed bed has a narrow zone of thinning of only 50 – 200 m long, leading away from the salt column. The other end-member is a wedge sequence that has a much wider zone of deformation (300 – 1000 m) leading away from the salt wall (Fig. 3.7). This implies that deformation bands which developed within 1000 m of the diapir stem would change orientation relative to when it first formed. Therefore, the modern orientation of the deformation bands would not represent the original orientation when the deformation band formed.

As well as faulting and fracturing resulting from rising salt structures, the dissolution of salt could also produce faults in overlying sediments (Clark et al., 1999). During the Triassic, the Zechstein salt layer passively intruded the Smith Bank Formation via circular collapse zones that had formed during the Early Triassic. The intruding salt than developed and grew into significant chimney structures within the sediment fill of the mini-basins (Clark et al., 1999). Dissolution of these salt chimneys near the surface by groundwater would have resulted in localised collapse structures, which would have resulted in differential erosion of the basin sediments.

While the development and evolution of salt-wall mini-basins may initially seem simple, the previously mentioned studies have shown that mini-basins are influenced by many factors, both constant throughout the evolution of the mini-basin and changing as the mini-basin develops. The movement of the salt may also yield many different structural products that can impact the final geometry, the overlying topography, properties of the sediment infill, and reservoir quality.

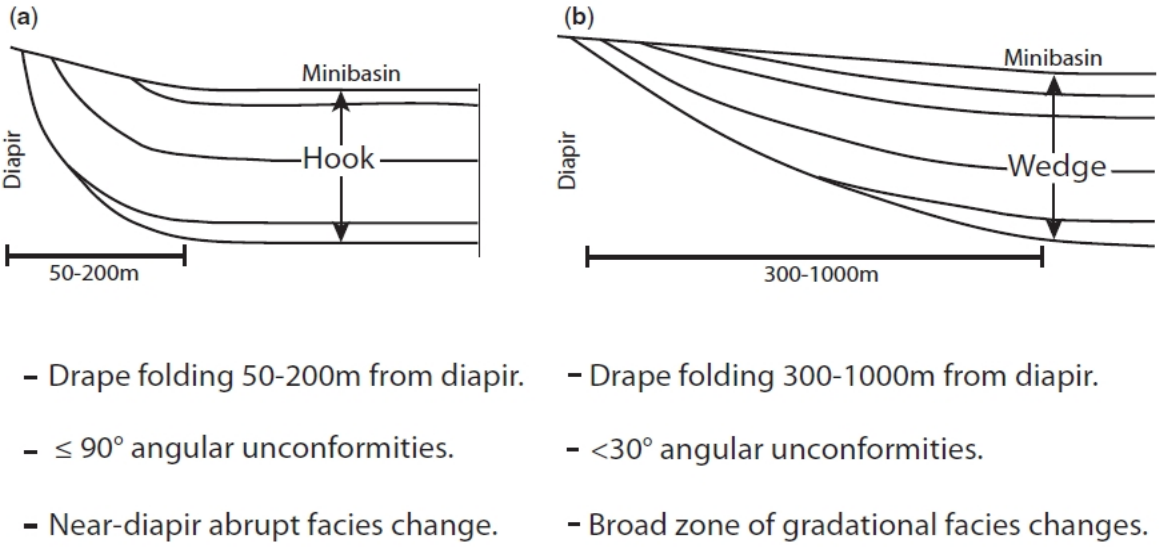

Figure 3.7: Two end-member types of halokinetic sequences: (a) hook halokinetic sequence; and (b) wedge halokinetic sequence. (From Giles & Rowan, 2012).

3.2 Geological Setting

The Central Graben of the CNS forms the southern arm of an incipient triple junction, with the Viking Graben forming the northern arm, and the Moray Firth Basin as the western arm. The Central Graben has been divided into east and west sections by the Josephine High and the Forties-Montrose High, separating the U.K. and Norwegian continental shelves and sectors (Fig. 1.8) (Cui et al., 2017). During the Early Triassic, sediments were deposited on the Upper Permian Zechstein salt layer, which deformed the salt layer and created sediment pods, or salt-wall mini-basins, within the Central Graben (Hodgson et al., 1992).

3.2.1 Structural framework and rifting phases

There have been several phases of rifting in the North Sea during the Late Palaeozoic and during the Mesozoic (Harding & Huuse, 2015). Two major extensional rifting phases occurred during the Permian to Early Triassic (290 – 210 Ma) and Late Jurassic (155 -140 Ma), (Goldsmith et al., 2003; Fraser et al., 2003; Stricker et al., 2018). The episode of Early Triassic extensional rifting has been considered as a response to the Hardegsen tectonic event, and was mostly accommodated by reactivation of pre-existing faults within the Rotliegend (McKie, 2014). Research suggests that reactivation of these faults during the Permian to Early Triassic (290—210 Ma) extensional rifting could have provided the instability in the overlying salt to initiate halokinesis (Hudec et al., 2009; Harding & Huuse, 2015). Faults with greater vertical offsets compared to the thickness of the salt layer appeared to have a more significant influence over the eventual position of the salt walls, and smaller offsets along the faults were not expressed in the position of the salt structures (Hudec et al., 2009; Karlo et al., 2014). The reactivation of these faults would have accentuated the horst and graben structures found across the Rotliegend, providing a mechanism for the mobilisation of the Zechstein salt layer (Hodgson et al., 1992). The combination of rifting and localised loading by continuous sediment deposition onto the salt cover of the CNS would have led to the development of a complex topography across the CNS (Hodgson et al., 1992; Smith et al., 1993; Matthews et al., 2007). The continuous sedimentation during the Hardegsen tectonic event and resultant rifting has caused the Triassic Smith Bank Formation to be considered syn-rift, and any overlying sediment to be post-rift, including the Skagerrak Formation (Hodgson et al., 1992; McKie et al., 2010). The uncertainty associated with the exact timing of this rifting phase has resulted in further uncertainty concerning the transition from syn-rift to post-rift sedimentation, and therefore the possible transition from the salt movement being controlled by tectonic phases or sediment loading.

An intra-Triassic unconformity which separates the Smith Bank Formation and the Bunter Sandstone Formation from the younger Skagerrak Formation sandstones has been linked to the Hardegsen Unconformity found in the Southern Permian Basin (Geluk, 2005; McKie, 2014). The next major phase of extensional rifting would occur during the Late Jurassic (155 -140 Ma) (Fraser et al., 2003; Stricker et al., 2018).

3.2.2 North Sea salt-wall mini-basins

The salt province of the CNS area is notable for featuring salt-walled mini-basin structures throughout the area (Fig. 3.8). The movement of salt during the Triassic allowed for an increase in accommodation space and therefore sediment deposition. However, the periods of time when salt evacuation and accommodation space creation stopped is different for each individual mini-basin due to the variable thickness of the salt layer and the rate of salt evacuation beneath the Triassic sediment (refer to section 3.1.5) (Goldsmith et al., 2003; McKie et al., 2010).

3.2.2.1 Initiation of the North Sea salt-wall mini-basins

When the location and orientation of faults in the Rotliegend and the location and orientation of salt structures are compared with each other, a correlation can be observed (Figs. 1.8 & 1.9). It has been suggested that extensional rifting and reactivation of the faults in the basement could have caused the required instability in the overlying salt to initiate halokinesis (Hudec et al., 2009; Harding & Huuse, 2015). Faults with greater vertical offsets appear to have a greater influence on the eventual location and orientation of the salt structures, which would suggest extensional rifting as a possible mechanism for how the formation of the salt-wall mini-basins initiated (Hudec et al., 2009). It should also be noted that the initiation mechanism of halokinesis in the North Sea has been previously discussed and debated (Erratt, 1993; Stewart & Clark, 1999). However, it is unlikely that the specific mechanism that initiated the salt movement would have any further influence over the eventual formation of the deformation bands within the mini-basins other than the initial position of the salt walls.

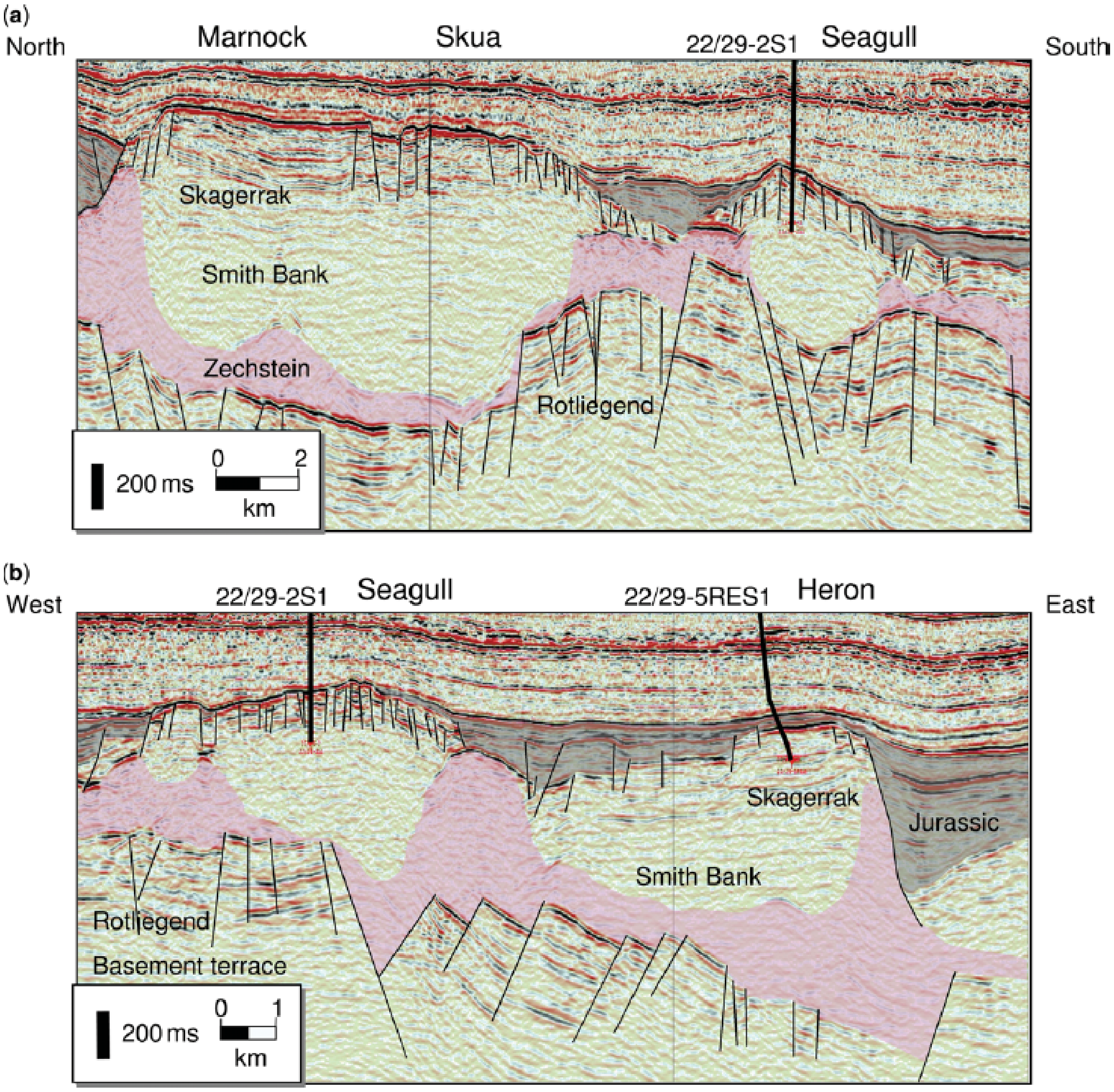

Figure 3.8: Illustrative seismic sections showing the preserved geometry of the Triassic Sandstones in the Heron Cluster area. (**a**) This section shows the geometry of the Marnock, Skua and Seagull fields. (**b**) A cross section across the Heron and Seagull Fields. The Jurassic units (darker grey) above the Skagerrak Formation are generally thicker over the Zechstein salt walls (light grey) which are adjacent to the mini-basin pods. (From McKie et al., 2010). This study utilises core imagery and well data from well 22/29-2S1, located towards the mini-basin centre, which displays a faulted turtle-back-anticline structure in the seismic image. Although the well is not located next to a salt wall, the presence of faults in the mini-basin centre may indicate a high abundance of deformation bands in well 22/29-2S1.

3.2.2.2 Influence of salt movement on sedimentation

Sedimentation into mini-basins during the Mid—Late Triassic fluctuated in response to the varying climate (Archer et al., 2010; Banham & Mountney, 2013b) and surface topography (Hodgson et al., 1992; McKie et al., 2010; Banham & Mountney, 2013b). Subsurface movement of the salt is thought to have been expressed at the surface as changes in topography. These changes in topography would alter the sediment transport pathways, resulting in some mini-basins becoming sediment starved while other mini-basins were filled and became sediment-rich (Hodgson et al., 1992; McKie et al., 2010).

The Judy and Joanne Sandstone members (Fig. 2.7) show variable thickness across the sandstone units, indicating that the surface that the sediments were being deposited on were not perfectly planar and could imply halokinesis or rifting during deposition (McKie et al., 2010; McKie, 2014).

These changes in thickness are gradational and the sandstones show similar facies characteristics across wide areas with little evidence of abrupt facies or lithology changes. This semi-uniformity within the sedimentary members across large areas would suggest that there was minimal surface expression of any underlying salt movement during the deposition of these fluvial sheets (McKie, 2014). There is evidence of Middle to Late Triassic sediments onlapping onto the salt walls, so there is some local surface expression of salt structures, but not a significant amount which would confine the sediments during sedimentation. Palaeocurrent analyses indicate that the fluvial sediments were deposited axially parallel to the salt walls, showing that the salt structures did have sufficient surface expression to influence the deposition of the sediment (McKie et al., 2014). This could be resolved by the lack of change in surface topography being the result of the sediment influx infilling the mini-basins at a similar rate to the development of accommodation space as the salt evacuated out from under the sedimentary mini-basin fills. Since most of the mini-basins had grounded on the Rotliegend by the end of the Triassic, it is likely that deposits during the Late-Triassic such as the Josephine sandstone unit (Fig 2.7) would only have been deposited and preserved in mini-basins which had not yet grounded and would therefore still produce accommodation space, prior to erosion during the Jurassic (Mid-Cimmerian Unconformity).

3.2.2.3 Sediment pods grounding on the Rotliegend

Based on the podology model (Hodgson et al., 1992), the grounding of the mini-basin pods may have started as early as the Mid-Triassic, while other basins may not have fully grounded until the mid-Jurassic. This was due to the variable thickness of the salt layer and rate of salt evacuation, with sediment in thicker layers of salt taking longer to subside than thinner layers of salt.

Topographically, the syncline form of the sedimentary infill within the mini-basin would change upon grounding on the Rotliegend, forming a topographic high over the depocentre of the mini-basin. The resulting structure is referred to as a ‘turtle-back-anticline’ which can be observed in seismic sections of the Skagerrak Formation across the CNS (Fig. 3.8) (Hodgson et al., 1992). After the grounding of the mini-basin pod on the underlying Rotliegend, the sediment would be deposited over the interpod areas (salt walls). These salt walls would then subside under the load of the sediment, similar to the mini-basin pods, or the salt structures would collapse due to dissolution from meteoric water. This process would result in the preservation of Upper Jurassic sediments between the Skagerrak Formation-filled mini-basins (Hodgson et al., 1992).

3.3 Methodology

3.3.1 Datasets (Well 22/29-3)

Orientation data for well 22/29-3 was recorded as tabulated core goniometry data in the well reports (Shell Exploration and Production, 1993a, b). Core goniometry can be used to measure the orientation of the deformation features from the core samples, which are then calibrated using wireline log data and dipmeter data from the borehole. The tabulated data listed the depth of the deformation band, as well as their dip, dip azimuth and strike (Appendix D).

Another set of data for well 22/29-3 from the well reports included interpreted Fullbore Formation MicroImager (FMI) data. This data is measured using a Formation MicroScanner Tool (FMS), a microresistivity imaging device that can display the data as eight Stratigraphic High-resolution Dipmeter Tool (SHDT) curves for dipmeter processing (Fig. 3.9) (Rider, 1996). The range of orientation data from the FMI log acquired occurred from 4181.2 m (13718 ft.) to 4269.6 m (14008 ft.) depth (Appendix E). However, this occurred over 6 sections of between 1.8 – 2.1 m (6 – 7 ft.) meaning that the data covered a total of 12.1 m (40 ft.) of the recorded 88.4 m (290 ft.) core section length (Fig. 3.10).

While this is a very small amount of data, the range over which the data is taken samples a broad range of the borehole depth. A gradual change in the dip direction of the deformation bands may be observed between the ‘snapshots’ provided by these dip logs and would capture the rotation of the deformation band orientations along the borehole length. Ideally, this data set would be combined with the core goniometry data to produce a larger data set. However difficulties in correlating the orientations for individual bands, since depth in the core goniometry data is accurate to 15 cm (0.5 ft.), so bands with similar orientations within 15-30 cm of each other could not be confidently separated. This means that simply combining the two data sets for this well would result in repeated band orientations and therefore produce inaccurate results when analysing the orientation data.

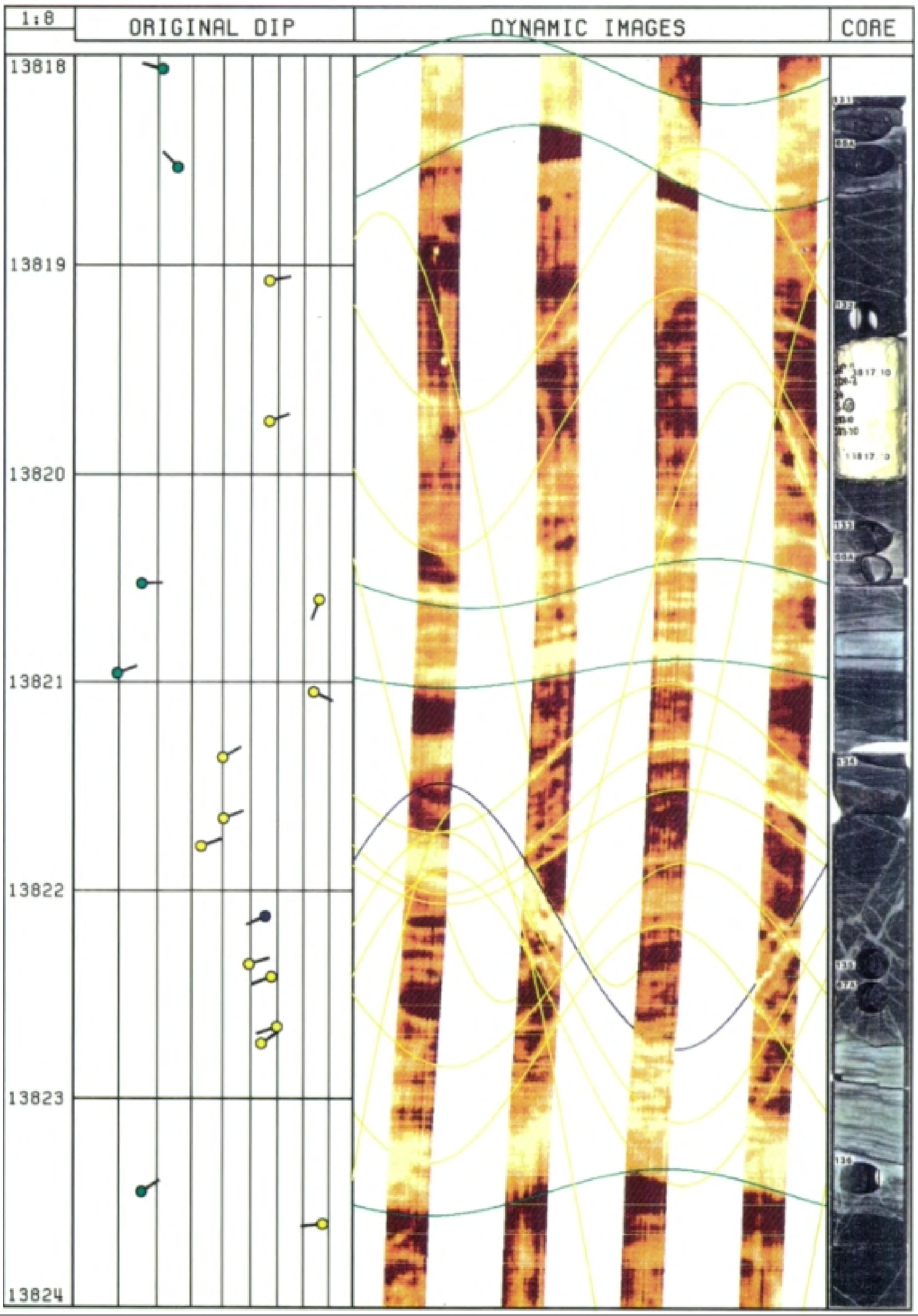

Figure 3.9: Interpreted FMS (FMI) data for a 1.8 m (6 ft.) interval of well 22/29-3 from Shell Exploration & Production (1993a). The image shows interpretations of deformation features (yellow), parallel bedding features (green), and faults (dark blue). The interpreted FMS data (tadpole) is shown alongside the FMS scan image, and the core sample from the same depth interval. The 'tadpole' denoting dip magnitude and dip direction consist of a dot and a headless arrow connected to the dot. The headless arrow indicates the direction of down dip away from the dot, with north being towards the top of the tadpole. The horizontal position of the dot across the dip log indicates the dip magnitude of the feature with each vertical bar from left-to-right representing 10^{O} of dip from horizontal. Depth is measured depth in feet (MD).

Figure 3.10: Diagram showing the division of deformation band orientations based on core goniometry data and FMI data in well 22/29-3 into the various core run intervals, as well as the depths for each of the dataset depth intervals. The plotted stereonet data for all deformation bands from each respective dataset is also shown against depth along the borehole. Stratigraphic log adapted from Shell Exploration and Production (1993). (d) shows the extent of the core section from Fig 3.9.

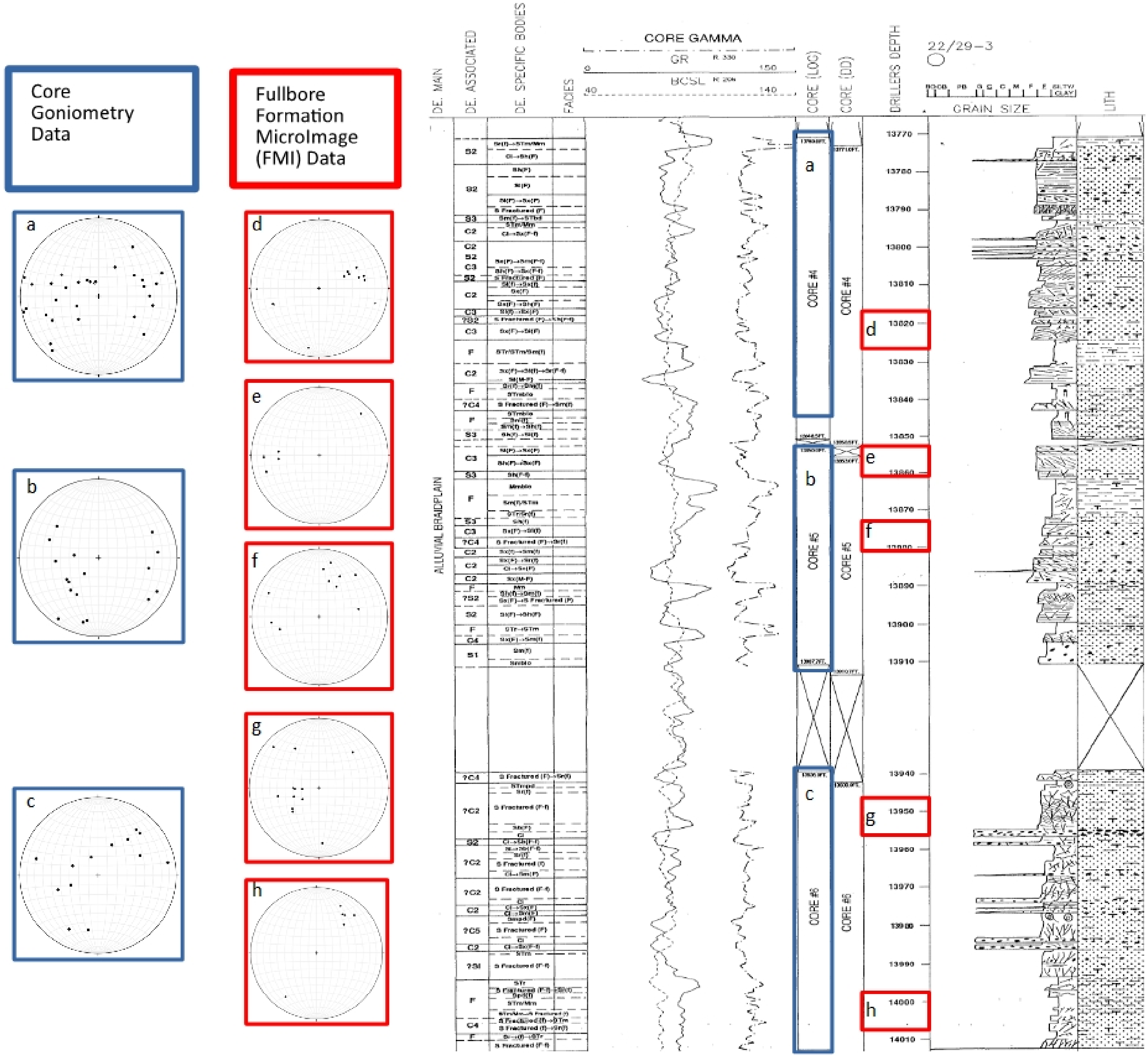

3.3.2 Datasets (Well 22/29-2S1)

The well reports for well 22/29- 2S1 provided two dipmeter logs which displayed the same deformation band orientation data set, so only one dip log was required for the conversion into tabulated dip and dip direction data (Appendix F). This dip log contained orientation data for the deformation bands and sedimentary beds along the borehole. The dip logs were interpreted from Formation Micro-Scanner (FMS) data, the same as the well 22/29-3 FMI dataset (Fig 3.9). This data was also presented as dip log 'tadpoles', which were then converted into tabulated dip and dip direction orientations. The large number of data points from the dip log allowed for the data to be separated into various data interval sizes. The intervals were 7.6 m (25 ft.), 15.2 m (50 ft.), and 30.5 m (100 ft.), which allowed any changes in the average orientation of the deformation bands to be observed at several scales while also allowing consecutive intervals to contain multiple measurements.

An uncertainty involved with using this dataset is that it did not include the original FMI data and only included the interpreted tadpole data. Therefore an assumption has to be made that the interpretation of the FMI log is accurate when picking out deformation bands.

Well 22/29- 2S1 sampled the Skagerrak Formation from 4114.8 m – 4477.5 m (13500 ft. – 14690 ft.) MD depth. This included 225 interpreted fracture orientations found along the entirety of the length of the sampled section. There were more interpreted orientations logged towards the base of the wellbore, and for the intervals 4245.9 m – 4279.4 m (13930 ft. – 14040 ft.) MD, and 4322.1 m – 4361.7 m (14180 ft. – 14310 ft.) MD, there is no orientation data. Due to the lack of core photographs for this sidetrack well, it is unknown if any deformation bands are present in these intervals and were not picked out by the FMS.

3.3.3 Stereonets

The first analysis performed was to plot the data on the stereonets using Stereonet9. The data was plotted as planes to poles with bottom hemisphere projection. As well as all of the orientation data from each set being plotted on the stereonets to observe significant clustering, the various datasets were plotted according to depth intervals to observe changes in orientation along the core section. For well 22/29- 3, the data was divided into core run intervals based on the well reports (Table 2.2), and further divided into 20 ft. intervals to better observe gradual changes to the orientation.

While these depth intervals are highly irregular, they provide a 'snapshot' of the orientation of deformation bands at that depth. These intervals were then further divided into 6 m (20 ft.)

intervals which were then plotted on the stereonets. The size of the intervals was selected to be 6 m (20 ft.) as this would provide a small enough interval to observe any changes in deformation band orientation while also containing enough data points (deformation bands) to generate a representative average orientation for the deformation bands over that interval. The core goniometry data did not contain orientation data for core runs #2 or #3, and only records orientations for the Kimmeridge Clay Formation and the Upper Skagerrak Formation. While the Kimmeridge Clay Formation is not the focus of this study, the orientation data from this interval was still used since it could give an indication of the final stress field in the Jurassic, and if any trend observed from the Skagerrak Formation continued from the Triassic into the Jurassic.

3.3.4 Orientation Trends

The software which generated the stereonets (Stereonet9) also generated eigenvalues for the various data sets. These eigenvalues would provide an 'average' orientation (refer to section 3.3.5 for more detail) for that interval of deformation band orientations. However, since most depth windows included conjugate sets, calculating the average orientation of the band would result in the dip tending towards vertical or horizontal orientations. Therefore, in order to have an accurate average orientation for deformation bands along that section of core, the orientation data would have to be separated into separate populations split out in oppositely dipping sets (easterly-dipping and westerly-dipping). However, this further division of the intervals would result in less statistically significant datasets that were more representative of the averaged orientation but had less abundant orientation data. Therefore, at this stage, eigenvalue analysis would be carried out on the combined conjugate sets and the separate conjugate sets. The eigenvalues for the combined conjugate sets could be used to generate the dip direction for the intersection between conjugate sets. In order to combine and resolve the oppositely dipping deformation bands in each depth window, the azimuth (dip direction) of the intersection between conjugate sets (ACI, or Azimuth of Conjugate Intersection) was recorded (Fig. 3.11).

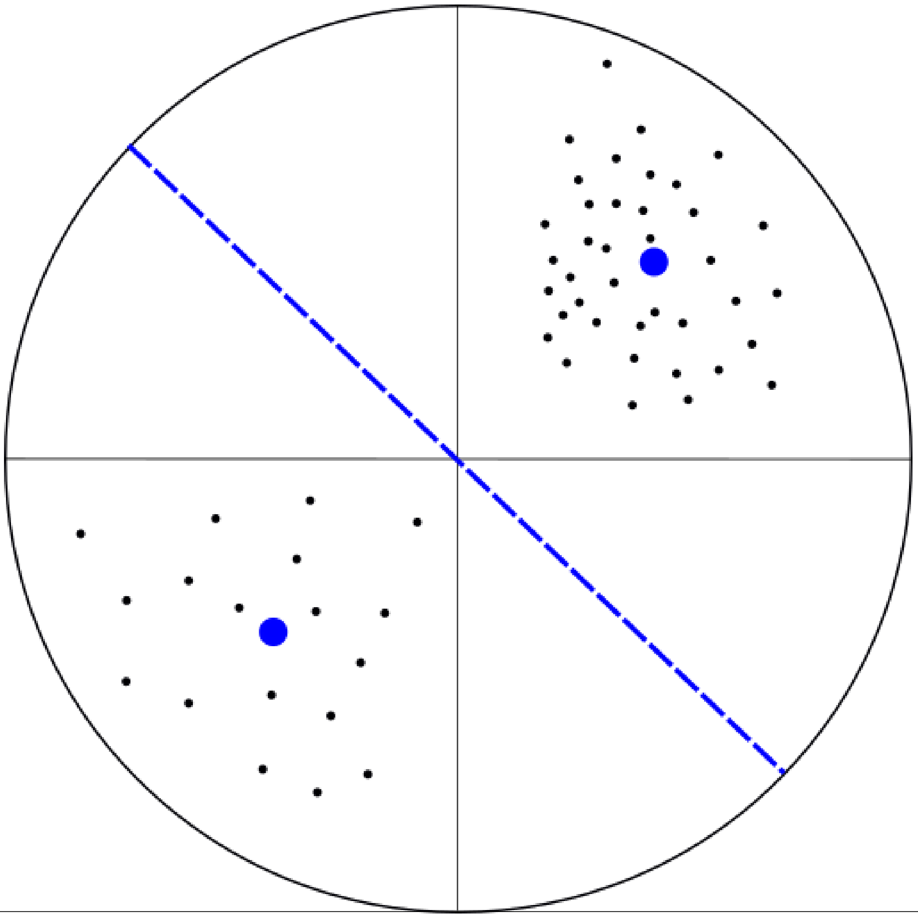

Figure 3.11: Sketch demonstrating the azimuth of the conjugate intersects (blue dashed line). The stereonet displays orientation data as two oppositely-dipping groups of poles-to-planes (black dots) with the northeast quadrant having a significantly higher population than the southwest quadrant. In order to measure a change in the average deformation band orientation, the average orientation of each oppositely-dipping cluster will be calculated (blue dots). Then the azimuth of the intersection between the averaged clusters can be calculated (blue dashed line). This method allows oppositely-dipping clusters to be resolved as a single dip direction so that successive 'depth intervals' of deformation bands can be grouped and averaged to observe potential changes of the overall deformation band orientations.

The analysis required to observe a change in the average orientation of deformation bands is similar in approach to that described by Guo et al. (2009). This study looked at the changes in dip magnitude and dip direction of deformation bands along a 40 m outcrop of Permo-Triassic sandstone in the Lake District, UK. One of the methods used in this study to display the changes in orientation, or spatial heterogeneity, of the features was to separate the data into intervals, or sampling windows, of varying size (3, 5, 10, and 20 m). The average orientation was then plotted on a graph of plunge vs azimuth, as well as a line of best fit for the data. The line of best fit highlights the change in deformation orientation across the outcrop. In effect, the sample line along the outcrop in Guo (2009) is geometrically equivalent to data collected from a borehole, and thus the methods applied would be equally viable for this thesis.

3.3.5 Statistical Analysis

The statistical viability of the stereonets were measured using the eigenvalues and the strength and spread of the data points. The eigenvalues would be denoted by S_1, S_2, and S_3, each of which are a normalised measure of the degree of clustering around the respective eigenvectors (v_n). The eigenvector, v_1, can be considered the estimate of the distribution mean for the data points, and v_3 can be considered the estimate of the pole to the best fit girdle to the data, assuming that the data does not form an axially symmetric cluster (Woodcock, 1977). The final eigenvector, v_2, is perpendicular to both v_1 and v_3. The methods and equations used to calculate and graphically display the results were taken from Woodcock (1977).

The shape that the data point distribution could take would vary from a circular cluster to a band or girdle of data points across the stereonet. This morphology of the data points can be assigned the value K, where:

$$K = \frac{\ln(S_1/S_2)}{\ln(S_2/S_3)}$$

K values that tend towards 0 form a girdle across the stereonet, and K values that tend towards ∞ (infinity) would form a smaller and more densely packed point. However, this would only quantify the shape of the data distribution. The density of the data points, or strength of the preferred orientation, is quantified by the value C:

$$C = \ln(S_1/S_3)$$

C values that tend towards 0 have a completely homogenous distribution across the stereonet, and higher values of C would have a more concentrated distribution of data points. These K and C values can be used to map areas on a graph of $\ln(S_1/S_2)$ against $\ln(S_2/S_3)$ to show the distribution shape and strength of the data points (Fig. 3.12).

However, the drawback of these values is that although the S_n values have been normalised using the number of data points, *N*, the K and C values do not reflect different values of *N* for each data set. In order to overcome this, the C values and K values were plotted with the number of data points used to generate that C value. Higher values of *N* would make the generated C values and K values more statistically reliable.

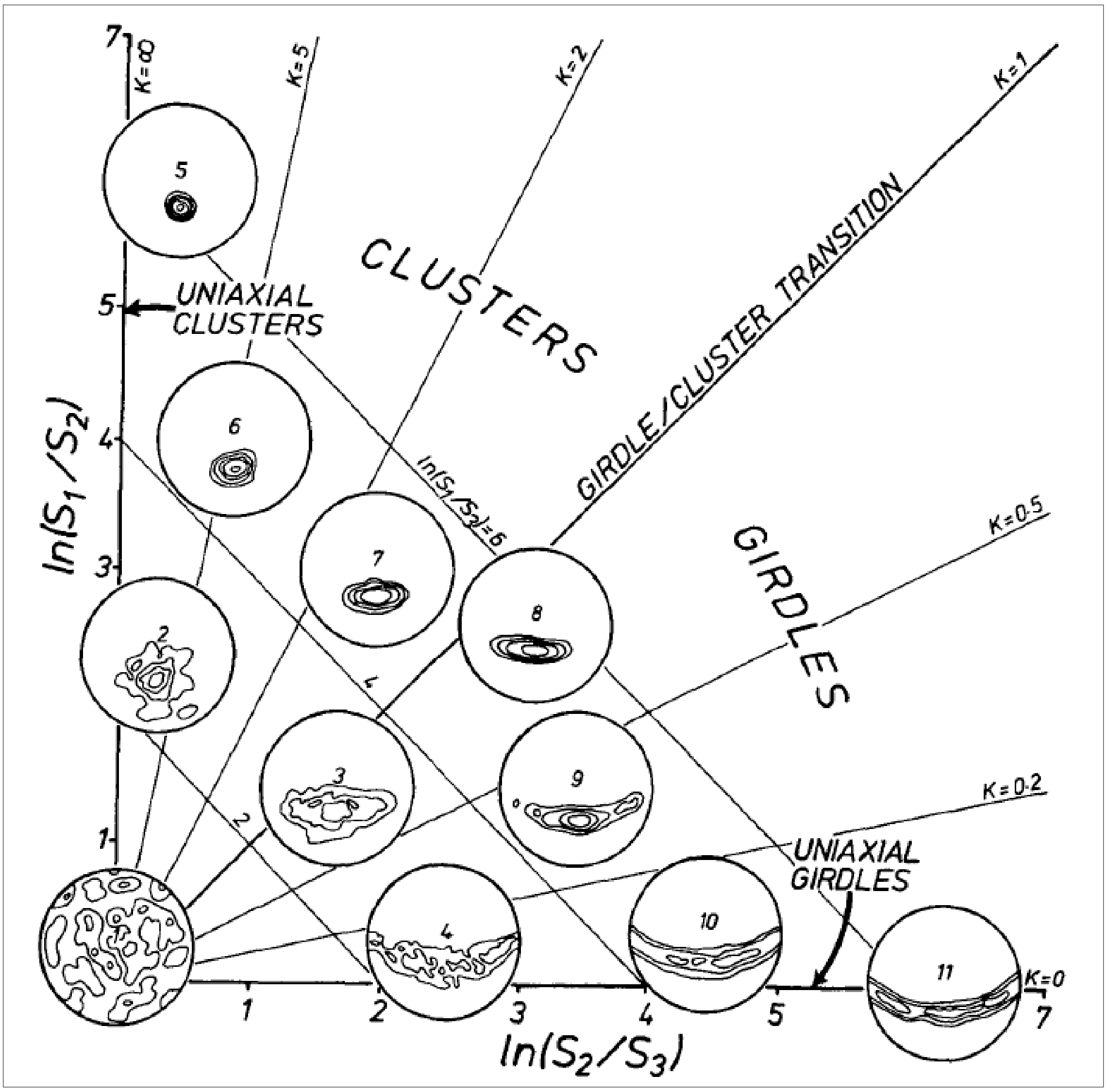

Figure 3.12: Two-axis logarithmic plot of ratios of normalised eigenvalues S_1, S_2, S_3 with examples of fabric shapes in different parts of the graph. K values determine the girdle/cluster form of the orientation data indicated by the gradients from the origin. C values determine the density of orientation data and are indicated in this graph by the gradients perpendicular to the girdle/cluster transition (K = 1 gradient). (From Woodcock, 1977).

3.4 Results

3.4.1 Well 22/29-3

3.4.1.1 Well 22/29-3 Data Reliability

While there was less available orientation data compared to well 22/29- 2S1, analyses were carried out on the orientation data for well 22/29- 3 in order to check the reliability of the available data. For the 6.1 m (20 ft.) intervals divided into the westerly- and easterly-dipping clusters, most of the average orientations have a K value less than 1, which would indicate that the orientation distribution tended towards a girdle rather than discrete clusters (Fig. 3.13). The distributions with K values greater than 1 have a C value of approximately 4, while the distributions with K values less than 1 show a distribution towards C values of 3 and 5. When the number of data points is plotted against the C values that the number of data points generated, it could be observed that a range of C values (2 – 5.5) can be generated by a small range of data points (3 - 7) (Fig. 3.13). The most common number of data points used to calculate C values was 5, which gave a C value range of 2.5 – 5. There did not appear to be a correlation between the number of data points and the C values generated, meaning that the apparent cluster density of deformation band orientations was independent of the number of deformation bands present in the plotted data set (Fig. 3.14). For this data set, an increase in the number of deformation bands did not increase the cluster density of deformation band orientations. Due to the smaller amount of data and patchy distribution of the FMI data set for this well, no reliability analyses were carried out on this data set.

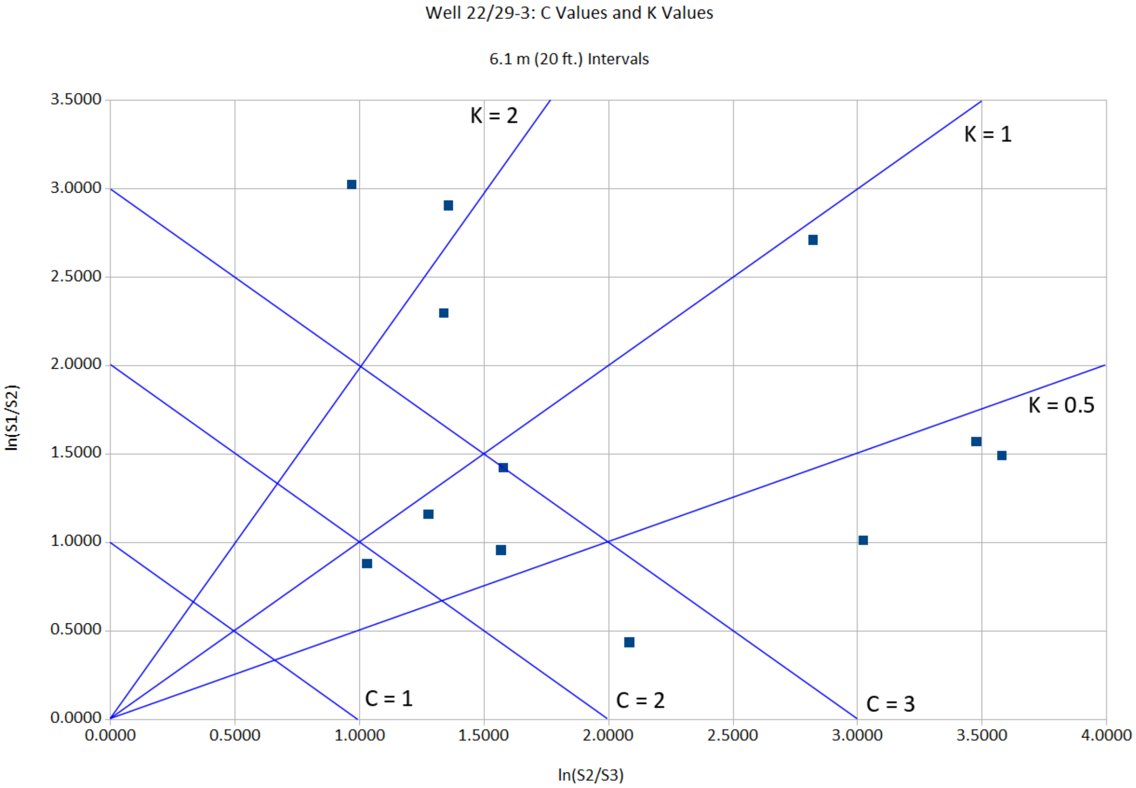

Figure 3.13: Graph showing the spatial and density distribution of the deformation bands in well 22/29-3 for every 6.1 m (20 ft.) interval of both the easterly- and westerly-dipping deformation bands from the core goniometry dataset. The solid blue lines are used to identify boundaries with certain K and C values for ease of comparison with the graphed examples from Woodcock (1977) (Fig 3.12).

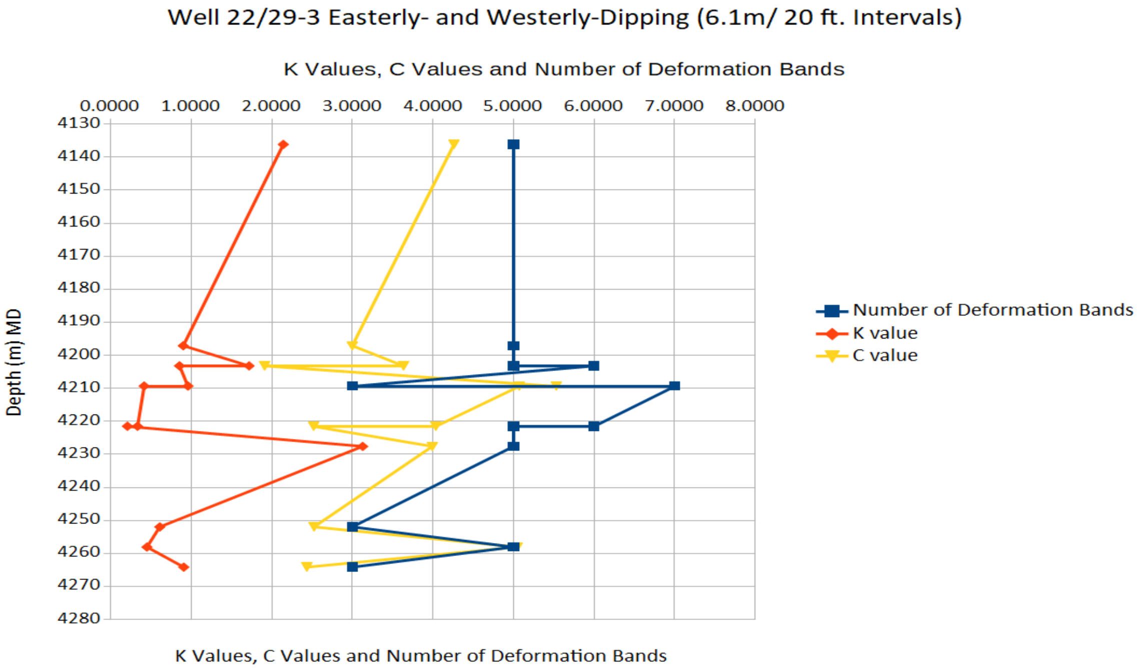

Figure 3.14: Graph showing the number of deformation band orientations used to generate the K values and C values for each 6.1 m (20 ft.) depth interval calculated in Figure 3.13. This is used to illustrate the number of data points used to calculate the C and K values.

3.4.1.2 Well 22/29-3 Orientation Analysis

The stereonet plots of all the orientation data for well 22/29-3 showed a low density girdle distribution, with contouring displaying a more diffuse distribution of orientations of deformation bands tilting towards the west compared to a stronger clustering of orientations dipping towards the east (Fig. 3.15a). The core goniometry dataset and FMI stereonets displayed similar azimuth ranges for the deformation bands and the core goniometry dataset displayed a higher range of dip magnitudes (from horizontal) and azimuths than the FMI dataset. The core goniometry dataset includes dip magnitudes of 20° to 80° for the easterly-dipping deformation bands and dip magnitudes of 15° to 83° for the westerly-dipping deformation bands with the average dip magnitude measuring 50° and azimuths measuring between 40° and 140° for the easterly-dipping deformation bands and 185° and 320° for the westerly-dipping deformation bands. The FMI stereonet highlighted a range of dip magnitudes of 19° to 79° for the easterly-dipping deformation bands and dip magnitudes of 40° to 73° for the westerly-dipping deformation bands with the average dip magnitude measuring 55° and azimuths measuring between 15° and 140° for the easterly-dipping deformation bands and 190° and 355° for the westerly-dipping deformation bands. The higher number of data points in the core goniometry dataset allowed for a higher population density of data points within the dip magnitude ranges.

The stereonet plot of all of the FMI data showed two girdle distributions around the central origin (Fig. 3.15d). These girdles displayed an overall orientation towards the western hemisphere, with the distribution ranging between the north and the south east, and the other girdle showed the distribution focussed in the north-east with the distribution of orientations ranging across the eastern hemisphere. When all of the deformation bands were divided into the 1.8 – 2.1 m (6-7 ft.) intervals, a slight clockwise rotation of the deformation band orientations around the centre towards the top of the core section can be observed (Fig. 3.10). Using the core photographs to identify deformation bands with shear offsets, the deformation bands could then be further divided into depth intervals and shear or dilational bands. Comparing the two different types of deformation band orientations revealed no observable differences in orientation between the different band types (Fig. 3.16). However, it should be considered that this was the smallest data set and therefore the other orientation data for well 22/29- 3 (core goniometry) would be used to corroborate the observations made from the FMI intervals.

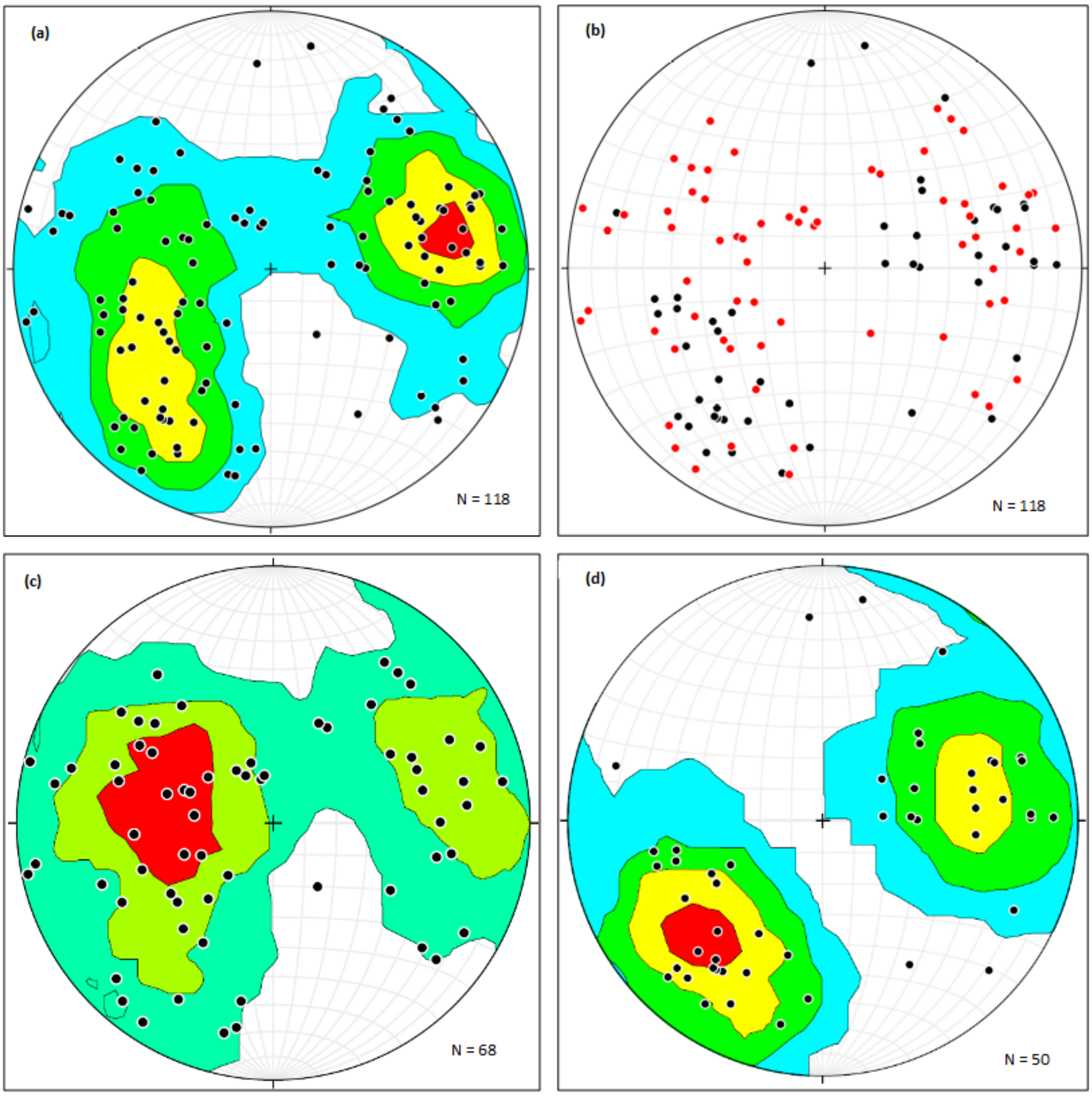

Figure 3.15: Stereonets for the deformation bands observed in well 22/29-3 with planes to poles, bottom hemisphere projection. **(a)** Contoured stereonet for all deformation bands from both the FMI dataset and the core goniometry dataset. **(b)** Stereonet from **(a)** without contours and displays the FMI data (black dots) and core goniometry data (red dots). **(c)** Contoured stereonet of the core goniometry dataset. **(d)** Contoured stereonet of the FMI dataset.

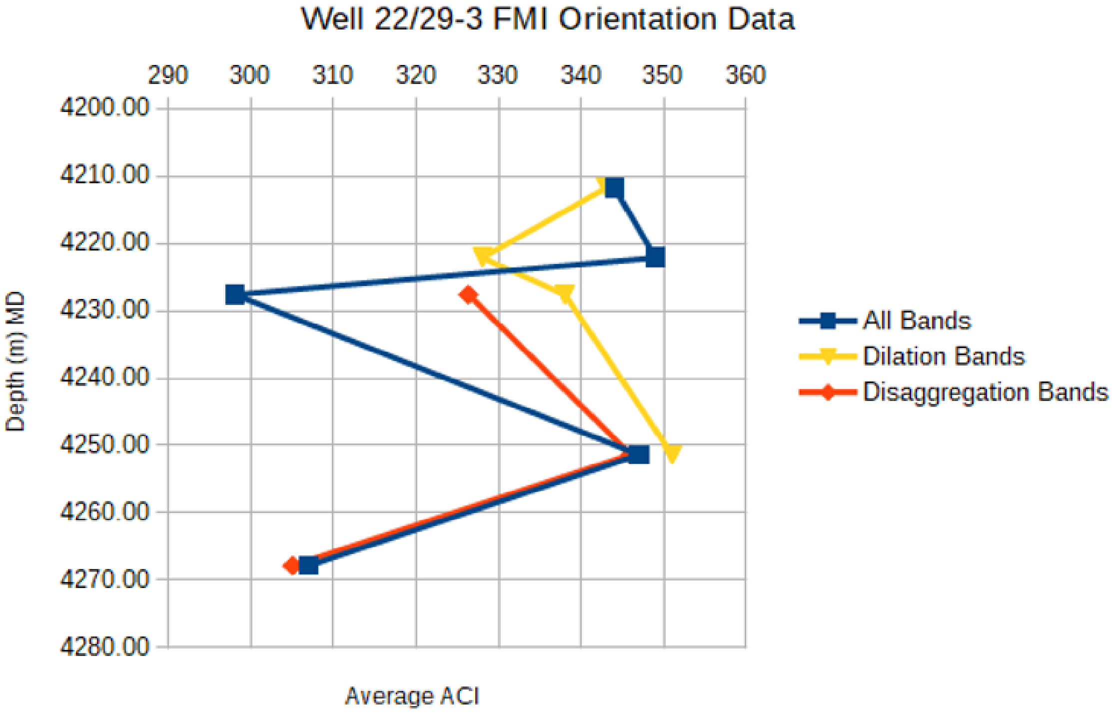

Figure 3.16: Graph showing the average ACI trend of the deformation bands, divided into dilation and disaggregation (shear) bands. The average trend is defined as the azimuth of the intersection between conjugate sets of the deformation band orientations. This is used in order to combine both clusters of the conjugate sets without having to divide the small amount of data further into easterly-dipping and westerly-dipping orientations.

A stereonet with all of the plotted core goniometry from well 22/29-3 showed that the spread of the deformation band orientations was greater than the stereonet for the FMI data, with a higher density distribution of orientations extending towards the north- and southwest for the westerly girdle, and north-east to south-east for the opposite girdle (Fig. 3.15c). The dip magnitudes of the deformation bands ranged from sub-vertical to shallowly dipping (~20^{O} from horizontal), the average dip magnitude for the easterly-dipping girdle appeared to be approximately 60^{O} from horizontal, and the average dip magnitude for the westerly-dipping girdle was approximately 45-50^{O}, slightly shallower compared to the easterly-dipping girdle.

Plotting the averaged dip magnitude against the averaged azimuth for the easterly-dipping deformation bands showed an overall gradual change in the averaged azimuth of the deformation bands from 130^{O} to 68^{O} with fluctuations in dip magnitude ranging from 63^{O} to 26^{O} towards the centre of the sampled core section (Fig. 3.17a). This trend was not reflected in the westerly-dipping deformation band dataset which displayed both clockwise (234^{O} – 311^{O} between 4209.09 m and 4227.58 m (13810 ft. and 13870 ft.) MD) and anticlockwise rotation (311^{O} – 231^{O} between 4227.58 m and 4258.06 m (13870 ft. and 13970 ft.) MD) (Fig. 3.17b).

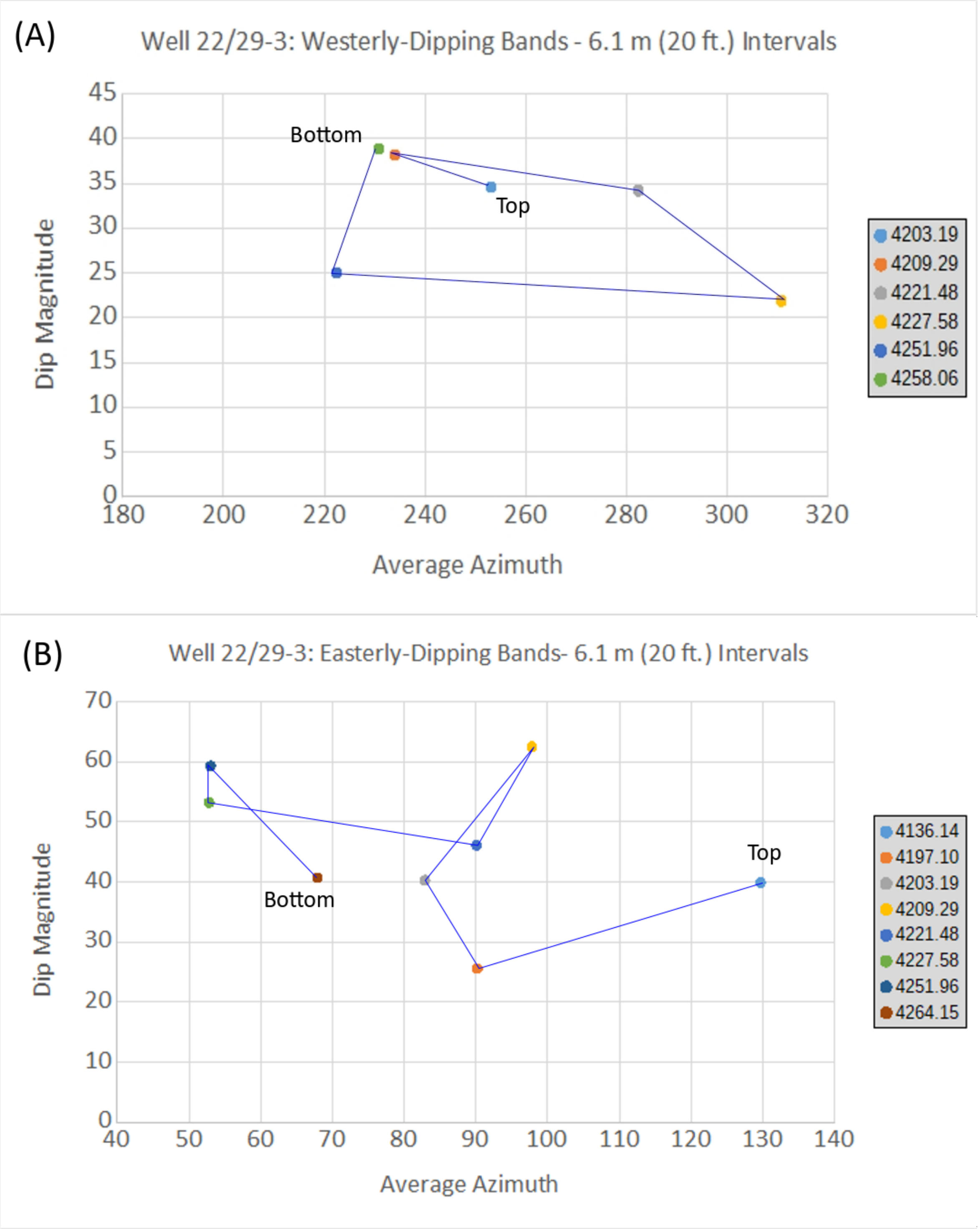

Figure 3.17: Graphs showing the dip magnitude vs. average azimuth of the deformation bands averaged over 6.1 m (20 ft.) intervals along well 22/29-3. (**A**) shows the averaged dip magnitude against the averaged azimuth of the westerly-dipping deformation bands for each 6.1 m (20 ft.) depth interval (depth key). **(B)** shows the averaged dip magnitude plotted against the averaged azimuth of the easterly-dipping deformation bands for each 6.1 m (20 ft.) depth interval (depth key). Depths are measured depths (MD) from the drilling floor datum, units in metres. The blue line highlights the change in average azimuth and dip magnitude down the well (top → bottom).

Plotting the averaged azimuths of conjugate intersections (ACI) orientations of the easterly-dipping and westerly-dipping deformation bands from the core goniometry dataset displayed an overall change in the average orientation of the deformation bands above 4250 m (MD) with dilation bands displaying the strongest linear change in ACI trend (Fig. 3.18). Plotting the averaged azimuth of the intersection between conjugate sets (ACI) for each 6.1 m (20 ft.) interval against depth showed a slight clockwise trend in ACI up the core section before a significant rotation counter-clockwise within the Kimmeridge Clay Formation (Fig. 3.18). The core photographs were used to separate the bands within each of the 6.1 m (20 ft.) intervals into bands that displayed shear offsets (disaggregation) and deformation bands which did not display offsets (dilation). The averaged ACI trends were then plotted against depth to identify any trends in the deformation band orientations (Fig. 3.18).

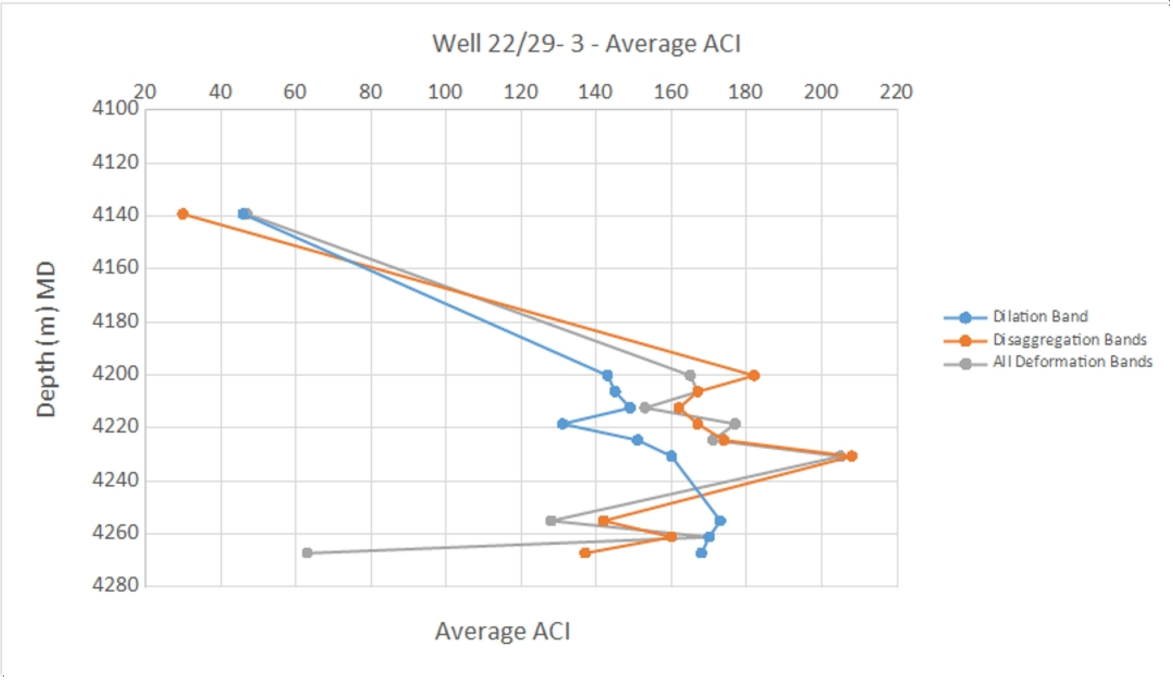

Figure 3.18: Graph showing the average orientation of the dilation bands, disaggregation bands, and all sets of deformation bands for well 22/29- 3 from the core goniometry data. The average orientation is taken to be the azimuth of the intersection between the conjugate sets (ACI) of deformation bands for that interval.

3.4.2 Well 22/29-2S1

3.4.2.1 Well 22/29-2S1 Data Reliability

The analyses carried out to check the validity of each of the interval datasets (7.6 m (25 ft.), 15.2 m (50 ft.), and 30.5 m (100 ft.) intervals) were compared with the two-axis graphical representation of data clustering on a stereonet from Woodcock (1977) (Figs.3.19 – 3.21). When separated into the easterly-dipping and westerly-dipping deformation orientations, the distribution of the orientation data tended towards clusters with a low – moderate data point density. There were still some intervals, at the 7.6 m (25 ft.) interval size that showed a girdle distribution (Fig. 3.19a). The lowest K value (tends towards a girdle distribution) recorded for the 7.6 m (25 ft.) interval was 0.2568, with a corresponding C value of 2.8015 (Fig. 3.19a).

The cluster/girdle distribution of the 3 data interval sizes shows a trend towards moderate C values (2 < C < 4) and slight grouping of the K values into compact clusters (>5) and girdle/cluster transition (K = 1). However, only 3 interval sizes were used, so it is unknown if the trend would be towards clusters or a combination of girdles and clusters.

Plotting the C values against the number of data points in each interval size showed that, for all interval sizes, similar C values (approximately 3.0000) were generated by largely variable numbers of data points, even as the number of data points used to generate the C values increased from the smaller intervals (7.6 m (25 ft.)) to the larger intervals (30.5 m (100 ft.)) (Figs. 3.19– 3.21).

Although, it could be observed that as the interval size increased, a lower proportion of high C values were generated using fewer data points. This was likely due to the increase in interval size incorporating more data points when calculating the C value for that depth interval.

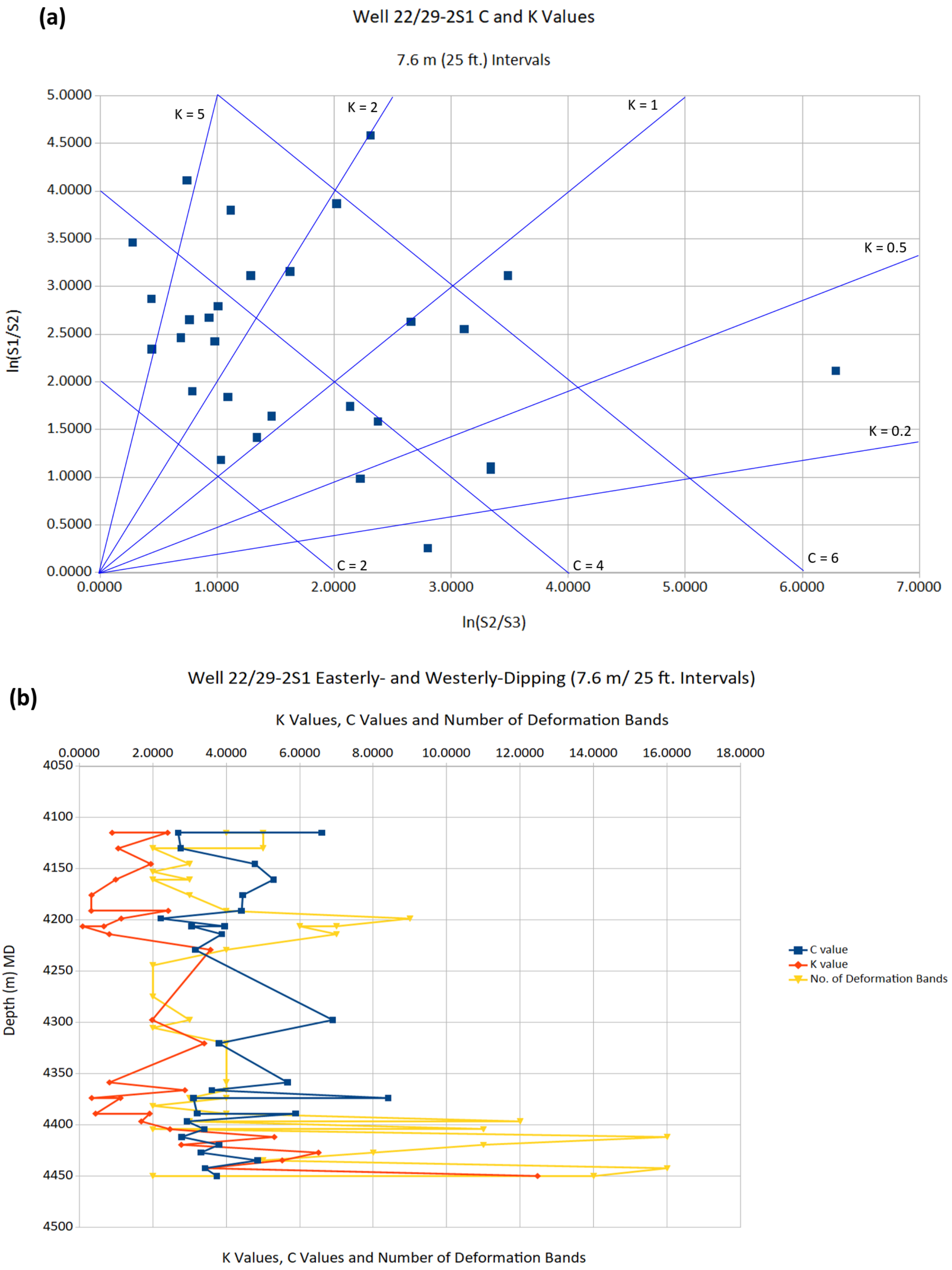

Figure 3.19: Graphs showing the spatial and density distribution of the deformation bands in well 22/29-2S1 for every 7.6 m (25 ft.) interval of both the easterly- and westerly-dipping deformation bands. (a) A graphical representation of the K and C values generated from the 7.6 m (25 ft.) intervals. The solid blue lines are used to identify boundaries of certain K and C values for ease of comparison with the graphed examples from Woodcock (1977) (Fig. 3.12). (b) shows the number of data points used to generate the C and K values, as well as the depths that the C and K values represent. This is used to identify the correlation between the number of data points used to calculate the C and K values, as well as the depths of the calculated K and C values.

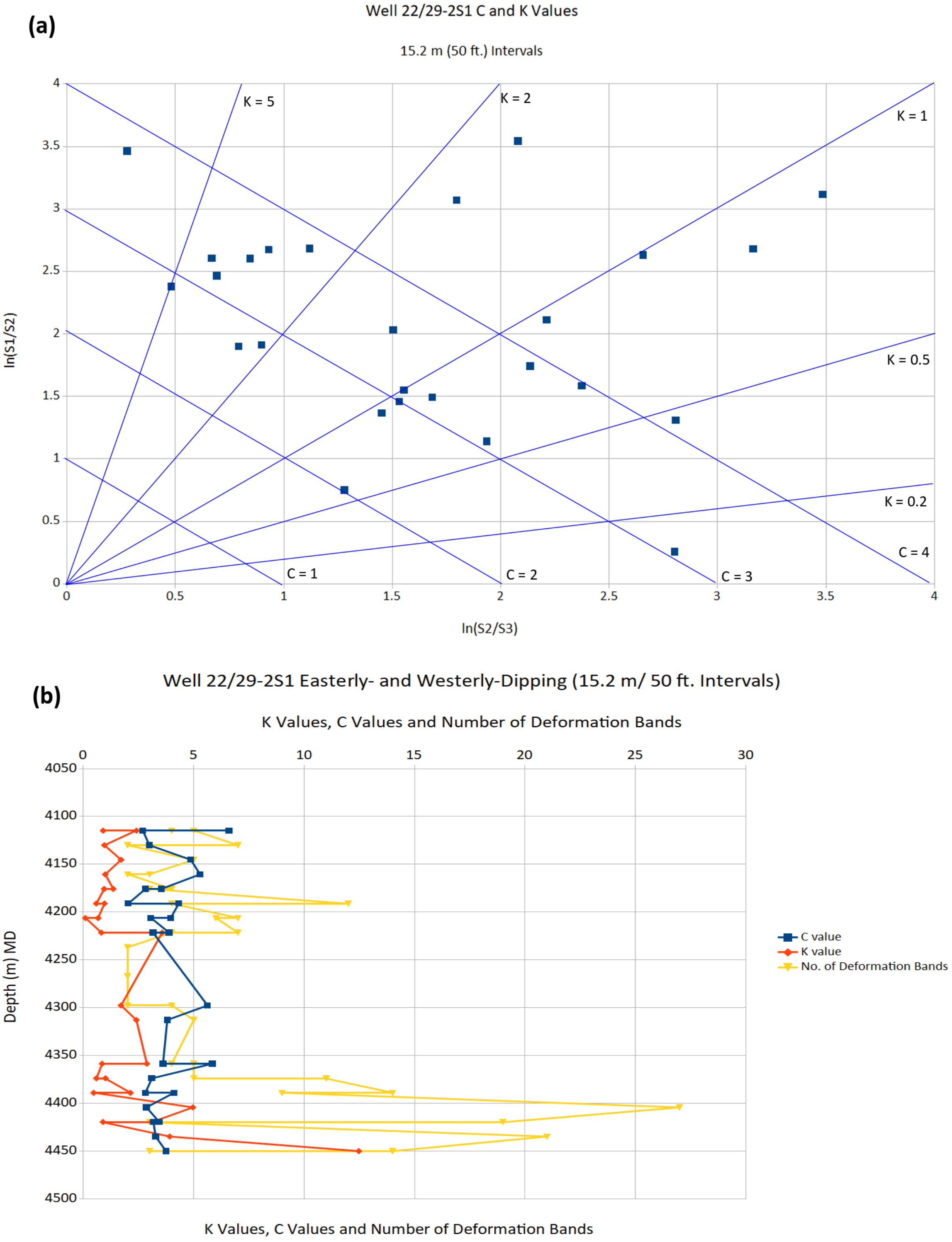

Figure 3.20: Graphs showing the spatial and density distribution of the deformation bands in well 22/29-2S1 for every 15.2 m (50 ft.) interval of both the easterly- and westerly-dipping deformation bands. (a) A graphical representation of the K and C values generated from the 15.2 m (50 ft.) intervals. The solid blue lines are used to identify boundaries of certain K and C values for ease of comparison with the graphed examples from Woodcock (1977) (Fig. 3.12). (b) shows the number of data points used to generate the C and K values, as well as the depths that the C and K values represent. This is used to identify the correlation between the number of data points used to calculate the C and K values, as well as the depths of the calculated K and C values.

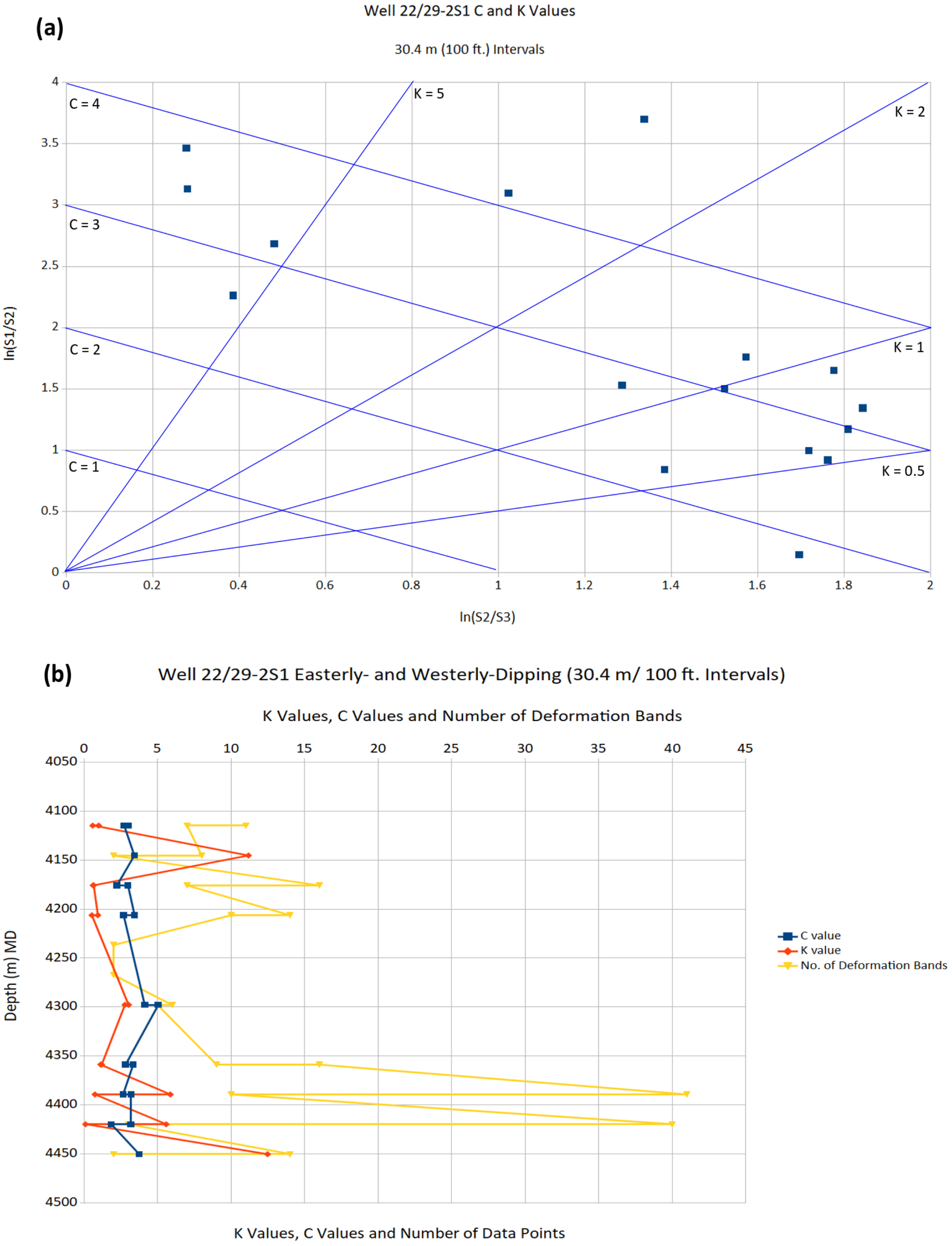

Figure 3.21: Graphs showing the spatial and density distribution of the deformation bands in well 22/29-2S1 for every 30.4 m (100 ft.) interval of both the easterly- and westerly-dipping deformation bands. (a) A graphical representation of the K and C values generated from the 30.4 m (100 ft.) intervals. The solid blue lines are used to identify boundaries of certain K and C values for ease of comparison with the graphed examples from Woodcock (1977) (Fig. 3.12). (b) shows the number of data points used to generate the C and K values, as well as the depths that the C and K values represent. This is used to identify the correlation between the number of data points used to calculate the C and K values, as well as the depths of the calculated K and C values.

3.4.2.2 Well 22/29-2S1 Orientation Analysis

As previously noted, well 22/29- 2S1 is approximately 1 km further from any salt walls compared to well 22/29- 3, so the results were plotted in order to observe if salt wall movement could still affect the orientation of deformation bands further away from the salt wall (Fig. 2.10). The data set for well 22/29- 2S1 was significantly larger than the combined data sets for well 22/29- 3 (well 22/29- 3FMI and core goniometry, N = 118; well 22/29- 2S1, N = 225) (Appendices D, E, and F).

The stereonets for all deformation bands interpreted from the FMI data showed a similar distribution of poles from planes as well 22/29-3, with increased clustering of poles from planes in the SW and NE quadrants (Fig. 3.22). However, the well 22/29-2S1 stereonets showed higher cluster densities in the SW quadrant compared to well 22/29-3 (Fig 3.15).

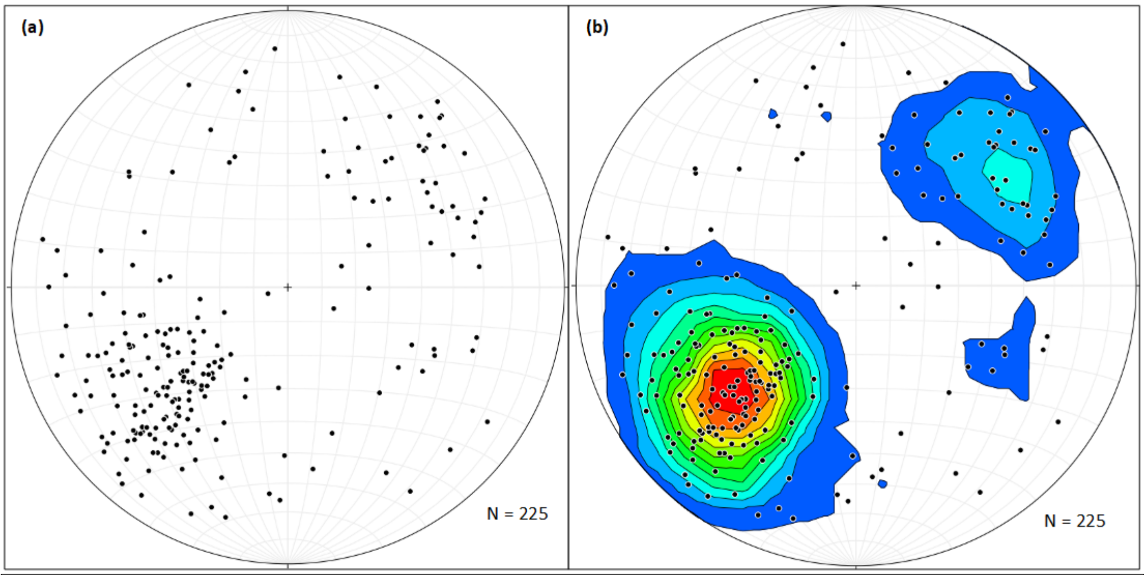

Figure 3.22: Stereonets for the deformation bands observed in well 22/29-2S1 with planes to poles, bottom hemisphere projection. **(a) S**tereonet for all deformation bands from the interpreted FMI dataset for well 22/29-2S1. **(b)** Stereonet from **(a)** with added contour lines to identify high density clusters of deformation band orientations.

Plotting the dip magnitude and azimuth of the average deformation band orientation for each interval showed that both dip magnitude and azimuth fluctuated along the length of the well, with no noticeable trend in the orientation data along the length of the well (Fig. 3.23 – 3.25).

Figure 3.23: Graphs showing the plunge vs. trend of the deformation bands averaged over 7.6 m (25 ft.) intervals along well 22/29-2S1. (**A**) shows the averaged dip magnitude against the averaged azimuth of the westerly-dipping deformation bands for each 7.6 m (25 ft.) depth interval (depth key). **(B)** shows the averaged dip magnitude plotted against the averaged azimuth of the easterly-dipping deformation bands for each 7.6 m (25 ft.) depth interval (depth key). Depths are measured depths (MD) from the drilling floor datum, units in metres. The blue line highlights the change in average azimuth and dip magnitude down the well (top → bottom).

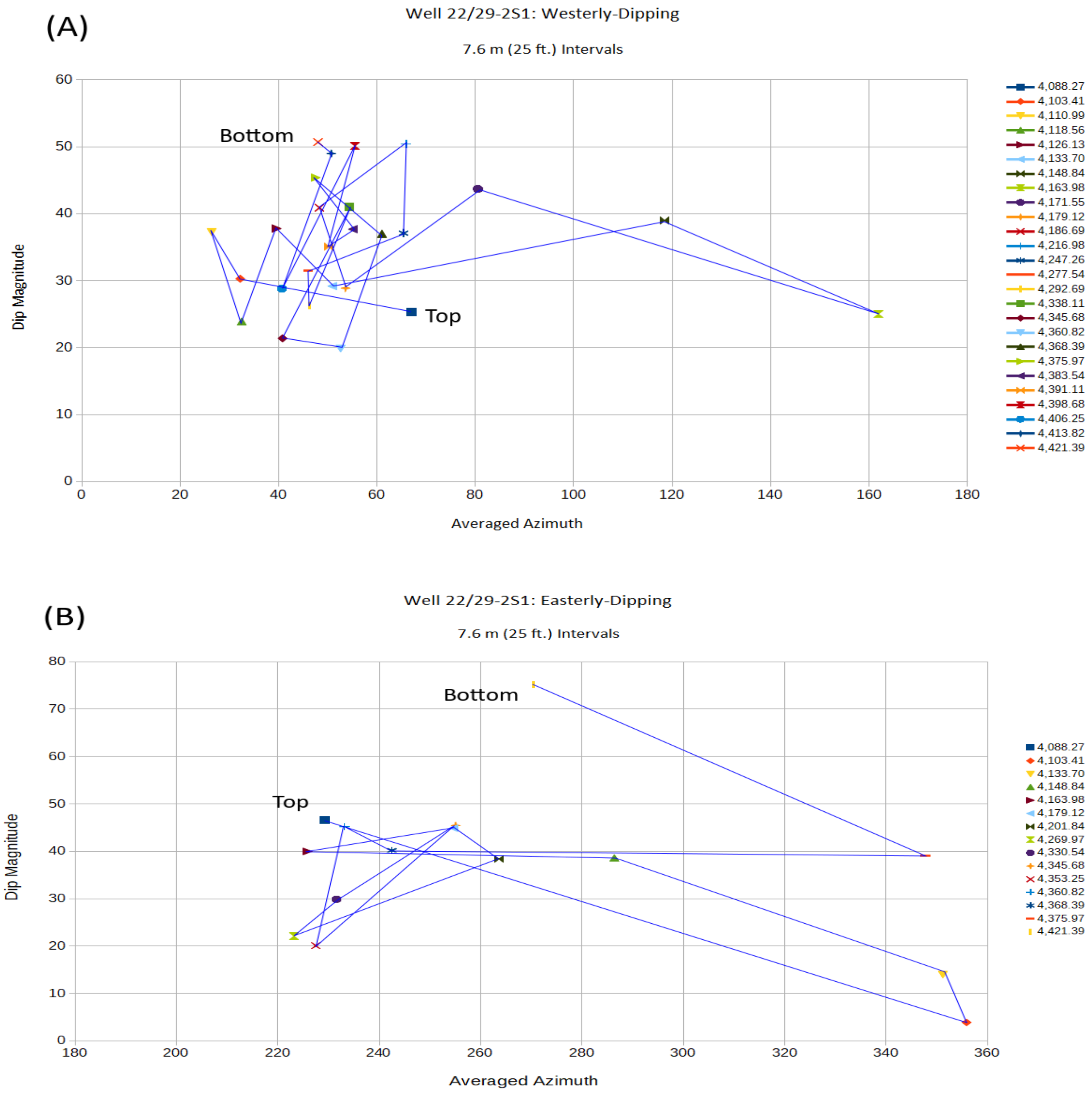

Figure 3.24: Graphs showing the plunge vs. trend of the deformation bands averaged over 15.2 m (50 ft.) intervals along well 22/29-2S1. (**A**) shows the averaged dip magnitude against the averaged azimuth of the westerly-dipping deformation bands for each 15.2 m (50 ft.) depth interval (depth key). **(B)** shows the averaged dip magnitude plotted against the averaged azimuth of the easterly-dipping deformation bands for each 15.2 m (50 ft.) depth interval (depth key). Depths are measured depths (MD) from the drilling floor datum, units in metres. The blue line highlights the change in average azimuth and dip magnitude down the well (top → bottom).

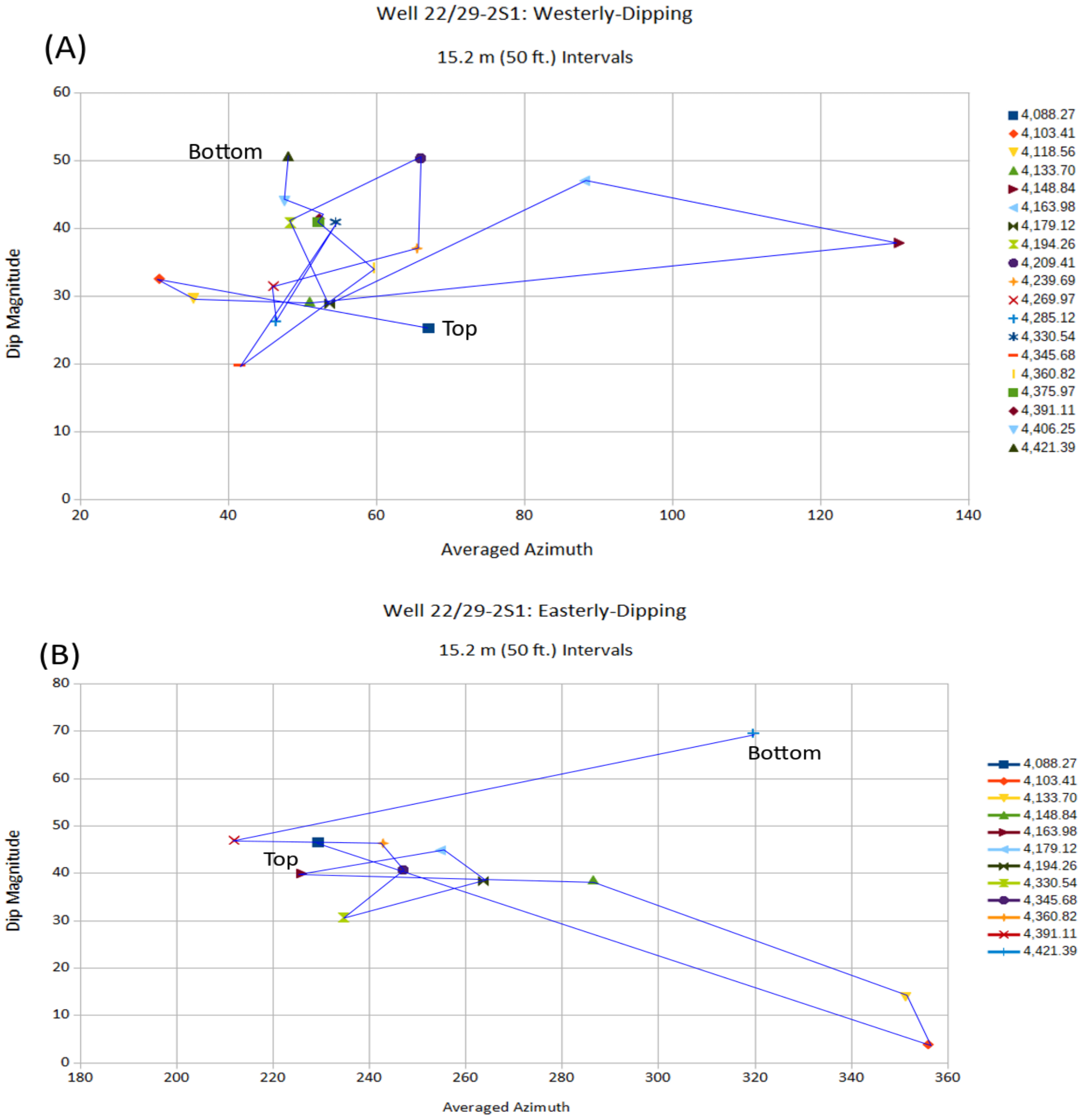

Figure 3.25: Graphs showing the plunge vs. trend of the deformation bands averaged over 30.4 m (100 ft.) intervals along well 22/29-2S1. (**A**) shows the averaged dip magnitude against the averaged azimuth of the westerly-dipping deformation bands for each 30.4 m (100 ft.) depth interval (depth key). **(B)** shows the averaged dip magnitude plotted against the averaged azimuth of the easterly-dipping deformation bands for each 30.4 m (100 ft.) depth interval (depth key). Depths are measured depths (MD) from the drilling floor datum, units in metres. The blue line highlights the change in average azimuth and dip magnitude down the well (top → bottom).

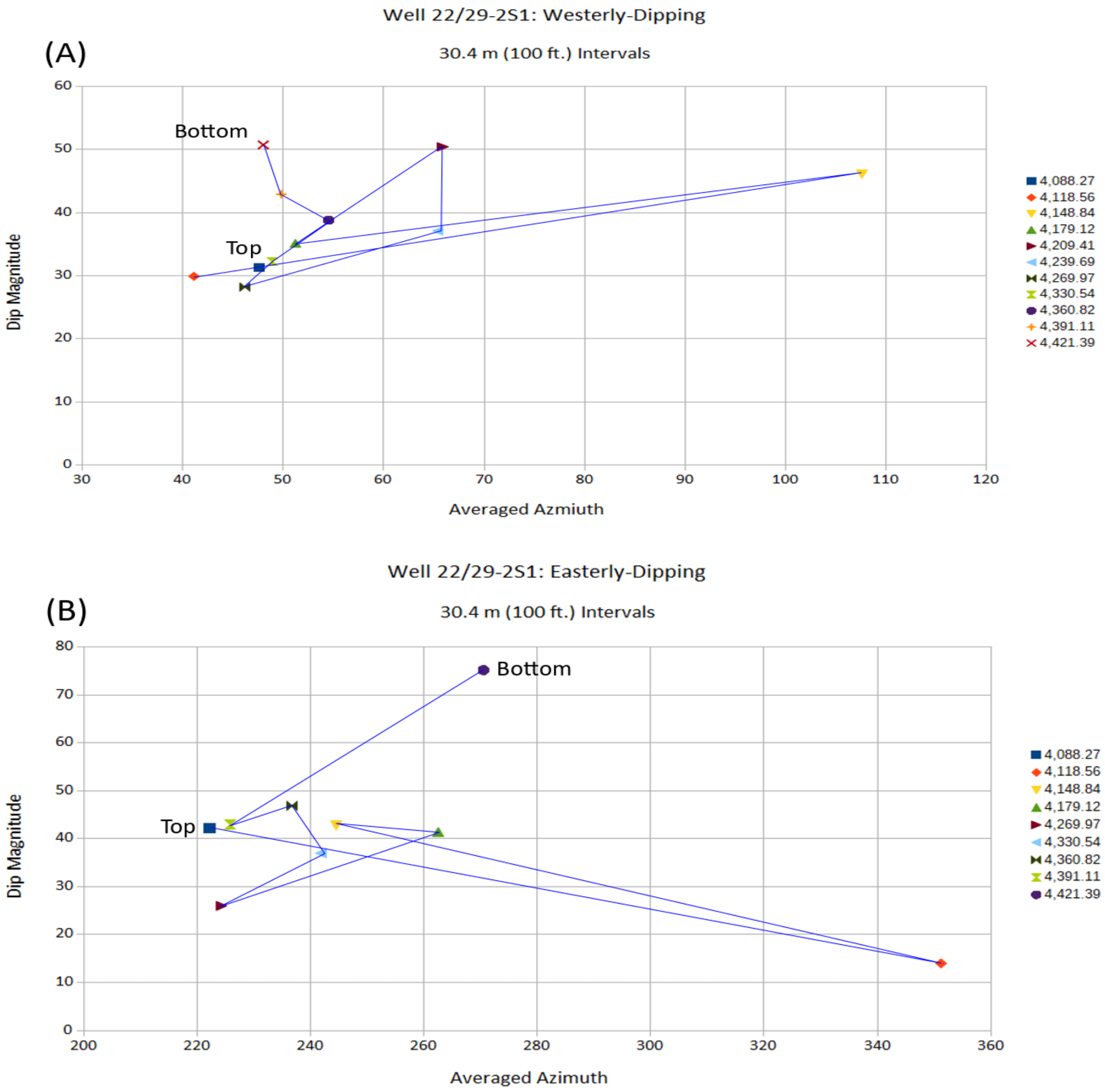

The averaged azimuth (ACI) against depth for all interval sizes showed that depths shallower than 4267.2 m (14000 ft.) MD, the averaged ACI fluctuated over a large range (160^{O} – 320^{O} for the 7.6 m (25 ft.) interval) (Fig. 3.26). However, these fluctuations decreased as the data intervals increased (210^{O} – 360^{O} for the 15.2 m (50 ft.) interval, and 300^{O} – 350^{O} for the 30. m (100ft.) interval). At depths greater than 4267.2 m (14000 ft.) for all sized intervals, the graphs showed a significant decrease in the fluctuation in the average ACI of the orientations. It should be noted that well 22/29- 3 did not sample below 4267.2 m (14000 ft.) so a comparison between the orientations in the two wells below this point could not be made. The average ACI for all of the data intervals originate from an orientation of ~325^{O} at the base of the core section and fluctuated without a significant trend in orientation either clockwise or counter-clockwise.

Tilting of the sedimentary beds could have produced the fluctuation in dip magnitude along the core section. As previously mentioned, the dip logs also showed the orientation data for the sedimentary bedding features, which included parallel bedding and cross-bedding. Visual comparison between the dip magnitude of the deformation features and dip magnitude of the bedding features showed that significant tilting of the sedimentary beds did not correlate with significant tilting of the deformation bands. However, this could be due to the formation of later deformation bands overprinting earlier deformation bands which have already experienced tilting. The sedimentary beds did show significant tilting of up to 50^{O}, although most sedimentary beds showed tilting of between 10^{O}-40^{O}, with a fluctuating dip azimuth between the south-west and south-east direction.

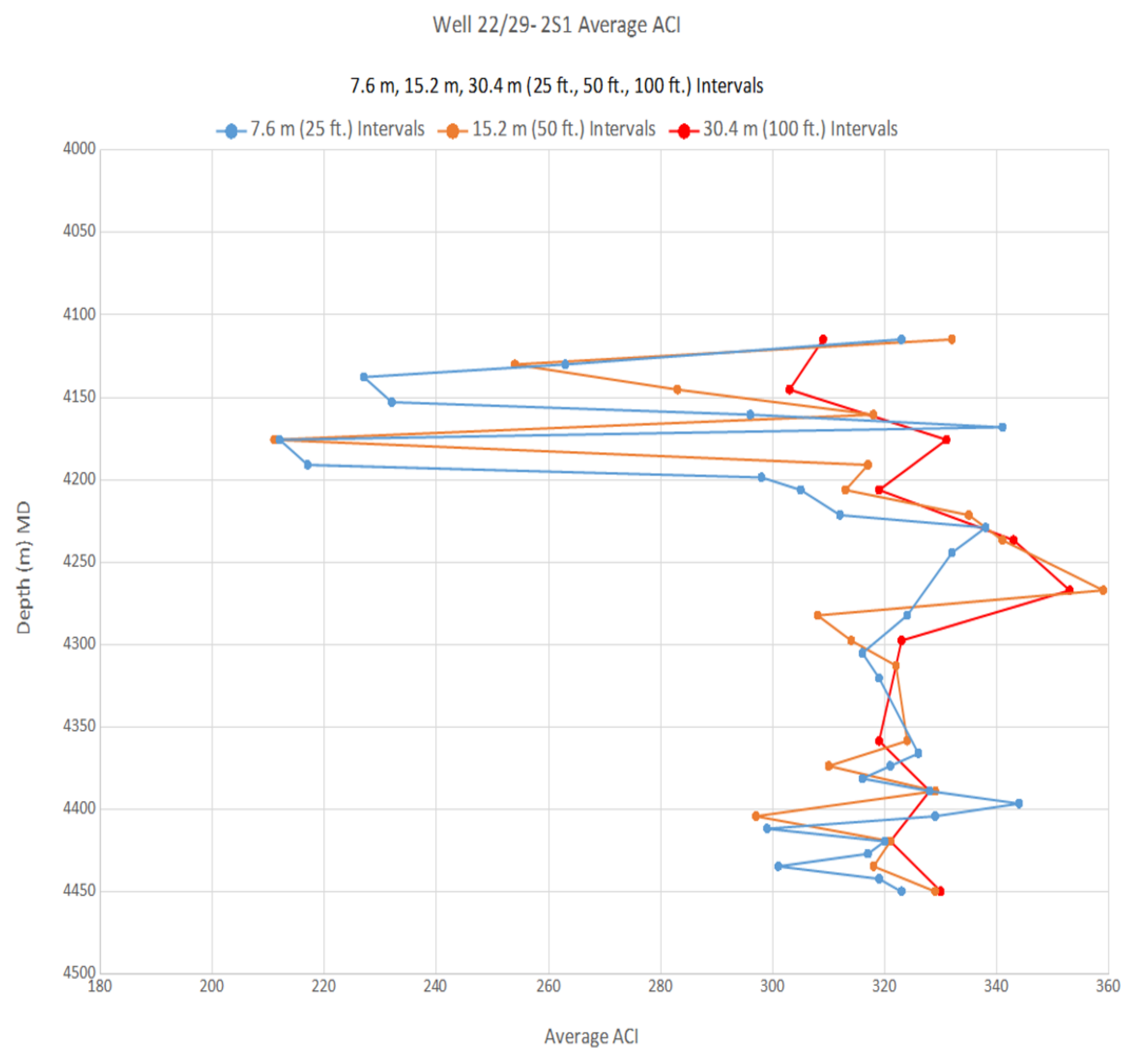

Figure 3.26: Graph showing the average ACI of the deformation bands plotted against depth for the interpreted FMI data for the 7.6 m, 15.2 m, and 30.4 m (25 ft., 50 ft., and 100 ft.) intervals for well 22/29-2S1. The average orientation is taken to be the azimuth of the intersection between the conjugate sets (ACI) of deformation bands for that interval.

3.5 Discussion

3.5.1 Interpreting stress fields from deformation band orientations

In a simplistic framework, deformation of unconsolidated sand and/or poorly consolidated sandstones at shallow depths of burial (<500m) promotes simple shear kinematics, non-cataclastic deformation and in some cases, also pure compaction and dilation of the sediments. Important factors recognised are the low levels of stress from the overburden, pore fluid overpressure, mineralogy, and potential early cementation. In granular sands, stress is transmitted across grain-to-grain contacts, and low stress across such contacts allows for grain disaggregation. Hence, the fact that stress related to overburden is low at shallow burial depths implies that grains can more easily move relative to one another, while the higher stress at deeper burial depths promotes cataclasis.

Tectonic stress alters the state of stress generated by the overburden. The strength of sediments, as well as their response to external loading, is a function of their loading history post-deposition (Terzaghi et al., 1996), and their diagenetic history (Laubach et al., 2010). Taking the stress history into account is especially critical in environments, such as those near salt diapirs that have undergone significant geological loading. In the Triassic Skagerrak Sandstones of the Central Graben the close interaction between the salt walls and porous poorly cemented sandstones have been clearly recognized with a series of deformation bands.

The evolution of salt diapirs has been studied extensively using kinematic restorations (Rowan and Ratliff, 2012). These studies aim to explain the present-day shape of the salt structure by modelling potential development histories of the salt body without investigation into the stresses within the sediments. Similarly, large-strain numerical studies (Schultz-Ela, 2003; Chemia et al., 2009; Gradmann et al., 2009; Albertz & Beaumont, 2010; Albertz et al., 2010; Beaumont, 2012; Goteti et al., 2012) have focused on the geological evolution of salt systems without a clear understanding of the wall rocks and their response to salt movement.

In this study the stress that created the deformation bands due to salt movement has been analysed with regard to the orientation of the deformation bands. The stress field which formed deformation bands can be inferred from the orientation and type of fractures being analysed (Fossen, 2016). Principal stresses in 3-dimensions are represented by σ (sigma) notation, σ_1, σ_2, and σ_3. The three stress notations are all perpendicular to each other with σ_1 representing the orientation of highest principal stress, and σ_3 representing the orientation of lowest principal stress. As previously mentioned, Mohr circles are graphical representations of stresses, and use the maximum and minimum principal stresses along with failure envelopes (calculated using experimental methods) to indicate when a stress state is stable, critical and on the verge of failure, and unstable where the stress state exceeds the strength of the rock (Fig. 1.2). Shear fractures are found to form 30^{O} from the maximum principle stress direction (σ_1). The intersection between conjugate shear fractures lies parallel to the intermediate principal stress (σ_2). Tensile fractures (open fractures) are inferred to be perpendicular to the minimum principle stress direction (σ_3).

3.5.2 Salt wall influence on Skagerrak Formation sandstone

The orientation of deformation bands in the Skagerrak Formation sandstones, with deformation bands from well 22/29-3 in particular showed that the overall NW-SE strike of the conjugate bands sets was parallel to the orientation of the salt wall (Fig 3.15). This implied that the plane of maximum and minimum principal stress could initially be estimated as perpendicular to the salt/sediment interface, with the intermediate principle stress running parallel to the length of the salt wall. The normal (downslope) shear offsets at sedimentary beds and cross-cutting interactions between deformation bands implied that the maximum principle stress is in the same orientation as the Vertical Effective Stress (VES) (Fig 2.18). The dip magnitudes of the band orientations displayed a range between approximately 30^{O} - 60^{O} (Fig. 5.8). Desrues et al. (2007) stated that in unconsolidated soils with high confining stresses would tend to produce steeper angles of failure. Higher confining stresses also produced greater clustering of bands that may occur in closer proximity to the salt wall. Decreases in porosity, grain-size and water content can also increase the size of the failure envelope (Fig. 1.2) (e.g. Schultz & Siddharthan, 2005). The Skagerrak sandstones at shallower depths (< 500 m) in well 22/29-3, the high porosity and fine-grained sandstones demonstrate minimal fluctuations in terms of grain size and macro-porosity. The arid to semi-arid palaeogeographic conditions of the CNS during deposition of the Triassic Skagerrak Formation highlighted variability in water content and a likely periodicity with episodic drying out and more arid occurrences (Fig. 2.7) (Archer et al., 2010; McKie & Shannon, 2011). Therefore, wetter periods with more pronounced fluvial channel activity and introduction of palaeosols decreases the stress required to cause the brittle failure of the sediment. Increased water content alone could not cause the deformation of the sediment itself, though it would increase the likelihood of stress from the salt wall causing failure in the adjacent sediment and more widely occurring deformation bands. Previous research suggested that the cohesion of unconsolidated sediments could increase with additional water content by utilising capillary forces between the grains (Kemper & Rosenau, 1984; Kim et al., 2009). Increasing the water content of unconsolidated sediment from 0.5% - 4% (weight %) produced a change in the tensile strength of the samples from 400 Pa to 950 Pa, although when the water content caused the pore pressure to increase to $10^2 - 10^3$ Pa this would exceed the capillary forces between grains and weaken the sediment (section 2.1.1.1).

Based on observations in this study, the salt wall of the Seagull field may have imposed the minimum principal stress on adjacent sediments, with the shallowly dipping disaggregation bands (~ 30^{O} from horizontal) in well 22/29-3 resulting from decreasing salt-induced stresses, larger grain sizes, and higher water content. Steeper disaggregation dips (~60^{O} from horizontal) would result from higher salt stresses, smaller grain sizes, and lower water content. Dilation bands may then have formed to accommodate shearing from the adjacent disaggregation bands instead of being strongly influenced by the salt wall. Experimental results have shown that deformation bands can form within confining stress ranges of 10 – 60 MPa (section 1.3.1), although values for the VES in well 22/29-3 did not exceed 10 MPa prior to the onset of rapid burial 90 Ma (Fig. 2.9) (Bésuelle et al., 2000; Desrue et al., 2007; Stricker et al., 2018).

Figure 3.14 showed that well 22/29-3 generated higher proportions of deformation band depth intervals with girdle distributions (K < 1). This demonstrated that the salt walls do not generate a uniform stress on the adjacent sediment, but can vary over short intervals (~6.1 – 7.6 m (20 - 25 ft.)). Figures 3.17a & b both showed gradual changes in the average azimuth along the formation. However, over specific depth intervals (4209.3 – 4227.6 m (13810 – 13870 ft.)), these average azimuths have counter-rotations, where the strike of the westerly-dipping bands changed from 235^{O} to 311^{O} through the formation, and the strike of the easterly-dipping bands changed from 97^{O} to 52^{O}. These opposite rotations of dip direction along the same depth interval are interpreted as changes in the stress state and was not a continuous process, but more disorderly and erratic over geological time.

This study represents one of the first examples that couples sedimentation with salt rise and captured the deformational effects of the Skagerrak Formation sandstones. Although, several authors note that the principal stresses rotate near a salt diapir (Zerwer, 1994; Dusseault et al., 2004; Bachrach et al., 2007). According to standard practice (Bradley, 1978; Perez et al., 2008), wells drilled through salt should exit the salt perpendicular to the salt/sediment interface, which echoes the fact that the maximum principal stress rotates to be perpendicular to this interface. More recently pore-elastic basin modeling results predicted that the maximum principal stress was radial around the upper parts of the diapir, and that it reached values even higher than the weight of the overburden (e.g. Nikolinakou et al., 2012,2014; Heridari et al., 2017). The results in this study showed that the maximum principal stress for the formation of the deformation bands occurred vertically due to the overburden, or perpendicular to the salt wall/sediment interface, contradicting the predictions proposed by Heidari et al., (2017). Other models showed the development of stress and deformation around salt structures (mainly diapirs) showing that initial fractures and faults form polygonal fracture rings and radial tensile fractures above the salt diapir in the overburden (Section 3.1.6) (Fig. 3.6). However, these models typically assumed that the overburden has some internal strength and can be modelled as a rigid layer, while the unconsolidated shallow Skagerrak Formation sediments would not be as structurally competent (Alsop, 1996; Withjack & Callaway, 2000; Nikolinakou et al., 2014; Heidari et al., 2017).

The rotation of the deformation bands in this study, and therefore stress state for well 22/29-3, was highly punctuated by discrete movements of the salt walls and reflected a less than regular rotation of dilation and deformation bands. The results highlighted the fact that the salt movement was not steady state and was punctuated by irregular movements linked to overburden. However, this research does further demonstrate the need for detailed stress histories close to salt walls and diapirs, such an understanding is critical for predicting stress, porosity, and pore pressure in and around salt systems.

3.5.3 Stresses in wall rocks and at distance from the salt wall

The stereonets of well 22/29-2S1 showed a NE-SW (45^{O} - 225^{O}) average azimuth of the majority of deformation bands, similar to well 22/29-3. This would initially indicate that the orientation of the salt wall had a degree of influence on the deformation bands orientations in well 22/29-2S1. The roughly parallel orientation of the deformation bands in well 22/29-2S1 could be caused by the salt wall confining the sediments, but not directly causing the formation of the bands. Rowan et al. (2012) described how salt-wall induced deformation is not observed beyond the 100's of metres limit away from the salt wall. In contrast, well 22/29-2 displayed deformation bands over 1000 m away from the salt wall. This contradiction could be rectified based on observations made in McKie et al. (2010) that described faults in the Skagerrak Formation that followed the trend of major faults in the underlying Rotliegend rock. The major fault in the Rotliegend rock would have had some measure of influence over the orientation and position of the salt wall, and may also have influenced the orientation of deformation bands in the overlying sandstones of the Skagerrak Formation. Figures 3.23 – 3.25 did not show any gradual changes in the general trends in the dip magnitudes and average azimuths along the core section, meaning that there were no gradual changes in the stress field. Well 22/29-2S1 showed a slightly stronger cluster distribution ($K > 1$) than well 22/29-3 (Figs 3.13 – 3.15 & Figs. 3.19 – 3.21). But the C values for both wells showed that the orientation data were equally dense ($2 < C < 4$). This meant that well 22/29-2S1 had a higher range of dip magnitudes than well 22/29-3 for each depth interval. This was likely due to the lack of influence the principal stress of the salt wall had on deformation band orientations further away.

A suggestion for the increased fluctuation of CIAs with the increased abundance of deformation bands towards the top of the Skagerrak Formation in well 22/29-2S1 could be as a result of the mini-basin sedimentary pod grounding on the underlying Rotliegend (McKie et al., 2010) (Fig. 3.8). The formation of a turtle-back anticline after grounding of the sediment pod would cause complex stress fields within the sediment, resulting in faults and fractures forming at the mini-basin centre, located proximal to well 22/29-2S1 (Hodgson et al., 1992). This hypothesis would constrain the time of formation for these deformation bands to after the sedimentary infill grounded on the basement rock.

3.6 Summary and conclusions

This research used detailed deformation band data from two wells (well 22/29-2S1 and well 22/29-3) of the Seagull field in the Central Graben, North Sea, UK where the datasets were analysed in order to identify if there was a change in the orientation of the deformation bands along the well length. This was carried out by dividing the datasets into various sized intervals and plotting the average orientation against depth. For well 22/29- 3, the orientations could be separated further into the different deformation band types (disaggregation and dilation). The spread of orientation data observed on the stereonets were then analysed for statistical viability based on the shape of the distribution (K values), and the density of the data point clusters (C values) using eigenvalues. These K values and C values were then measured against the number of data points used to generate these values in order to test the reliability of the generated eigenvalues.

In conclusion:

- Deformation bands formed in sediments adjacent to a salt wall showed a wide range of orientations with the average azimuth perpendicular to the salt/sediment interface. Measured changes in the orientations of deformation bands reflected changes in the principal stresses imposed on the sediment.
- Assuming that the orientation of the deformation bands recorded palaeostresses at the time of formation, these orientations indicated that the principle stresses that produced the deformation bands would originate in the vertical orientation and perpendicular to the salt/sediment interface. The intermediate principal stress was parallel to the salt/sediment interface.

- Deformation bands closer to the salt wall displayed a larger variation in orientations compared to deformation bands towards the mini-basin centre. This could be attributed to the irregular movement of the salt wall having a stronger influence on the adjacent sediment.
- Sediment towards the salt-wall mini-basin pod centre can have a strong structural grain imposed at the time of grounding.
- There is minimal evidence for any gradual rotation of the azimuth of deformation band orientation towards the mini-basin centre, but bands closer to the salt wall did display a gradual rotation of the averaged CIA of each depth interval up the sampled formation. Of the different types of deformation bands identified closer to the salt, dilation bands showed the clearest trend for a change in orientation up the formation, with disaggregation bands showing the weakest gradual change.
- Previous pore elastic basin models demonstrated that the stresses induced adjacent to salt diapirs indicated that the maximum principal stress was perpendicular to the salt wall and the intermediate principal stress was equal to the VES. The results in this study showed that the minimum and maximum principal stresses could vary between the VES and perpendicular to the salt/sediment interface for shallow, unconsolidated sediment.
- A potential explanation of the deformation bands orientation towards the mini-basin centre is that the deformation bands were a result of the mini-basin pod grounding on the underlying Rotliegend, with the orientation and position of both the salt wall and mini-basin centre deformation bands resulting from the underlying major faults.

Chapter 4. Discussion and Implications

4.1 Implications

Dilatant deformation features which form at shallow depths are usually removed or overprinted during burial, and often have little to no lasting influence on sandstone quality at depth (Fossen, 2007). As this study demonstrates, early deformation band production can impact the evolution of the sandstone at depth when combined with diagenetic alteration and development. In the case of the sandstones of the Central Graben, North Sea, complex networks of disaggregation and dilatant deformation bands were produced in the sandstones of the Skagerrak Formation proximal to the salt wall. These deformation bands are initially characterised by the increase in porosity compared to the host rock which then allows for the extensive infiltration of clay minerals into the unconsolidated sediment before developing into pore-filling diagenetic clay minerals and drastically reducing the porosity of the sandstone. Previous work on deforming unconsolidated sediments indicated that factors such as confining pressure, grain size, and water content could produce deformation bands which increase in porosity or decrease in porosity compared to the host sediment (Fossen, 2007; Fossen & Bale, 2007). The enhanced porosity of deformation bands in the Skagerrak Formation resulted in poor quality sandstones due to enhanced clay mineral infiltration. Deformation bands observed in other wells across the Central Graben (i.e. Huntington and Puffin) reveal that the phenomenon of deformation bands adjacent to salt walls is not unique to the Seagull Field of the Central Graben. It is highly probable that similar deformation bands have formed adjacent to salt walls in other salt-walled mini-basins in other salt provinces (Banham & Mountney, 2013b) (Fig. 1.7).

This study focused on fine-grained to very-fine grained sediment at shallow depths although previous work has shown that deformation bands can form and develop at depth (Fossen, 2007). It is therefore possible that compaction or cataclastic bands may form in other wells at higher confining stresses and inhibit the infiltration of clay minerals, helping to preserve porosity at greater depth or potentially forming structural baffles to upward-migrating fluids. The petrography of the sediment may also have to be considered since grain size, mineralogy and other factors influence the formation and morphology of the resultant deformation bands (Fossen & Bale, 2007; Griffiths et al., 2016). Therefore, salt wall movement adjacent to coarse-grained sediment or mudstone may also produce highly complex networks of deformation bands adjacent to the salt wall. This study also demonstrates that deformation in sediments approximately 1000 m from the salt wall may still be indirectly influenced by salt movement as salt that has completely evacuated from underneath a mini-basin can result in the sediment pod grounding on the underlying rock, producing faulted turtle-back anticline structures.

Another implication of this study is that the deformation features provide a record for stresses in the sediment during formation, presenting the opportunity to infer the movement of the salt wall in the past. For the salt walls in the Central Graben, North Sea, these deformation bands recorded the irregular movement of the salt wall of adjacent sediments.

These findings will influence the development of complex models for mini-basins, which will have to consider the effect of sub-seismic deformation band features combined with diagenetic processes.

4.2 Discussion

4.2.1 Alternative interpretation options

4.2.1.1 Stylolites

Stylolites are deformational features that occur in sediments due to mechanical compaction with a concentration of clays along their length associated with their formation and composition (Aharonov & Katsman, 2009; Fossen, 2016). They are typically characterised by pressure solution and irregular sinusoidal surfaces. The sandstones investigated in this thesis did display evidence of compaction, although the mechanical compaction did not appear to have caused excessive pressure solution between the grains within the deformation bands in thin section (section 2.4.2). Also, the deformation features from the Skagerrak Formation are typically linear planar features with a decreased grain framework density within the band compared to the host rock. This is not characteristic of stylolites, which exhibit sinuous and irregular deformation surfaces and the grain framework density within the stylolite is significantly higher with pressure solution and recrystallisation of the grains, compared to the host rock. However, it is possible that stylolites may appear in sediments buried at great depths with high VES in other wells across the CNS.

4.2.1.2 Dessication cracks

Dessication cracks are dilatant features that form at the surface and allow for the infiltration of fluids and sedimentary material into the underlying sediment (Hallet & Newson, 2005). A feature of dessication cracks is that the soil dilation propagates from the surface and typically produces a vertically orientated crack in the soil that are several mm wide at the surface and tapers down towards a point (Hallet & Newson, 2005; Shin & Santamarina, 2011). The deformation features in this study were tabular and displayed a uniform thickness along their length (Fig. 2.18). The deformation bands were also observed to cross cut and interact with other deformation bands, a feature not observed in dessication cracks (Hallet & Newson, 2005; Shin & Santamarina, 2011). However, this does not eliminate the possibility of dessication cracks occurring in the CNS, as the climate during the Triassic fluctuated between semi-arid and arid. It is possible that some features observed in well 29-05a-7 (Fig. 2.18a) may have resulted from the formation of dessication cracks.

4.2.1.3 Deformation during the Jurassic

The deformation bands may have originated during the regional thermal doming event during the Mid-Jurassic, resulting in the upheaval of the CNS and widespread erosion, producing the Mid-Cimmerian Unconformity (Erratt, 1993). This significant tectonic event would impart similar stresses on the sediments that can be observed in a turtle-back anticline (Fig. 3.8) (Hodgson et al., 1992). As previously discussed, the deformation bands in well 22/29-2S1 could have formed from faulting of the Upper Skagerrak Formation due to the turtle-back anticline (section 3.5.3). It is therefore possible that a regional upheaval of the CNS during the Mid-Late Jurassic could have produced faults and associated deformation bands within the Skagerrak Formation. The thermal doming would also preferentially result in dilation bands since confining pressure and VES would decrease due to uplifting of the sediment, and the erosion of the overlying Late-Triassic and Early-Jurassic sediments (Fossen et al., 2007. Based on the burial history of the Skagerrak Formation, it is plausible that prior to uplift during the Jurassic, the Triassic sediments may not have deformed yet due to the VES not exceeding 10 MPa prior to 90 Ma (section 3.5.2) (Fig. 2.9) (Bésuelle et al., 2000; Desrue et al., 2007; Stricker et al., 2018).

Deformation of the sediments during the Jurassic instead of the Triassic would have implications that detrital smectite from the Jurassic sediments were able to infiltrate into the Triassic sediments during the thermal doming, rather than smectite sourced from Triassic sedimentation. Formation of the dilational deformation bands during the Mid-Jurassic would create preferential pathways for the smectite clay to infiltrate into the sediment (Du Bernard et al., 2002). Testing this would require comparison between smectite in Triassic sediments and smectite in Jurassic sediments, utilising electron microscopy, infrared spectroscopy, and chemical analysis. Although it may need to be considered that the detrital smectite may have altered along different diagenetic pathways between the Triassic and Jurassic sandstones (Worden & Morad, 2009).

It is unlikely that the deformation bands formed later than the Mid- Late-Jurassic, such as during the Late Jurassic – Early Cretaceous rifting, as the sediment overlying the Skagerrak Formation would have exceeded 3000 m, and deformation of the Triassic sediments would likely display some evidence of cataclasis or grain fracturing which is not observed in the thin section samples (section 2.4.2) (Fraser et al., 2002).

4.2.2 Deformation band genesis

As evidenced by the micrographs (Figs. 2.24 – 2.27), the deformation bands could be identified in thin section by the lower grain framework density within the deformation bands compared to the host rock, and these deformation bands had a noticeable difference in terms of the pore-filling diagenetic material between the deformation band and the host rock. The decreased grain framework density would only occur at shallow depths (< 500 m) so these deformation bands are examples of early deformation features being preserved at depths greater than 3500 m due to the development of diagenetic material.

Some of the micrographs displayed a larger proportion of darker clay minerals compared to the host rock which is suggestive of different diagenetic developments between the deformation band and the host rock. One possible process could be that the decreased grain framework density allowed larger precursor clay particles (likely smectite) to infiltrate the deformation bands, but the transition to a higher grain framework density into the host rock prevented further movement of the clay particles into the surrounding host rock. The greater abundance of precursor clay mineral combined with the higher influx of hypersaline pore fluids sourced from the dissolution of the adjacent salt wall by meteoric water would then result in the preferential conversion of this precursor mineral into the mixed illite-chlorite found in the deformation bands. The high abundance of diagenetic material observed in the host rock and subsequent low porosity showed that the presence of initially higher porosity deformation bands was highly detrimental to the reservoir quality of the sandstone adjacent to the salt wall (Fig. 4.1).

Chapter 3 highlighted that syn-depositional salt movement produced deformation bands proximal to the salt wall and further afield towards the mini-basin centre with deformation bands being observed approximately 1000 m from the salt wall (Fig. 4.2). These far-field deformation bands would have occurred at a range greater than would be expected to be influenced by the salt wall, so a more likely cause for these deformation bands would be due to the formation of faults proximal to the mini-basin centre (McKie et al., 2010). These faults could have formed as the mini-basin grounded on the underlying Rotliegend (Hodgson et al., 1992).

The orientations of the deformation bands also suggested that the maximum principal stress direction was perpendicular to the salt wall/sediment interface or parallel to the overburden. However, the movement of the salt wall produced minor variations in the lateral orientation of the deformation bands which suggested a minor rotation of the principal stress in the horizontal plane adjacent to the salt wall.

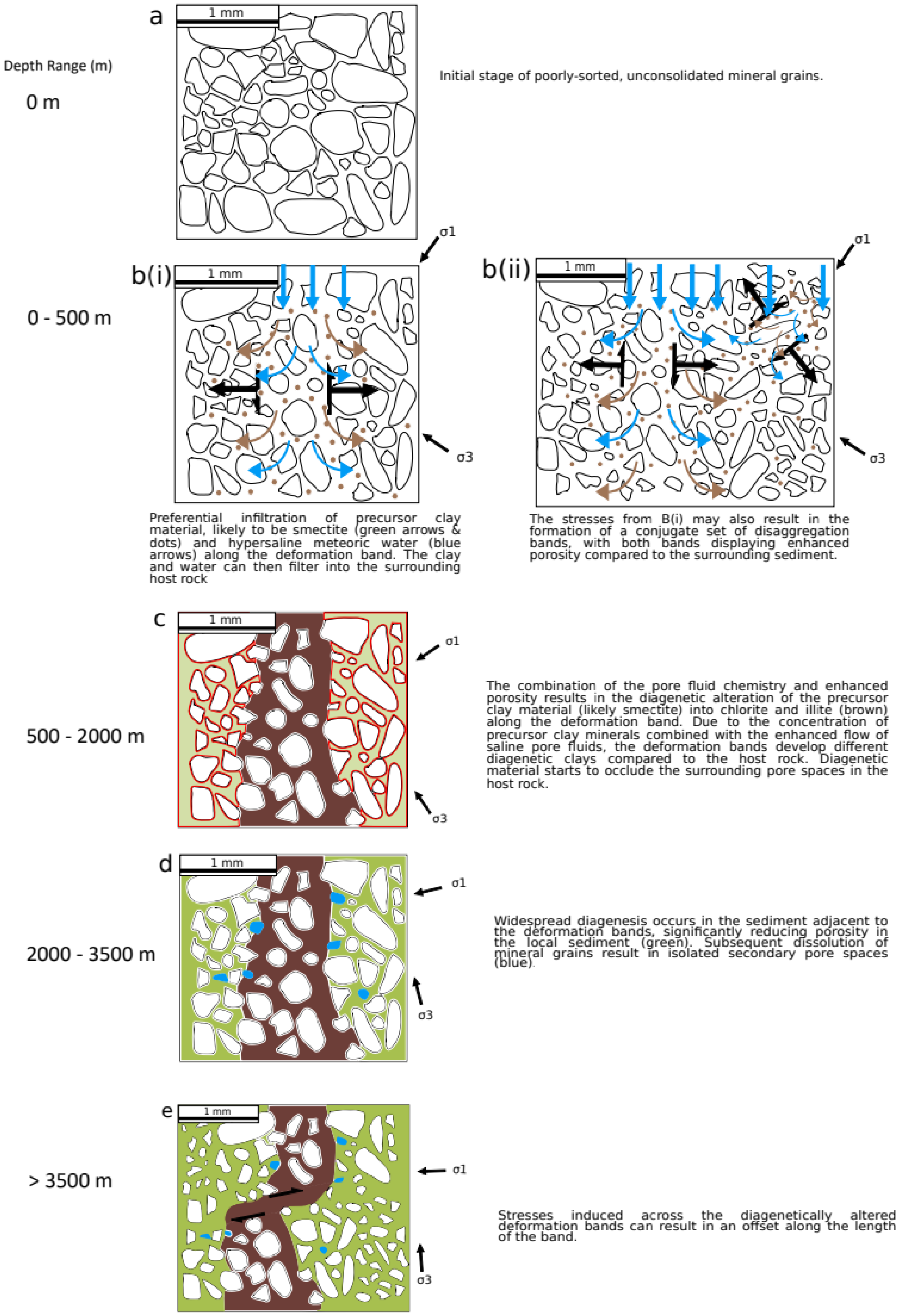

Initial stage of poorly-sorted, unconsolidated mineral grains.

Preferential infiltration of precursor clay material, likely to be smectite (green arrows & dots) and hypersaline meteoric water (blue arrows) along the deformation band. The clay and water can then filter into the surrounding host rock

The stresses from B(i) may also result in the formation of a conjugate set of disaggregation bands, with both bands displaying enhanced porosity compared to the surrounding sediment.

The combination of the pore fluid chemistry and enhanced porosity results in the diagenetic alteration of the precursor clay material (likely smectite) into chlorite and illite (brown) along the deformation band. Due to the concentration of precursor clay minerals combined with the enhanced flow of saline pore fluids, the deformation bands develop different diagenetic clays compared to the host rock. Diagenetic material starts to occlude the surrounding pore spaces in the host rock.

Widespread diagenesis occurs in the sediment adjacent to the deformation bands, significantly reducing porosity in the local sediment (green). Subsequent dissolution of mineral grains result in isolated secondary pore spaces (blue).

Stresses induced across the diagenetically altered deformation bands can result in an offset along the length of the band.

Figure 4.1: Schematic diagram demonstrating the formation and development of the deformation bands. The column of depth ranges refer to the depths where these processes would be expected to occur. Principal stresses have been added to the diagrams to demonstrate the expected stresses the sediment was subjected to at increasing depths.

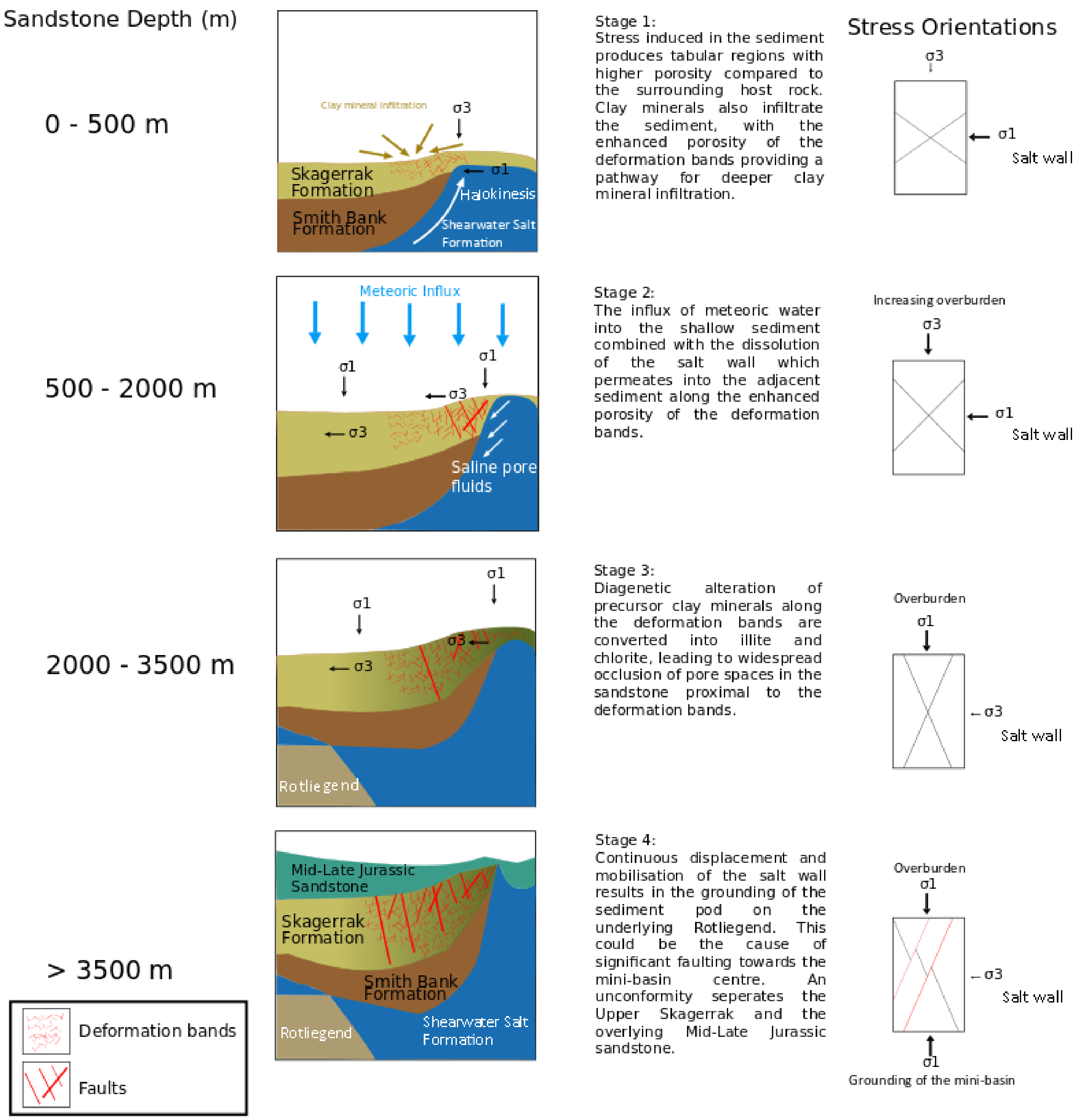

Stage 1:
Stress induced in the sediment produces tabular regions with higher porosity compared to the surrounding host rock. Clay minerals also infiltrate the sediment, with the enhanced porosity of the deformation bands providing a pathway for deeper clay mineral infiltration.

Stage 2:
The influx of meteoric water into the shallow sediment combined with the dissolution of the salt wall which permeates into the adjacent sediment along the enhanced porosity of the deformation bands.

Stage 3:
Diagenetic alteration of precursor clay minerals along the deformation bands are converted into illite and chlorite, leading to widespread occlusion of pore spaces in the sandstone proximal to the deformation bands.

Stage 4:
Continuous displacement and mobilisation of the salt wall results in the grounding of the sediment pod on the underlying Rotliegend. This could be the cause of significant faulting towards the mini-basin centre. An unconformity seperates the Upper Skagerrak and the overlying Mid-Late Jurassic sandstone.

Figure 4.2: Schematic diagram demonstrating the movement of the salt wall in relation to the thickness of the mini-basin sediment-fill. The sandstone depth correlate to the depth ranges from fig. 4.1. The stress orientations refer to the expected average orientation of deformation bands for each depth, with the final stress orientation at > 3500 m depth indicating the formation of new deformation bands producing offsets along previous deformation bands, as well as the reactivation of previous deformation bands at this depth. The size and thickness of the principal stress arrows for the stress orientation column indicate the relative magnitude between the maximum and minimum principal stresses at each depth range.

Chapter 5. Conclusions and Further Work

5.1 Conclusions

- Salt-wall mini-basins have been found to produce high-yield hydrocarbon reservoirs, dependant on the reservoir quality of the sandstone. As these high-production reservoirs are depleted, exploration may have to take place closer to the mini-basin margins. This study investigated the quality of the sandstones adjacent to the salt walls of the mini-basins with regard to sub-seismic deformation features.
- Deformation bands have been found in multiple wells across the Central Graben, North Sea. These deformation bands were located in Triassic sandstone deposits which comprise the Skagerrak Formation within the salt-walled mini-basins across the area.
- Deformation bands are found in sediments both adjacent to the salt wall (well 22/29-3) and in sediments closer to the mini-basin centre (well 22/29-2S1).
- The deformation bands are interpreted to have formed at shallow depths with low confining stress (<500 m).
- The preserved grain framework density showed that grain framework density decreased in the deformation bands compared to the host rock, indicative of salt movement producing deformation bands with higher porosity compared to the host rock. This allowed for the infiltration of clay minerals into the sediment along with enhanced meteoric water influx.
- The combination of enhanced meteoric water and hypersaline pore fluids from dissolution of the salt wall infiltrating the sediment caused diagenetic development of the clay minerals into pore-occluding illite and chlorite. The illite and chlorite have occupied almost all of the porosity in the sandstone adjacent to the salt wall (< 5% available macro pore space).
- The orientation of deformation bands implied that they formed from compressive stresses induced by the salt wall at low confining pressures at shallow depths and vertical effective stress (VES) at greater confining pressures during burial.
- Sediments proximal and distal to the salt wall both showed equally varying deformation dip azimuths, but sediments closer to the salt wall have a smaller variation in dip azimuths than deformation bands further from the salt wall.
- Deformation bands can be used as a record of changing stresses within the sediment and by extension, the movement of the salt wall. This study demonstrates that stresses imposed by salt walls are not steady state and are punctuated by irregular movements linked to the overburden.

- The deformation bands are detrimental to reservoir quality in proximity to a salt wall when combined with diagenetic processes. Further research may show that compressive and cataclastic deformation bands form in higher stress regimes, or very fine-grained sediment may not be as detrimental to the sandstone as these factors would not favour the infiltration of minerals for diagenesis at depth.
- This study will have implications for hydrocarbon exploration and production adjacent to salt walls in mini-basins, for stress modelling around salt walls and for predictions of sandstone reservoir quality in salt-walled mini-basins.
- The null hypothesis stated in the introduction of this thesis (section 1.2) that deformation band abundance increased towards the salt wall could be rejected, since well 22/29-2 displayed an equal or greater abundance of deformation features compared to well 22/29-3. However, due to the position of well 22/29-2 on a faulted turtle-back anticline, this null hypothesis could still be tested in further work. The secondary hypothesis that the salt wall would have a stronger influence on deformation band orientations on local sediments compared to distal sediments has not been rejected, although more wells will need to be investigated in order to demonstrate that this is consistent for all mini-basins.

5.2 Further Work

- Investigate unfaulted wells across the CNS to continue testing the null hypothesis presented in this thesis. Investigating wells with sandstones that are unfaulted and do not contain deformation bands would act as a set of control wells for sandstones in salt-wall mini-basins. This would allow for indepth comparisons between undeformed and deformed wells, rather than undeformed and deformed sections from the same well. Based on Figure 3.8, the Marnock wells could make excellent candidates for exploring and comparing wells that do not sample faulted sandstones from the CNS.

- Incorporating more data types such as handling the core samples, production history, and seismic surveys. Handling the core samples for the wells should provide a better insight into the lithology of the wells and the nature of the deformation features than well reports and core photographs. Production history may further strengthen the impact of deformation bands on hydrocarbon flow and production in wells that display a high abundance of deformation bands against wells that do not display significant deformation. Quiescence or acoustic complexity on seismic surveys may be able to act as a proxy for dense clusters of deformation bands, improving the location of exploration wells.

- Corroborate deformation band petrography and orientation observations in wells 22/29-2S1 and 22/29-3 with other wells across the CNS (i.e. Huntington, Fiddich, Puffin). Orientation data for the deformation bands in these wells would be tested to confirm if lateral movement of the salt wall could be expressed as a rotation of the deformation bands. As previously stated, salt walls can cause differences in sedimentary deposits between adjacent mini-basins. These differences may be reflected in the petrographic analyses for each of these mini-basins with minor changes to the initial detrital clay minerals found in each mini-basin resulting in measurably different diagenetic pathways and eventual sandstone quality.
- Investigate similar salt-walled mini-basins in other halokinetic provinces. One such location would be the Paradox Basin which contains the upper Triassic Chinle Formation, a succession of channel-fill sandstones analogous to the fluviolacustrine deposits of the Triassic Skagerrak Formation in this study (Kluth & DuChene, 2009; Matthews et al., 2007). This location would demonstrate if the observations from the mini-basins of the Central Graben have been reproduced in similar mini-basins from other halokinetic provinces.
- Investigate salt-walled mini-basins with a different sedimentary environment. One possible target could be the Magnolia Formation in the Gulf of Mexico, which is comprised of turbidite deposits and sandstone-mudstone successions (Kneller & McCaffrey, 1995; Kane et al., 2012). This sandstone formation also developed early overpressure, leading to preserved porosity at depth (Sathar & Jones, 2016; Stricker & Jones, 2016). The larger range of grain sizes in the turbidite deposits would alter the stresses required for the formation of any deformation bands and any deformation bands that are produced would display a lager variation in deformation band thickness and morphology, potentially creating a complex network of dilational and compaction bands. The diagenetic pathways of clay minerals within the sediment may also undergo drastically different alteration pathways and may alter the petrophysical properties of the turbidite sandstone to be significantly better quality than that measured in the Skagerrak Formation sandstones.
- Investigate each of the factors associated with deformation band formation. Changing the composition, sorting and size of the sediment would influence the nature of the resultant deformation bands. Larger grains would be expected to produce thicker bands and require higher stresses to deform the sediment, potentially fracturing the grains and occluding the enhanced porosity with grain fragments (Johansen & Fossen, 2008). Increasingly higher compressive stresses would produce compaction and cataclastic bands that would inhibit fluid flow into the sandstone, preventing the infiltration of meteoric pore fluids into the

sandstone and suppressing subsequent pore-filling diagenetic material. These higher stresses are likely to occur in compressive halokinetic regimes compared to the extensional regime of the Central Graben, North Sea (Solum et al., 2010).

- Apply the conclusions from this thesis and subsequent similar studies to poro-elastic basin modelling, with consideration of dilational and disaggregation bands that form at shallow depths (< 500 m depth). Previous models of salt-wall mini-basins have focussed on large-scale faulting around the salt structures with no analysis of small-scale deformation features (Nikolinakou et al., 2014; Heidari et al., 2017). This research highlights the requirement for future modelling of salt-walled mini-basins to include the effects of deformation band formation and the interaction with diagenetic processes at depth.

References:

Aharonov, E., & Katsman, R. (2009). Interaction between pressure solution and clays in stylolite development: Insights from modeling. *American Journal of Science*, Vol: 309, pp: 607-632.

Albertz, M., & Beaumont, C., (2010). An investigation of salt tectonic structural styles in the Scotian Basin, offshore Atlantic Canada: 2. Comparison of observations with geometrically complex numerical models. *Tectonics* 29, TC4018.

Albertz, M., Beaumont, C., Shimeld, J.W., Ings, S.J., Gradmann, S., (2010). An investigation of salt tectonic structural styles in the Scotian Basin, offshore Atlantic Canada: 1. Comparison of observations with geometrically simple numerical models. *Tectonics* 29, TC4017.

Alsop, G. I. (1996). Physical modelling of fold and fracture geometries associated with salt diapirism. *Geological Society, London, Special Publications*, Vol: 100, pp: 227-241.

Andersen, L. T., Hansen, D. L., & Huuse, M. (2005). Numerical modelling of thrust structures in unconsolidated sediments: implications for glaciotectonic deformation. *Journal of Structural Geology,* Vol: 27, pp: 587-596.

Andrie, J. R., Giles, K. A., Lawton, T. F., & Rowan, M. G. (2012). Halokinetic-sequence stratigraphy, fluvial sedimentology and structural geometry of the Eocene Carroza Formation along La Popa salt weld, La Popa Basin, Mexico. *Geological Society, London, Special Publications*, Vol: 363, pp: 59-79.

Antonellini, M.A., Aydin, A. and Pollard, D.D. (1994). Microstructure of deformation bands in porous sandstones at Arches National Park, Utah. *Journal of Structural Geology,* Vol: 16, pp: 941-959.

Archer, S., Ward, S., Menad, S., Shahim, I., Grant, N., Sloan, H., & Cole, A. (2010). The Jasmine discovery, Central North Sea, UKCS. In: Vining, B. A. & Pickering, S. C. (eds.) *Geological Society, London, Petroleum Geology Conference series*, Vol: 7, pp: 225-243.

Archer, S. G., Alsop, G. I., Hartley, A. J., Grant, N. T., & Hodgkinson, R. (2012). Salt tectonics, sediments and prospectivity: an introduction. *Geological Society, London, Special Publications*, Vol: 363, pp: 1-6.

Aydin, A. (1978). Small faults formed as deformation bands in sandstone. *Pure and Applied Geophysics*, Vol: 116, pp: 913-930.

Aydin, A., Borja, R.I. & Eichhubl, P. (2006). Geological and mathematical framework for failure modes in granular rock. *Journal of Structural Geology*, Vol: 28, pp: 83–98.

Bachrach, R., Sengupta, M., & Salama, A., (2007). Stress and seismic anisotropy near salt bodies—numerical modeling and observation from wide-azimuth marine data. In: EAGE 69th Conference & Exhibition, London, UK.

Banham, S. G., & Mountney, N. P. (2014). Climatic versus halokinetic control on sedimentation in a dryland fluvial succession. *Sedimentology*, Vol: 61, pp: 570-608.

Banham, S. G., & Mountney, N. P. (2013a). Controls on fluvial sedimentary architecture and sediment-fill state in salt-walled mini-basins: Triassic Moenkopi Formation, Salt Anticline Region, SE Utah, USA. *Basin Research*, Vol: 25, pp: 709-737.

Banham, S.G. and Mountney, N.P. (2013b). Evolution of fluvial systems in salt-walled mini-basins: A review and new insights. *Sedimentary Geology*, Vol: 296, pp: 142-166.

Barde, J. P., Chamberlain, P., Galavazi, M., Gralla, P., Harwijanto, J., Marsky, J., & van den Belt, F. (2002). Sedimentation during halokinesis: Permo-Triassic reservoirs of the Saigak field, Precaspian basin, Kazakhstan. *Petroleum Geoscience*, Vol: 8, pp: 177-187.

Bardet, J. P. (1990). A comprehensive review of strain localization in elastoplastic soils. *Computers and geotechnics*, Vol: 10, pp: 163-188.

Bense, V. F., Van den Berg, E. H., & Van Balen, R. T. (2003). Deformation mechanisms and hydraulic properties of fault zones in unconsolidated sediments; the Roer Valley Rift System, The Netherlands. *Hydrogeology Journal*, Vol: 11, pp: 319-332.

Bésuelle, P., Desrues, J., & Raynaud, S. (2000). Experimental characterisation of the localisation phenomenon inside a Vosges sandstone in a triaxial cell. *International Journal of Rock Mechanics and Mining Sciences*, Vol: 37, pp:1223-1237.

Bjørlykke, K., Aagaard, P., (1992). Clay minerals in North Sea sandstones, Origin, diagenesis, and petrophysics of clay minerals in sandstones. *Society for Sedimentary Geology (SEPM), Tulsa, OK, United States*. Vol: 47, pp: 65–80.

Bolton, M. D. (1986). The strength and dilatancy of sands. *Geotechnique*, Vol: 36(1), pp: 65-78.

Borradaile, G. J. (1981). Particulate flow of rock and the formation of cleavage. *Tectonophysics*, Vol: 72, pp: 305-321.

Bourquin, S., Bercovici, A., López-Gómez, J., Diez, J. B., Broutin, J., Ronchi, A., Durand, M., Arché, A., Linol, B., & Amour, F. (2011). The Permian–Triassic transition and the onset of Mesozoic sedimentation at the northwestern peri-Tethyan domain scale: palaeogeographic maps and geodynamic implications. *Palaeogeography, Palaeoclimatology, Palaeoecology*, Vol: 299, pp: 265-280.

Bradley, W. B. (1978). Bore hole failure near salt domes. In *SPE Annual Fall Technical Conference and Exhibition*. Society of Petroleum Engineers.

Brun, J. P., & Fort, X. (2011). Salt tectonics at passive margins: Geology versus models. *Marine and Petroleum Geology*, Vol: 28, pp: 1123-1145.

Buck, B. J., Lawton, T. F., & Brock, A. L. (2010). Evaporitic paleosols in continental strata of the Carroza Formation, La Popa Basin, Mexico: record of Paleogene climate and salt tectonics. *Geological Society of America Bulletin*, Vol: 122, pp: 1011-1026.

Carr, A. D. (2003). Thermal history model for the South Central Graben, North Sea, derived using both tectonics and maturation. *International Journal of Coal Geology*, Vol: 54, pp: 3-19.

Cashman, S. M., Baldwin, J. N., Cashman, K. V., Swanson, K., & Crawford, R. (2007). Microstructures developed by coseismic and aseismic faulting in near-surface sediments, San Andreas Fault, California. *Geology*, Vol: 35, pp: 611-614.

Chemia, Z., Schmeling, H., & Koyi, H. (2009). The effect of the salt viscosity on future evolution of the Gorleben salt diapir, Germany. *Tectonophysics,* Vol*:* 473, pp: 446-456.

Chuhan, F. A., Kjeldstad, A., Bjørlykke, K., & Høeg, K. (2002). Porosity loss in sand by grain crushing —Experimental evidence and relevance to reservoir quality. *Marine and Petroleum Geology*, Vol: 19, pp: 39-53.

Clark, J.A., Cartwright, J.A., Stewart, S.A. (1999). Mesozoic dissolution tectonics on the West Central Shelf, UK Central North Sea. *Marine and Petroleum Geology*. Vol: 16, pp: 283-300. DOI: 10.1016/S0264-8172(98)00040-3.

Cui, Y., Jones, S. J., Saville, C., Stricker, S., Wang, G., Tang, L., Fan, X., & Chen, J. (2017). The role played by carbonate cementation in controlling reservoir quality of the Triassic Skagerrak Formation, Norway. *Marine and Petroleum Geology*, Vol: 85, pp:316-331.

Davison, I., Alsop, G. I., Evans, N. G., & Safaricz, M. (2000). Overburden deformation patterns and mechanisms of salt diapir penetration in the Central Graben, North Sea. *Marine and Petroleum Geology*, Vol: 17, pp: 601-618.

Davison, I., Alsop, I., & Blundell, D. (1996). Salt tectonics: some aspects of deformation mechanics. *Geological Society, London, Special Publications*, Vol: 100, ppg1-10.

Desrues, J., Bésuelle, P., & Lewis, H. (2007). Strain localization in geomaterials. *Geological Society, London, Special Publications*, Vol: 289, pp: 47-73.

Desrues, J., & Viggiani, G. (2004). Strain localization in sand: an overview of the experimental results obtained in Grenoble using stereophotogrammetry. *International Journal for Numerical and Analytical Methods in Geomechanics*, Vol: 28, pp: 279-321.

Du Bernard, X., Eichhubl, P., & Aydin, A. (2002). Dilation bands: A new form of localized failure in granular media. *Geophysical Research Letters*, Vol: 29, 2176.

Dusseault, M. B., Maury, V., Sanfilippo, F., & Santarelli, F. J. (2004). Drilling around salt: risks, stresses, and uncertainties. In *Gulf Rocks 2004, the 6th North America Rock Mechanics Symposium (NARMS)*. American Rock Mechanics Association.

Erratt, D. (1993). Relationships between basement faulting, salt withdrawal and Late Jurassic rifting, UK Central North Sea. In: Parker, J. R. (ed.) *Geological Society, London, Petroleum Geology Conference series*, Vol: 4, pp. 1211-1219.

Evans, D., Graham, C., Armour, A. (2003) The Millennium Atlas: Petroleum geology of the central and northern North Sea: Geological Society, London.

Exner, U., Kaiser, J., Gier, S. (2013). Deformation bands evolving from dilation to cementation bands in a hydrocarbon reservoir (Vienna Basin, Austria). *Marine and Petroleum Geology*. Vol: 43, pp: 504-515. DOI: 10.1016/j.marpetgeo.2012.10.001.

Fisher, Q. J., & Knipe, R. (1998). Fault sealing processes in siliciclastic sediments. *Geological Society, London, Special Publications*, Vol: 147, pp: 117-134.

Fisher, M. J., & Mudge, D. C. (1998). Triassic.IN: K. W.. Glennie, ed. *Introduction to the Petroleum Geology of the North Sea.* Oxfrod: Blackwell Scientific Publications, pp: 212-244.

Fort, X., Brun, JP., Chauvel, F. (2004) Salt tectonics on the Angolan margin, synsedimentary deformation processes. *AAPG Bulletin*, Vol: 88, pp: 1523-1544. DOI: 10.1306/06010403012.

Fossen, H. (2016). *Structural geology (2nd edition)*. Cambridge University Press.

Fossen, H. (2010). Deformation bands formed during soft-sediment deformation: Observations from SE Utah. *Marine and Petroleum Geology*, 27, pp: 215-222.

Fossen, H., Schultz, R.A., Shipton, Z.K. and Mair, K. (2007). Deformation bands in sandstone: a review. *Journal of the Geological Society,* Vol: 164, pp: 755-769.

Fossen, H & Bale. A. (2007). Deformation bands and their influence on fluid flow. *AAPG Bulletin*, Vol: 91, pp: 1685-1700. DOI: 10.1306/07300706146.

Fossen, H., & Hesthammer, J. (1998). Deformation bands and their significance in porous sandstone reservoirs. *First Break*, Vol: 16, pp: 21-25.

Fraser, S. I., Robinson, A. M., Johnson, H. D., Underhill, J. R., Kadolsky, D. G. A., Connell, R., Johannessen, P., & Ravnås, R. (2003). Upper Jurassic *In:* Evans, D., Graham, C., Armour, A. & Bathurst, P. (eds) *The Millennium Atlas: Petroleum Geology of the Central and Northern North Sea. The Geological Society.* The Geological Society, London, pp: 157-189.

Geluk, M. C. (2005). Stratigraphy and tectonics of PermoTriassic basins in the Netherlands and surrounding areas. PhD thesis, University of Utrecht.

Gerbersdorf, S. U., & Wieprecht, S. (2015). Biostabilization of cohesive sediments: revisiting the role of abiotic conditions, physiology and diversity of microbes, polymeric secretion, and biofilm architecture. *Geobiology*, Vol: 13, pp: 68-97.

Giles, K. A., & Rowan, M. G. (2012). Concepts in halokinetic-sequence deformation and stratigraphy. *Geological Society, London, Special Publications*, Vol: 363, pp: 7-31.

Glennie, K. W., Higham, J., & Stemmerik, L. (2003). Permian. *In:* Evans, D., Graham, C., Armour, A. & Bathurst, P. (eds) *The Millennium Atlas: Petroleum Geology of the Central and Northern North Sea*. The Geological Society, London, pp: 91–103.

Goldsmith, P. J., Rich, B., & Standring, J. (1995). Triassic correlation and stratigraphy in the south Central Graben, UK North Sea. In: Boldy S. A. R. (ed.) *Geological Society, London, Special Publications*, Vol: 91, pp: 123-143.

Goldsmith, P. J., Hudson, G., & Van Veen, P. (2003) Triassic. *In:* Evans, D., Graham, C., Armour, A. & Bathurst, P. (eds) *The Millenium Atlas: Petroleum Geology of the Central and Northern North Sea.* The Geological Society, London, pp: 105–127.

Goteti, R., Ings, S.J., & Beaumont, C., (2012). Development of salt minibasins initiated by sedimentary topographic relief. *Earth & Planetary Science Letters.* Vol: 339/340, pp: 103-116.

Gradmann, S., Beaumont, C., & Albertz, M., (2009). Factors controlling the evolution of the Perdido Fold Belt, northwestern Gulf of Mexico, determined from numerical models. *Tectonics,* Vol: 28.

Grant, N. T., Middleton, A. J., & Archer, S. (2014). Porosity trends in the Skagerrak Formation, Central Graben, United Kingdom Continental Shelf: The role of compaction and pore pressure history. *AAPG bulletin*, 98, pp: 1111-1143.

Griffiths, J., Faulkner, D. R., Edwards, A. P., & Worden, R. H. (2016). Deformation band development as a function of intrinsic host-rock properties in Triassic Sherwood Sandstone. *Geological Society, London, Special Publications*, Vol: 435, SP435-11.

Guo, J., McCaffrey, K., Jones, R., & Holdsworth, R. (2009). The spatial heterogeneity of structures in high porosity sandstones: Variations and granularity effects in orientation data. *Journal of Structural Geology*, Vol: 31, pp: 628-636.

Guven, N., Hower, W. F., & Davies, D. K. (1980). Nature of authigenic illites in sandstone reservoirs. *Journal of Sedimentary Research*, Vol: 50, pp: 761-766.

Hallett, P. D., & Newson, T. A. (2005). Describing soil crack formation using elastic–plastic fracture mechanics. *European Journal of Soil Science*, Vol: 56, pp: 31-38.

Harding, R., Huuse, M. (2015). Salt on the move: Multi stage evolution of salt diapirs in the Netherlands North Sea. *Marine and Petroleum Geology*. Vol: 61, pp: 39-55. DOI: 10.1016/j.marpetgeo.2014.12.003.

Heidari, M., Nikolinakou, M. A., Flemings, P. B., & Hudec, M. R. (2017). A simplified stress analysis of rising salt domes. *Basin Research*, Vol: 29, pp: 363-376.

Hodgson, N. A., Farnsworth, J., & Fraser, A. J. (1992). Salt-related tectonics, sedimentation and hydrocarbon plays in the Central Graben, North Sea, UKCS. *Geological Society, London, Special Publications*, Vol: 67, pp: 31-63.

Hudec, M. R., Jackson, M. P., & Schultz-Ela, D. D. (2009). The paradox of minibasin subsidence into salt: Clues to the evolution of crustal basins. *Geological Society of America Bulletin*, Vol: 121, pp: 201-221.

Hudec, M. R., & Jackson, M. P. (2007). Terra infirma: Understanding salt tectonics. *Earth-Science Reviews,* Vol: 82, pp: 1-28.

Humphreys, B., Smith, S. A., Strong, G. E. (1989). Authigenic chlorite in Late Triassic sandstones from the Central Graben, North Sea. *Clay Minerals*, Vol: 24, pp: 427-444.

Ings, S. J., & Beaumont, C. (2010). Shortening viscous pressure ridges, a solution to the enigma of initiating salt 'withdrawal' minibasins. *Geology*, Vol: 38, pp: 339-342.

Jackson, C. A., Jackson, M. P., Hudec, M. R., & Rodriguez, C. (2014). Internal structure, kinematics, and growth of a salt wall: Insights from 3-D seismic data. *Geology*, 42, pp: 307-310.

Jackson, M. P., & Talbot, C. J. (1986). External shapes, strain rates, and dynamics of salt structures. *Geological Society of America Bulletin*, Vol: 97, pp: 305-323.

Jackson, M. P. A., & Talbot, C. J. (1991). *A glossary of salt tectonics*. Bureau of Economic Geology, University of Texas at Austin.

Johansen, T. E. S., & Fossen, H. (2008). Internal geometry of fault damage zones in interbedded siliciclastic sediments. *Geological Society, London, Special Publications*, Vol: 299, pp: 35-56.

Jones, S. (2017). Goo, glue, and grain binding: Importance of biofilms for diagenesis in sandstones. *Geology*, Vol: 45, pp: 959-960.

Kane, I. A., McGee, T. D., & Jobe, Z. R. (2012). Halokinetic effects on slope equilibrium profiles: Submarine channel evolution and implications for facies architecture in Magnolia field, Gulf of Mexico. *Salt tectonics, sediments and prospectivity: Geological Society (London) Special Publication*, Vol: 363, pp: 289-302.

Kaproth, B. M., Cashman, S. M., & Marone, C. (2010). Deformation band formation and strength evolution in unlithified sand: the role of grain breakage. *Journal of Geophysical Research: Solid Earth*, Vol: 115 p. B12103.

Karlo, J. F., van Buchem, F. S., Moen, J., & Milroy, K. (2014). Triassic-age salt tectonics of the Central North Sea. *Interpretation*, Vol: 2, SM19-SM28.

Kemper, W. D., & Rosenau, R. C. (1984). Soil cohesion as affected by time and water content. *Soil Science Society of America Journal,* Vol: 48, pp: 1001-1006.

Kemper, W. D., Rosenau, R. C., & Dexter, A. R. (1987). Cohesion development in disrupted soils as affected by clay and organic matter content and temperature. *Soil Science Society of America Journal*, Vol: 51, pp: 860-867.

Kim, T. H., Nam, J. M., Yun, J. M., Lee, K. I., & You, S. K. (2009) Relationship between cohesion and tensile strength in wet sand at low normal stresses. In *Proc. of 17 th Intern. Conf. on Soil Mechanics and Geotechnical Engineering.–Olexandria, 2009.–Amsterdam, Berlin, Tokyo, Washington: JOS Press.–2009.–P. 364* (Vol. 367).

Kluth, C. F., & DuChene, H. R. (2009). Late Pennsylvanian and Early Permian structural geology and tectonic history of the Paradox Basin and Uncompahgre Uplift, Colorado and Utah. *In: The Paradox Basin Revisited-New Developments in Petroleum Systems and Basin Analysis* (Ed. by W.S. Houston, L.L. Wray & P.G. Moreland), pp. 178–197. RMAG Special Publication – The Paradox Basin, Denver, CO.

Kneller, B. C., & McCaffrey, W. D. (1995). Modelling the effects of salt-induced topography on deposition from turbidity currents. In *Salt, sediment and hydrocarbons: Gulf Coast Section SEPM* (pp. 137-145).

Laubach, S. E., Eichhubl, P., Hilgers, C., & Lander, R. H. (2010). Structural diagenesis. *Journal of Structural Geology*, Vol: 32, pp: 1866-1872.

Lawton, T. F., & Buck, B. J. (2006). Implications of diapir-derived detritus and gypsic paleosols in Lower Triassic strata near the Castle Valley salt wall, Paradox Basin, Utah. *Geology*, Vol: 34, pp: 885-888.

Lemon, N. M. and Cubitt, C. J. (2009). Illite Fluorescence Microscopy: A New Technique in the Study of Illite in the Merrimelia Formation, Cooper Basin, Australia. In Clay Mineral Cements in Sandstones (eds R. H. Worden and S. Morad).

Lommatzsch, M., Exner, U., Gier, S. and Grasemann, B. (2015a). Structural and chemical controls of deformation bands on fluid flow: Interplay between cataclasis and diagenetic alteration. *AAPG Bulletin*, Vol: 99, pp: 689-710.

Lommatzsch, M., Exner, U., Gier, S., & Grasemann, B. (2015b). Dilatant shear band formation and diagenesis in calcareous, arkosic sandstones, Vienna Basin (Austria). *Marine and petroleum geology*, Vol: 62, pp: 144-160.

Main, I. G., Kwon, O., Ngwenya, B. T., & Elphick, S. C. (2000). Fault sealing during deformation-band growth in porous sandstone. *Geology*, Vol: 28, pp: 1131-1134.

Malarkey, J., Baas, J. H., Hope, J. A., Aspden, R. J., Parsons, D. R., Peakall, J., Paterson, D. M., Schindler, R. J., Ye, L., Lichtman, I. D., Bass, S. J., Davies, A. G., Manning, A. J., & Thorne, P. D. (2015). The pervasive role of biological cohesion in bedform development. *Nature communications*, Vol: 6, p. 6257.

Mange-Rajetzky, M. (1995). Subdivision and correlation of monotonous sandstone sequences using high resolution heavy mineral analysis, a case study: the Triassic of the Central Graben. In: Dunay, R. E. & Hailwood, E. A. (eds) Non-biostratigraphical Methods of Dating and Correlation. *Geological Society, London, Special Publications*, Vol: 89, pp: 23–30.

Matthews, W. J., Hampson, G. J., Trudgill, B. D., & Underhill, J. R. (2007). Controls on fluviolacustrine reservoir distribution and architecture in passive salt-diapir provinces: Insights from outcrop analogs. *AAPG bulletin*, Vol: 91, pp: 1367-1403.

McKie, T., & Audretsch, P. (2005). Depositional and structural controls on Triassic reservoir performance in the Heron Cluster, ETAP, Central North Sea. In: Doré, A. G. & Vining, B. A. (eds). *Geological Society, London, Petroleum Geology Conference series,* Vol. 6, No. 1, pp. 285-297.

McKie, T., & Williams, B. (2009). Triassic palaeogeography and fluvial dispersal across the northwest European Basins. *Geological Journal*, Vol: 44, pp: 711-741.

McKie, T. (2014). Climatic and tectonic controls on Triassic dryland terminal fluvial system architecture, central North Sea. *From Depositional Systems to Sedimentary Successions on the Norwegian Continental Margin (eds Martinius AW, Ravn R., Howell JA, Steel RJ & Wonham JP)*, pp: 19-58.

McKie, T., Jolley, S. J. and Kristensen, M. B. (2010). Stratigraphic and structural compartmentalisation of dryland fluvial reservoirs: Triassic Heron Cluster, Central North Sea. *Geological Society, London, Special Publications,* Vol: 347, pp: 165-198.

McKie, T., & Shannon, P. M. (2011). Comment on "The Permian–Triassic transition and the onset of Mesozoic sedimentation at the northwestern peri Tethyan domain scale: Palaeogeographic maps and geodynamic implications" by S. Bourquin, A. Bercovici, J. López-Gómez, JB Diez, J. Broutin, A. Ronchi, M. Durand, A. Arché, B. Linol and F. Amour.[Palaeogeography, Palaeoclimatology, Palaeoecology. Vol: 299 pp: 265–280. *Palaeogeography, Palaeoclimatology, Palaeoecology*, Vol: 311, pp: 136-143.

Mello, U. T., Karner, G. D., & Anderson, R. N. (1995). Role of salt in restraining the maturation of subsalt source rocks. *Marine and Petroleum Geology*, Vol: 12, pp: 697-716.

Newell, A. J., Benton, M. J., Kearsey, T., Taylor, G., Twitchett, R. J., & Tverdokhlebov, V. P. (2012). Calcretes, fluviolacustrine sediments and subsidence patterns in Permo-Triassic salt-walled minibasins of the south Urals, Russia. *Sedimentology*, Vol: 59, pp: 1659-1676.

Nikolinakou, M. A., Flemings, P. B., & Hudec, M. R. (2014). Modeling stress evolution around a rising salt diapir. *Marine and Petroleum Geology*, Vol: 51, pp: 230-238.

Nikolinakou, M. A., Luo, G., Hudec, M. R., & Flemings, P. B. (2012). Geomechanical modeling of stresses adjacent to salt bodies: Part 2—Poroelastoplasticity and coupled overpressures. *AAPG bulletin*, Vol: 96, pp: 65-85.

Nguyen, B. T. T., Jones, S. J., Goulty, N. R., Middleton, A. J., Grant, N., Ferguson, A. and Bowen, L. (2013). The role of fluid pressure and diagenetic cements for porosity preservation in Triassic fluvial reservoirs of the Central Graben, North Sea. *AAPG Bulletin*, Vol: 97, pp: 1273–1302.

Ogilvie, S. R.; J. M., & Glover, P. W. J. (2001). The influence of deformation bands upon fluid flow using profile permeametry and positron emission tomography. *Geophysical Research Letters*, Vol: 28, pp: 61-64.

Owen, G. (1987). Deformation processes in unconsolidated sands. *Geological Society, London, Special Publications*, Vol: 29, pp: 11-24.

Parsons, D. R., Schindler, R. J., Hope, J. A., Malarkey, J., Baas, J. H., Peakall, J., Manning, A. J., Ye, L., Simmons, S., Paterson, M. P., Aspden, R. J., Bass, S. J., Davies, A. G., Lichtman, I. D., & Thorne, P. D. (2016). The role of biophysical cohesion on subaqueous bed form size. *Geophysical research letters*, Vol: 43, pp: 1566-1573.

Peel, F. J. (2014). How do salt withdrawal minibasins form? Insights from forward modelling, and implications for hydrocarbon migration. *Tectonophysics*, Vol: 630, pp: 222-235.

Penge, J., Munns, J. W., Taylor, B., & Windle, T. M. F. (1999, January). Rift–raft tectonics: examples of gravitational tectonics from the Zechstein basins of northwest Europe. In *Geological Society, London, Petroleum Geology Conference series,* Vol. 5, pp. 201-213.

Penge, J., Taylor, B., Huckerby, J. A., & Munns, J. W. (1993). Extension and salt tectonics in the East Central Graben. In *Geological Society, London, Petroleum Geology Conference series.* Vol. 4, No. 1, pp. 1197-1209.

Perez, M.A., Clyde, R., D'Ambrosio, P., Israel, R., Leavitt, T., Nutt, L., Johnson, C., & Wiliamson, D., (2008). Meeting the subsalt challenge. Oilfield Rev. Vol: 20, pp: 32-45

Pichat, A., Hoareau, G., Callot, J. P., & Ringenbach, J. C. (2016). Diagenesis of Oligocene continental sandstones in salt-walled mini-basins—Sivas Basin, Turkey. *Sedimentary Geology*, Vol: 339, pp: 13-31.

Pittman, E. D. (1981). Effect of fault-related granulation on porosity and permeability of quartz sandstones, Simpson Group (Ordovician), Oklahoma. *AAPG Bulletin*, Vol: 65, pp: 2381-2387.

Prather, B. E., Booth, J. R., Steffens, G. S., & Craig, P. A. (1998). Classification, lithologic calibration, and stratigraphic succession of seismic facies of intraslope basins, deep-water Gulf of Mexico. *AAPG bulletin*, Vol: 82, pp: 701-728.

Prochnow, S. J., Atchley, S. C., Boucher, T. E., Nordt, L. C., & Hudec, M. R. (2006). The influence of salt withdrawal subsidence on palaeosol maturity and cyclic fluvial deposition in the Upper Triassic Chinle Formation: Castle Valley, Utah. *Sedimentology*, Vol: 53, pp: 1319-1345.

Quinta, A., Tavani, S., Roca, E. (2012). Fracture pattern analysis as a tool for constraining the interaction between regional and diapir-related stress fields: Poza de la Sal Diapir (Basque Pyrenees, Spain). in: G.I. Alsop, S.G. Archer, A.J. Hartley, N.T. Grant, R. Hodgkinson (Eds.), Salt Tectonics, Sediments and Prospectivity, *Geological Society, London, Special Publications*, Vol. 363, pp: 521–532. DOI: 10.1144/SP363.25

Rawling, G.C. & Goodwin, L.B. (2003). Cataclasis and particulate flow in faulted, poorly lithified sediments. *Journal of Structural Geology*, Vol: 25, pp: 317–331.

Rider, M. H. (1996). *The geological interpretation of well logs (2nd Edition),* Whittles Publishing.

Rossetti, D. D. F. (1999). Soft-sediment deformation structures in late Albian to Cenomanian deposits, São Luís Basin, northern Brazil: evidence for palaeoseismicity. *Sedimentology*, Vol: 46, pp: 1065-1081.

Rowan, M. G., Peel, F. J., Vendeville, B. C., & Gaullier, V. (2012). Salt tectonics at passive margins: Geology versus models–Discussion. *Marine and Petroleum Geology*, Vol: 37, pp: 184-194.

Rowan, M. G., & Ratliff, R. A. (2012). Cross-section restoration of salt-related deformation: Best practices and potential pitfalls. *Journal of Structural Geology*, Vol: 41, pp: 24-37.

Rowan, M. G., & Vendeville, B. C. (2006). Foldbelts with early salt withdrawal and diapirism: Physical model and examples from the northern Gulf of Mexico and the Flinders Ranges, Australia. *Marine and Petroleum Geology*, Vol: 23, pp: 871-891.

Rowan, M. G., F. J. Peel, & B. Vendeville, (2004). Gravity-driven foldbelts on passive margins, in K. R. McClay, ed., Thrust tectonics and hydrocarbon systems: AAPG Memoir 82, pp: 157– 183.

Sathar, S., & Jones, S. (2016). Fluid overpressure as a control on sandstone reservoir quality in a mechanical compaction dominated setting: Magnolia Field, Gulf of Mexico. *Terra Nova*, Vol: 28, pp: 155-162.

Schultz, R. A., & Siddharthan, R. (2005). A general framework for the occurrence and faulting of deformation bands in porous granular rocks. *Tectonophysics*, Vol: 411, pp: 1-18.

Schultz-Ela, D.D., (2003). Origin of drag folds bordering salt diapirs. *AAPG Bulletin,* Vol: 87, pp: 757-780.

Shell (U.K.) Exploration and Production (1991). Core Photograph Reports; Well 22/29-2.

Shell (U.K.) Exploration and Production (1992). Special Core Analysis Study; Well: 22/29-2.

Shell (U.K.) Exploration and Production (1993a). Structural and sedimentological study of Formation MicroScanner and Dipmeter data; Wells 22/29-2 S1, 22/29-3, 22/24d-10 & 22/30a-6.

Shell (U.K.) Exploration and Production (1993b). Core Sedimentology And Core Analysis Results of the cored Triassic and Jurassic intervals of Shell/Esso; Well 22/29-3.

Shin, H., & Santamarina, J. C. (2011). Desiccation cracks in saturated fine-grained soils: particle-level phenomena and effective-stress analysis. *Géotechnique*, Vol: 61, pp: 961-972.

Shipton, Z. K., & Cowie, P. A. (2001). Damage zone and slip-surface evolution over µm to km scales in high-porosity Navajo sandstone, Utah. *Journal of Structural Geology*, Vol: 23, pp: 1825-1844.

Smith, R. I., Hodgson, N., & Fulton, M. (1993). Salt control on Triassic reservoir distribution, UKCS central North Sea. In: Parker, J. R. (ed) *Geological Society, London, Petroleum Geology Conference series.* Vol. 4, pp. 547-557.

Soliva, R., Ballas, G., Fossen, H., & Philit, S. (2016). Tectonic regime controls clustering of deformation bands in porous sandstone. *Geology*, Vol: 44, pp: 423-426.

Solum, J. G., Brandenburg, J. P., Naruk, S. J., Kostenko, O. V., Wilkins, S. J., & Schultz, R. A. (2010). Characterization of deformation bands associated with normal and reverse stress states in the Navajo Sandstone, Utah. *AAPG bulletin*, Vol: 94, pp: 1453-1475.

Spark, I. S. C., & Trewin, N. H. (1986). Facies related diagenesis in the main Claymore oilfield sandstones. *Clay Minerals*, Vol: 21, pp: 479-496.

Stricker, S., & Jones, S. J. (2016). Enhanced porosity preservation by pore fluid overpressure and chlorite grain coatings in the Triassic Skagerrak, Central Graben, North Sea, UK. *Geological Society, London, Special Publications*, Vol: 435, pp:321-341.

Stricker, S., Jones, S. J., Meadows, N., & Bowen, L. (2018). Reservoir quality of fluvial sandstone reservoirs in salt-walled mini-basins: an example from the Seagull field, Central Graben, North Sea, UK. *Petroleum Science*, Vol: 15, pp: 1-27.

Stricker, S., Jones, S. J., Sathar, S., Bowen, L., & Oxtoby, N. (2016). Exceptional reservoir quality in HPHT reservoir settings: examples from the Skagerrak Formation of the Heron Cluster, North Sea, UK. *Marine and Petroleum Geology*, Vol: 77, pp: 198-215.

Sternlof, K. R., Chapin, J. R., Pollard, D. D. and Durlofsky, L. J. (2004). Permeability effects of deformation band arrays in sandstone. *AAPG Bulletin*, Vol: 88, pp: 1315-1329.

Stewart, S. A., & Clark, J. A. (1999). Impact of salt on the structure of the Central North Sea hydrocarbon fairways. In: Fleet, A. J. & Boldy, S. A. R. (eds) *Geological Society, London, Petroleum Geology Conference series* (Vol. 5, pp. 179-200). Geological Society of London.

Terzaghi, K., Peck, R. B., & Mesri, G. (1996). *Soil mechanics in engineering practice*. John Wiley & Sons.

Torabi, A., Fossen, H., & Braathen, A. (2013). Insight into petrophysical properties of deformed sandstone reservoirs. *AAPG Bulletin*, Vol: 97, pp: 619-637.

Torabi, A., & Fossen, H. (2009). Spatial variation of microstructure and petrophysical properties along deformation bands in reservoir sandstones. *AAPG bulletin*, Vol: 93(7), pp: 919-938.

Trudgill, B. D. (2011). Evolution of salt structures in the northern Paradox Basin: Controls on evaporite deposition, salt wall growth and supra-salt stratigraphic architecture. *Basin Research*, Vol: 23, pp: 208-238.

Tucker, M. E. (1991). Sequence stratigraphy of carbonate-evaporite basins: models and application to the Upper Permian (Zechstein) of northeast England and adjoining North Sea. *Journal of the Geological Society*, Vol: 148, pp: 1019-1036.

Underhill, J. R. (2003). The tectonic and stratigraphic framework of the United Kingdom's oil and gas fields. *Geological Society, London, Memoirs*, Vol: 20, pp: 17-59.

Venus, J. H., Mountney, N. P., & McCaffrey, W. D. (2015). Syn-sedimentary salt diapirism as a control on fluvial-system evolution: an example from the proximal Permian Cutler Group, SE Utah, USA. *Basin Research*, Vol: 27, pp: 152-182.

Weibel, R. (1999). Effects of burial on the clay assemblages in the Triassic Skagerrak Formation, Denmark. *Clay Minerals*, Vol: 34, pp: 619-635.

Wilkins, A. D., Hurst, A., Wilson, M. J., & Archer, S. (2018). Palaeo-environment in an ancient low-latitude, arid lacustrine basin with loessite: The Smith Bank Formation (Early Triassic) in the Central North Sea, UK Continental Shelf. *Sedimentology*, Vol: 65, pp: 335-359.

Willson, S.M., Edwards, S., Heppard, P.D., Li, X., Coltrin, G., Chester, D.K., Harrison, H.L., & Cocales, B.W., (2003). Wellbore stability challenges in the deep water, Gulf of Mexico: case history examples from the Pompano Field. *In: SPE Annual Technical Conference and Exhibition. Society of Petroleum Engineers, Denver, Colorado.*

Withjack, M. O., & Callaway, S. (2000). Active normal faulting beneath a salt layer: an experimental study of deformation patterns in the cover sequence. *AAPG bulletin*, Vol: 84, pp: 627-651.

Withjack, M. O., Olson, J., & Peterson, E. (1990). Experimental models of extensional forced folds (1). *AAPG Bulletin*, Vol: 74, pp: 1038-1054.

Withjack, M. & Scheiner, C. (1982). Fault patterns associated with domes–an experimental and analytical study. *AAPG Bulletin*, Vol: 66, pp: 302–316.

Woodcock, N. H. (1977). Specification of fabric shapes using an eigenvalue method. *Geological Society of America Bulletin,* Vol: 88, pp: 1231-1236.

Worden, R., & Morad, S. (Eds.). (2009). *Clay mineral cements in sandstones* (Vol. 19). John Wiley & Sons.

Zerwer, A., (1994). Using Borehole Breakouts to Map Horizontal Stress Trajectories in the Gulf of Mexico (MSc thesis). Dept. of Earth Science, University of Waterloo, p. 290.

Zuluaga, L. F., Fossen, H., Ballas, G., & Rotevatn, A. (2017). Structural and petrophysical effects of overthrusting on highly porous sandstones: the Aztec Sandstone in the Buffington window, SE Nevada, USA. *Geological Society, London, Special Publications*, Vol: 459, SP459-8.

Appendix A – Well 22/29-2 Wireline logs

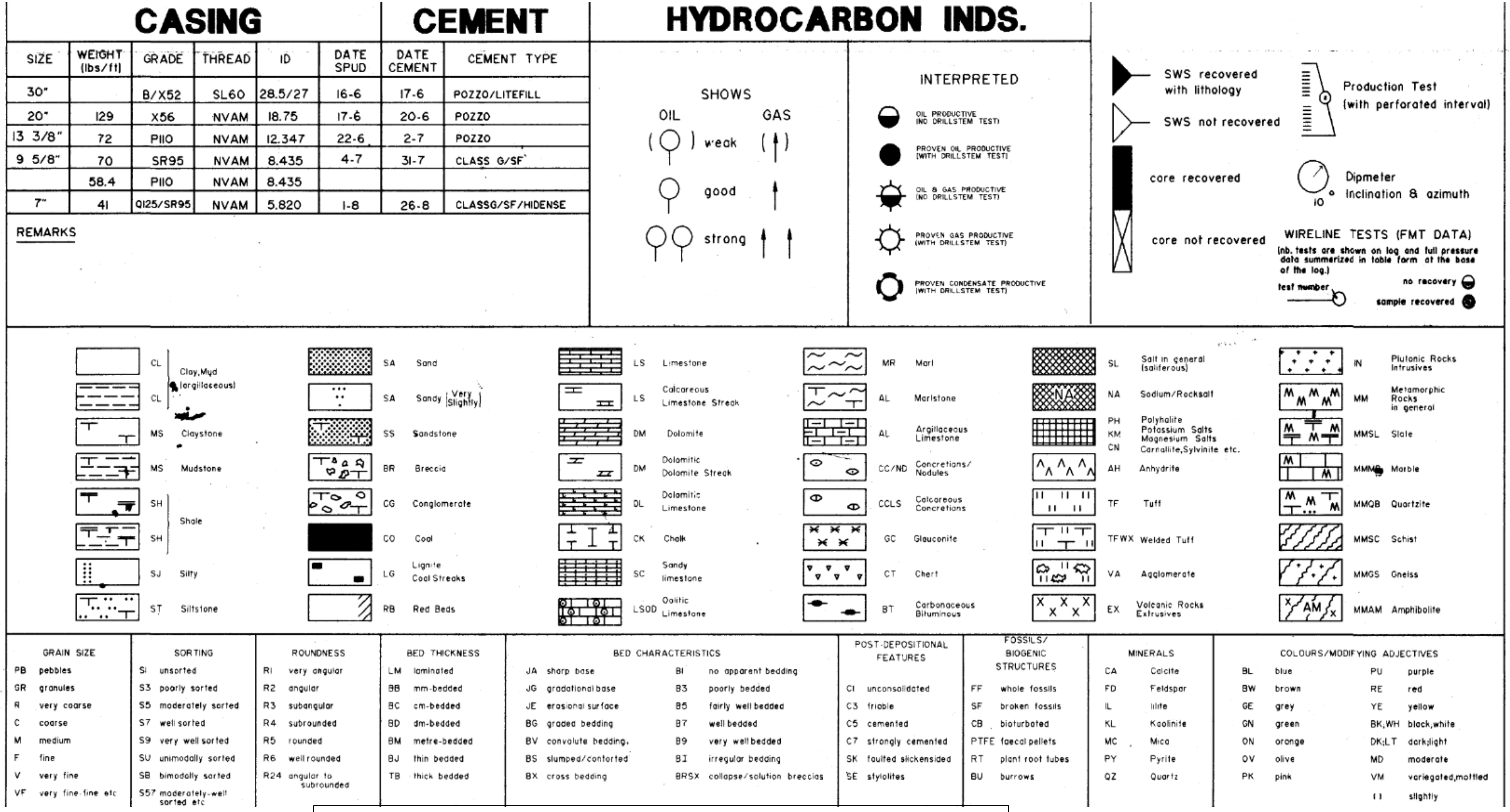

CASING						CEMENT	
SIZE	WEIGHT (lbs/ft)	GRADE	THREAD	ID	DATE SPUD	DATE CEMENT	CEMENT TYPE
30"		B/X52	SL60	28.5/27	16-6	17-6	POZZO/LITEFILL
20"	129	X56	NVAM	18.75	17-6	20-6	POZZO
13 3/8"	72	P110	NVAM	12.347	22-6	2-7	POZZO
9 5/8"	70	SR95	NVAM	8.435	4-7	31-7	CLASS G/SF
	58.4	P110	NVAM	8.435			
7"	41	Q125/SR95	NVAM	5.820	1-8	26-8	CLASSG/SF/HIDENSE

REMARKS

HYDROCARBON INDS.

SHOWS

OIL GAS

weak

good

strong

INTERPRETED

OIL PRODUCTIVE (NO DRILLSTEM TEST)

PROVEN OIL PRODUCTIVE (WITH DRILLSTEM TEST)

OIL & GAS PRODUCTIVE (NO DRILLSTEM TEST)

PROVEN GAS PRODUCTIVE (WITH DRILLSTEM TEST)

PROVEN CONDENSATE PRODUCTIVE (WITH DRILLSTEM TEST)

SWS recovered with lithology

SWS not recovered

core recovered

core not recovered

Production Test (with perforated interval)

Dipmeter Inclination & azimuth

WIRELINE TESTS (FMT DATA)

(nb. tests are shown on log and full pressure data summerized in table form at the base of the log.)

test number

no recovery

sample recovered

CL Clay,Mud
CL (argillaceous)
MS Claystone
MS Mudstone
SH Shale
SH
SJ Silty
ST Siltstone

SA Sand
SA Sandy (Very Slightly)
SS Sandstone
BR Breccia
CG Conglomerate
CO Coal
LG Lignite Coal Streaks
RB Red Beds

LS Limestone
LS Calcareous Limestone Streak
DM Dolomite
DM Dolomitic Dolomite Streak
DL Dolomitic Limestone
CK Chalk
SC Sandy limestone
LSOD Oolitic Limestone

MR Marl
AL Marlstone
AL Argillaceous Limestone
CC/ND Concretions/Nodules
CCLS Calcareous Concretions
GC Glauconite
CT Chert
BT Carbonaceous Bituminous

SL Salt in general (saliferous)
NA Sodium/Rocksalt
PH KM CN Polyhalite Potassium Salts Magnesium Salts Carnallite,Sylvinite etc.
AH Anhydrite
TF Tuff
TFWX Welded Tuff
VA Agglomerate
EX Volcanic Rocks Extrusives

IN Plutonic Rocks Intrusives
MM Metamorphic Rocks in general
MMSL Slate
MMMB Marble
MMQB Quartzite
MMSC Schist
MMGS Gneiss
MMAM Amphibolite

GRAIN SIZE	
PB	pebbles
GR	granules
R	very coarse
C	coarse
M	medium
F	fine
V	very fine
VF	very fine-fine etc

SORTING	
S1	unsorted
S3	poorly sorted
S5	moderately sorted
S7	well sorted
S9	very well sorted
SU	unimodally sorted
SB	bimodally sorted
S57	moderately-well sorted etc

ROUNDNESS	
R1	very angular
R2	angular
R3	subangular
R4	subrounded
R5	rounded
R6	well rounded
R24	angular to subrounded

BED THICKNESS	
LM	laminated
BB	mm-bedded
BC	cm-bedded
BD	dm-bedded
BM	metre-bedded
BJ	thin bedded
TB	thick bedded

BED CHARACTERISTICS			
JA	sharp base	B1	no apparent bedding
JG	gradational base	B3	poorly bedded
JE	erosional surface	B5	fairly well bedded
BG	graded bedding	B7	well bedded
BV	convolute bedding.	B9	very well bedded
BS	slumped/contorted	BI	irregular bedding
BX	cross bedding	BRSX	collapse/solution breccias

POST-DEPOSITIONAL FEATURES	
C1	unconsolidated
C3	friable
C5	cemented
C7	strongly cemented
SK	faulted slickensided
SE	stylolites

FOSSILS/ BIOGENIC STRUCTURES	
FF	whole fossils
SF	broken fossils
CB	bioturbated
PTFE	faecal pellets
RT	plant root tubes
BU	burrows

MINERALS	
CA	Calcite
FD	Feldspar
IL	Illite
KL	Kaolinite
MC	Mica
PY	Pyrite
QZ	Quartz

COLOURS/MODIFYING ADJECTIVES			
BL	blue	PU	purple
BW	brown	RE	red
GE	grey	YE	yellow
GN	green	BK;WH	black,white
ON	orange	DK;LT	dark;light
OV	olive	MD	moderate
PK	pink	VM	variegated,mottled
		( )	slightly

Figure A.1: Key and symbols for the wireline log (with resistivity log).

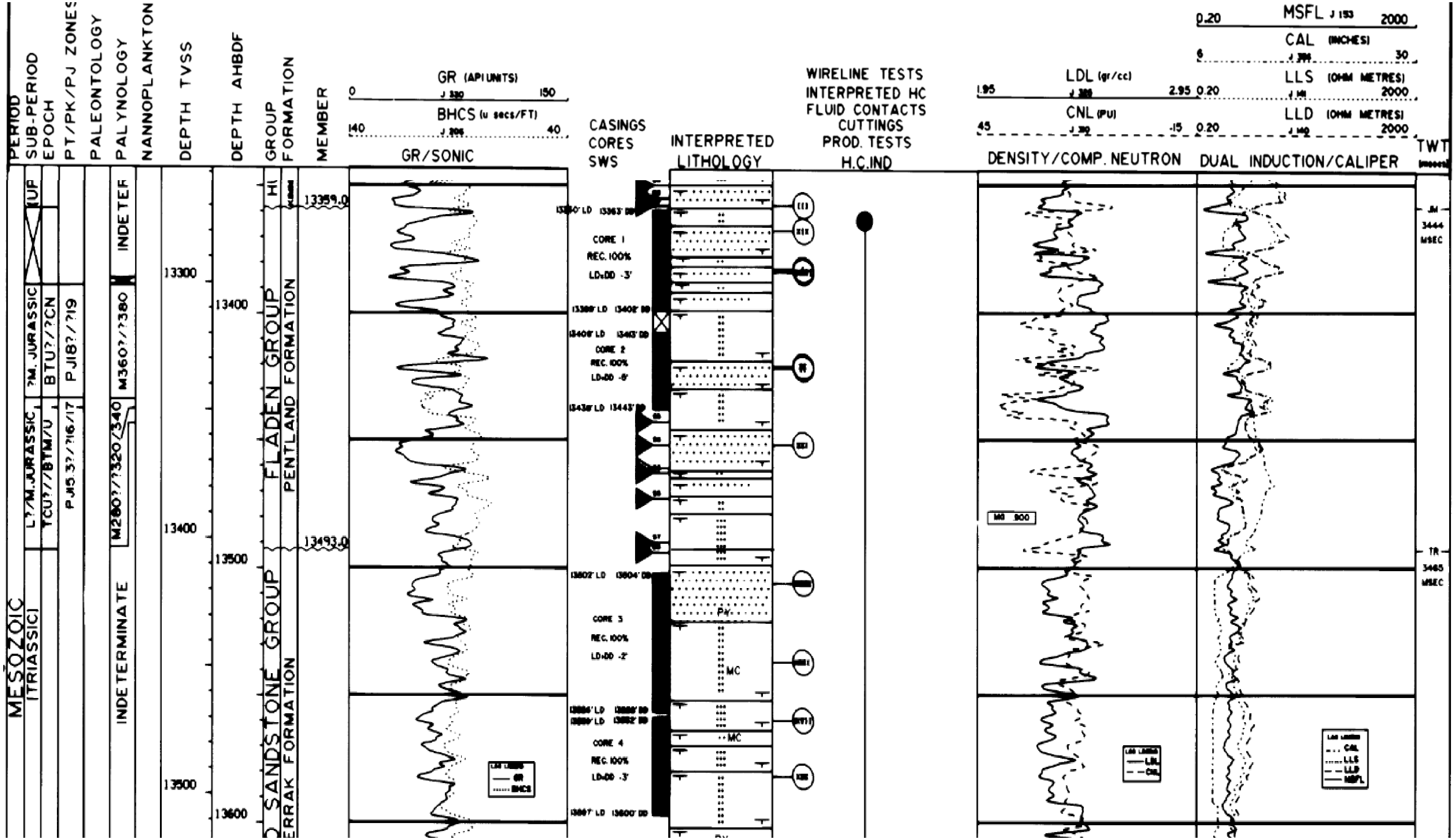

Figure A.2: Snapshot of wireline log for well 22/29-2 core runs 1 – 4 (with resistivity log).

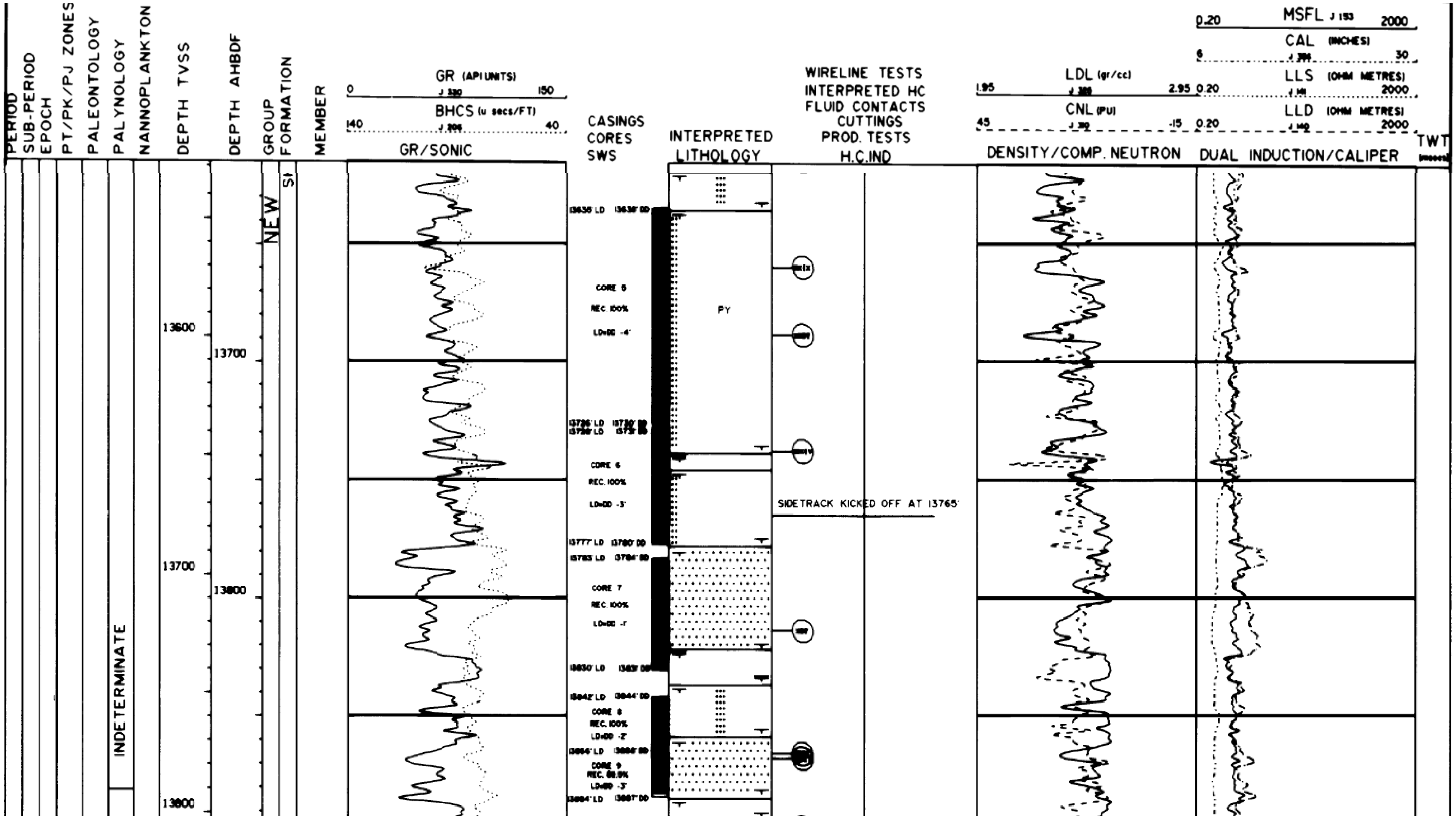

Figure A.3: Snapshot of wireline log for well 22/29-2 core runs 4 - 9 (with resistivity log).

Figure A.4: Key of symbols and lithology types for wireline log with helium porosity and permeability columns.

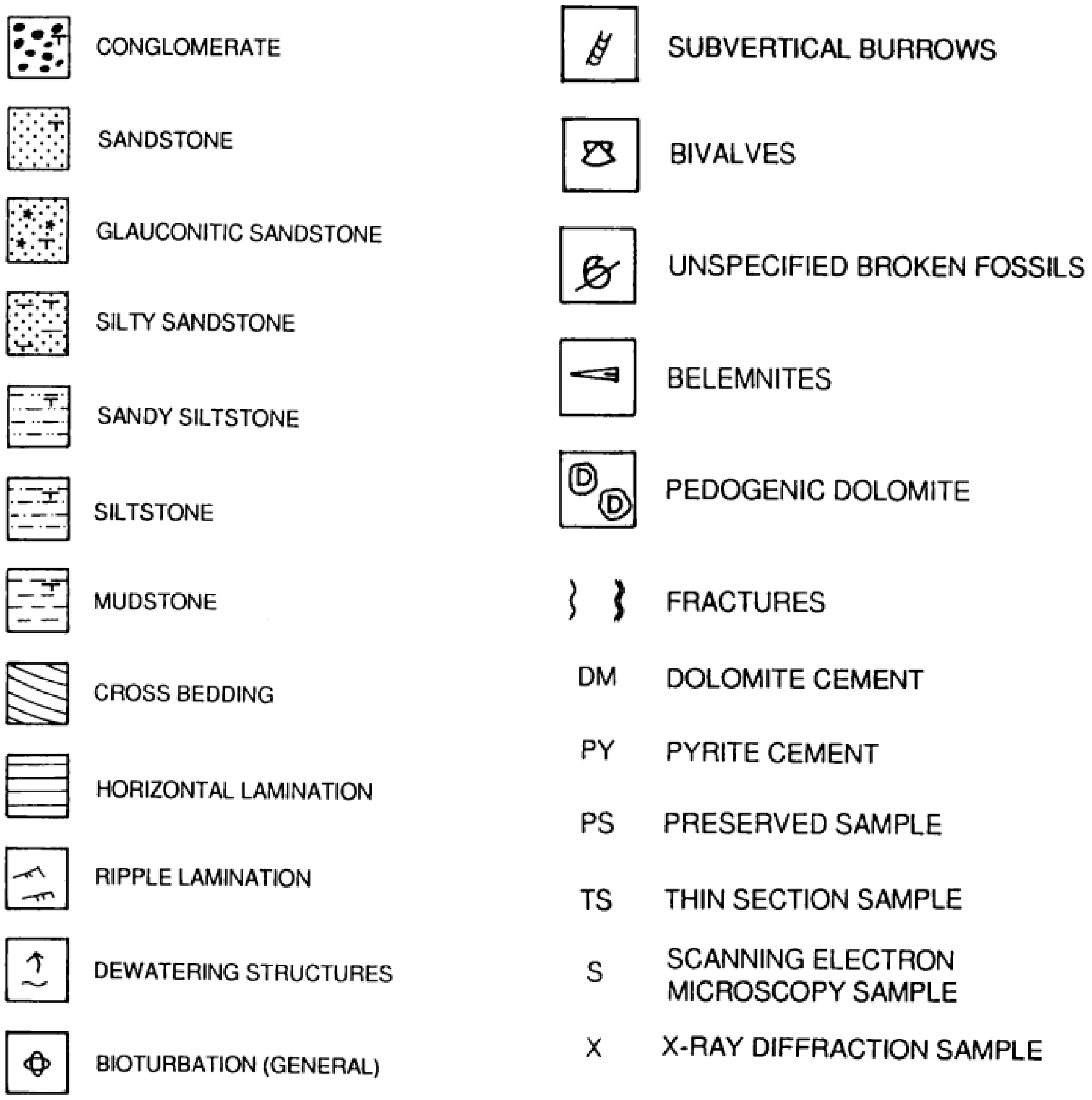

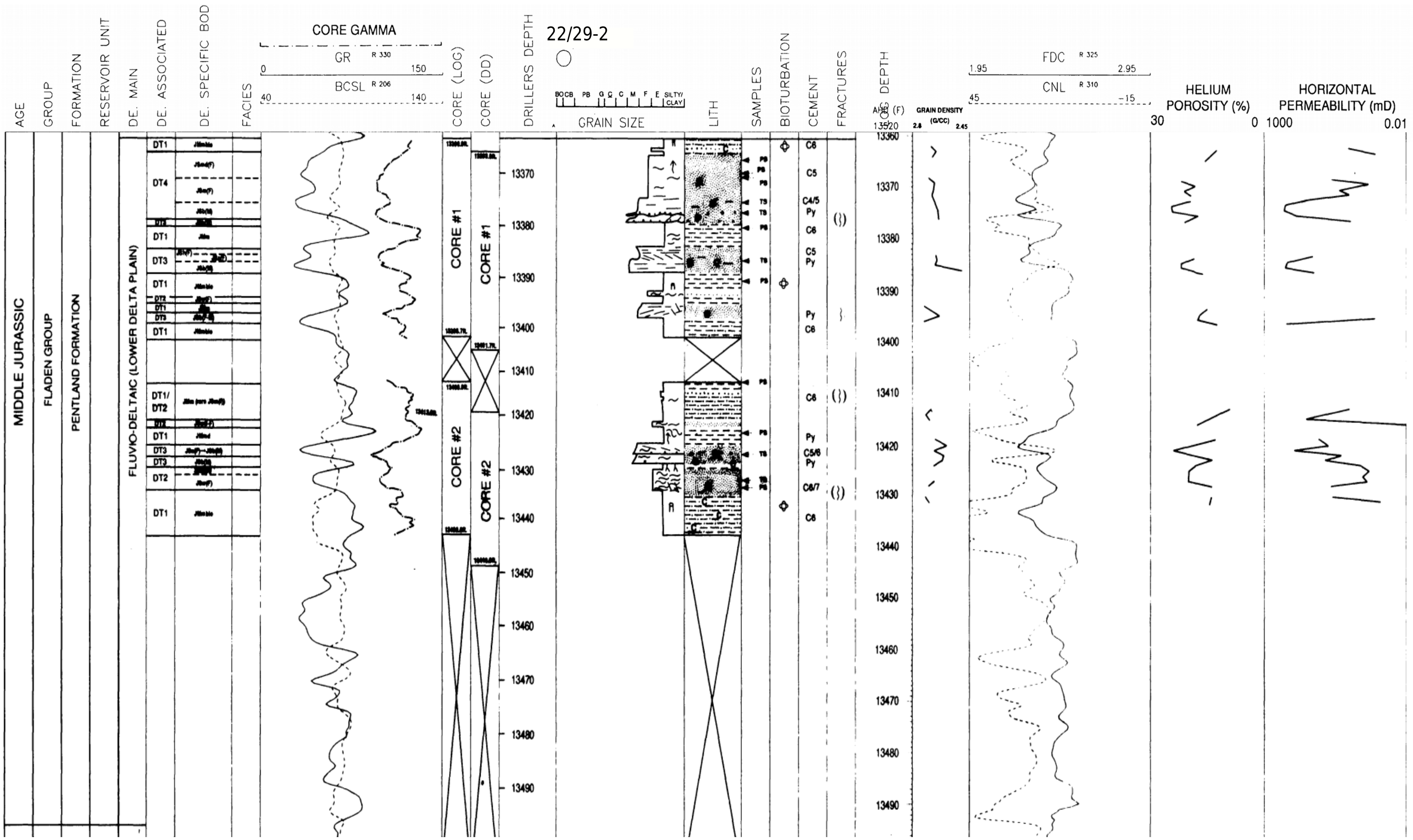

Figure A.4: Snapshot of wireline log for well 22/29-2 core runs 1 & 2 (with porosity log).

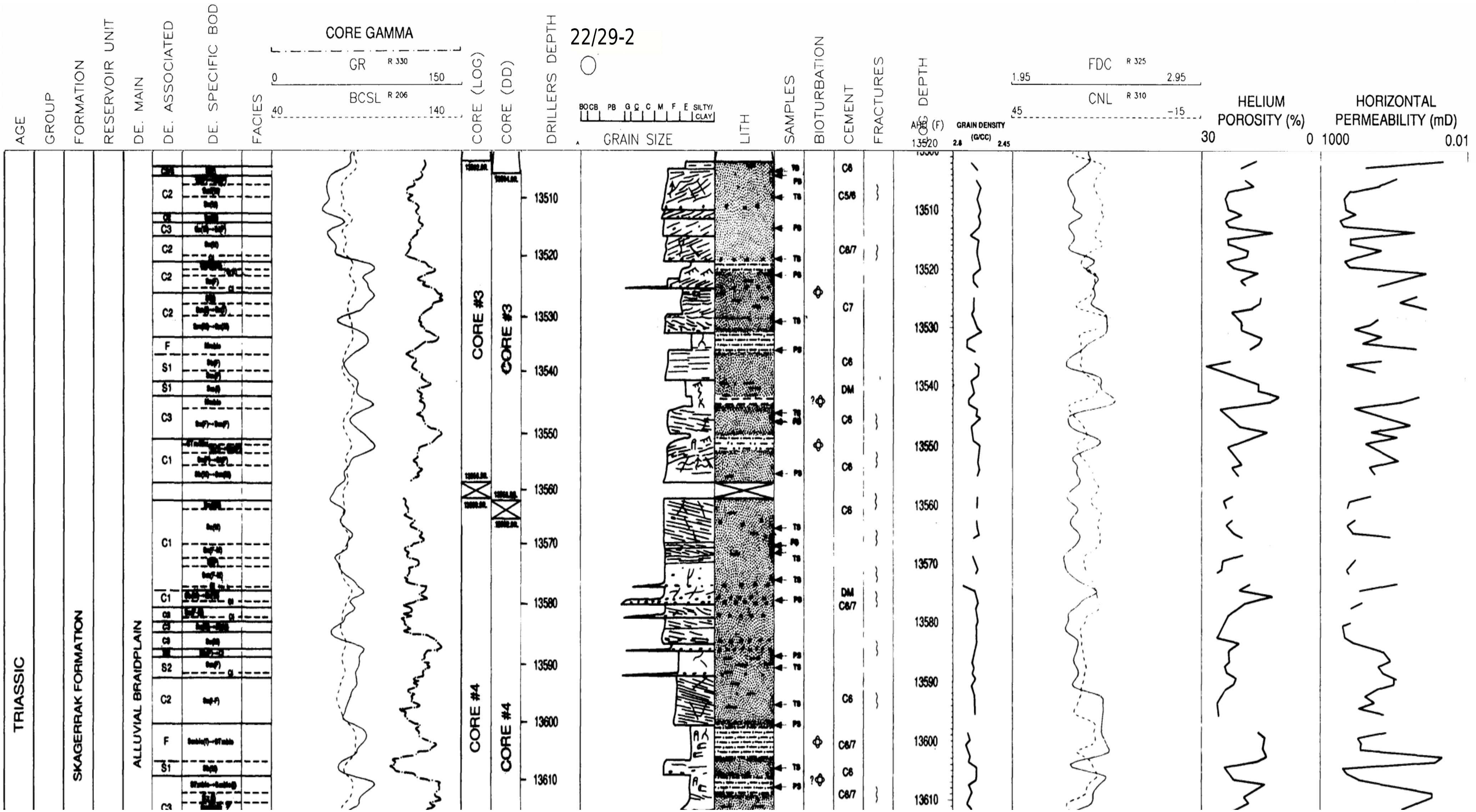

Figure A.5: Snapshot of wireline log for well 22/29-2 core runs 3 & partially 4 (with porosity log).

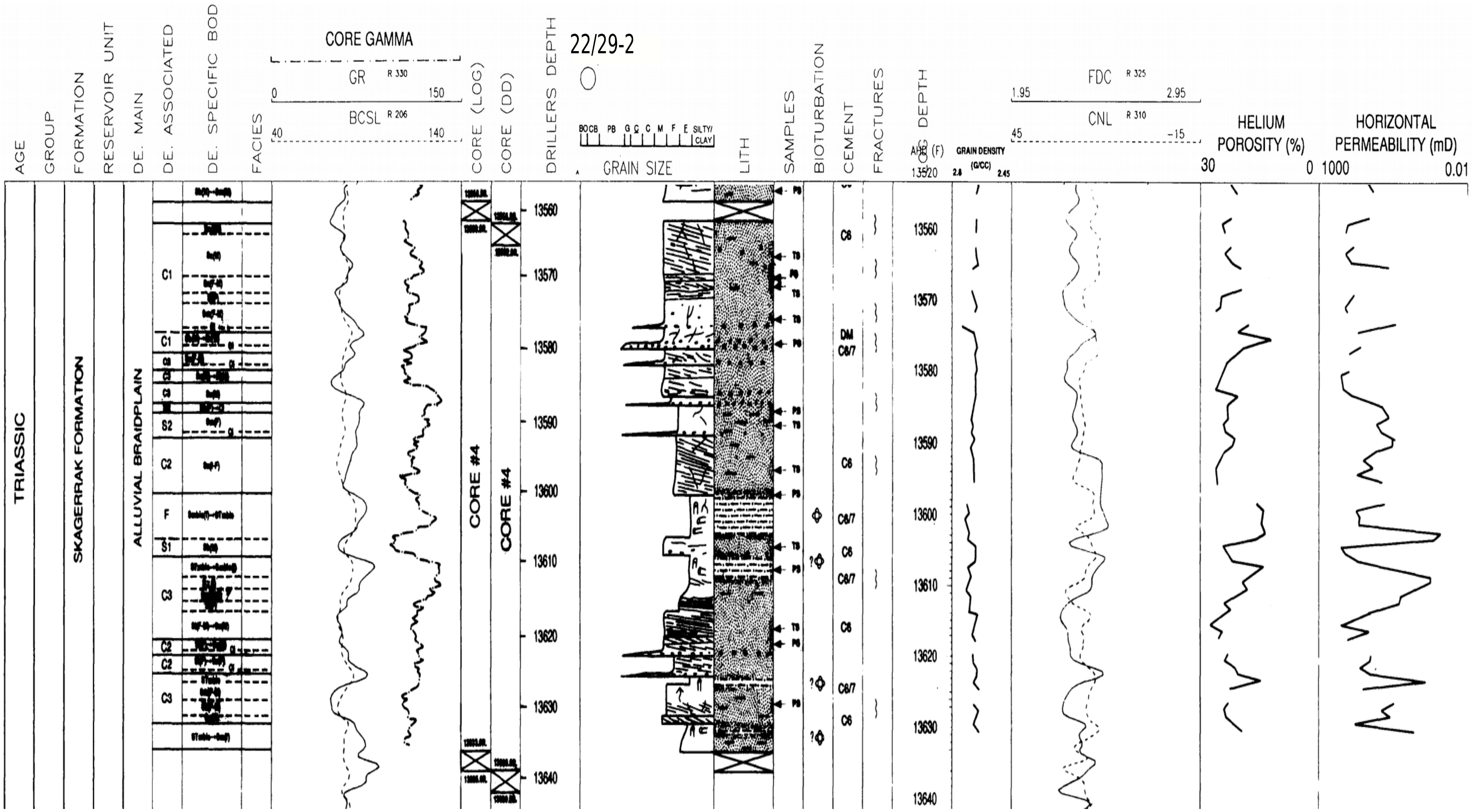

Figure A.6: Snapshot of wireline log for well 22/29-2 core run 4 (with porosity log).

Appendix B – Well 22/29-3 Wireline logs

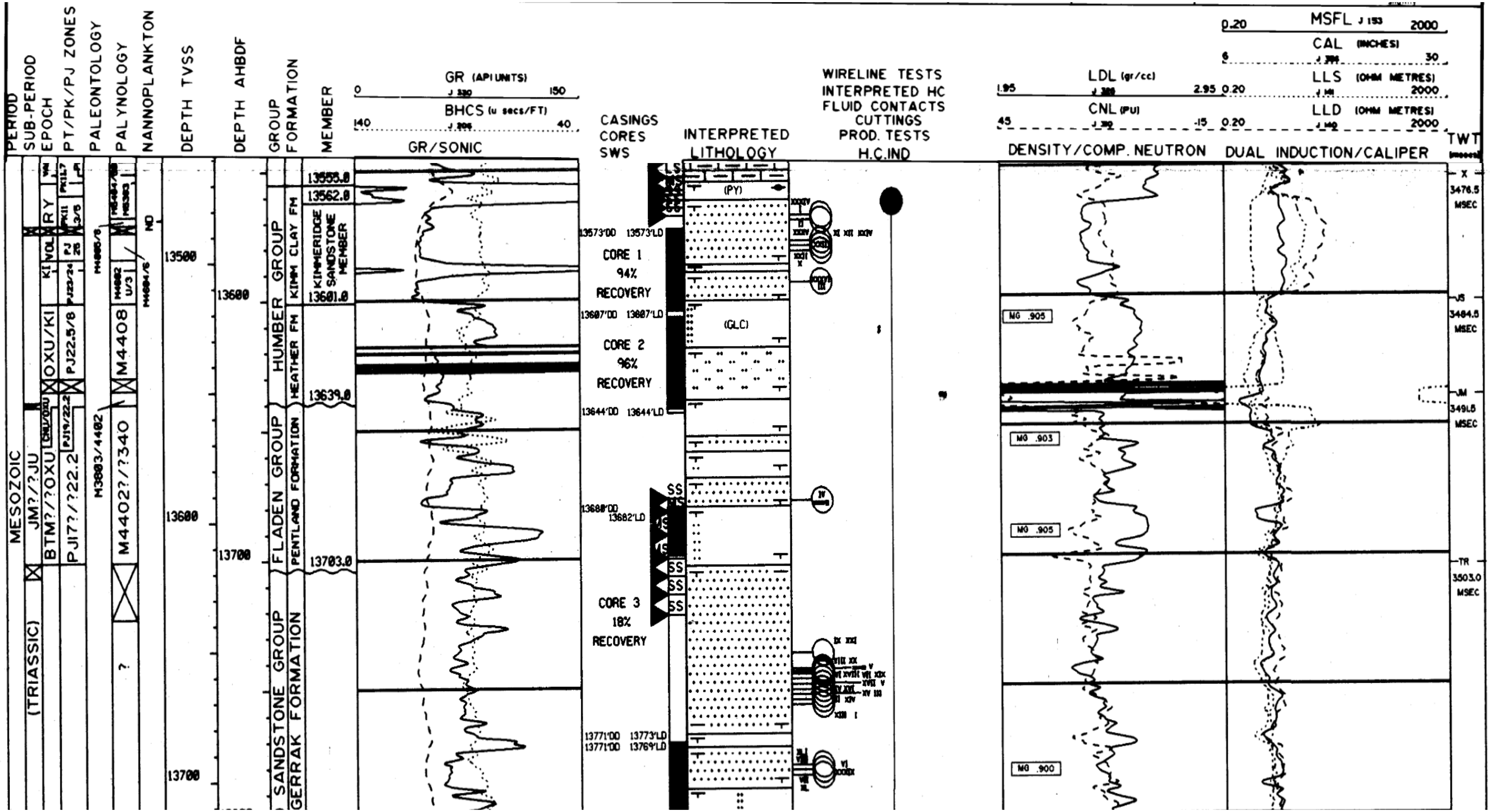

Figure B.1: Snapshot of wireline log for well 22/29-3 core runs 1 - 3 (with resistivity log).

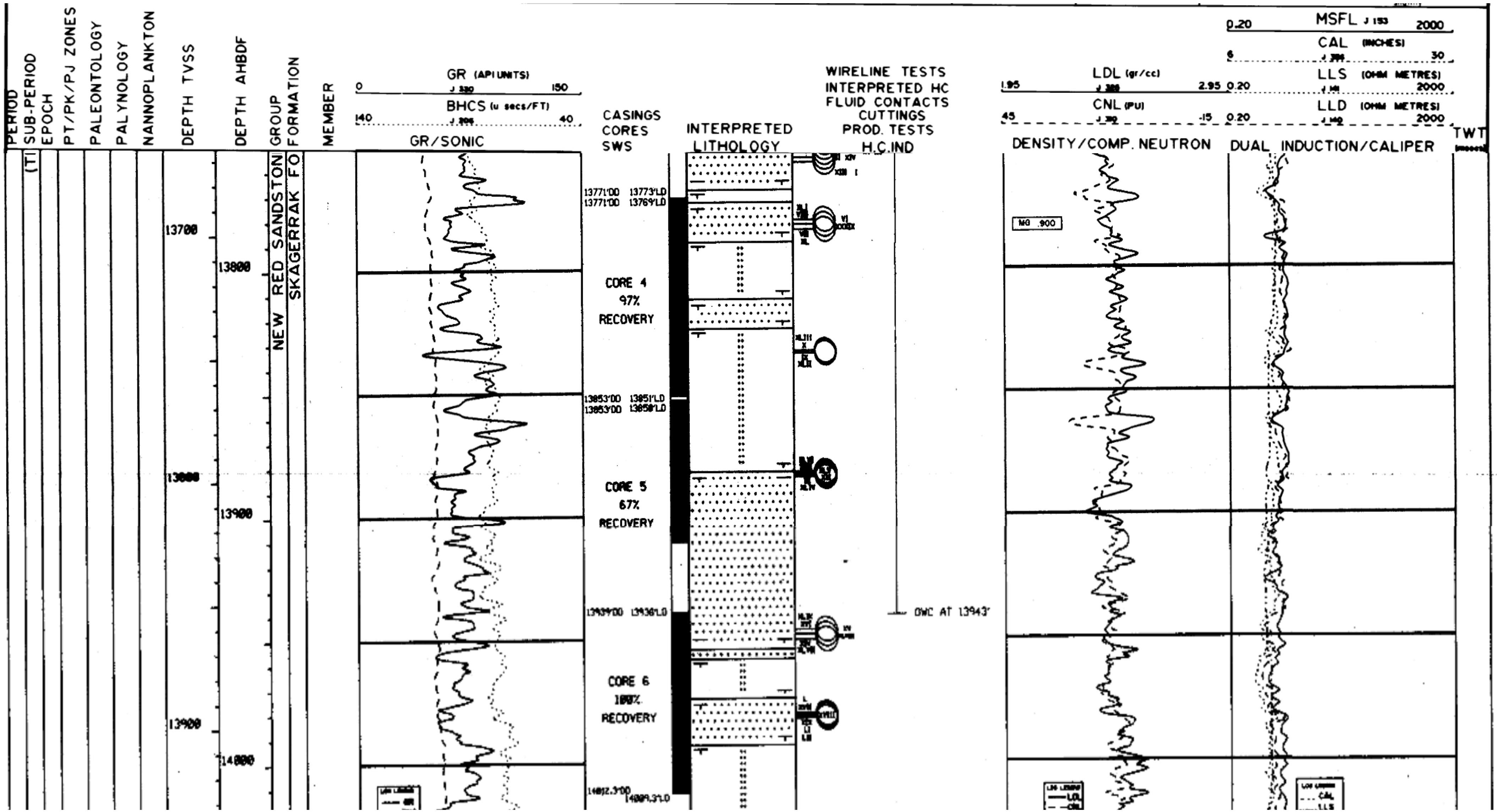

Figure B.2: Snapshot of wireline log for well 22/29-3 core runs 4 - 6 (with resistivity log).

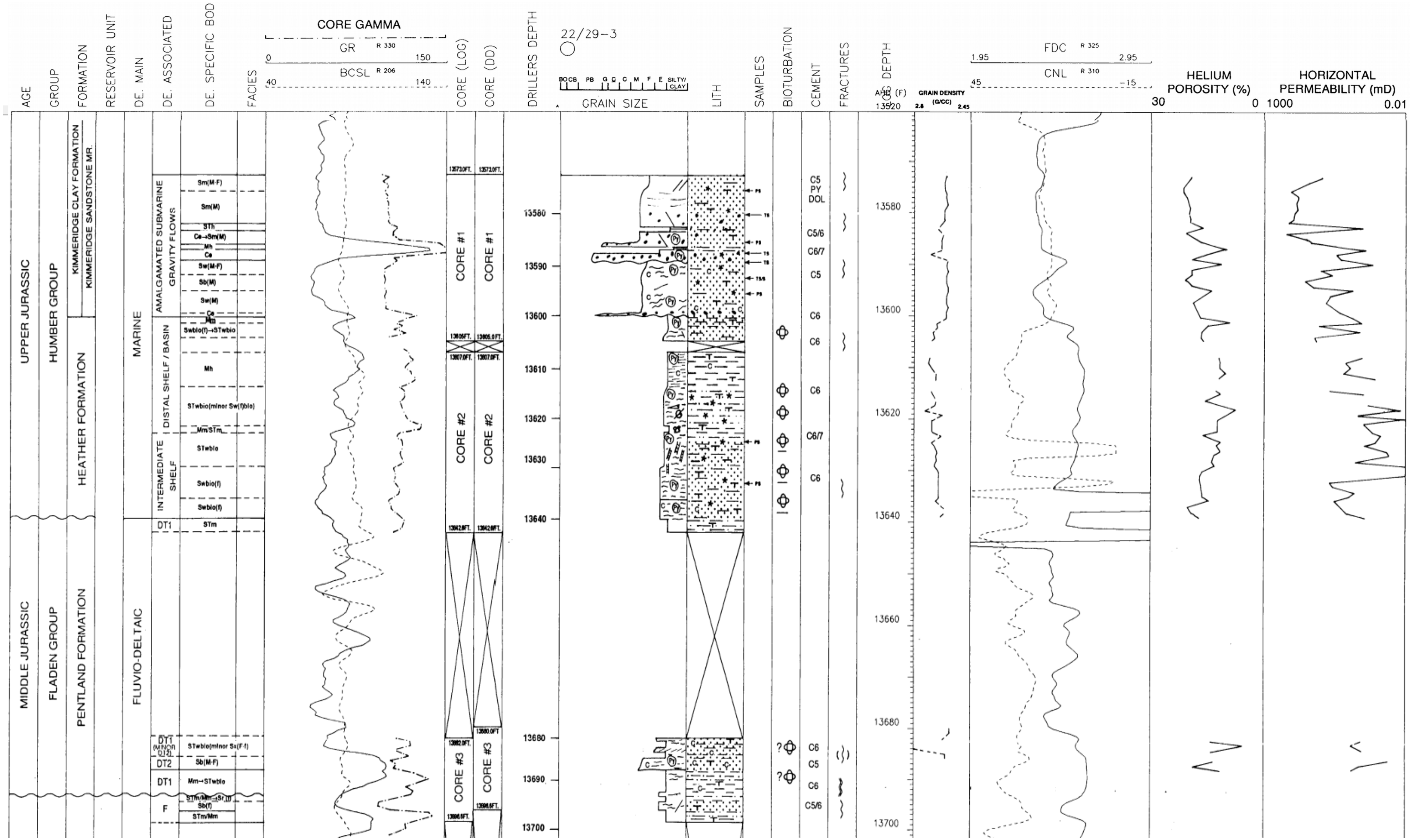

Figure B.3: Snapshot of wireline log for well 22/29-3 core runs 1 - 3 (with porosity log).

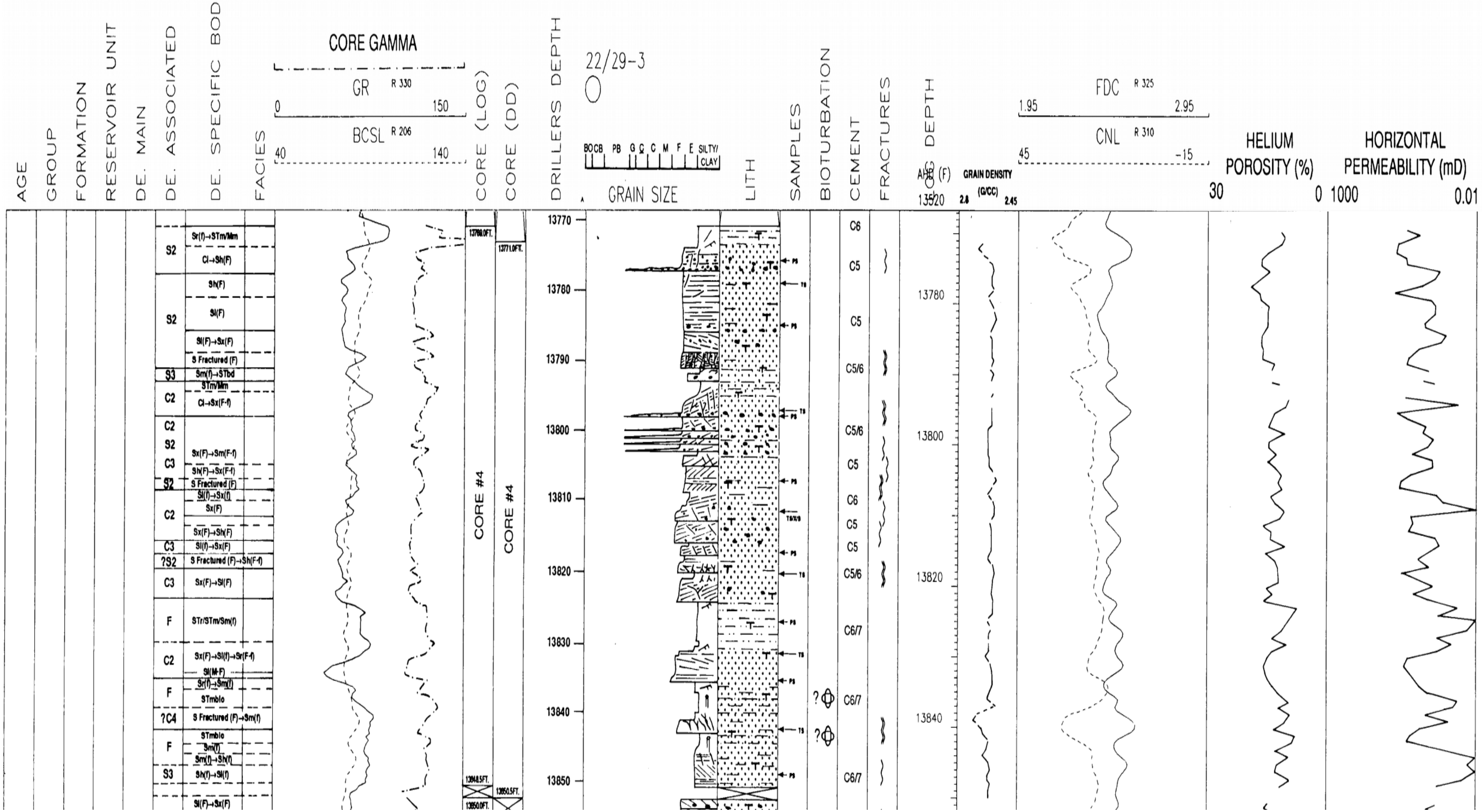

Figure B.4: Snapshot of wireline log for well 22/29-3 core run 4 (with porosity log).

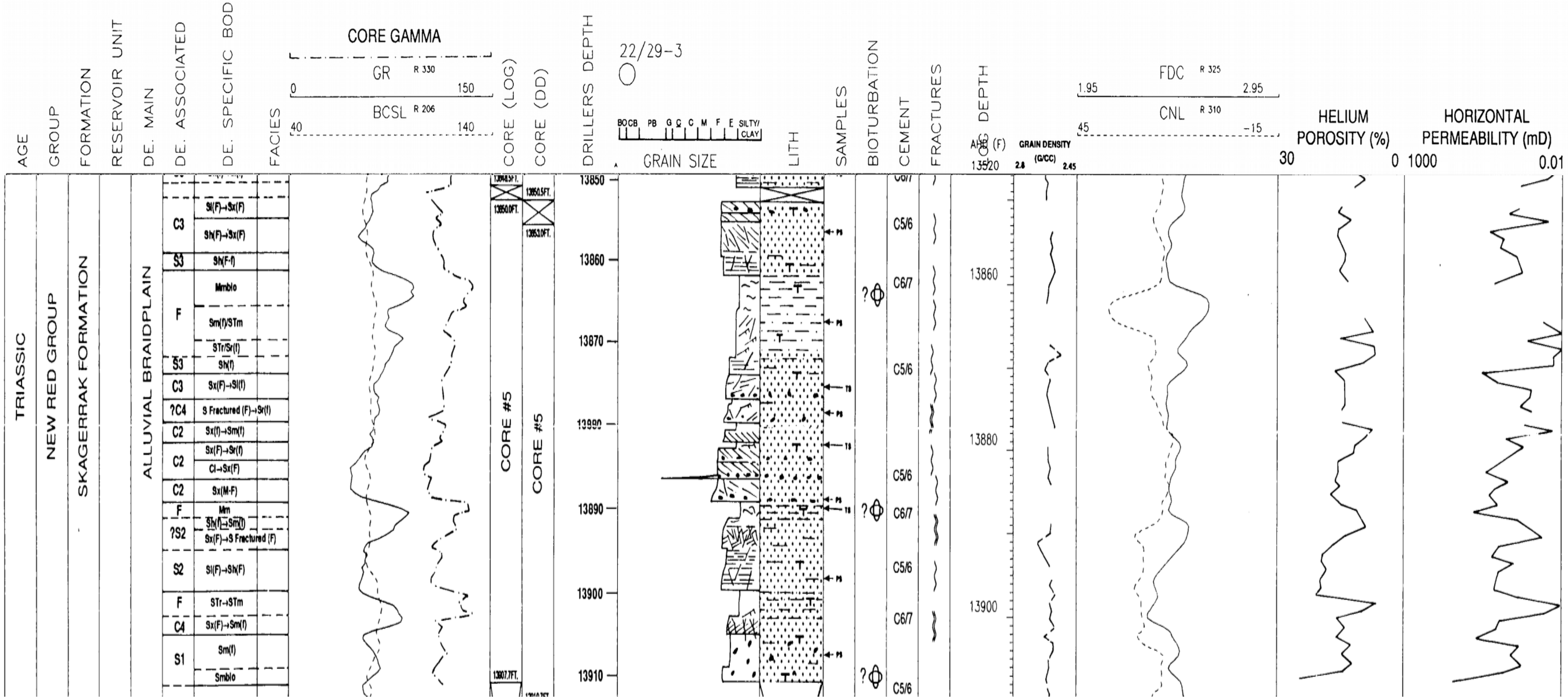

Figure B.5: Snapshot of wireline log for well 22/29-3 core run 5 (with porosity log).

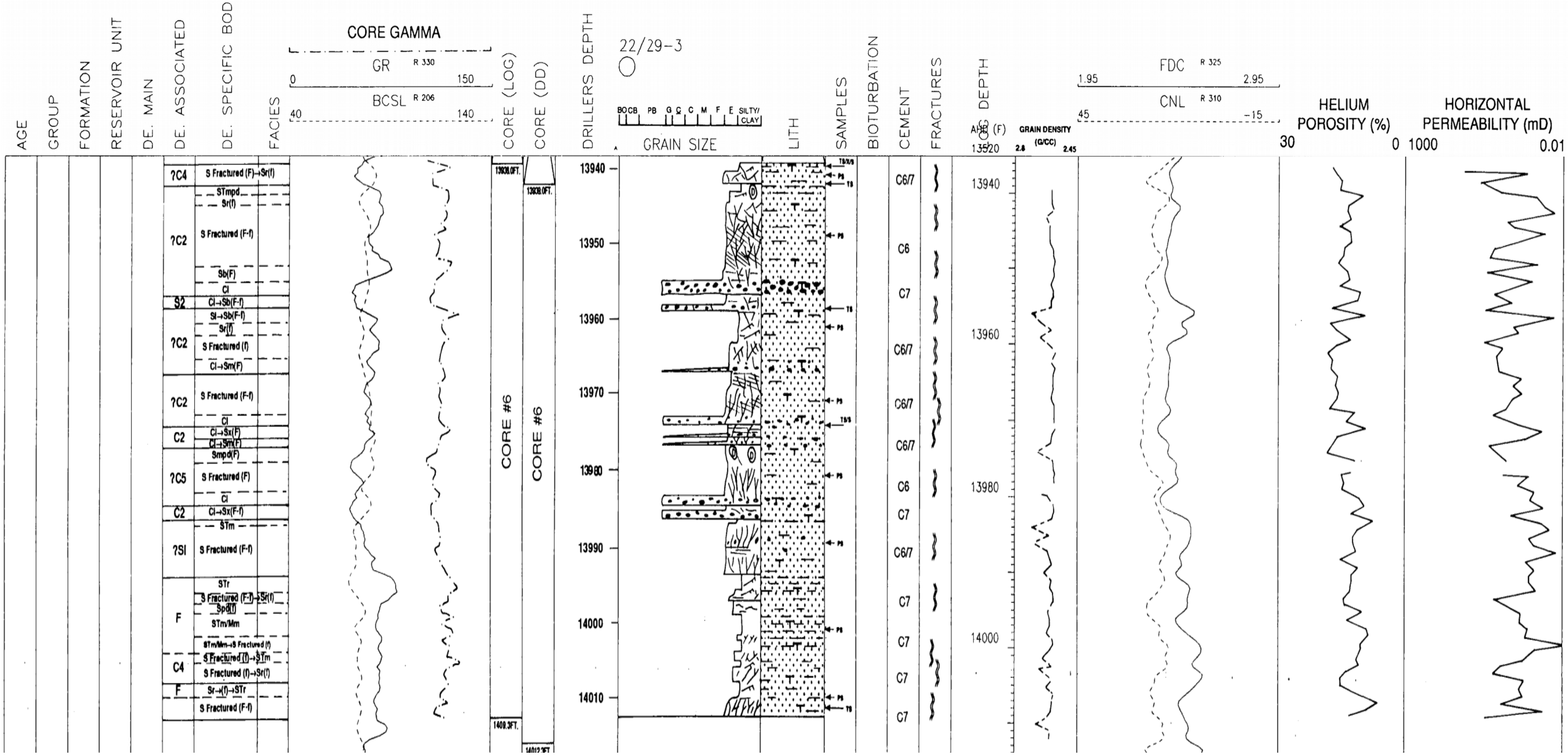

Figure B.6: Snapshot of wireline log for well 22/29-3 core run 6 (with porosity log).

Appendix C – Petrographic and point count data for well 22/29-3 (from Stricker et al., 2018)

Table C.1: Petrographic and point count data for the well 22/29-3 sample set, with sample depth in metre and feet TVDSS, facies type [channel sand (CF), unconfined fluvial (UCF), lacustrine shoreface (LSF)], grain size (GS), coated grains with > 80% coated surface (CG), and point count values for detrital quartz grains (Qtz), detrital feldspar grains (Feld), lithic fragments (Lith), mica (Mica), clay mineral cements (CM), carbonate cements (Carb) and porosity (PPC). (From Stricker et al., 2018).

Depth					Point count (300)						
TVDSS, m	TVDSS, ft	Facies, [–]	GS, mm	CG, %	Qtz, %	Feld, %	Lith, %	Mica, %	CM, %	Carb, %	P_{PC}, %
4172.71	13,690.00	CF	0.154	72.0	47.3	8.3	7.0	2.7	30.0	0.0	4.7
4173.09	13,691.25	CF	0.124	76.0	50.3	10.0	7.7	2.7	28.3	0.3	0.7
4173.78	13,693.50	CF	0.134	78.3	44.0	11.7	6.3	0.7	34.7	0.0	2.7
4174.64	13,696.33	CF	0.121	39.3	49.7	10.3	4.3	3.3	32.3	0.0	0.0
4176.45	13,702.25	CF	0.141	61.6	44.7	9.7	5.0	2.3	35.7	0.3	2.3
4177.54	13,705.83	CF	0.143	40.6	51.7	11.0	7.0	3.0	25.0	0.0	2.3
4180.18	13,714.50	CF	0.146	58.3	45.3	10.0	3.3	5.0	35.0	0.0	1.3
4181.96	13,720.33	CF	0.127		44.7	8.3	3.0	3.7	36.0	0.0	4.3
4185.06	13,730.50	CF	0.189	35.6	54.3	7.7	7.0	0.7	28.3	0.0	2.0
4187.06	13,737.08	CF	0.163	54.0	55.3	6.0	6.3	2.0	27.0	0.0	3.3
4188.89	13,743.08	LSF	0.097		33.3	16.7	0.3	7.3	36.0	0.0	6.3
4190.72	13,749.08	UCF	0.210	44.3	49.7	14.7	5.3	2.7	20.0	0.0	7.7
4192.63	13,755.33	LSF	0.096	56.0	37.0	17.7	6.7	4.3	29.7	0.0	4.7
4194.05	13,760.00	LSF	0.120		39.7	8.0	4.7	7.3	35.0	0.0	5.3
4195.42	13,764.50	CF	0.142		39.3	20.3	3.3	13.3	21.7	0.0	2.0
4196.79	13,769.00	CF	0.167		40.7	11.3	7.3	7.0	33.0	0.0	0.7
4201.54	13,784.58	LSF	0.107		39.0	17.3	1.3	3.3	38.7	0.3	0.0
4203.29	13,790.33	UCF	0.127		44.0	13.7	4.7	2.3	34.7	0.0	0.7
4205.33	13,797.00	CF	0.163		43.3	9.7	12.0	3.3	30.7	0.3	0.7
4206.90	13,802.17	CF	0.183		45.3	14.7	6.0	4.0	29.7	0.0	0.3
4209.34	13,810.17	CF	0.153	86.0	55.0	11.7	6.7	1.3	24.0	0.0	1.3
4210.58	13,814.25	CF	0.146	98.3	42.7	16.3	5.7	3.3	28.0	0.0	4.0
4213.86	13,825.00	LSF	0.159	96.0	42.0	17.7	5.3	1.3	27.0	0.0	6.7
4226.18	13,865.42	CF	0.114		42.0	22.3	4.0	3.3	24.7	0.0	3.7
4231.16	13,881.75	CF	0.109		37.7	19.7	3.0	2.7	29.3	5.3	2.3
4232.45	13,886.00	CF	0.118		43.3	27.3	2.3	3.0	17.3	0.0	6.7
4234.10	13,891.42	CF	0.123	99.0	37.0	27.3	4.3	3.0	21.3	0.0	7.0
4235.63	13,896.42	CF	0.165		42.3	16.0	11.3	3.7	24.3	0.3	2.0
4237.76	13,903.42	UCF	0.115		45.3	16.3	5.3	1.3	31.7	0.0	0.0

Appendix D – Well 22/29-3 Core Goniometry Data

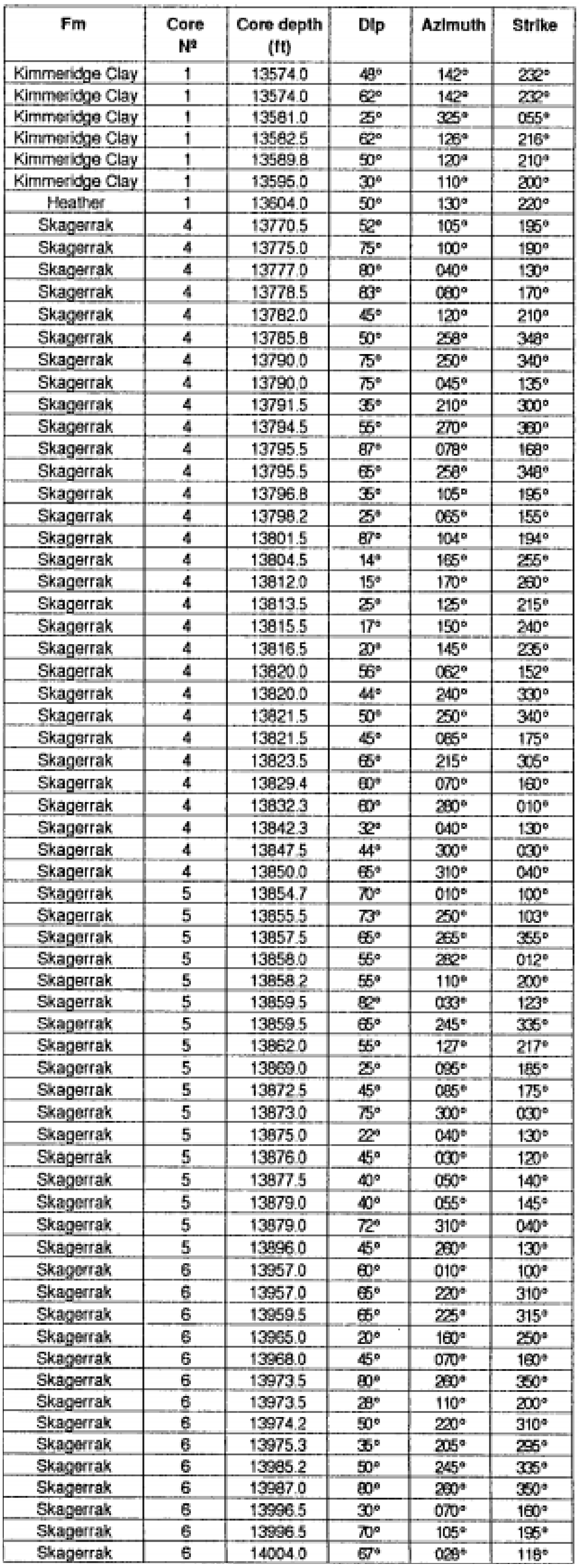

Fm	Core Nº	Core depth (ft)	Dip	Azimuth	Strike
Kimmeridge Clay	1	13574.0	48°	142°	232°
Kimmeridge Clay	1	13574.0	62°	142°	232°
Kimmeridge Clay	1	13581.0	25°	325°	055°
Kimmeridge Clay	1	13582.5	62°	126°	216°
Kimmeridge Clay	1	13589.8	50°	120°	210°
Kimmeridge Clay	1	13595.0	30°	110°	200°
Heather	1	13604.0	50°	130°	220°
Skagerrak	4	13770.5	52°	105°	195°
Skagerrak	4	13775.0	75°	100°	190°
Skagerrak	4	13777.0	80°	040°	130°
Skagerrak	4	13778.5	83°	080°	170°
Skagerrak	4	13782.0	45°	120°	210°
Skagerrak	4	13785.8	50°	258°	348°
Skagerrak	4	13790.0	75°	250°	340°
Skagerrak	4	13790.0	75°	045°	135°
Skagerrak	4	13791.5	35°	210°	300°
Skagerrak	4	13794.5	55°	270°	360°
Skagerrak	4	13795.5	87°	078°	168°
Skagerrak	4	13795.5	65°	258°	348°
Skagerrak	4	13796.8	35°	105°	195°
Skagerrak	4	13798.2	25°	065°	155°
Skagerrak	4	13801.5	87°	104°	194°
Skagerrak	4	13804.5	14°	165°	255°
Skagerrak	4	13812.0	15°	170°	260°
Skagerrak	4	13813.5	25°	125°	215°
Skagerrak	4	13815.5	17°	150°	240°
Skagerrak	4	13816.5	20°	145°	235°
Skagerrak	4	13820.0	56°	062°	152°
Skagerrak	4	13820.0	44°	240°	330°
Skagerrak	4	13821.5	50°	250°	340°
Skagerrak	4	13821.5	45°	085°	175°
Skagerrak	4	13823.5	65°	215°	305°
Skagerrak	4	13829.4	60°	070°	160°
Skagerrak	4	13832.3	60°	280°	010°
Skagerrak	4	13842.3	32°	040°	130°
Skagerrak	4	13847.5	44°	300°	030°
Skagerrak	4	13850.0	65°	310°	040°
Skagerrak	5	13854.7	70°	010°	100°
Skagerrak	5	13855.5	73°	250°	103°
Skagerrak	5	13857.5	65°	265°	355°
Skagerrak	5	13858.0	55°	282°	012°
Skagerrak	5	13858.2	55°	110°	200°
Skagerrak	5	13859.5	82°	033°	123°
Skagerrak	5	13859.5	65°	245°	335°
Skagerrak	5	13862.0	55°	127°	217°
Skagerrak	5	13869.0	25°	095°	185°
Skagerrak	5	13872.5	45°	085°	175°
Skagerrak	5	13873.0	75°	300°	030°
Skagerrak	5	13875.0	22°	040°	130°
Skagerrak	5	13876.0	45°	030°	120°
Skagerrak	5	13877.5	40°	050°	140°
Skagerrak	5	13879.0	40°	055°	145°
Skagerrak	5	13879.0	72°	310°	040°
Skagerrak	5	13896.0	45°	260°	130°
Skagerrak	6	13957.0	60°	010°	100°
Skagerrak	6	13957.0	65°	220°	310°
Skagerrak	6	13959.5	65°	225°	315°
Skagerrak	6	13965.0	20°	160°	250°
Skagerrak	6	13968.0	45°	070°	160°
Skagerrak	6	13973.5	80°	260°	350°
Skagerrak	6	13973.5	28°	110°	200°
Skagerrak	6	13974.2	50°	220°	310°
Skagerrak	6	13975.3	35°	205°	295°
Skagerrak	6	13985.2	50°	245°	335°
Skagerrak	6	13987.0	80°	260°	350°
Skagerrak	6	13996.5	30°	070°	160°
Skagerrak	6	13996.5	70°	105°	195°
Skagerrak	6	14004.0	67°	028°	118°

Table D.1: The tabulated core goniometry data for the fractures found in well 22/29-3. From Shell (U.K.) Exploration and Production (1993b)

Appendix E – Well 22/29-3 Tabulated FMI data

Depth (ft.)	Dip	Dip Direction
13819	57	80
13819	57	75
13820	77	190
13821	73	105
13821	40	60
13821	40	65
13821	33	65
13822	50	75
13822	59	250
13822	60	251
13822	52	61
13823	79	269
13852	50	265
13852	50	275
13855	75	45
13855	70	269
13855	70	268
13875	70	252
13875	70	253
13871	56	27
13871	70	41
13873	42	30
13873	71	295
13874	60	263
13875	45	15
13876	49	79
13876	70	12
13876	59	5
13876	51	252
13948	50	258
13948	42	227
13949	40	231

13949	23	234
13950	19	265
13950	69	176
13950	31	250
13951	55	329
13951	30	269
13952	28	267
13953	76	312
13954	60	44
14002	69	27
14003	60	34
14004	61	36
14004	61	37
14005	70	215
14005	50	44
14007	70	45

Appendix F – Well 22/29-2S1 Tabulated FMI data

Depth (ft.)	Dip Direction	Dip
13500	225	64
	66	67
	250	62
	251	65
	260	70
13510	20	35
	27	47
	38	48
	115	41
13550	357	75
13560	24	68
	229	55
	149	75
13570	243	60
	181	51
	215	59
	182	66
13590	238	46
13600	223	54
13620	217	72
	199	73
13630	212	56
	228	49
13650	239	76
13660	226	41
	14	67
13680	139	42
	226	65
13700	56	51
13710	275	35
13720	126	41
	305	59
	306	60
	124	76
13740	346	62

13750	39	50
	15	42
	224	36
13760	43	59
	84	59
13770	349	68
	334	70
	230	61
	223	55
	281	58
13780	254	51
	238	63
	270	75
	251	6
13790	338	42
	335	41
13800	245	69
	229	75
	349	55
	19	54
13810	152	65
	45	60
	28	39
	249	50
	231	48
	225	63
	226	62
13820	135	72
13840	109	60
13850	212	51
	225	48
13860	219	56
	224	40
	230	51
	245	60
	334	53

13890	91	24
	105	60
	75	59
	69	64
13930	291	46
	205	51
14040	249	51
	242	55
14080	38	48
14120	43	64
	48	65
	39	75
14130	223	59
	229	58
14160	199	62
14170	52	68
14180	231	51
	241	70
	231	75
14310	38	67
14330	68	56
	31	61
	71	61
14340	223	62
	65	57
	231	41
	219	38
	262	61
14350	63	27
	220	40
	122	48
	79	51
	64	56
14360	37	33
	220	82
	45	59

	113	48
	115	49
	42	72
	222	80
14390	215	81
	53	69
	42	71
	315	49
14400	64	52
14410	218	65
14420	52	52
	49	40
	45	36
	249	78
14430	55	55
	61	50
	73	45
	203	78
	279	73
	253	74
	218	61
	221	51
	217	50
	250	37
14440	224	47
	281	79
	251	41
	259	44
	243	47
	163	46
	172	56
14450	249	35
	223	74
	278	47
	231	36
	242	28

14460	216	65
14470	221	62
	225	48
	205	45
	217	41
	220	31
	251	28
14480	262	26
	222	80
	243	75
	219	54
14490	185	64
	227	65
	219	66
	273	69
	10	45
	231	45
	228	42
	243	40
	261	50
	234	53
	239	52
	242	57
14500	228	78
14510	51	76
	251	45
	225	61
	220	51
	218	47
	252	56
	231	40
14520	222	29
	235	64
	225	67
	226	69
14530	220	56

	230	27
	259	45
	246	55
	250	51
14540	221	45
	32	16
	204	30
	248	20
14560	230	71
	223	55
14570	210	65
	225	61
	175	58
	215	55
	208	60
14580	235	34
	240	41
	268	56
14590	224	31
	219	35
	249	39
	240	32
	195	75
	250	59
	230	51
	245	32
	222	35
	239	38
	201	35
	223	43
14600	245	41
	230	39
	273	38
	220	26
	232	59
	225	49

	229	41
	221	34
	225	33
14610	69	17
	115	15
	185	30
	221	39
	225	40
	230	47
14630	222	49